NEUTRON SCATTERING CROSS SECTION AND ANALYZING POWER MEASUREMENTS FOR ^{208}Pb FROM 6 TO 10 MeV AND OPTICAL MODEL ANALYSES

by

Mark L. Roberts

Department of Physics
Duke University

Date: 23 November 1988

Approved:

Richard L Walter
Richard L. Walter, Supervisor

Frank DeLucia

Dissertation submitted in partial fulfillment of
the requirements for the degree of Doctor
of Philosophy in the Department of
Physics in the Graduate School
of Duke University

1988

ABSTRACT

(Physics-Nuclear)

NEUTRON SCATTERING CROSS SECTION AND ANALYZING POWER MEASUREMENTS FOR ^{208}Pb FROM 6 TO 10 MeV AND OPTICAL MODEL ANALYSES

by

Mark L. Roberts

Department of Physics
Duke University

Date: 23 November 1988

Approved:

Richard L Walter
Richard L. Walter, Supervisor

Werner Tornow

Frank DeLucia

Henry R Weller

An abstract of a dissertation submitted in partial fulfillment
of the requirements for the degree of Doctor
of Philosophy in the Department of
Physics in the Graduate School
of Duke University

1988

ABSTRACT

NEUTRON SCATTERING CROSS SECTION AND ANALYZING POWER MEASUREMENTS FOR ^{208}Pb FROM 6 TO 10 MeV AND OPTICAL MODEL ANALYSES

by

Mark L. Roberts

Differential cross sections and analyzing powers have been obtained for the scattering of neutrons from the ground and first excited states of ^{208}Pb. These new measurements include differential cross sections for elastic and inelastic neutron scattering at 8.0 MeV, and analyzing powers for elastic and inelastic neutron scattering at 6.0, 7.0, 8.0, 9.0, and 10.0 MeV. These data complement earlier work performed at Triangle Universities Nuclear Laboratory (TUNL) for elastic scattering of neutrons from ^{208}Pb at 10.0, 14.0, and 17.0 MeV. All data were obtained using the TUNL pulsed beam facility and time-of-flight spectrometer. The data have been corrected for the effects of finite geometry, flux attenuation, and multiple scattering. The present elastic scattering data have been combined with the previously measured TUNL data and data measured elsewhere in order to obtain a detailed and high accuracy data set for neutron elastic scattering from ^{208}Pb over the 4.0 to 40.0 MeV energy range. This comprehensive data set has been described using the spherical optical model in which constant geometry fits, energy-dependent geometry fits, and fits incorporating the dispersion relation were performed. Although the overall description of the elastic n+^{208}Pb scattering data was reasonably good using the various optical potentials, small systematic discrepancies remained at the backward angles of both the cross section and analyzing power data, and no optical model solution based on conventional Woods-Saxon form factors was found which could describe all of the details seen in the scattering data. To relax the constraint of having a Woods-Saxon form factor, the real central part of the optical model potential was modified using a Fourier-Bessel expansion of the real central potential. Individual fits at 6.0, 7.0, 8.0, 9.0, and 10.0 MeV, and fits to the combined 6.0 to 10.0 MeV data set were obtained using a Fourier-Bessel expansion of the real central potential and compared to fits using a conventional Woods-Saxon form factor.

ACKNOWLEDGMENTS

It is doubtful that any graduate student has ever written a dissertation totally alone. Somewhere along the line, he had assistance; often that assistance is great. This dissertation is no exception.

First, I would like to thank my research advisor, Dr. Richard L. Walter, for the help and guidance he has given me throughout my graduate career at Duke University. I am indebted to Dr. Calvin Howell for his insight and knowledge of pulsed beam techniques and general workings of the Laboratory. I am grateful to Dr. Werner Tornow for his help and advice, including discussions regarding optical model potentials, dispersion relations, and Fourier-Bessel expansions of the optical potential. A special thanks to Dr. Thomas Clegg for his supervision and help concerning the polarized ion source. I would also like to acknowledge Dr. Dan Horen for his suggestions and frequent discussions.

I would like to especially thank the members of the neutron time-of-flight group who participated in these experiments and without whom these often time consuming measurements could not have been made: Dr. Harold Pfützner, Dr. Kim Murphy, Paul Felsher, Anli Li, Gary Weisel, and M. AlOhali.

A special thanks to the staff of TUNL. Sidney Edwards and Patrick Mulkey are acknowledged for their help in electronic design and continuing efforts to repair electronics faster than they can be broken. Bob Rummel and Paul Carter are recognized for maintaining and repairing equipment in the Laboratory. I am also grateful to Alton Lovette for his patience and help in building new apparatus and repairing broken accelerator parts. I am also indebted to Karen Mitchell and Kathryn Carpenter for their help in proofreading this manuscript.

Last, but most importantly, I would like to thank my wife and family for their continuous support and encouragement.

This work was supported in part by the United States Department of Energy, Office of High Energy and Nuclear Physics, under Contract No. DE-AC05-76ER01067.

TABLE OF CONTENTS

LIST OF FIGURES

LIST OF TABLES

CHAPTER I

INTRODUCTION

The nuclear optical model potential has long been a fundamental tool in nuclear physics for analyses of nucleon-nucleus elastic scattering data. Although the optical model contains a large number of adjustable parameters, experience has shown that elastic nucleon scattering data over a wide range of target nuclei and incident nucleon energies can be described in terms of global optical model potentials in which the various optical model parameters show a smooth and sensible variation with energy and with the neutron and proton number of the target nucleus.

While nucleon scattering from many nuclei has been studied, there has recently been a great deal of interest in determining the precise energy dependence and geometry of the n+^{208}Pb optical potential (Johnson 1987, Mahaux 1987, and Annand 1985). For a single-nucleus study, the interaction of neutrons with ^{208}Pb has several theoretically and experimentally attractive features. First, because ^{208}Pb is "doubly-magic" in the formalism of the shell model (i.e., both proton and neutron shells are closed), it is expected that the ground state of the ^{208}Pb nucleus is nearly spherical. This property suggests that nucleon elastic-scattering data from ^{208}Pb are ideally suited for analyses using the spherical optical model. Second, since the neutron-nucleus interaction is not complicated by the effects of the long range Coulomb force, as is the proton-nucleus interaction, neutron scattering from ^{208}Pb gives direct information about the strong interaction. Third, there is a relatively large energy separation between the ground and first excited states of ^{208}Pb. This large energy separation (2.614 MeV) is important for neutron time-of-flight experiments where energy resolution can be a limiting factor.

In the recent parametrizations of the n+^{208}Pb optical model potential, however, gross features have been established mainly from analyses of differential and total cross section data. While high accuracy differential cross section measurements place severe constraints on the various optical model parameters, certain ambiguities can only be resolved by detailed measurements of analyzing powers. Therefore, in order to better determine the details of the n+^{208}Pb optical model potential, analyzing powers and one complementary differential cross section have been obtained for the scattering of neutrons from the ground and first excited states of ^{208}Pb. These new measurements include the differential cross section for elastic and inelastic neutron scattering at 8.0 MeV, and analyzing powers for elastic and inelastic neutron scattering at 6.0, 7.0, 8.0, 9.0, and 10.0 MeV. All data were obtained using the Triangle Universities Nuclear Laboratory (TUNL) pulsed beam facility and time-of-flight spectrometer. These data complement earlier work performed at TUNL by Floyd (Floyd 1981) for elastic scattering of neutrons from ^{208}Pb at 10.0, 14.0, and 17.0 MeV. The data have been corrected for the effects of finite geometry, flux attenuation, and multiple scattering. At 6.0 and 7.0 MeV the elastic scattering analyzing power data were also adjusted for compound nucleus contributions using the observed cross sections and calculated compound nucleus cross sections reported by Annand *et al.* (Annand 1985). Although the inelastic scattering data will not be used in the present analyses, cross sections and analyzing powers for inelastic neutron scattering from the first excited state of ^{208}Pb ($J^{\pi}=3^{-}$, Q=-2.614 MeV) are reported since the data would be appropriate for future descriptions of n+^{208}Pb scattering in the coupled-channels formalism.

The present n+^{208}Pb elastic scattering data have been combined with the ^{208}Pb differential cross section and analyzing power data previously measured at TUNL (Floyd 1981), ^{208}Pb differential cross section data from Ohio (Annand 1985, Finlay 1984, and Rapaport 1978) and Michigan State University (DeVito 1979), and ^{nat}Pb (52% ^{208}Pb) total cross section data (Larson 1980) to obtain a detailed and high accuracy data set for neutron elastic scattering from Pb from 4.0 to 40.0 MeV. This comprehensive n+Pb data set, hereafter referred to as the n+^{208}Pb data set, has been described using the spherical optical model in which constant geometry fits, energy-dependent geometry fits, and fits incorporating the dispersion relation were performed. The dispersion relation, which connects the real and imaginary parts of the optical potential, allows extrapolation of the scattering potential to negative energies so that energy dependences can be further tested by comparing predicted single-particle bound state energies to values extracted from measurements. Comparisons of the newly derived optical model parametrizations were also made to those of existing n+^{208}Pb optical models.

Although the overall description of the elastic n+^{208}Pb scattering data was reasonably good using the various optical potentials, small systematic discrepancies remained at the backward angles for both the cross section and analyzing power, and no optical model solution based on conventional Woods-Saxon form factors was found which could describe all of the details seen in the scattering data. To relax the constraint of having a Woods-Saxon form factor, the real central part of the optical model potential was modified using a Fourier-Bessel expansion of the real central potential. Individual fits at 6.0, 7.0, 8.0, 9.0, and 10.0 MeV and fits to the combined 6.0 to 10.0 MeV data set were obtained using a Fourier-Bessel expansion of the real central potential and compared to fits using a conventional Woods-Saxon form factor.

In addition to the ^{208}Pb data obtained, differential cross sections at 11.01 and 13.76 MeV were measured for the scattering of neutrons to the ground and first excited state of ^{12}C. These ^{12}C data were obtained to provide a confirmation of the 11.05 and 13.75 MeV calibration data obtained at Physikalisch-Technische Bundesanstalt (PTB), Braunschweig, Federal Republic of Germany. These PTB results are in disagreement with the ENDF/B-V (Evaluated Nuclear Data File, Library B, Version V, National Neutron Cross Section Center, Brookhaven National Laboratory, USA) ^{12}C cross section evaluation and call into question earlier data obtained at TUNL and Bruyères-le-Châtel.

CHAPTER II

EXPERIMENTAL TECHNIQUES

A. Introduction

Cross sections $\sigma(\theta)$ and analyzing powers $A_y(\theta)$ were measured using the neutron time-of-flight facilities at Triangle Universities Nuclear Laboratory. With the exception of the ion source used, both types of measurements utilized similar or identical equipment and followed somewhat similar procedures. Since most of the time-of-flight equipment and procedures have been extensively documented in dissertations and publications (Beyerle 1981, El-Kadi 1981 and 1982, Floyd 1981 and 1983, Guss 1982, Hogue 1977, Howell 1984, and Lisowski 1973 and 1975), this work will only give descriptions for techniques that are new or important to the presentation.

A floor plan of the laboratory is shown in Figure 2.1. Ion sources are shown in the upper left-hand corner of the figure, the accelerator in the upper center of the figure, and the neutron time-of-flight room in the lower right-hand corner of the figure.

B. Cross-section measurements

1. Neutron beam production

For the $\sigma(\theta)$ measurements a direct extraction negative ion source was used to produce a 50 keV dc deuteron beam. The deuteron beam was chopped and bunched to obtain a pulsed beam. The chopping and bunching systems will be described in Chapter III. The pulsed deuteron beam was accelerated by a model FN tandem Van de Graaff accelerator. To provide energy determination after acceleration, the deuteron beam was deflected through 38° using an analyzing magnet. Once inside the neutron time-of-flight target room, the pulsed deuteron beam passed through a capacitive pickoff unit (described by Howell (Howell 1984)) and entered a gas cell containing deuterium. The resulting ^{2}H(d,n)^{3}He reaction (Q-value = +3.269 MeV) produced a high intensity cone of nearly monoenergetic neutrons centered around 0°. The ^{2}H(d,n)^{3}He reaction was used as a source of neutrons because the neutrons emitted at 0° are the most energetic neutrons produced in this reaction, the neutron cross section is high at 0°, and both the neutron energy and cross section decrease rapidly with increasing angle.

For the present $\sigma(\theta)$ measurements, the beam of pulsed deuterons typically had a

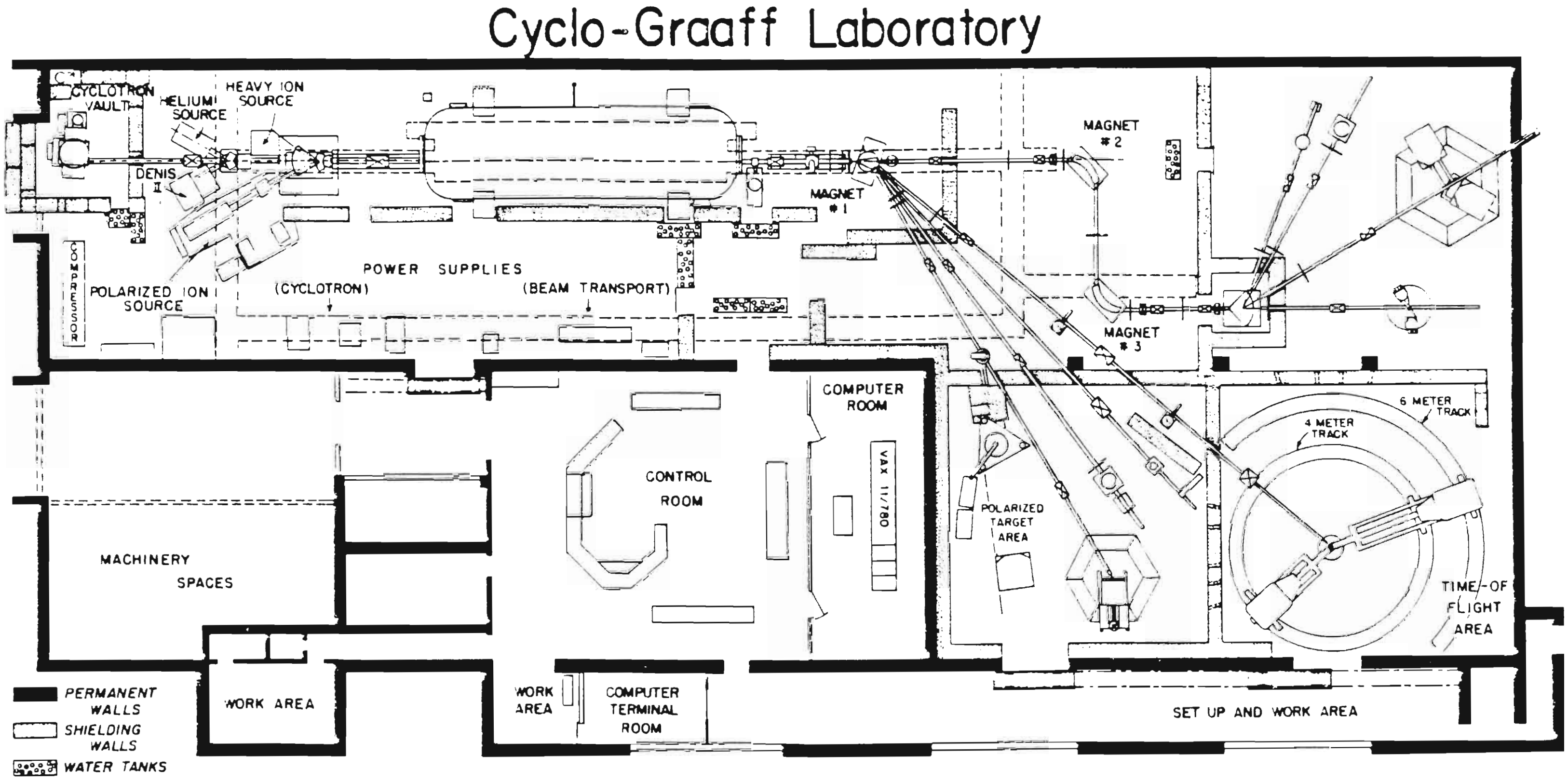

Figure 2.1. Floor plan of the Triangle Universities Nuclear Laboratory

time-averaged intensity of 2 µA. The repetition rate of beam pulses was 2 MHz, and the pulses had a full-width-at-half-maximum (FWHM) of less than 2 ns. Deuterium gas pressures and the beam energy loss in the Havar entrance foil and gas cell for $\sigma(\theta)$ measurements are listed in Table 2.1.

Table 2.1

Deuterium gas cell pressures and beam energy loss calculations for $\sigma(\theta)$ measurements

All energies are in MeV

Neutron Sample	Deuterium Gas Energy	Deuteron Energy at Pressure	Thickness of Havar Cell Center	Energy Loss in Foil	Energy Loss in Havar Foil	Gas Cell
^{12}C	11.050	2.0 atm	7.921	2.54 µm	0.120	0.118
13.810	2.0 atm	10.828	2.54 µm	0.096	0.091	
^{208}Pb	8.000	2.0 atm	4.751	6.35 µm	0.410	0.180

2. Scattering samples

The scattering samples used in the $\sigma(\theta)$ measurements were right circular cylinders suspended by a thin steel wire above the pivot point of the neutron detectors. The scattering samples were located at a reaction angle of 0° for neutrons produced via the ^{2}H(d,n)^{3}He reaction, with the axes of symmetry of the samples perpendicular to the horizontal scattering plane. The distance from the center of the gas cell to the center of the sample was 12.4 cm. Table 2.2 describes the samples used.

Table 2.2

Scattering Sample Parameters

Sample	Mass	Diameter	Height	Isotopic Purity
^{12}C	12.53 g	1.90 cm	2.54 cm	98.9 %
^{208}Pb	116.33 g	2.00 cm	3.25 cm	99.7 %
Polyethylene$^{a)}$		3.37 g	1.44 cm	2.28 cm
^{12}C$^{a)}$	2.91 g	0.95 cm	2.38 cm	99.0 %

a) Used for normalizing data to published n-p cross sections.

3. Neutron detectors

For $\sigma(\theta)$ measurements, the time-of-flight spectrometer facility consisted of two main detectors, a neutron flux monitor, and a pulse timing monitor. The arrangement of the two main detectors relative to the scattering sample is shown in Figure 2.2. All of the detectors were liquid organic scintillators coupled to photomultiplier tubes. The right neutron detector and flux monitor contained NE-218 scintillator fluid, while the left neutron detector and timing monitor contained NE-213 scintillator fluid. Both types of scintillator and associated photomultiplier tubes allowed good pulse-shape discrimination between neutron and γ-ray events.

The main right and left detectors were heavily shielded and mounted on movable carts that could be positioned over an angular range of 0° to 162°. At each angle where a measurement was made, tungsten shadow bars were positioned so that the detector, the front edge of the detector collimator, and much of the detector casing were shielded from the direct flux of source reaction neutrons. The detectors were cylindrical in shape with the detector on the right (i.e., for a neutron scattered to the right side of the incident beam axis) having a diameter of 8.8 cm and the left detector having a diameter of 12.7 cm. Both detectors were 5.08 cm thick. The right and left detectors had adjustable flight paths, where the flight path is defined to be the distance between the center of the sample and the center of the scintillator. The range of flight paths possible for the right detector was 2.77 to 3.76 m, while the range for the left detector was 3.76 to 5.70 m. For ^{12}C $\sigma(\theta)$ measurements, maximum flight paths of 3.76 and 5.70 m were used for both the right and left detectors. For ^{208}Pb $\sigma(\theta)$ measurements, flight paths of 2.92 and 3.89 m were used for the right and left detectors, respectively.

A neutron flux monitor was suspended from the ceiling of the target room and used to monitor the neutron flux from the source reaction. This flux monitor was housed in a copper shield with the cylindrical axis of the detector pointing at the gas cell at an angle of about 50° from the horizontal. The flight path of the flux monitor was about two meters.

The pulse timing monitor, used to monitor the time distribution of neutrons emerging from the gas cell, was located near 0° at a flight path of about four meters. Because the pulse timing monitor was exposed to the direct flux of neutrons produced in the gas cell, count rates in this detector were large and good counting statistics could be obtained in about 60 s. The beam pulsing system was adjusted so that the neutron source reaction peak in the time-of-flight spectrum of the timing monitor had the narrowest time width possible.

4. Detector electronics

Electronic modules were used to measure the time-of-flight of an incident particle, to determine that the energy deposited in the detector due to an event was greater than a

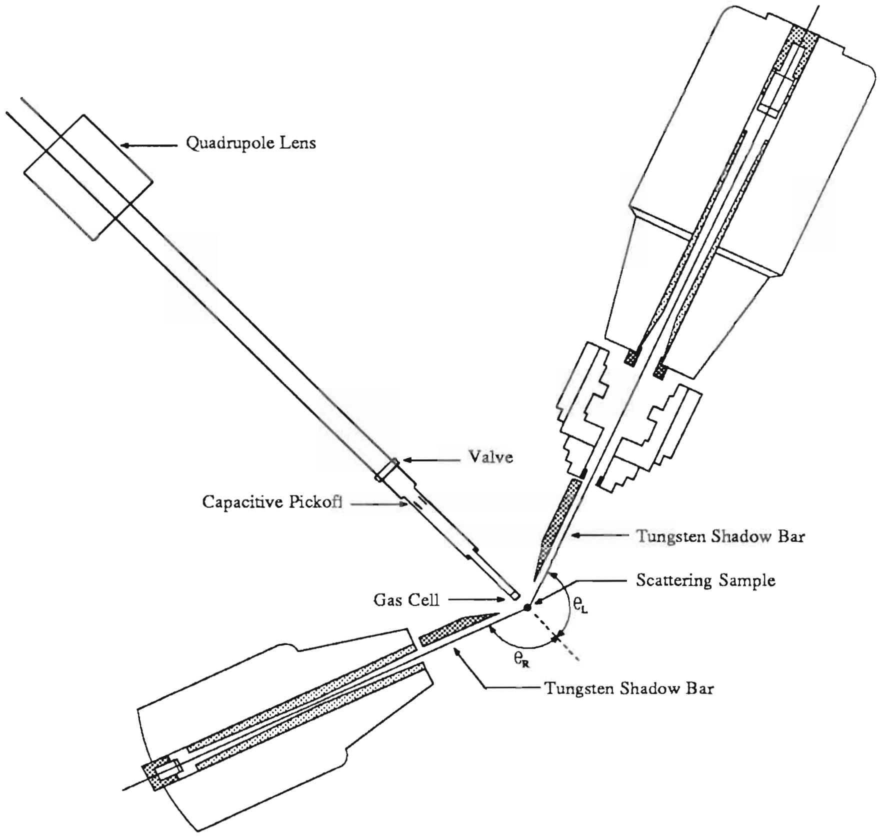

Figure 2.2. Arrangement of the main neutron detectors relative to the scattering sample and beam line for $\sigma(\theta)$ measurements.

specific energy bias, and to determine that the event in the detector was caused by a neutron and not by a γ-ray. For $\sigma(\theta)$ measurements, the four anode signals and the signal from the capacitive pickoff unit were brought from the target area into the control room on 50 Ω low loss cable. Once in the control room, the anode signal from each detector was sent to a different set of identical electronics. A block diagram of the electronics used in $\sigma(\theta)$ experiments is shown in Figure 2.3.

The liquid organic scintillators used for neutron detection at TUNL are of the proton recoil type. In a proton recoil type detector, the incoming neutron transfers some of its energy to a nucleus (usually a proton) in the scintillator via a nuclear interaction. This recoiling nucleus has an energy proportional to the incident neutron energy, with a maximum recoil energy equal to the incident neutron energy. The recoiling nucleus deposits its energy into the scintillator through ionization or excitation, and photons are emitted when the free electrons and cations recombine or when the excited atoms decay into their ground state. These photons eventually exit the scintillator and bombard a photomultiplier tube which generates an electric signal proportional to the energy lost by the recoiling nucleus. To determine that this electric signal was greater than some cutoff level and therefore that the energy deposited in the detector was greater than some chosen energy bias, the incoming photomultiplier anode signal was amplified and fed into a linear amplifier with single channel analyzer (AMP+SCA) module. The SCA of the AMP+SCA module had a lower level threshold, or bias, set to coincide with the approximate energy of the Compton recoil edge produced by 0.662 MeV γ-rays from ^{137}Cs. Signals with amplitudes smaller than this bias did not produce logic pulses, or gates, at the SCA output. This energy bias corresponded to a proton recoil energy of about 2 MeV and helped to reduce backgrounds in the time-of-flight spectra.

Because the liquid organic scintillators used for neutron detection in the present measurements were sensitive to both neutrons and γ-rays, it was necessary to use pulse shape analysis to determine that an event in the detector was caused by a neutron and not by a γ-ray. To discriminate γ-rays from neutrons, the incoming anode signal from each detector was fed into a constant fraction discriminator (CFD) module and a pulse shape discriminator (PSD) module. The CFD produced an output pulse at a constant fraction of the leading edge of the input signal, while the PSD module produced an output pulse at a constant fraction of the trailing edge of the input signal. Because the γ-rays interacted primarily with the electrons and the neutrons interacted primarily with the protons in the scintillator, and since the decay response of the scintillator was different for the low ionizing electrons than for the highly ionizing protons, the decay time of a signal produced by a γ-ray interaction was different than the decay time of a signal produced by

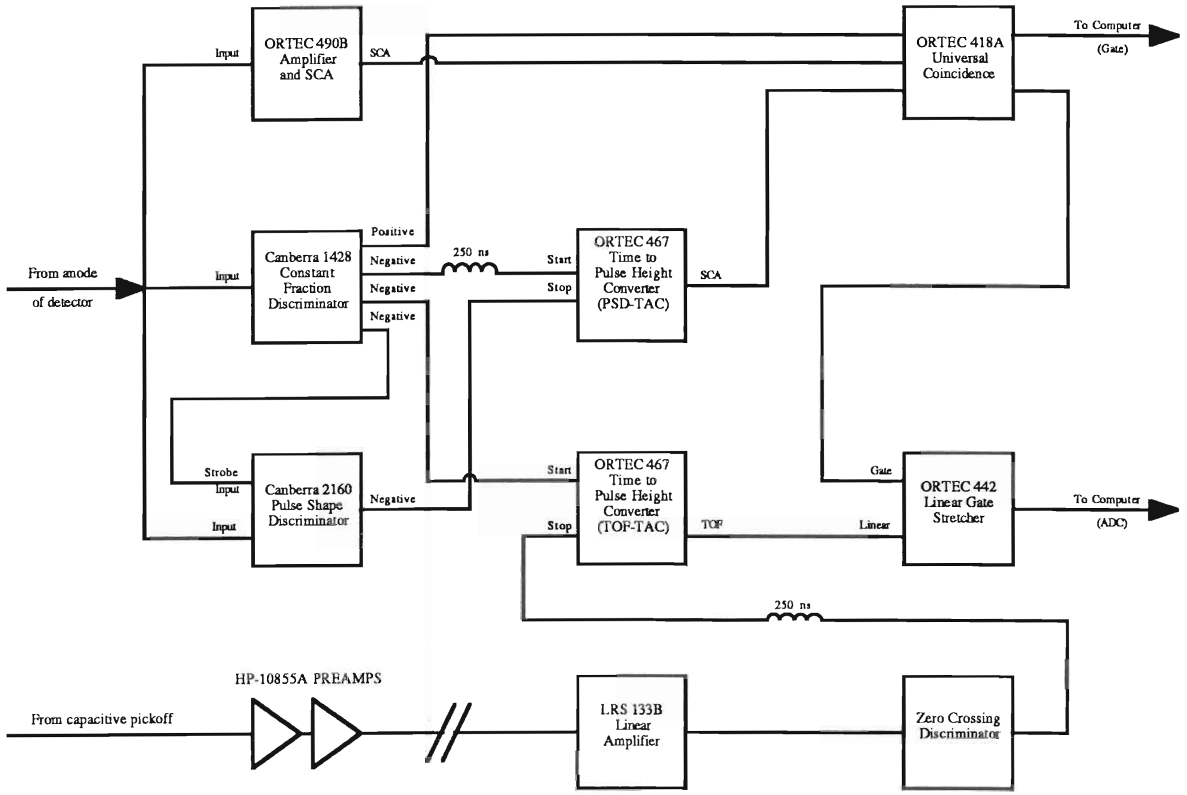

Figure 2.3. Block diagram of the electronics used in $\sigma(\theta)$ measurements.

a neutron interaction. Therefore, the time difference between the output of a signal from the CFD module and the output of a signal from the PSD module was different for γ-rays than for neutrons. To convert this time difference to a voltage, a time to amplitude converter (PSD-TAC) was used that was started by an output of the CFD and stopped by an output of the PSD module. The output voltage of the PSD-TAC was directly proportional to the time difference between the start and stop signals and was different for γ-rays than for neutrons. Since signals produced by the γ-rays had a faster decay time than signals produced by neutrons, the output voltage of the PSD-TAC was lower for γ-rays than for neutrons. A window was set on this output voltage such that only output voltages that corresponded to a valid neutron event would produce a logic pulse or gate.

Time-of-flight information was determined from the time difference between a start and a stop signal. A capacitive beam pickoff signal (obtained from the capacitive beam pickoff located immediately before the gas cell) was amplified and fed into a discriminator to produce a stop signal. This signal was delayed and used to stop a time-to-amplitude converter (TOF-TAC) that was started by a second output of the CFD module. Beam pickoff signals were used as the stop of the TOF-TAC because the capacitive pickoff signals arrived every 500 ns and would have caused the TAC to become paralyzed if used as the start of the TOF-TAC. Signals out of the TOF-TAC had an amplitude linearly related to the time difference between the start and stop signals fed into it and therefore an amplitude linearly related to the TOF of a neutron. The output of the TOF-TAC was shaped by a linear gate stretcher that was gated by the logic output of a universal coincidence module. The universal coincidence module was used to produce a logic output or gate when the input gates from the CFD, SCA, and PSD were in coincidence. The stretched TOF-TAC signals and the logic output from the universal coincidence module were sent to the computer interface where the TOF-TAC signals were digitized by an analog-to-digital converter (ADC).

5. Data acquisition

Data acquisition and storage at TUNL for $\sigma(\theta)$ measurements was controlled using a Digital Equipment Corporation VAX-11/780 computer. The hardware for data acquisition was based on CAMAC modules controlled by a Microprogrammed Branch Driver MBD-11. An overview of the hardware system can be found elsewhere (see Gould 1981, Roberson 1981). Control of the MBD and ADC's, data sorting, online calculations, and graphic displays of spectra was accomplished with the aid of the TUNL XSYStem software package. The XSYStem package contains a set of general purpose commands useful to all experiments performed at TUNL. DEC Command Language programs incorporating these XSYStem commands were written specifically for $\sigma(\theta)$ measurements and were combined into a neutron time-of-flight data acquisition package called NTOF. The programs in NTOF made it possible to set windows on peaks of interest within a spectrum, define backgrounds, calculate differences, and obtain yields.

Using NTOF, $\sigma(\theta)$ measurements were made from 16° to 40° in 4° increments and from 45° to 160° in 5° increments. Data were accumulated for the two experimental configurations of sample-in or sample-out. Data taken with the ^{12}C or ^{208}Pb sample in place were referred to as sample-in data while data accumulated with an empty wire hanger in place were referred to as sample-out data. From 16° to 40° both detectors were used to obtain measurements at the same scattering angle simultaneously, with one detector on each side of the beam axis. Such measurements were useful in checking for normalization differences between the two detectors and for scattering angle shifts. Scattering angle shifts can be caused by beam steering effects, an incorrect detector angle scale, or a misaligned scattering sample position. In the forward angle region, a slight scattering angle shift can give a noticeably different measured cross section. For example, in the n+^{208}Pb case, a change of 0.5° at 8.0 MeV can cause a 4.6% change in $\sigma(\theta)$ near 16°.

At the beginning, middle, and end of an angular distribution measurement, the yield for neutron scattering from hydrogen was measured for normalization purposes and as a check of systematic drifts in the system. Normalization measurements were made by measuring neutron scattering from a polyethylene ($(CH_2)_n$) sample and a carbon sample. The polyethylene and carbon samples are described in Table 2.2. The difference between the polyethylene and carbon spectra gave the spectra for n-p scattering. Normalization measurements were made at an angle ($\theta_{lab} \approx 30°$) chosen to maximize the resolution of the hydrogen scattering peak from the inelastic scattering peaks of carbon.

C. Analyzing power measurements

1. Neutron beam production

For $A_y(\theta)$ measurements a Lamb-shift polarized ion source (PIS) was used to produce a polarized beam of deuterons. The beam was ramped, bunched, and chopped to obtain a pulsed beam. The ramping and bunching system will be described in Chapter III. As with $\sigma(\theta)$ measurements, the pulsed polarized deuteron beam was accelerated by a model FN tandem Van de Graaff accelerator. To provide energy determination after acceleration, the deuteron beam was deflected through 38° using an analyzing magnet. Once inside the neutron time-of-flight target room, the pulsed deuteron beam passed through a capacitive pickoff unit and entered a gas cell containing deuterium. The resulting ^{2}H(d,n)^{3}He reaction produced a high intensity cone of nearly monoenergetic polarized neutrons centered around 0°. The polarization of the deuteron beam was determined by the quench ratio method which has been discussed elsewhere (Lisowski 1975, Pfützner 1987). The polarization of the neutrons was determined from the measured deuteron beam polarization using the polarization transfer function determined by Lisowski *et al.* (Lisowski 1975).

For the present $A_y(\theta)$ measurements, the beam of pulsed polarized deuterons typically had a time-averaged intensity of 150 nA and a polarization that ranged from 60% to 70%, of which approximately 90% was transferred to the neutron beam. The repetition rate of the beam bursts was 4 MHz, and the pulses had a FWHM of less than 2 ns. Deuterium gas pressures and the beam energy loss in the Havar entrance foil and gas cell for $A_y(\theta)$ measurements are listed in Table 2.3.

Table 2.3

Deuterium gas cell pressures and beam energy loss calculations for ^{208}Pb(n,n)^{208}Pb $A_y(\theta)$ measurements

All energies are in MeV

Neutron Energy	Deuterium Gas Pressure	Deuteron Energy at Cell Center	Thickness of Havar Foil	Energy Loss in Havar Foil	Energy Loss in Gas Cell
6.000	2.5 atm	2.735	6.35 μm	0.549	0.353
7.000	3.0 atm	3.733	6.35 μm	0.467	0.329
8.000	4.0 atm	4.751	6.35 μm	0.406	0.361
9.000	4.5 atm	5.783	6.35 μm	0.360	0.345
10.000	6.6 atm	6.823	6.35 μm	0.323	0.441

2. Scattering sample

The ^{208}Pb scattering sample used for $A_y(\theta)$ measurements was the same scattering sample as was used for $\sigma(\theta)$ measurements and has been discussed earlier in Section B-2 of this chapter.

3. Neutron detectors

For $A_y(\theta)$ measurements, the time-of-flight spectrometer facility consisted of seven detectors. Six detectors were used to detect neutrons scattered from the sample while a seventh detector was used as a pulse timing monitor. The six detectors were arranged in three pairs, with each pair consisting of a detector placed at an equal angle on the left and right side of the incident beam axis. Simultaneous measurements with detectors placed at equal angles helped minimize instrumental effects. The arrangement of the detectors relative to the scattering sample is shown in Figure 2.4. All of the detectors were liquid organic scintillators coupled to photomultiplier tubes. The right detector of detector pair #1 in Figure 2.4 contained NE-218 scintillator fluid, while the rest of the detectors contained NE-213 scintillator fluid. Both types of scintillator and associated photomultiplier tubes provided good pulse-shape discrimination between neutrons and γ-rays.

The right and left detectors of detector pair #1 were the same detectors used for $\sigma(\theta)$ measurements. At each angle where a measurement was made, tungsten shadow bars were positioned so that each detector was shielded from the direct flux of source reaction neutrons. The minimum and maximum angles for simultaneous measurements with both detectors at equal angles were 16° and 159°, respectively. In $A_y(\theta)$ measurements, a flight path of 2.98 m was used for the right detector in detector pair #1, while a flight path of 3.91 m was used for the left detector in detector pair #1.

Detector pairs #2 and #3 were heavily shielded and mounted on movable tables. Copper and polyethylene shadow bars were positioned at each angle so that the detectors and detector shielding could not view the direct flux of source reaction neutrons. Detector pair #2 was used over an angular range of 105° to 149°, while detector pair #3 was used over an angular range of 120° to 164°. All four detectors used in detector pairs #2 and #3 were rectangular in shape. Detectors used in detector pair #2 were 7.62 cm wide, 12.70 cm tall, and 5.08 cm thick and were placed at a flight path of 2.59 m. Detectors used in detector pair #3 were 7.62 cm wide, 15.24 cm tall, and 5.08 cm thick and were placed at a flight path of 2.66 m.

The pulse timing monitor used in $A_y(\theta)$ experiments was the same monitor used in $\sigma(\theta)$ experiments. This monitor was again located near 0° at a flight path of about four meters and was used to monitor the time distribution of neutrons emerging from the gas cell. The beam pulsing system was adjusted so that the neutron source reaction peak in the time-of-flight spectrum of the timing monitor had the narrowest time width possible. The overall time resolution of the system (FWHM of the peak) was about 3.4 ns at $E_n = 6.0$ MeV and about 2.6 ns at $E_n = 10.0$ MeV.

4. Detector electronics

As with $\sigma(\theta)$ measurements, the electronics for $A_y(\theta)$ measurements were used to measure the time-of-flight of an incident particle, to determine that the energy deposited in the detector due to an event was greater than a specified energy bias, and to determine that

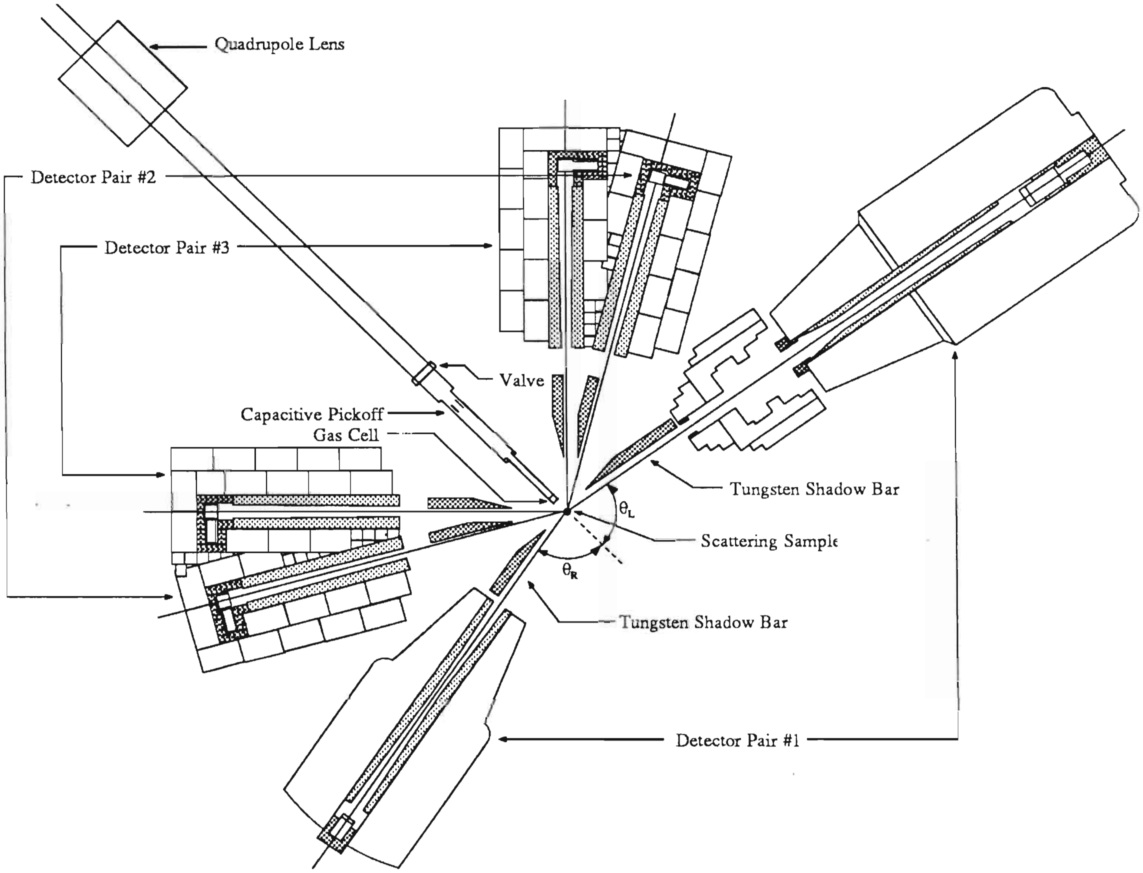

Figure 2.4. Arrangement of the main neutron detectors relative to the scattering sample and beam line for $A_y(\theta)$ measurements.

the event in the detector was caused by a neutron and not by a γ-ray. For $A_y(\theta)$ measurements, the seven anode signals and the signal from the capacitive pickoff unit were brought from the target area into the control room on 50 Ω low loss cable. The anode signal from the pulse timing monitor was sent to a set of electronics that was identical to the electronics used in $\sigma(\theta)$ measurements. The anode signals for the remaining six detectors were sent in pairs to three identical sets of the electronics. Each pair of signals corresponded to detectors placed at equal angles on the left and right side of the beam axis. A block diagram of the electronics used in $A_y(\theta)$ experiments is shown in Figure 2.5. To determine that the energy deposited in the detector due to an event was greater than our energy bias, the incoming anode signals from the left and right detectors were summed using a linear fan-in/out module. An output from the linear fan-in/out module was amplified and fed into a linear amplifier with single channel analyzer (AMP+SCA) module. As with $\sigma(\theta)$ measurements, the SCA of the AMP+SCA had a lower level threshold, or bias, set to coincide with proton recoil energies of about 2 MeV. Signals with amplitudes smaller than this bias did not produce logic pulses, or gates, at the SCA output and so were discriminated according to pulse height.

As with $\sigma(\theta)$ measurements, pulse shape analysis was used to determine that an event in the detector was caused by a neutron and not by a γ-ray. To discriminate γ-rays from neutrons, the incoming anode signals were fed into separate constant fraction discriminator (CFD) modules, while the sum of the two anode signals was fed into a pulse shape discriminator (PSD) module. As was described in Section B-4 of this chapter, the time difference between the output of a signal from the CFD module and an output from the PSD module was a measure of the decay time of the incoming anode pulse. Time differences between outputs of the CFD and PSD were converted to voltages using a time-to-amplitude converter (PSD-TAC). A window was set on the output of the PSD-TAC such that only output voltages which corresponded to valid neutron events would produce logic pulses or gates.

Time-of-flight information was determined from the time difference between a start and a stop signal. As with $\sigma(\theta)$ measurements, pickoff signals were delayed and used to stop a time-to-amplitude converter (TOF-TAC). The TOF-TAC was started by the summed output of the CFD modules. Signals out of the TOF-TAC had an amplitude linearly related to the time difference between the start and stop signals fed into it and therefore an amplitude linearly related to the TOF of a neutron. The output of the TOF-TAC was shaped by a linear gate stretcher and sent to the computer interface, where it was gated by an output from a universal coincidence module and digitized by an analog-to-digital converter (ADC). The universal coincidence module was used to

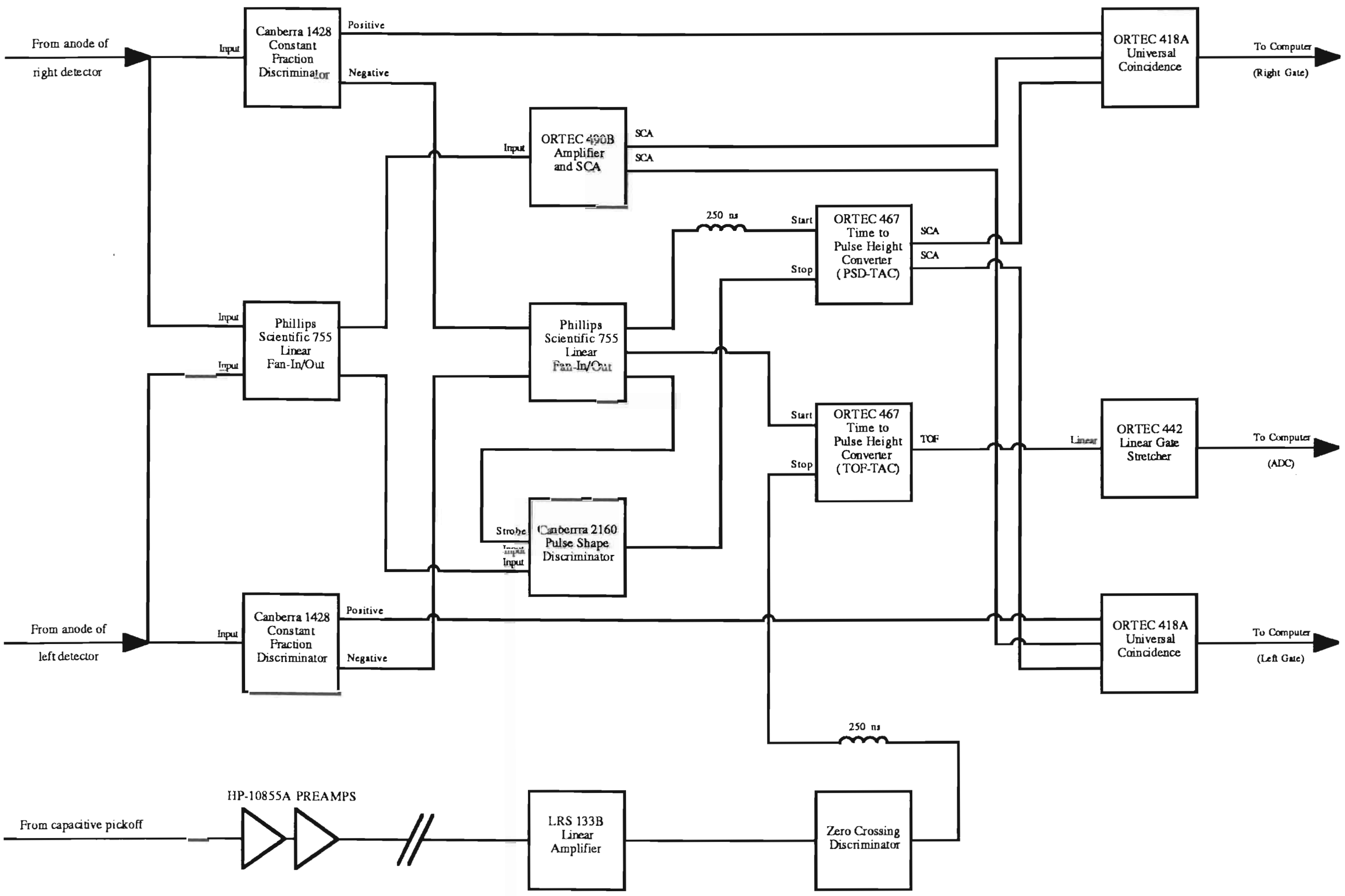

Figure 2.5. Block diagram of the electronics used in $A_y(\theta)$ measurements.

produce a logic output or gate when the input gates from the CFD, SCA, and PSD were in coincidence.

5. Data acquisition

The data acquisition and storage system for $A_y(\theta)$ measurements is similar to the system described earlier for $\sigma(\theta)$ measurements. Command Language programs incorporating XSYStem commands were written and combined into a polarized neutron time-of-flight data acquisition package called PTOF. The programs in PTOF made it possible to set windows on peaks of interest within a spectrum, define backgrounds, calculate differences, obtain yields, and generate analyzing powers.

Using PTOF, $A_y(\theta)$ measurements were made from 16° to 40° in 4° increments and from 45° to 160° in 5° increments. Data were accumulated for four experimental configurations: sample-in spin-up, sample-in spin-down, sample-out spin-up, and sample-out spin-down. Data taken with the ^{208}Pb sample in place were referred to as sample-in data while data accumulated with an empty sample wire in place were referred to as sample-out data. Spin-up and spin-down refer to the polarization direction of the incident neutron beam. The direction of the incident neutron beam spin was flipped about every twenty minutes by changing the direction of the deuteron spin at the polarized ion source. The deuteron beam polarization was measured about every ten minutes.

Depending on cross section, sufficient time was spent on each experimentally measured angle to obtain a 0.6% to 3.0% statistical uncertainty on each measured analyzing power. Time spent at each angle ranged from 1 hr to obtain a 0.6% statistical uncertainty on the 10.0 MeV ^{208}Pb elastic analyzing power data point at $\theta_{lab} = 16°$ to 12 hrs to obtain a 3.3% statistical uncertainty on the 6.0 MeV ^{208}Pb elastic analyzing power data point at $\theta_{lab} = 130°$. Since the cross section for inelastic scattering from the first excited state ($J^\pi = 3^-$, Q = -2.614 MeV) of ^{208}Pb was small compared to the elastic scattering cross section, analyzing power values for inelastic scattering from the first excited state of ^{208}Pb had much larger statistical uncertainties. Statistical uncertainties of the inelastic analyzing power values ranged from 4.5% to 27.4% and were rarely below 10%. Large statistical uncertainties on inelastic analyzing power values were not a major concern, however, because the focus of this work was on the physics of the elastic scattering data and not on the physics of the inelastic scattering data.

CHAPTER III

BEAM PULSING

A. Introduction

Because neutrons are uncharged, they are harder to detect and their energy more difficult to measure than charged particles such as protons, deuterons, and alphas. The neutron detection process usually involves a nuclear reaction or an elastic scattering process through which the neutron produces a detectable charged particle. At Triangle Universities Nuclear Laboratory (TUNL), neutrons are detected by observing recoil protons from neutron-proton collisions in an organic scintillator containing hydrogen, while neutron energies are determined using time-of-flight techniques. With time-of-flight techniques the time-of-flight of a neutron over a known path length from target to detector is measured, and neutron energies are determined from a calculation of velocity. To achieve good energy resolution when using time-of-flight techniques, however, the incident beam must be pulsed into bursts as narrow as possible, and the time between arriving beam bursts must be sufficiently long to allow all reaction products of interest from one beam burst to reach the detectors before the arrival of any reaction products from the next beam burst. Since some of the developmental contributions of the present author involve beam pulsing, a brief review of the beam pulsing system at TUNL and recent improvements made to the system will follow.

B. Cross section measurements

To obtain a pulsed beam for $\sigma(\theta)$ measurements at TUNL, a standard chopping and bunching system was used which operated on the following principle. After a continuous ion beam was extracted from the direct extraction negative ion source, it entered a set of horizontal deflection plates, called main chopping plates, to which a 2 MHz sinusoidal voltage was applied. Beam passing through the chopping plates at the zero crossing of the sine wave received little or no deflection, while the remainder of the beam was swept across a defining circular aperture before the buncher tube. Since the sine wave applied to the main chopping plates or main chopper had two zero crossings every period, beam emerging from the main chopper had a repetition rate of 4 MHz (4 million pulses per second). This process was called chopping because it chopped the dc beam into packets or segments.

After chopping by the main chopper, the beam passed through a vertical set of deflection plates that were usually driven by a 2 MHz square wave. These deflection plates, called auxiliary chopping plates, deflected or removed alternate beam segments that emerged from the main chopper. The frequency of the square wave applied to the auxiliary chopping plates could be varied from 2 MHz to 31 kHz, allowing the experimenter to vary the beam repetition rate from 2 MHz to 31 kHz.

After the beam was chopped by the main and auxiliary choppers it entered a double-gap buncher. The double-gap buncher modulated the velocity of particles in the beam segment in such a way that particles in the segment that were initially separated in space were made to arrive at the target at nearly the same time. At TUNL, the double-gap buncher is a cylindrical tube consisting of three electrically insulated sections separated by two gaps. The sections on either end are grounded while the longer middle section is driven by a sinusoidal rf voltage. The phase of the chopping waveforms is adjusted relative to the phase of the voltage on the buncher so that the potential across the first bunching gap is negative when the beam segment enters the first gap. This causes the front of the negative-ion beam segment to be repulsed or slowed down. As the center of the beam segment passes through the buncher gap, the gap voltage is zero and the center of the beam segment is neither sped up nor slowed down. When the rear of the beam segment reaches the bunching gap, the gap voltage has reversed and the rear of the beam segment is accelerated. In a double-gap buncher, the distance between the first and second gaps of the buncher is such that the voltage at the second bunching gap acts on the beam pulse in the same manner as the voltage at the first bunching gap. After bunching, the beam segment has a non-uniform energy or velocity distribution and as the beam segment drifts to target it forms a narrow beam burst.

For the present $\sigma(\theta)$ measurements, this standard method of chopping and bunching delivered approximately 2% of the initial direct current emitted by the ion source to target at a repetition rate of 2 MHz with a full width at half maximum (FWHM) of less than 2 ns.

C. Analyzing power measurements

Because of the low intensity of the polarized ion source at TUNL (i.e., a dc beam of about 400 nA), the use of a standard chopping and bunching system to obtain pulsed polarized beams would produce a prohibitively low intensity beam on target. Therefore, for $A_y(\theta)$ measurements another technique was necessary. Pulsing polarized beams involved ramping of the very low beam-energy supply in the polarized ion source, bunching the beam by a pair of double-gap bunching tubes, and chopping away background beam occurring between pulses.

In the polarized ion source at TUNL, an initially unpolarized beam is formed by extracting ions from a duoplasmatron. For deuterons, the beam energy inside the polarized ion source is established by biasing the anode of the duoplasmatron at 1100 V with respect to the rest of the source. Before acceleration to 50 keV, the beam drifts approximately 1.5 meters while being converted to a polarized beam. This long drift path at relatively low energy allowed prebunching or ramping of the beam by a modest voltage modulation of the duoplasmatron. For $A_y(\theta)$ measurements at TUNL, a 4 MHz ramp wave with a peak-to-peak voltage of about 70 V was applied to the anode of the polarized ion source. The ramp circuit and theory of operation has been described in detail by Howell (Howell 1984). The ramp on the polarized ion source modulated the deuteron beam energy in such a way that about 90% of the initial direct current of the beam was compressed into about 30% of a cycle by the time that it reached the end of the polarized ion source.

After being ramped, the beam emerging for the polarized ion source was further compressed by a two-stage double-drift bunching system. Two-stage double-drift bunching systems (described in detail by Milner (Milner 1979)) consist of two double-gap bunchers that are separated in space, independently driven, but phase-locked together. At TUNL, the first stage of this bunching system used the same buncher as was used for $\sigma(\theta)$ measurements. As with $\sigma(\theta)$ measurements, this first buncher decelerated the leading portion of beam segments and accelerated the trailing portions. Because only about 20 to 30% of the sinusoidal waveform applied to the first buncher was sufficiently linear to produce bunching of the quality required, the highest efficiency we could expect from this single buncher was between 20 and 30%. In a two-stage double-drift bunching system, a second buncher is used which operates at twice the frequency of the first buncher and 180° out of phase. The effect of this second buncher is to produce an effective bunching system which has a more linear bunching voltage over an extended range in time. The maximum efficiency of a two-stage double-drift bunching system depends on the ratio of the separation between the two bunchers and the total drift distance to target. For our installation, the separation distance between the two bunchers was fixed by physical limitations in the low energy transport system to be about 55 cm, and typical efficiencies of about 60% were obtained (i.e., if an initial dc beam entered the double-drift bunching system, 60% of the beam would be compressed into a beam burst of about 2.0 ns FWHM by the time it reached the target).

The final element in the polarized beam pulsing system at TUNL was a post bunching chopper, commonly called the low energy chopper. The low energy chopper removed time-uncorrelated background that occurred between beam pulses. The low energy chopper is located at the entrance or low energy end of the Van de Graaff Accelerator (hence the name low energy chopper) and consisted of two parallel plates with a 4 MHz sinusoidal voltage applied to one side. The voltage applied to the low energy chopper was phased so that ions present between the beam bursts produced by the ramp and bunching system were deflected out of the beam.

For the current $A_y(\theta)$ measurements, ramping of the polarized ion source into the phase acceptance of the double-drift bunching system and chopping away the background beam that occurred between beam pulses allowed about 80% of the the initial direct current emitted by the polarized ion source to reach target with a FWHM of less than 2 ns at a repetition rate of 4 MHz.

D. Improvements to the system

One of the major objectives of the neutron program at TUNL has been to measure $\sigma(\theta)$ and $A_y(\theta)$ neutron scattering data accurately from a variety of nuclei. In order to reduce ambiguities in phenomenological optical model analyses and coupled channel analyses, and to provide sensitive observables for testing microscopic calculations, measurements must be conducted on many nuclei. However, since many nuclei have excited states that are not well separated from their ground state, it is necessary to have good energy resolution. Because time spreads in the beam are interpreted as energy spreads in time-of-flight spectra, it is important to minimize the time spread in the incident beam.

Prior to 1985, time widths for beam bursts produced by the standard chopping and bunching system were substantially broader than predicted by calculations. To first order, the time spread of two particles that cross the bunching plane simultaneously but differ in energy by an amount ΔE can be determined from:

$$\Delta t = \frac{1}{2} \cdot \frac{t_0}{E_0} \cdot \Delta E \ , \qquad (3\text{-}1)$$

where E_0 is the average energy of the particles at the buncher and t_0 is the time that a particle takes to travel from the buncher to target. If the beam emerging from the direct extraction ion source is assumed to have the same intrinsic energy spread as deduced by

Howell *et al.* (Howell 1982) for the TUNL polarized ion source ($\Delta E = 25\ eV$), then 50 keV deuterons accelerated to 10.0 MeV and focused on target in the target room ($t_0 = 3000\ ns$) should have a time spread of $\Delta t = 0.75$ ns FWHM. In practice, beam burst widths were observed to be greater than 2 ns FWHM. Several possible causes for this poor timing were examined: dc voltages applied to the buncher's rf power supply were checked for stability, possible time spread due to path length differences in trajectories of beam particles after exiting the buncher was calculated, and effects due to a larger than assumed beam energy spread at the buncher were investigated.

The ripple on the voltages applied to the buncher's rf power amplifier were checked and found to be negligible. In estimating time spread due to path length differences, only path length differences of beam particles before the accelerator were considered. An upper limit on the path length difference can be obtained by assuming that the outermost particles in the beam follow a triangular path between the buncher and the low energy base plate of the tandem. Assuming that the beam has a maximum radial size at the center of all focusing elements and a crossover between focusing elements, a time spread of $\Delta t \cong 0.68$ ns is obtained for 50 keV deuterons. Combining the time spread due to path length differences and the assumed time dispersion due to the intrinsic energy spread in the beam gives a resultant time spread of $\Delta t = 1.01$ ns, which is well below the observed time spread of $\Delta t \cong 2.00$ ns.

The last possible cause for the poor timing was that the intrinsic beam energy spread at the buncher was larger than assumed. The routine beam timing spread of 2 ns FWHM suggested that the energy spread in the beam at the buncher was larger than 65 eV. Two possible causes for the enhanced beam energy spread were ripple on the accelerating voltage of the negative ion source and effects due to chopping. The ripple on the acceleration voltage of the negative ion source was found to have a sawtooth waveform with an amplitude of 400 volts peak-to-peak out of 50 kV and a repetition rate of 120 Hz. Because of its low frequency, effects of accelerating voltage ripple on timing were negligible. To investigate the influences of the chopper on timing, time profile spectra of the beam were accumulated both with and without chopping. These spectra, shown in Figure 3.1, were accumulated by accelerating deuterons to 7.0 MeV and elastically scattering them from a gold foil. Details of a similar experimental setup have been discussed by Howell (Howell 1984). The improvement in timing obtained when the main chopper was turned off suggested that the width of the beam pulses was dominated by an energy spread introduced by chopping.

This energy spread was caused by fringe electric fields at the entrance and exit of the chopper plates and can be explained as follows. As is shown in Figure 3.2, fringe

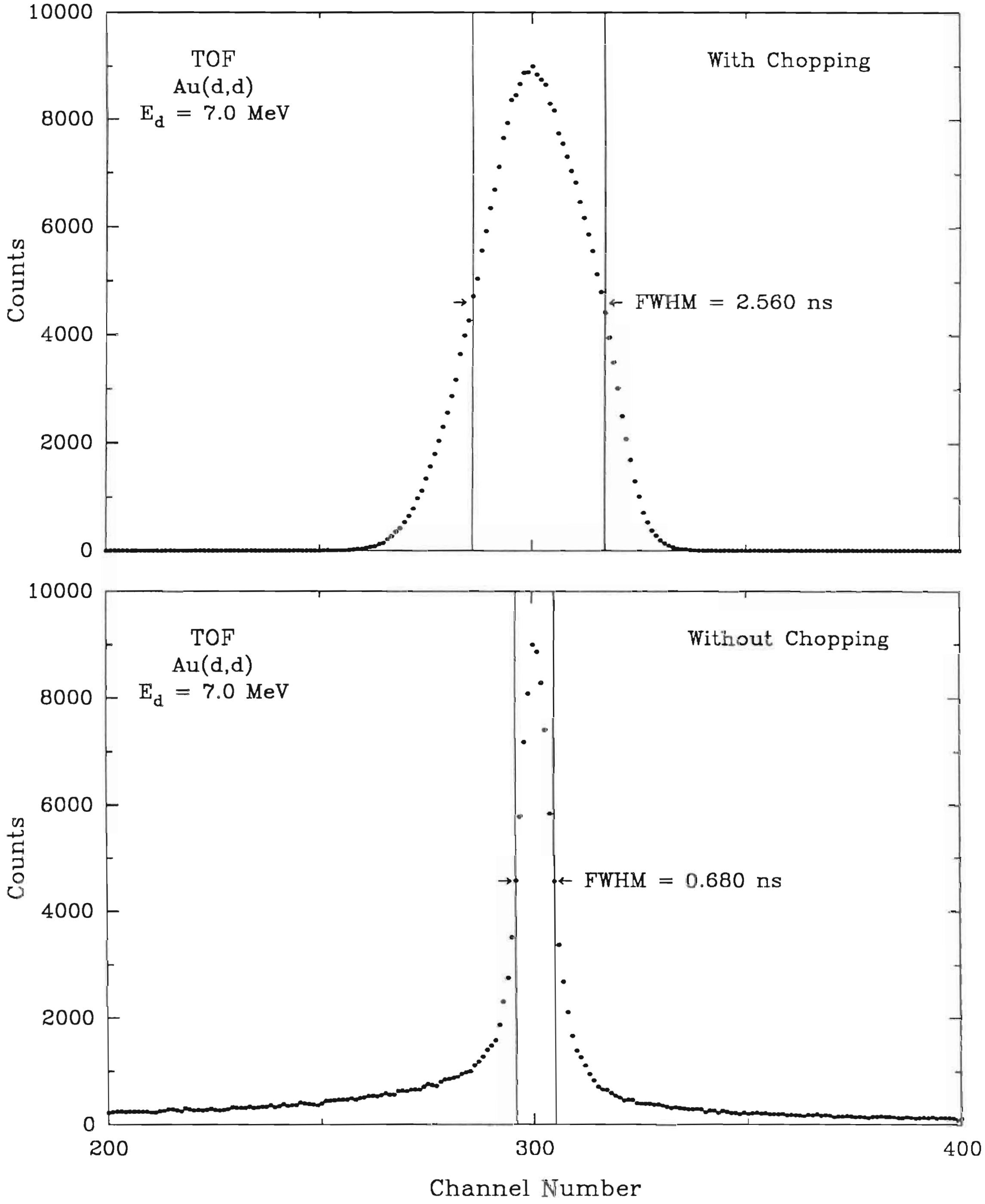

Figure 3.1. Beam profile spectra accumulated with and without chopping.

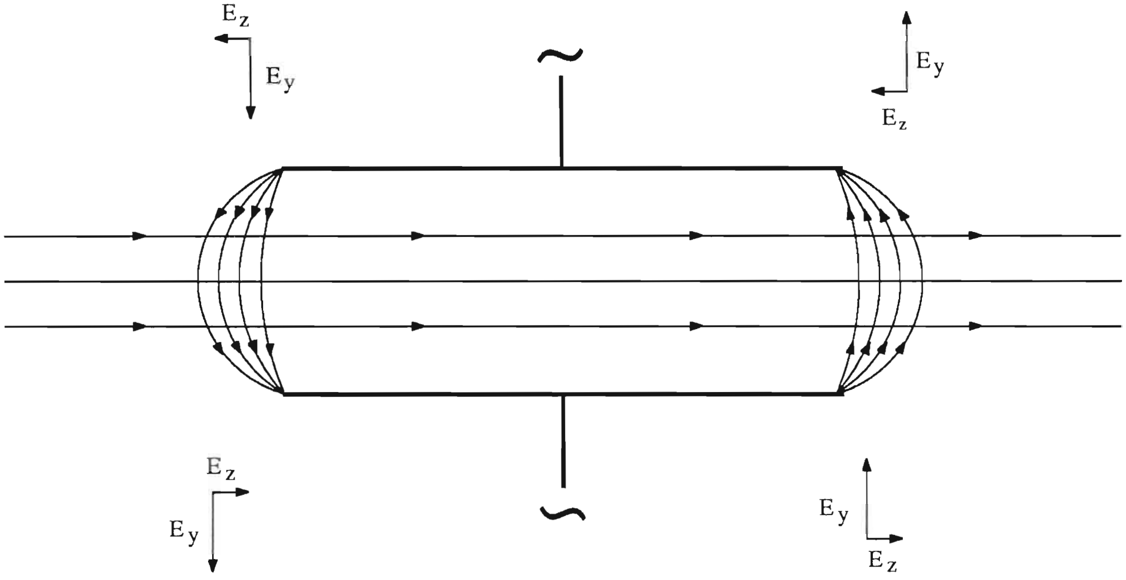

Figure 3.2. Fringe electric fields at the entrance and exit of the chopper. Fringe electric fields can cause a change in the longitudinal component of velocity for particles which traverse the chopper off axis.

electric fields of the main chopper cause a change in the longitudinal component of velocity for particles which traverse the chopper off axis. The magnitude of the change in the longitudinal component of velocity varies as a function of beam position. For particles which traverse the chopper on axis there is no change in the longitudinal component of velocity. However, for particles which enter and exit the chopper on the same side of the beam axis, the change in the longitudinal component of velocity is a maximum. As a consequence of the position dependence of the change in longitudinal component of velocity, the energy of particles exiting the chopper varies as a function of radial position, and the energy spread of a beam segment that traverses the chopper is increased. To minimize the energy spread introduced by chopping, the beam leg after the negative ion source was modified. The modifications are illustrated in Figures 3.3 and 3.4. The choppers were moved about one meter further away from the exit of the analyzing magnet and a new set of horizontal and vertical slits was placed in the chopper's old position. The new set of slits is used in conjunction with a small circular aperture in front of the buncher to help tune the beam through the center of the chopping plates. An electrostatic quadrupole triplet lens was also inserted before the chopping plates to form a focus or crossover at the center of the chopper. Not only did the beam focus at the center of the chopper reduce the energy spread in the emerging beam segment because of the smaller radial size of the beam, but the beam crossover caused the longitudinal component of velocity introduced by the chopping system to be cancelled to first order. After exiting the chopper, the beam was focused again by another electrostatic quadrupole triplet lens. Typical output timing with the new lens system is between 0.9 and 1.0 ns FWHM for 50 keV deuteron beam pulses. A comparison between beam profile spectra accumulated using the old chopping system and the new chopping system is shown in Figure 3.5.

As shown in Equation 3-1, time resolution can be further improved by increasing the injection energy of ions entering the tandem. To accommodate higher injection energies, a new bunching system featuring two variable length bunchers was designed and has been installed. A side view of the first or main buncher is shown in Figure 3.6. The length of the new bunching tubes can be varied external to the vacuum. Improvements on the phase stability of the system were also accomplished with the addition of a new phase control circuit. This new phase control circuit uses phase-locked loops to maintain phase stability between components and has automatic gain control circuits to reduce voltage drift caused by temperature changes in tuned circuits and to compensate for capacitance drift caused by vacuum changes. A block diagram of the new phase control

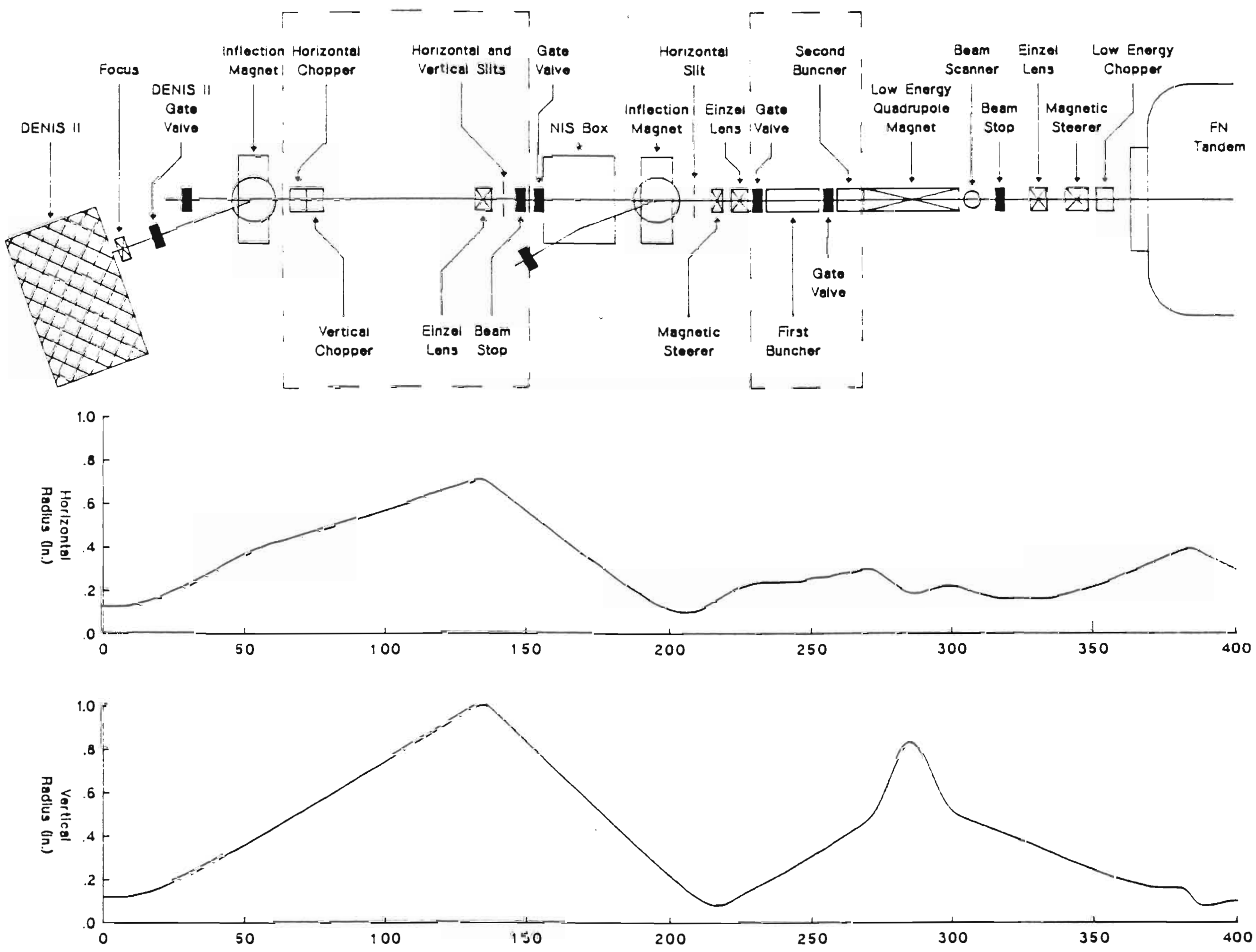

Figure 3.3. Negative ion source beam leg before modification. Vertical and horizontal beam profiles calculated from the computer code OPTIC are also shown.

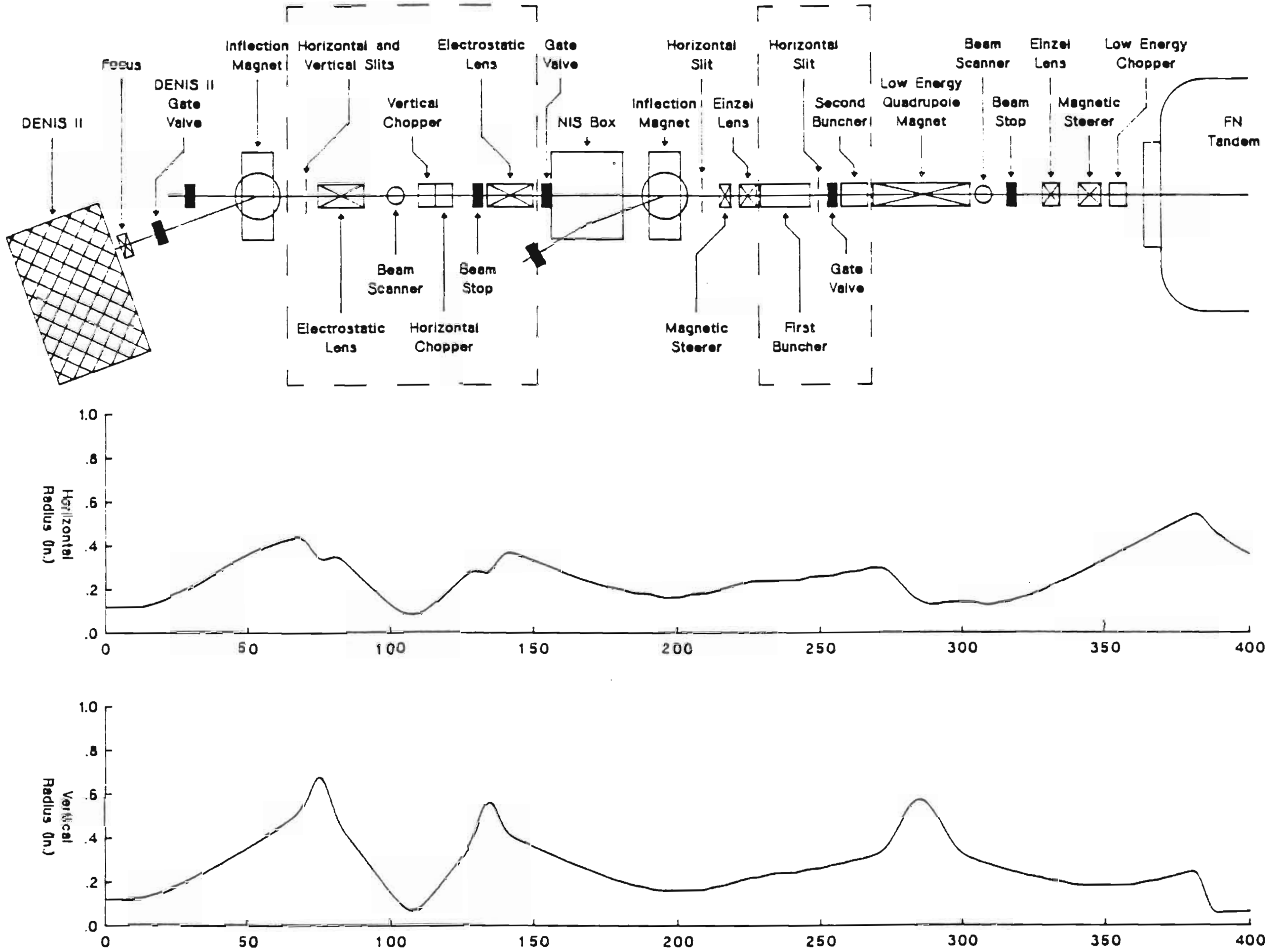

Figure 3.4. Negative ion source beam leg after modification. Vertical and horizontal beam profiles calculated from the computer code OPTIC are also shown.

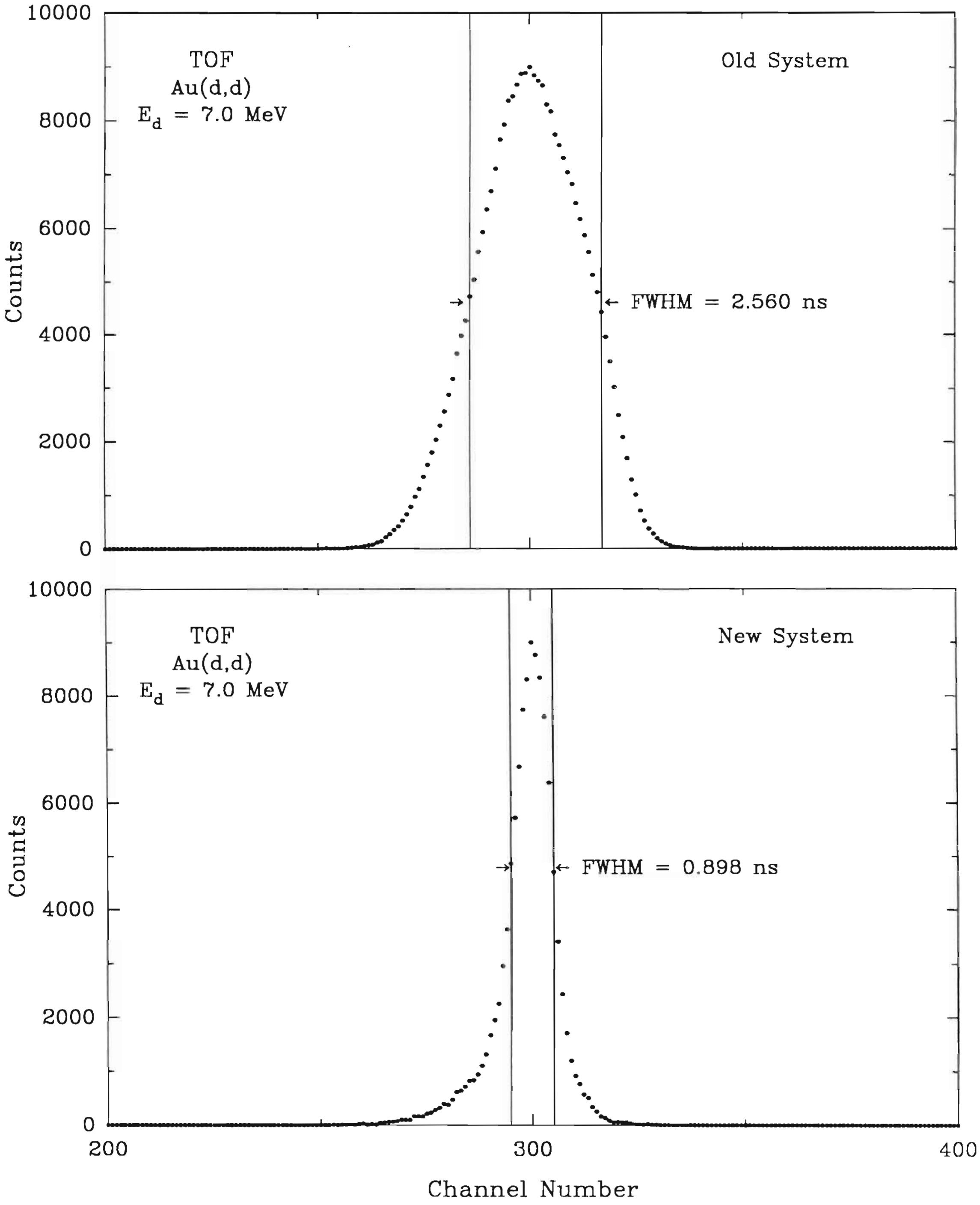

Figure 3.5. Beam profile spectra accumulated with the old beam pulsing system and the new beam pulsing system.

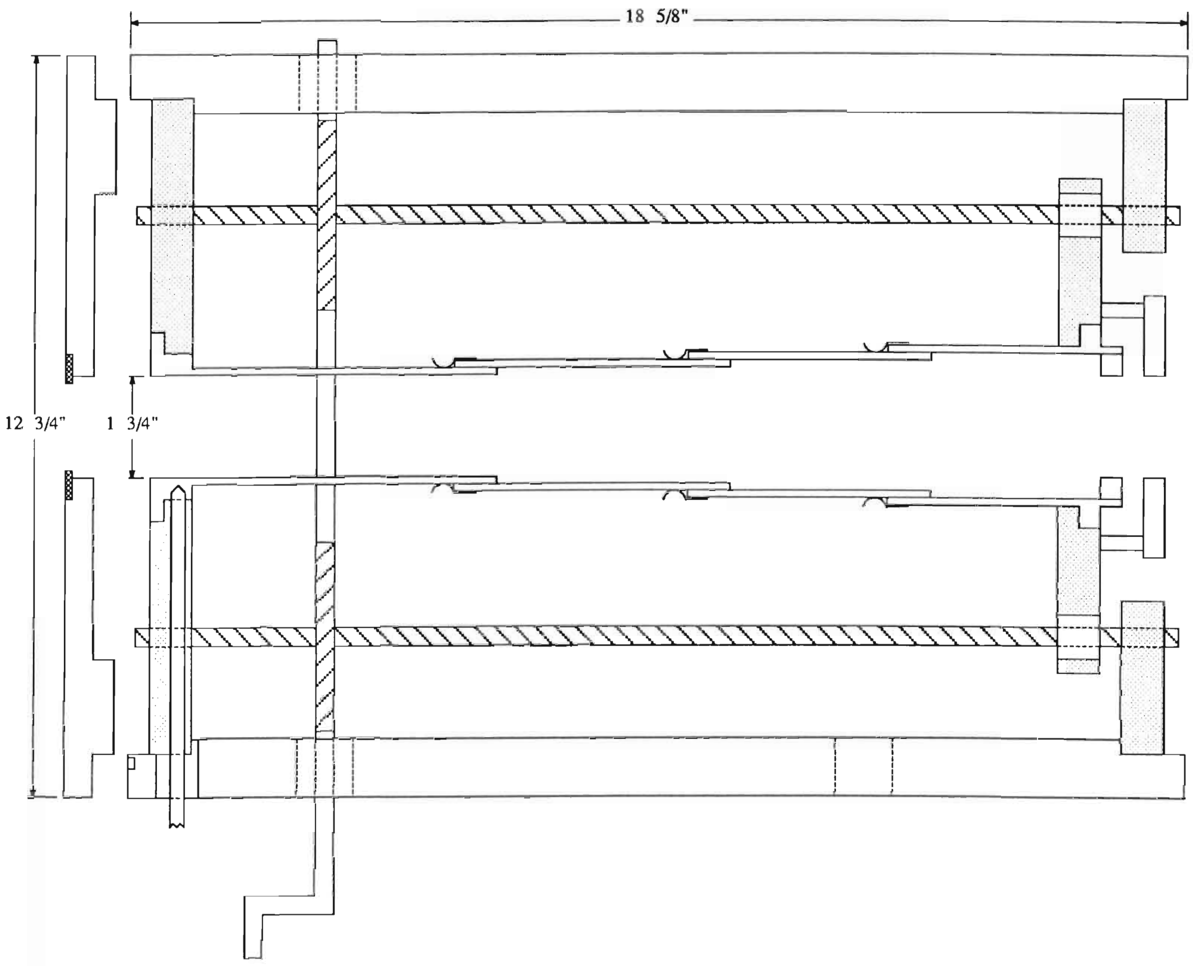

Figure 3.6. Side view of the main buncher tube. The length of the buncher can be varied external to the vacuum to allow a broad variety of ions to be bunched over a wide range of injection energies.

circuitry is shown in Figure 3.7. The new bunching system permits a broad variety of ion beams to be bunched over a wide range of injection energies into the tandem accelerator.

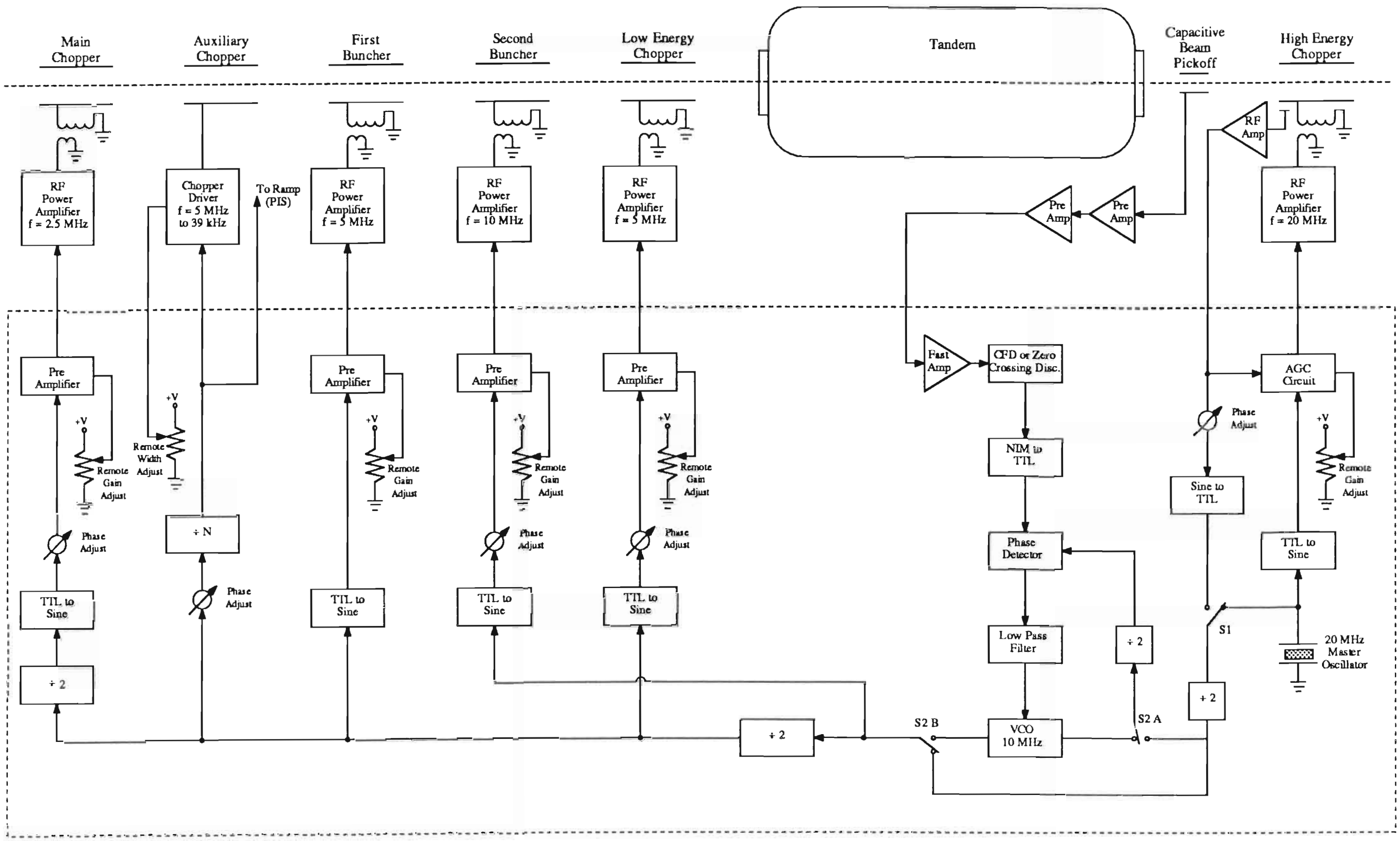

Figure 3.7. Block diagram of the phase control circuitry for beam pulsing.

CHAPTER IV

DATA REDUCTION AND PRESENTATION

A. Cross section measurements

1. Neutron yield extraction

To obtain differential cross sections ($\sigma(\theta)$), neutron yields had to be extracted from time-of-flight spectra. Neutron yields were obtained by setting windows about peaks of interest, and events within these windows were counted and stored using a self-contained data analysis package called NTOFOFF. The analysis package NTOFOFF contains a series of programs operating under the TUNL XSYStem software package that can display, normalize, subtract or add spectra together, draw polynomial backgrounds, set windows, and store yields.

Using NTOFOFF, the first step in extracting $\sigma(\theta)$ values from time-of-flight spectra was to obtain a monitor yield (Y_M) from the neutron flux monitor. A sample monitor spectrum is shown in Figure 4.1. First, a monitor background was selected to estimate the level of background neutron events lying under the discrete peak. This background was calculated by fitting regions on either side of the peak with a least-squares fitting routine. After the monitor background was drawn, a monitor window was set on the narrow peak of neutrons coming directly from the ^{2}H(d,n)^{3}He (Q = +3.269 MeV) ground state reaction in the gas cell. The monitor window was chosen to be narrow enough to include as few breakup neutrons as possible in the monitor yield, but wide enough to avoid steep slopes on the peak. A window which was too wide could, at lower deuteron energies, contain breakup neutrons produced from the collision of deuterons in the gas cell through the ^{2}H(d,np)d reaction (Q = -2.225 MeV), while at higher energies contain neutrons produced through the ^{2}H(d,np)np reaction (Q = -4.450 MeV). A window which was too narrow, however, could be sensitive to small timing shifts that could effect the monitor yield. After the background and window were set in the monitor spectrum, neutron events inside the window and above the background were summed to obtain Y_M for both the sample-in and the sample-out cases. To insure a proper normalization of the entire data set, the same window and similar backgrounds were used for all sample-in and sample-out neutron flux monitor spectra, including spectra from polyethylene and carbon normalization measurements.

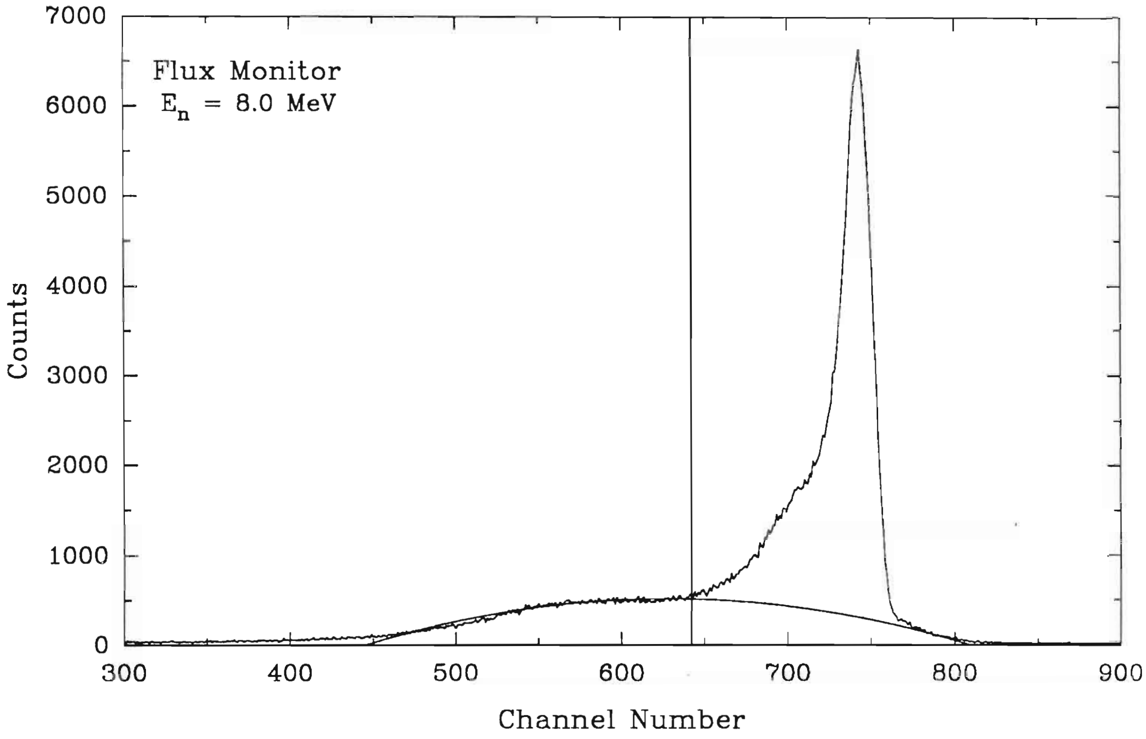

Figure 4.1. Neutron flux monitor spectra at $E_n = 8.0$ MeV. The smooth curve is the background estimate in the region of the peak, while the two vertical lines indicate the limits of the windows chosen. The flux monitor was located at an angle of about 50° relative to the ^{2}H(d,n)^{3}He source reaction.

The second step in extracting $\sigma(\theta)$ values was to calculate difference spectra. To obtain difference spectra (DIFF), sample-out time-of-flight spectra (OUT) were scaled by the ratio of sample-in to sample-out monitor yields and subtracted from the corresponding sample-in time-of-flight spectra (IN) according to the following formula:

$$\mathrm{DIFF} = \mathrm{IN} - \frac{Y_{M_{SI}}}{Y_{M_{SO}}} \cdot \mathrm{OUT} , \qquad (4\text{-}1)$$

where Y_{MSI} is the sample-in monitor yield and Y_{MSO} the sample-out monitor yield. An example of an IN, a normalized OUT, and a DIFF spectrum are shown in Figure 4-2. After difference spectra were formed, backgrounds were drawn in the difference spectra to remove sample-correlated backgrounds not measured in the sample-out count. In most cases, a linear function adequately described the residual background. After backgrounds were drawn, windows were chosen about peaks of interest and a yield per monitor (designated Y_S) was calculated. The yield per monitor is the number of events inside the window and above the background in the difference spectra divided by the number of events inside the window and above the background in the monitor spectra.

2. Data normalization

After neutron yields were extracted from time-of-flight spectra, absolute differential cross sections were calculated by comparing yields for neutron scattering from the sample to yields for neutron scattering from hydrogen and published n-p scattering cross sections. The measured experimental cross section at each scattering angle θ_L in the laboratory system was calculated as:

$$\sigma(\theta_L, E_n) = \frac{Y_S(\theta_L)}{Y_P(\theta_P)} \cdot \frac{1}{\mathrm{PCF}(\theta_P)} \cdot \frac{n_H}{n_S} \cdot \sigma_{np}(\theta_P, E_n) , \qquad (4\text{-}2)$$

where $Y_S(\theta_L)$ is the monitor normalized yield for neutron scattering from the sample and $Y_P(\theta_P)$ is the monitor normalized yield for neutron scattering from hydrogen at angle θ_p. $PCF(\theta_p)$ is a correction factor for relative efficiency, attenuation, finite geometry, and multiple scattering effects applied to the hydrogen sample. The number of hydrogen nuclei in the polyethylene sample divided by the number of nuclei in the scattering sample

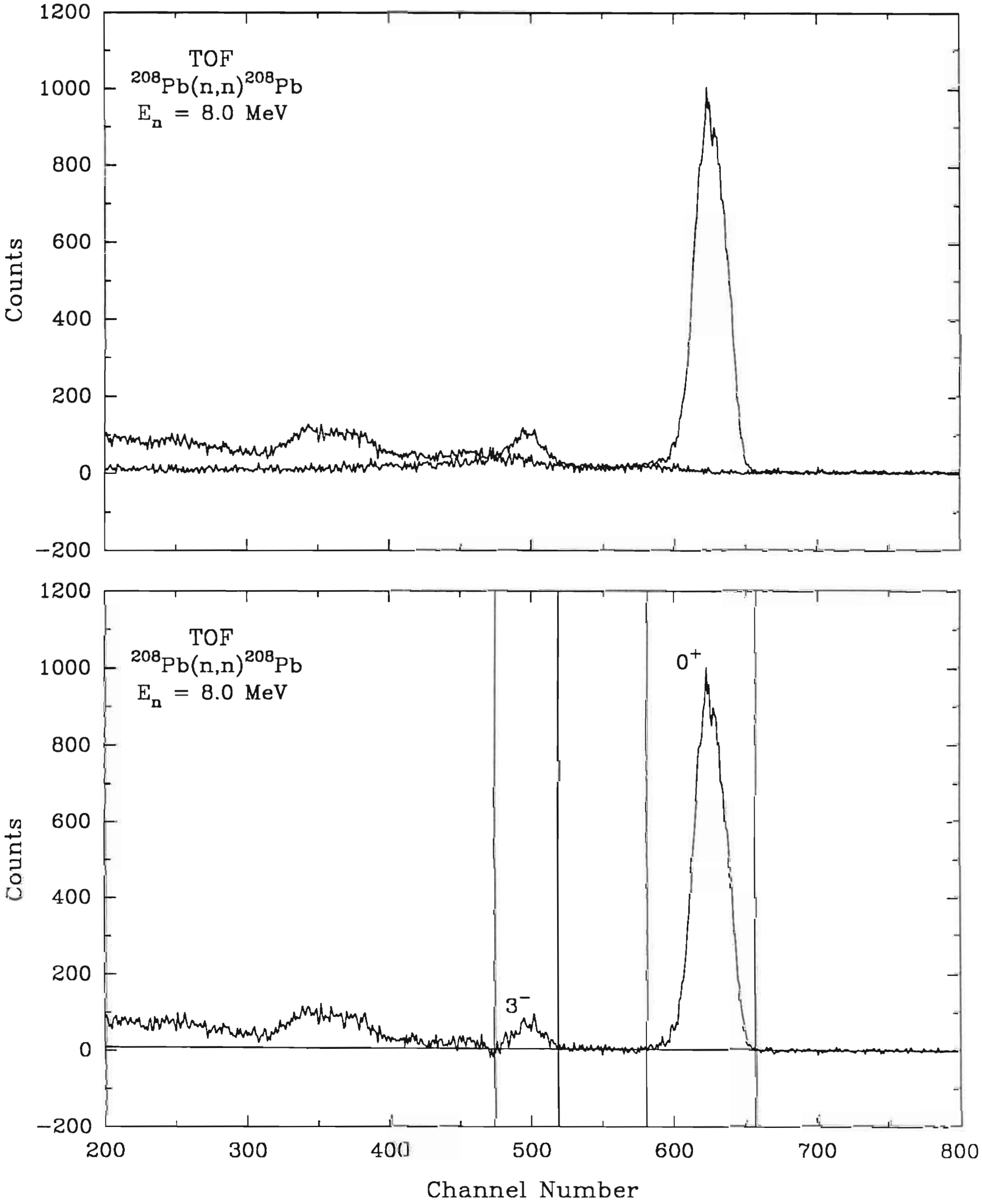

Figure 4.2. IN, OUT, and DIFF spectra for the scattering of 8.0 MeV neutrons from ^{208}Pb through a laboratory angle of 85°. The peaks for elastic and inelastic scattering peaks are labeled 0^+ and 3^-, respectively. In the difference spectrum, the solid line is the background estimate in the region of the peaks, while the four vertical lines indicate the limits of the two windows chosen.

is n_H/n_S . The known n-p scattering cross section value as reported by Hopkins and Breit (Hopkins 1971) is $\sigma_{np}(\theta_p,E_n)$.

3. Finite geometry, attenuation, and multiple scattering corrections

The observable σ(θ) is defined for scattering from a point sample into a point detector, i.e., a sample and detector of negligible cross-sectional area. Since neutron time-of-flight measurements require large samples and detectors, the effects of finite geometry, flux attenuation, and multiple scattering on the observed yield or cross section cannot be ignored and corrections are necessary. At TUNL, corrections to σ(θ) data are calculated by a Monte Carlo code called EFFIGY15. This code simulates an experiment in the lab system and calculates corrections to the data using an iterative procedure. In each iteration of the correction process, the experiment is simulated by using a library of total and differential cross sections and physical parameters of the experiment to generate time-of-flight spectra at each angle for which measurements were made.

The initial cross section library contains total cross sections for the scatterer, coefficients from a Legendre polynomial fit made to the original experimental σ(θ) data (obtained from uncorrected yields), and Legendre polynomial coefficients from fits to σ(θ) data at other energies. The simulation generates time-of-flight spectra by following individual neutron histories from their production at the gas cell through the scattering and detection processes. A single history is a set of random sites (hence the term Monte Carlo) in the gas cell, scattering sample, and detector, where the respective neutron was created, scattered, and detected. The first scattering in the sample is forced, and a weighted random selection process is used to determine whether or not the neutron scatters more than once, and if so by what process. As in the actual experiment, the statistical accuracies of the peaks of interest in the simulated time-of-flight spectra are checked periodically to determine whether sufficient neutron histories have been run. When sufficient histories have been obtained, values generated from the current cross section library are used with yields calculated from the simulated time-of-flight spectra to generate correction factors. The correction factors are applied to the experimental data to obtain corrected σ(θ) values. After an initial iteration of EFFIGY15, calculated yields are compared to experimental yields to check for convergence. Convergence is said to occur when the calculated yields and the experimental yields agree to within a set percentage. If convergence is not achieved, the cross section library is updated with coefficients from a Legendre polynomial fit to the corrected experimental data of the present iteration, and a new iteration is begun. The iteration process terminates with the achievement of convergence.

In EFFIGY15, corrections are calculated simultaneously for both elastic and inelastic scattering. The mean energy of the incident neutrons and the mean scattering angles are also obtained. The corrected experimental $\sigma(\theta)$ data of the converged iteration are converted to the center-of-mass system to give final $\sigma(\theta)$ data. The significance of finite geometry, attenuation, and multiple scattering corrections to ^{208}Pb(n,n)^{208}Pb elastic $\sigma(\theta)$ data at E_n=8.0 MeV is seen in Figure 4.3. The dominant correction is the flux attenuation of scattered neutrons as they traverse the scattering sample, which causes a lowering of the experimental yields by approximately the same factor across the entire distribution. Corrections for finite geometry and multiple scattering tend to deepen the valleys in the vicinity of $\sigma(\theta)$ minima and flatten the peaks in the vicinity of $\sigma(\theta)$ maxima.

4. Uncertainties in the data

There are three types of errors or uncertainties associated with the present differential cross section data: relative, normalization, and energy. Relative errors represent uncertainties in the shape of the distributions. For the ^{12}C $\sigma(\theta)$ scattering data, relative errors vary from 1.1% to 4.1% for elastic scattering and from 2.8% to 4.4% for inelastic scattering. Relative errors for the ^{208}Pb $\sigma(\theta)$ scattering data vary from 2.9% to 5.0% for elastic scattering and from 3.3% to 8.5% for inelastic scattering. Normalization errors represent scale uncertainties, and for all of the present $\sigma(\theta)$ data were taken to be 3.0%. Energy uncertainty represents uncertainty in knowledge of the exact or absolute energy at which measurements were made. In the present data, the mean incident energy of a 9.0 MeV neutron beam was believed to be known to within 60 keV. Error bars shown in figures and quoted later in Appendix A include only relative errors.

Relative errors include the uncertainties from neutron scattering yields, relative detector efficiencies, and multiple scattering corrections. The uncertainty in neutron scattering yields is due to counting statistics and uncertainty in the background underneath peaks of interest. Sample yield uncertainties ranged from 0.6% to 2.9% for elastic scattering and from 1.0% to 6.8% for inelastic scattering.

Uncertainty in the relative efficiency of the detectors is due to uncertainty in the shape of the efficiency curves. Because the present $\sigma(\theta)$ data were measured relative to n-p scattering, the detector efficiency enters into the expression for $\sigma(\theta)$ as a ratio, and both the absolute detector efficiency and the uncertainty in the absolute detector efficiency cancel. However, the uncertainty in the shape of the efficiency curve increases relative errors in the data due to the energy span covered by the scattered neutrons. Depending on scattering angle and whether they scatter elastically or inelastically, neutrons that scatter from the ^{12}C or ^{208}Pb target usually have a different energy than neutrons that

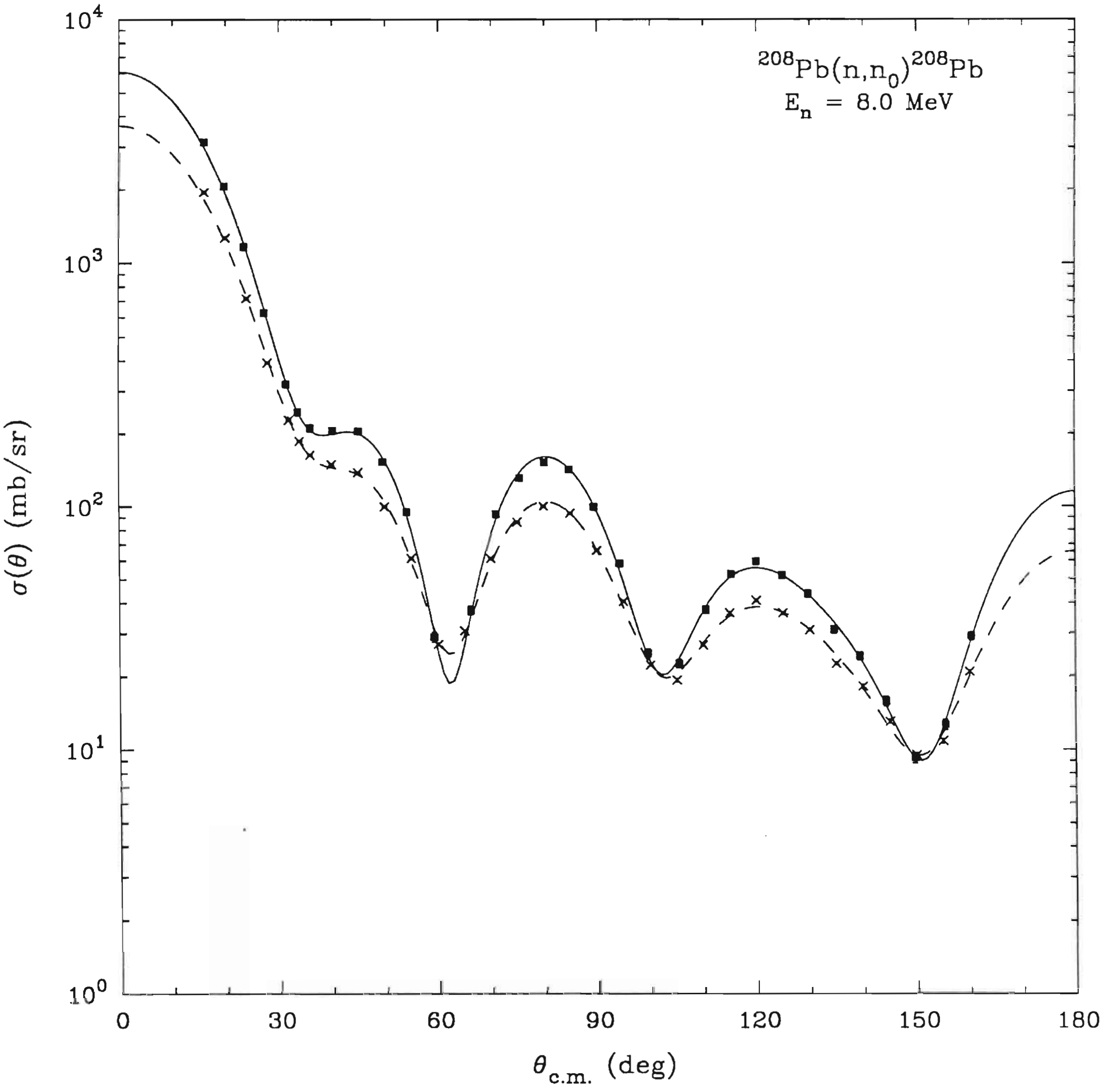

Figure 4.3. Attenuation, finite geometry, and multiple scattering corrections to elastic ^{208}Pb(n,n)^{208}Pb σ(θ) data at E_n=8.0 MeV. Normalized yields, uncorrected for attenuation, finite geometry, or multiple scattering, are indicated by x's and are connected by a dashed curve calculated from a Legendre polynomial fit. EFFIGY15 corrected differential cross sections are indicated by closed squares and are connected by a solid curve calculated from a Legendre polynomial fit.

scatter from the hydrogen nuclei in the polyethylene sample. Since the detectors used in the measurement have an efficiency that varies as a function of energy, the relative efficiency for detecting different energy neutrons must be determined and used when normalizing scattering data to n-p cross sections. Relative errors are increased because of uncertainty in this relative efficiency. Errors due to uncertainties in the relative detector efficiency range from 0% to 2.5%.

Uncertainty in the multiple scattering corrections contains the combined uncertainties in corrections for flux attenuation, multiple scattering, and angle corrections. Multiple scattering corrections were generally computed to a statistical accuracy such that the uncertainty in the corrections themselves had a negligible effect on the final quoted uncertainties. However, when the results of the multiple scattering calculations were applied to the data, statistical errors in the data were increased, particularly in the minimum of the $\sigma(\theta)$. This error enhancement was caused by the subtraction of multiple scattered neutrons from the observed neutron scattering yields, which effectively reduced the valid number of neutrons in the peaks of interest and increased the statistical errors. Therefore, uncertainties due to multiple scattering corrections were more dependent on the magnitude of the corrections than on the precision of the simulation.

In addition to uncertainties in neutron scattering yields, relative detector efficiencies and multiple scattering corrections, there is also an uncertainty in the angle at which measurements were made. Angular uncertainty represents uncertainty in the exact angular positions of the detectors relative to the optical beam axis and effects due to possible misalignment of the scattering sample along the beam axis or of the deuteron beam in the deuterium gas cell. The uncertainty in the cross section due to angular uncertainty is the range of possible cross sections $\delta\sigma = \pm(\sigma(\theta+\delta\theta)-\sigma(\theta-\delta\theta))/2$ within the angular uncertainty $\delta\theta$. Relative errors assigned to the present $\sigma(\theta)$ data do not include these angular uncertainties, however, because $\delta\theta$ is unknown. A reasonable angular uncertainty of $\pm 0.1°$, however, would cause an average increase of about 0.2% in the relative errors of ^{208}Pb forward angle $\sigma(\theta)$ data. Angle uncertainty effects would be largest in the forward angle region where the slope of $\sigma(\theta)$ is steep. Angular uncertainty effects on ^{12}C $\sigma(\theta)$ data and back angle ^{208}Pb $\sigma(\theta)$ data would be less because of the smaller variation in $\sigma(\theta)$ as a function of angle.

Normalization uncertainty includes uncertainties in electronic dead time, yields from n-p scattering used for normalization purposes, analytic corrections applied to n-p scattering yields, n-p cross sections, and the ratio n_H/n_S. No uncertainty was assigned to electronic dead time because the counting rates in the present measurements were much slower than the speed of the electronics. Uncertainty in n-p scattering yields due to counting statistics and uncertainty in the background underneath the n-p scattering peak were usually smaller than 0.6%. Analytic factors applied to n-p yields to correct the measured n-p yields for attenuation, finite geometry and multiple scattering within the polyethylene sample were determined to better than 1.4%. Uncertainties in the n-p cross section values were calculated by combining the 0.7% to 1.4% uncertainties reported by Hopkins and Breit (Hopkins 1971) with an additional angle uncertainty to cover the ±0.1° uncertainty in the n-p scattering angle. Uncertainty in the number of hydrogen nuclei in the polyethylene sample divided by the number of nuclei in the scattering sample (n_H/n_S) was less than 1.0%.

There is an uncertainty in the exact or absolute energy at which measurements were made. To obtain an estimate of the magnitude of this uncertainty, a 6.310 MeV deuteron beam (which, depending on deuterium gas cell pressure, would produce a neutron beam of ~9.0 MeV), which had been originally deflected by 38° into the time-of-flight beam leg, was deflected into the energy calibrated 52° beam leg. As the magnetic field of the analyzing magnet was raised from the 38° setting to the calibrated 52° setting, it was necessary to increase the terminal voltage on the Tandem Van de Graaff by 30 keV to properly center the deuteron beam on the control slits of the 52° beam leg. This 30 keV increase in the terminal voltage indicated an actual deuteron beam energy of about 6.250 MeV, almost 60 keV lower than originally thought. This 60 keV decrease in the deuteron beam energy would produce a decrease of the mean neutron energy of approximately 60 keV. A more exact determination of the energies at which measurements were made would require calibrating the 38° time-of-flight beam leg against known thresholds or resonances. When this is done, the energies of the present experiments can be adjusted accordingly.

5. Presentation of final data

After the differential cross section data were corrected for finite geometry, attenuation, and multiple scattering, they were described in the center-of-mass system by an expansion of Legendre polynomials, with the following form:

$$\sigma(\theta,E) = \sum_{l=0}^{n} A_l(E)\cdot P_l(\cos\theta) \qquad (4\text{-}3)$$

where $A_l(E)$ are the Legendre polynomial expansion coefficients. The computer code MACRO was used to obtain the Legendre polynomial expansion coefficients such that total chi-square (χ^2):

$$\chi^2 = \sum_{i=1}^{n} \left[\frac{\sigma^{exp}(\theta_i) - \sigma^{cal}(\theta_i)}{\Delta\sigma^{exp}(\theta_i)} \right]^2 \tag{4-4}$$

is a minimum, where, $\sigma^{exp}(\theta_i)$ is the differential cross section measured at θ_i in the center-of-mass system, $\sigma^{cal}(\theta_i)$ is the cross section calculated by MACRO at θ_i, and $\Delta\sigma^{exp}(\theta_i)$ is the uncertainty associated with $\sigma^{exp}(\theta_i)$.

Differential cross sections at 11.01 and 13.76 MeV for elastic neutron scattering from ^{12}C and for inelastic neutron scattering from the first excited state of ^{12}C ($J^\pi=2^+$, Q=-4.439 MeV) are shown in Figures 4.4 and 4.5, respectively. Differential cross sections at 8.0 MeV for elastic neutron scattering and inelastic neutron scattering to the first excited state of ^{208}Pb ($J^\pi=3^-$, Q=-2.614 MeV) are shown in Figure 4.6. The curves in Figures 4.4, 4.5, and 4.6 are Legendre polynomial fits to the data.

Corrected differential cross section data for ^{12}C and ^{208}Pb are tabulated in Appendix A. The tabulations include coefficients derived from Legendre polynomial fits to the data, normalized uncorrected lab data, corrected center-of-mass data, and relative uncertainties for the data.

B. Analyzing power measurements

1. Neutron yield extraction

To obtain the current analyzing power ($A_y(\theta)$) values, neutron yields had to be extracted from time-of-flight spectra. Neutron yields were obtained by setting windows about peaks of interest in difference spectra, and events within that window were counted and stored using a self-contained data analysis package called PTOFOFF. This analysis package contains a series of programs operating under the TUNL XSYStem software package that can display spectra, normalize spectra, subtract or add spectra together, draw polynomial backgrounds, set windows, and store yields. PTOFOFF is similar to NTOFOFF, the data analysis code for $\sigma(\theta)$ data, with the exception that difference spectra must be calculated for spin-up and spin-down measurements for both the right and left detectors.

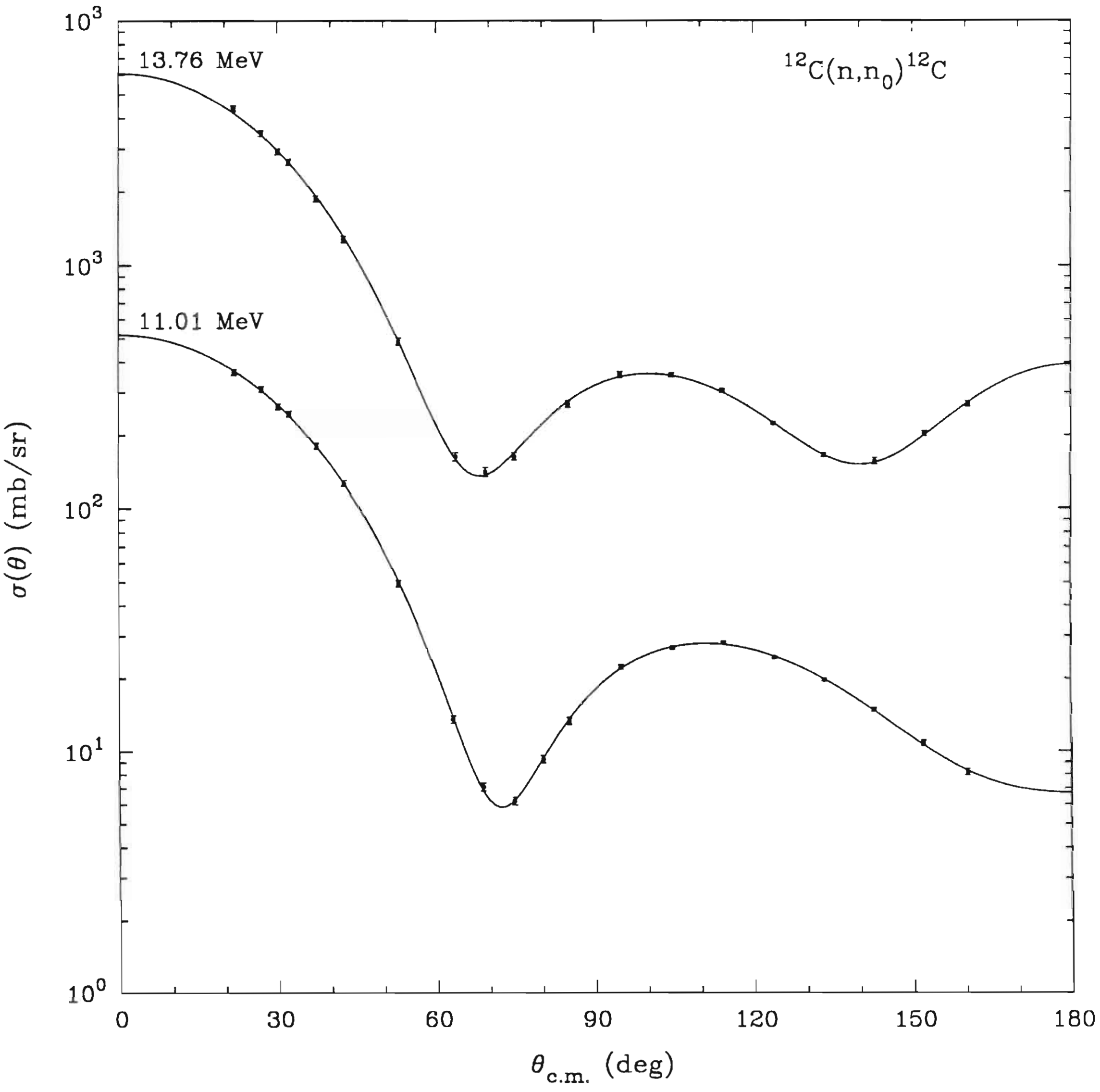

Figure 4.4. Differential cross sections for elastic neutron scattering from ^{12}C at 11.01 MeV and 13.76 MeV in the center-of-mass system. The curves are Legendre polynomial fits to the data.

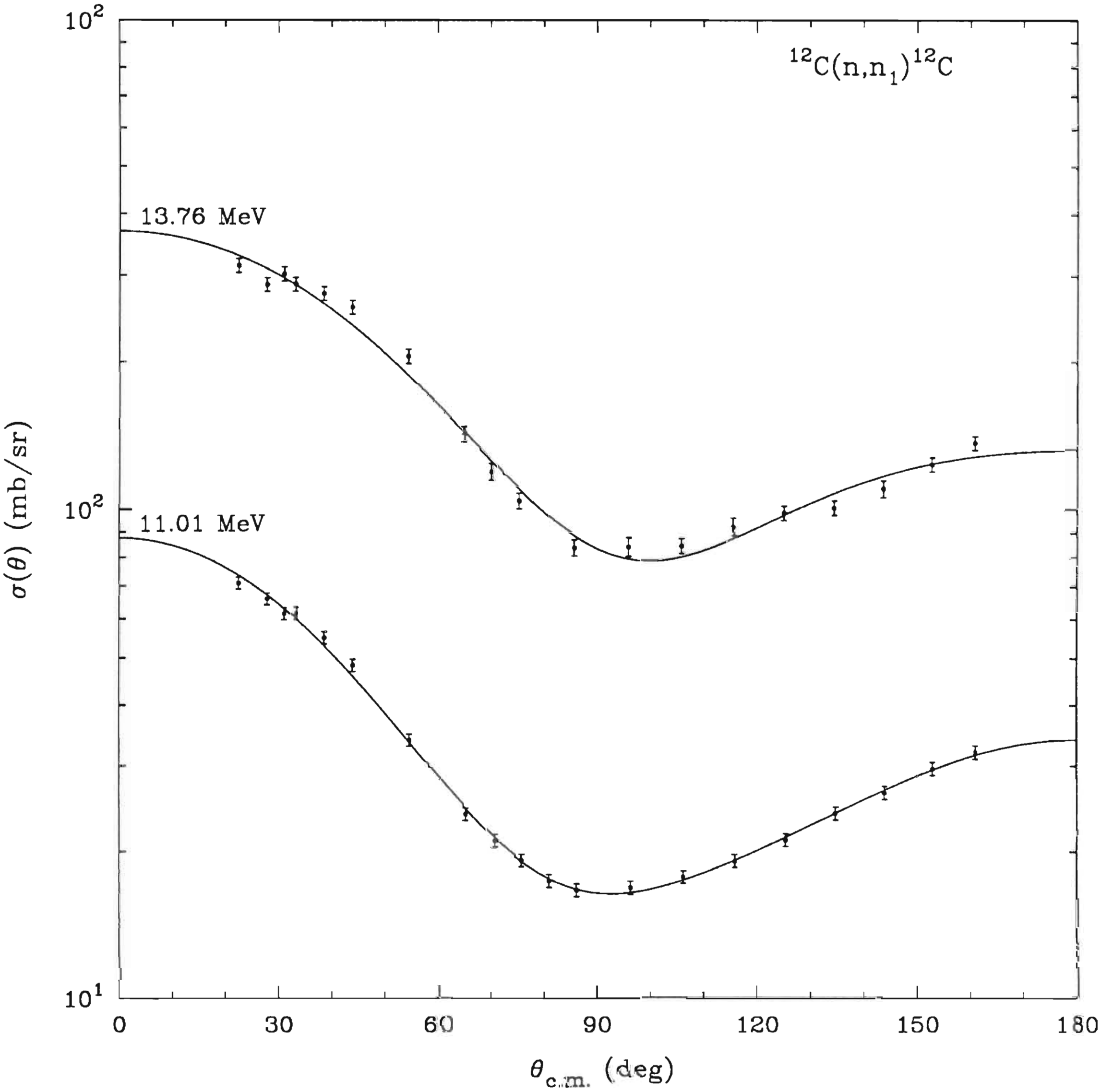

Figure 4.5. Differential cross sections for inelastic neutron scattering from the first excited state ($J^{\pi}=2^+$, Q=-4.439 MeV) of ^{12}C at 11.01 MeV and 13.76 MeV in the center-of-mass system. The curves are Legendre polynomial fits.

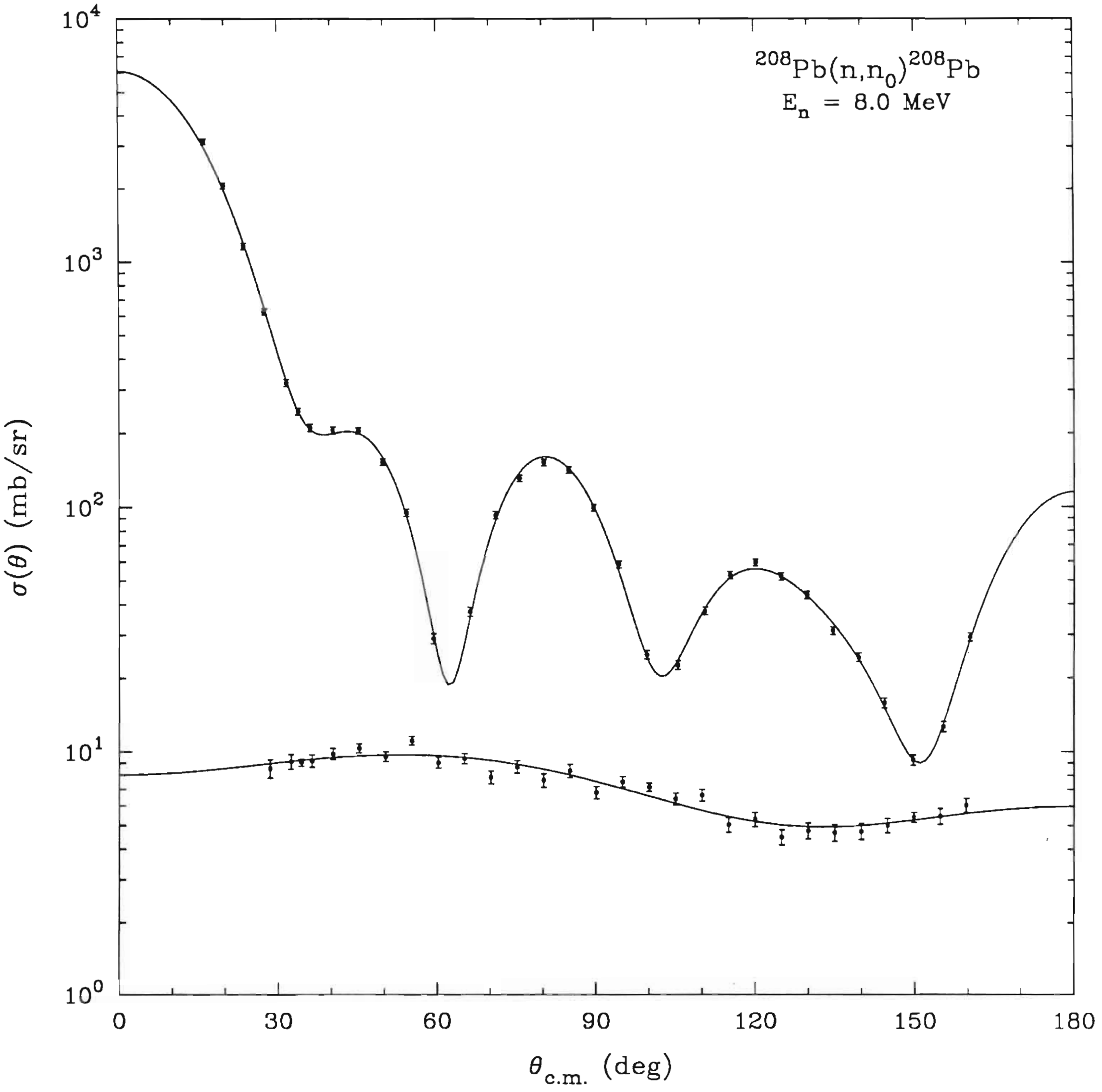

Figure 4.6. Differential cross sections for elastic neutron scattering from ^{208}Pb and inelastic neutron scattering from the first excited state ($J^{\pi}=3^-$, Q=-2.614 MeV) of ^{208}Pb at 8.0 MeV in the center-of-mass system. The curves are Legendre polynomial fits.

To obtain difference (DIFF) spectra, sample-out (OUT) time-of-flight spectra for spin-up and spin-down for both the right and left detectors were scaled by the ratio of sample-in to sample-out integrated beam current and then subtracted from the corresponding sample-in (IN) time-of-flight spectra:

$$\mathrm{DIFF} = \mathrm{IN} - \frac{\text{BCI-IN}}{\text{BCI-OUT}} \cdot \mathrm{OUT}\,, \tag{4-5}$$

where BCI-IN is the sample-in integrated beam current and BCI-OUT is the sample-out integrated beam current. An example of a sample-in time-of-flight spectrum, a normalized sample-out time-of-flight spectrum, and difference spectrum is shown in Figure 4.7. After difference spectra were formed, backgrounds were drawn in the difference spectra to remove sample correlated backgrounds not measured in the out count. Within statistical uncertainties, the background usually had the same level for both the spin-up and spin-down spectra and could be adequately described with a linear function. After backgrounds were drawn, windows were chosen about peaks of interest, and yields were calculated by summing the number of events inside the window and above the background. In contrast to the $\sigma(\theta)$ case, where all good neutron events had to be included in the chosen window, it is often desirable to choose narrow windows about the peaks of interest in $A_y(\theta)$ difference spectra . Narrow windows can optimize the signal-to-noise ratio (i.e., the ratio of yield to background) and improve statistical uncertainties in neutron scattering yields. For each state, there were four yields of interest: left detector spin-up (Y_{LU}), left detector spin-down (Y_{LD}), right detector spin-up (Y_{RU}), and right detector spin-down (Y_{RD}).

2. Calculation of analyzing powers

The four neutron yields obtained at each angle for each state of interest were combined to obtain the quantity $\alpha(\theta)$ as follows:

$$\alpha(\theta) = \sqrt{\frac{Y_{LU}(\theta)}{Y_{LD}(\theta)} \frac{Y_{RD}(\theta)}{Y_{RU}(\theta)}} \tag{4–6}$$

with Y_{LU} , Y_{LD} , Y_{RU} , and Y_{RD} as defined above. Analyzing power values were calculated from $\alpha(\theta)$ using the formula:

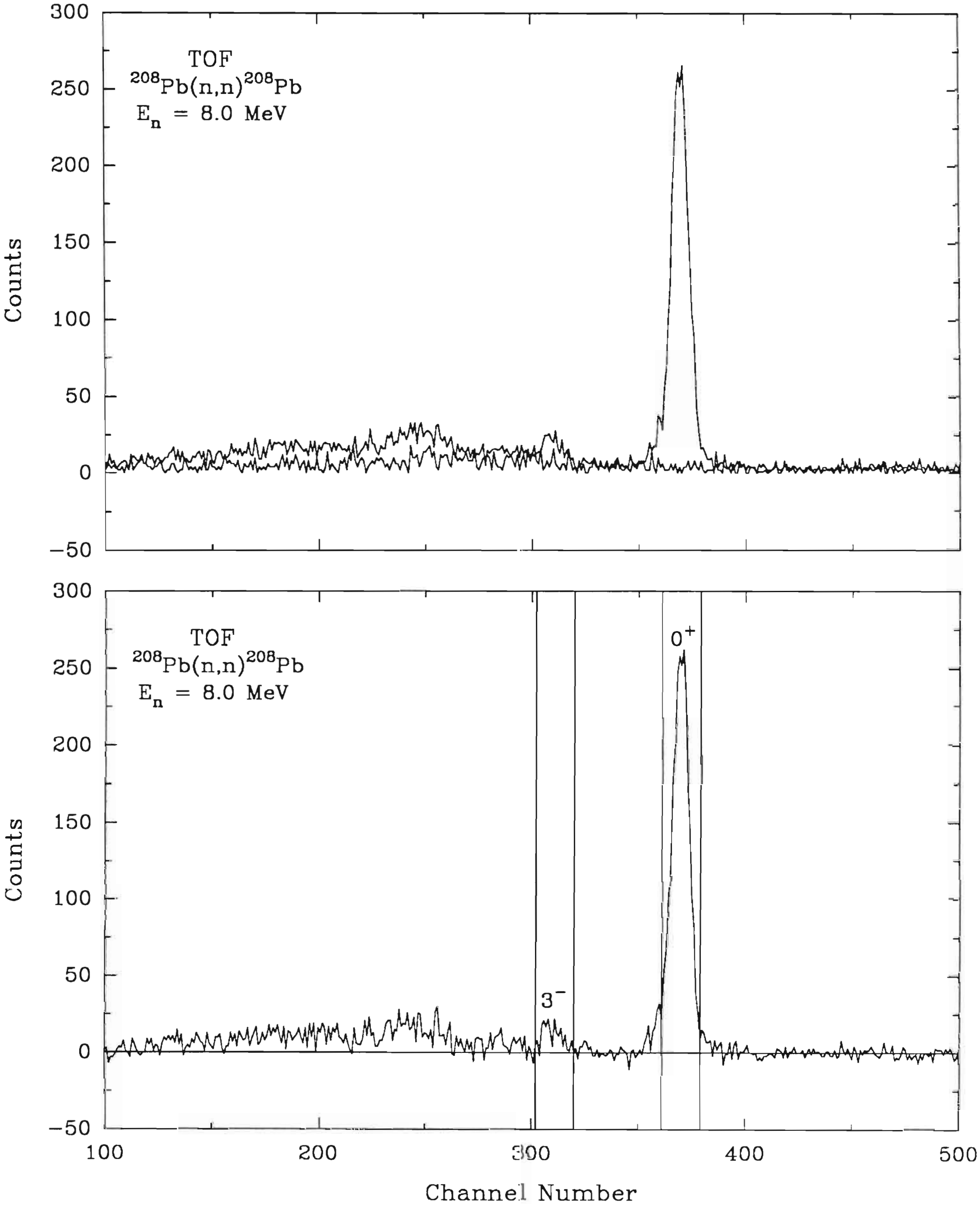

Figure 4.7. IN, OUT, and DIFF spectra for the scattering of 8.0 MeV polarized neutrons from ^{208}Pb through a laboratory angle of 85°. The elastic and inelastic scattering peaks are labeled 0^+ and 3^-, respectively. In the difference spectrum, the solid line is the background estimate in the region of the peaks, while the four vertical lines indicate the limits of the two windows chosen.

$$A_y(\theta) = \frac{1}{p_n}\left[\frac{\alpha - 1}{\alpha + 1}\right] \qquad (4\text{–}7)$$

where p_n is the polarization of the neutron beam.

Neutron beam polarizations were calculated from the incident deuteron beam vector polarization (p_z) using the polarization transfer function reported by Ohlsen and Keaton (Ohlsen 1973) for the ^{2}H(d,n)^{3}He neutron source reaction:

$$p_n(0°,E_d) = \frac{\frac{3}{2}\cdot K_y^y(0°,E_d)\cdot p_z}{1 - \frac{1}{4}\cdot A_{zz}(0°,E_d)\cdot p_{zz}} \qquad (4\text{-}8)$$

where $A_{zz}(0°,E_d)$ is the zero degree tensor analyzing power, $K_y^y(0°,E_d)$ is the zero degree polarization transfer coefficient, and p_{zz} is the tensor polarization of the incident deuteron beam and is equal to the vector polarization of the incident beam ($p_{zz} = p_z$) in our mode of operation of the polarized ion source.

The zero degree tensor analyzing powers and zero degree polarization transfer coefficients were calculated using least-squares fits to data measured by Lisowski *et al.* (Lisowski 1975). The zero degree tensor analyzing powers were described by Lisowski *et al.* (Lisowski 1975) with a third-order polynomial for deuteron energies below 3.0 MeV:

$$A_{zz}(0°,E_d) = -0.8838 + 0.3218E_d - 0.0776E_d^2 + 0.0055E_d^3\ , \qquad (4\text{-}9)$$

while for deuteron energies above 3.0 MeV, the data were described by a constant:

$$A_{zz}(0°,E_d) = -0.461\ . \qquad (4\text{-}10)$$

The zero degree polarization transfer coefficients were described by Lisowski *et al.* (Lisowski 1975) with a third-order polynomial for deuteron energies below 4.0 MeV:

$$K_y^y(0°,E_d) = 0.2475 + 0.2604E_d - 0.0588E_d^2 + 0.0046E_d^3\ , \qquad (4\text{-}11)$$

while for deuteron energies above 4.0 MeV, the data were fit with a first-order polynomial:

$$K_y^y(0°,E_d) = 0.6624 - 0.0032E_d \,. \tag{4-12}$$

3. Finite geometry, attenuation, and multiple scattering corrections

As with $\sigma(\theta)$ data, the observable $A_y(\theta)$ is defined for scattering from a point sample into a point detector, i.e., a sample and detector of negligible cross-sectional area. Since polarized neutron time-of-flight measurements require large samples and detectors, the effects of finite geometry, flux attenuation, and multiple scattering on the observed analyzing power cannot be ignored and corrections must be made. At TUNL, corrections for attenuation, multiple scattering and finite geometry to analyzing power data are calculated using a TUNL version of a Monte Carlo code called JANE (written by E. Woye, unpublished) and a data manipulation code called CORE. As with EFFIGY15, the equivalent Monte Carlo code used for correcting $\sigma(\theta)$ data, JANE simulates an experiment in the lab system and calculates corrections to $A_y(\theta)$ data using an iterative procedure. Since JANE must distinguish scattering to the left from scattering to the right and keep track of the neutron polarization after successive scattering processes, the procedure for correcting $A_y(\theta)$ data is more complicated than correcting $\sigma(\theta)$ data. A brief description of the corrections will be presented below.

Because of the combination of finite-sized neutron source, finite-sized scattering sample, and finite-sized detector, the measured analyzing power is the average analyzing power for a range of angles. For the present work, using the ^{208}Pb sample, the range in scattering was approximately 5°. The main contribution to this 5° was the scattering angle subtended by the sample as seen by the source volume of the gas cell.

Attenuation of the neutron beam in the sample causes the portion of the sample closest to the neutron source to be more highly illuminated than the rest of the sample. This attenuation shifts the effective center of the sample closer to the neutron source and causes the effective scattering angle to be smaller than the nominal laboratory angle.

In JANE, finite geometry and attenuation effects are combined into a single finite geometry correction factor (*F*) defined as:

$$F = A_s(\theta_p) - A_s(\theta_f) \,, \tag{4-13}$$

where $A_s(\theta_p)$ is the desired single-scattering (s) analyzing power for a point source, sample, and detector, and $A_s(\theta_f)$ is the single-scattering analyzing power in which the finite geometry effects of the source, scattering sample, and detector are taken into account. The finite geometry correction factor (F) involves both a change in the magnitude of the analyzing power and a shift in the scattering angle. The largest finite geometry correction factors occur when both the cross section and analyzing power are changing rapidly. The effect (recently discussed by Tornow *et al.* (Tornow 1988)) of an instrumental asymmetry caused by an apparent shift in the center of the scattering sample due to the analyzing power in the ^{2}H(d,n)^{3}He source reaction was not included in the finite geometry correction factor (F) because its effect was negligible when compared to the uncertainties in the present measurement.

Because of the large scattering sample used in the present $A_y(\theta)$ measurements, some neutrons can scatter more than once in the sample and still be detected. When neutrons scatter more than once in the sample, the observed analyzing power ($A_e(\theta_f)$) can be expressed as a weighted sum of the effective analyzing powers for scattering processes of different order (single (s), double (d), triple (t), and so on):

$$\begin{aligned} A_e(\theta_f) &= P_s A_s(\theta_f) + P_d A_d(\theta_f) + P_t A_t(\theta_f) + \cdots \\ &= P_s\,(\,A_s(\theta_f) + R_{ds}A_d(\theta_f) + R_{ds}R_{td}A_t(\theta_f) + \cdots) \end{aligned} \tag{4-14}$$

where the absolute scattering probabilities (P_i) have been rewritten in terms of ratios between successive scattering probabilities ($R_{i,i-1}$):

$$\begin{aligned} 1 &= P_s + P_d + P_t + \cdots \\ &= P_s\,(\,1 + R_{ds} + R_{ds}R_{td} + \cdots) \end{aligned} \tag{4-15}$$

By inverting Equation 4-14, the desired single-scattering finite-geometry result ($A_s(\theta_f)$) can be expressed in terms of the experimentally observed total-scattering value ($A_e(\theta_f)$):

$$A_s(\theta_f) = A_e(\theta_f)/P_s - R_{ds}A_d(\theta_f) - R_{ds}R_{td}A_t(\theta_f) - \cdots \tag{4-16}$$

To truncate the infinite series in Equation (4-16) and limit the necessary Monte Carlo calculations to a particular level of multiple scattering, two approximations were made. The first approximation was the assumption that the analyzing power for triple and higher order scatterings was zero. The second approximation was that the ratio of successive probabilities ($R_{i,i-1}$) was assumed to approach a constant value for $i > 2$. This limiting value, defined R_∞, was approximately equal to the average value of R_{ds} at back angles and permitted P_s to be calculated by summing higher-order terms in Equation (4-15) as a geometric series in powers of R_∞, giving:

$$P_s = \frac{1 - R_\infty}{1 - R_\infty + R_{ds}} . \tag{4-17}$$

Both assumptions have been investigated by the author and others (Guss 1982, Byrd 1984) and have been shown to introduce a negligible error when compared to the uncertainties in the present measurement.

With these approximations, only a double-scattering calculation was needed to convert the experimentally measured total-scattering analyzing power into the corrected single-scattering result:

$$A_s(\theta_p) = A_e(\theta_f)\cdot(1 - R_\infty + R_{ds})/(1 - R_\infty) - R_{ds}A_d(\theta_f) + F . \tag{4-18}$$

Using the computer code JANE, the experiment was simulated with a library of analyzing powers, total and differential cross sections, and physical parameters of the experiment to generate time-of-flight spectra at each angle for which measurements were made. In the first iteration of JANE, experimentally observed finite-geometry analyzing powers were used for the initial analyzing power library. In each iteration of JANE, for every experimentally measured angle, 10 000 single scattering histories and 40 000 double scattering histories were generated. A single history is a set of random sites in the gas cell, scattering sample, and detector, where the respective neutron was created, scattered, and detected. At each angle, simulated time-of-flight spectra were created for spin-up or spin-down and singly or doubly scattered neutrons. From the simulated time-of-flight spectra, JANE calculated the ratio of doubly to singly scattered neutrons (R_{ds}), the analyzing power of doubly scattered neutrons ($A_d(\theta_f)$), and the finite geometry correction factor (F). The quantities calculated in JANE and the uncorrected experimental data were input into the data manipulation code CORE. The code CORE used Equation 4-18 to compute corrected single-scattering analyzing powers. The corrected single-scattering analyzing powers were fit with an associated Legendre polynomial expansion which was used to create a revised version of the JANE analyzing power library. Successive iterations of JANE were performed and the analyzing power library updated after each iteration. After each iteration of JANE, corrected analyzing powers were checked to see if convergence was achieved. Convergence is reached when the corrected analyzing powers of the present iteration do not disagree significantly from the corrected analyzing powers of the previous iteration. In practice, only three iterations of JANE were usually needed to achieve convergence. The single-scattering analyzing powers computed by CORE in the last iteration are considered to be the final corrected $A_y(\theta)$ values. The significance of finite geometry and multiple scattering corrections on ^{208}Pb(n,n)^{208}Pb elastic $A_y(\theta)$ data at E_n=8.0 MeV is shown in Figure 4.8. The dominant effect of multiple scattering is to decrease the magnitude of the experimentally observed analyzing power, since the contributions from multiply scattered neutrons yield a smaller analyzing power.

4. Uncertainties in the data

As with $\sigma(\theta)$ data, the present $A_y(\theta)$ data have relative, normalization, and energy uncertainties. Relative errors represent uncertainties in the shape of the distributions and vary from 0.7% to 8.6% for elastic scattering and from 5.9% to 35% for inelastic scattering. Normalization errors represent scale uncertainties and were taken in the present data to be 3.0%. Energy uncertainty represents uncertainty in knowledge of the exact or absolute energy at which measurements were made. As was discussed for the $\sigma(\theta)$ data in section A-4 of this chapter, the mean incident energy of a 9.0 MeV neutron beam was believed to be known to within 60 keV. Error bars shown in figures and quoted later in Appendix B include only relative uncertainties.

Relative errors include uncertainties from sample yields and multiple scattering corrections. The uncertainty in neutron scattering yields is due to counting statistics and uncertainty in the background underneath peaks of interest. Neutron scattering yield uncertainties range from 0.6% to 6.4% for elastic scattering and from 4.5% to 27% for inelastic scattering.

Uncertainty in the multiple scattering corrections contains the combined uncertainties in corrections for finite geometry, flux attenuation, and multiple scattering. Multiple scattering corrections were generally computed to a statistical accuracy such that the uncertainty in the corrections themselves had a negligible effect on the the final quoted

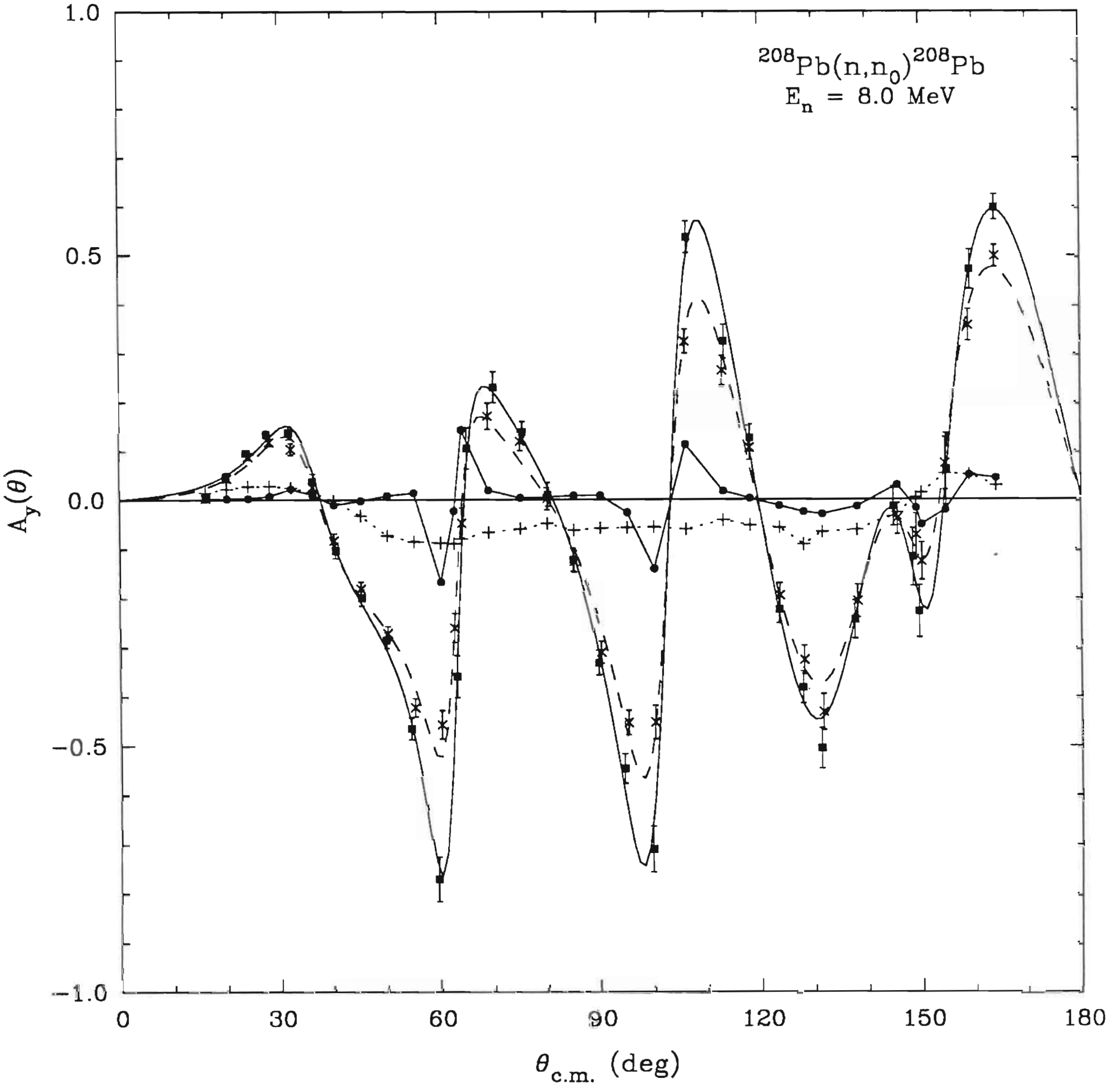

Figure 4.8. Attenuation, finite geometry, and multiple scattering corrections to elastic ^{208}Pb(n,n)^{208}Pb $A_y(\theta)$ data at E_n=8.0 MeV. Experimentally measured total-scattering analyzing powers are indicated by x's and are connected by a dashed curve calculated from an associated Legendre polynomial fit. Double-scattering analyzing powers, calculated by JANE, are represented by crosses and are connected by a dashed line. Finite geometry correction factors are represented by closed circles and are connected by a solid line. The largest geometry correction factors occur when both the cross section and analyzing power are changing rapidly. Final single-scattering analyzing powers, calculated by CORE, are represented by closed squares and are connected by a solid curve calculated from an associated Legendre polynomial fit.

uncertainties. However, when the results of the multiple scattering calculations were applied to $A_y(\theta)$ data, statistical errors in the data were increased, particularly for analyzing power measurements taken near the minimum of the cross section. This error enhancement was caused by the subtraction of multiple scattered neutrons from the observed neutron scattering yields, which effectively reduced the valid number of neutrons in the peaks of interest and increased statistical errors. Therefore, uncertainties due to multiple scattering corrections were more dependent on the magnitude of the effects than on the precision of the simulation.

Normalization or scale uncertainty includes uncertainties in electronic dead time, beam polarization measurements, zero degree tensor analyzing powers, and zero degree vector polarization transfer coefficients. As with $\sigma(\theta)$ data, no uncertainty was assigned to electronic dead time for $A_y(\theta)$ measurements because the counting rates in these experiments were much lower than the speed of the electronics. To cover uncertainties in quench ratio techniques and instabilities of the beam during quench ratio measurements, an error of ±0.01 to ±0.02 was assigned to the deuteron beam polarization values. Tensor analyzing powers and vector polarization transfer coefficients used to obtain the neutron beam polarization at zero degrees were measured by Lisowski (Lisowski 1973) and were reported to a statistical accuracy of better than ±0.017 and ±0.010, respectively. Combining the uncertainty in beam polarization measurements, zero degree tensor analyzing powers, and zero degree vector polarization gives an overall uncertainty in the neutron polarization of between ±0.02 and ±0.03.

5. Presentation of final data

After the analyzing power data were corrected for attenuation, finite geometry, and multiple scattering, they were described in the center-of-mass system with functions that were derived from fitting an associated Legendre polynomial expansion to the product $A_y(\theta,E)\cdot\sigma(\theta,E)$. The expansion has the form:

$$A_y(\theta,E)\cdot\sigma(\theta,E) = \sum_{l=1}^{n} B_l(E)\cdot P_l^1(\cos\theta) \qquad (4\text{-}19)$$

where $B_l(E)$ are the associated Legendre polynomial expansion coefficients. The computer code MACRO was used to obtain the associated Legendre polynomial expansion coefficients such that total chi-square (χ^2):

$$\chi^2 = \sum_{i=1}^{n} \left[\frac{A_y^{exp}(\theta_i) - A_y^{cal}(\theta_i)}{\Delta A_y^{exp}(\theta_i)} \right]^2 \qquad (4\text{-}20)$$

is a minimum, where $A_y^{exp}(\theta_i)$ is the analyzing power measured at θ_i in the center-of-mass system, $A_y^{cal}(\theta_i)$ is the analyzing power calculated by MACRO at θ_i, and $\Delta A_y^{exp}(\theta_i)$ is the uncertainty associated with $A_y^{exp}(\theta_i)$. The cross sections used in calculating the fits were determined from Legendre polynomial fits to $\sigma(\theta)$ data.

Analyzing powers at 6.0, 7.0, 8.0, 9.0, and 10.0 MeV for elastic neutron scattering from ^{208}Pb are shown in Figure 4.9. Figure 4.10 shows a comparison of the present ^{208}Pb 10.0 MeV elastic neutron analyzing power data to data previously measured by Floyd (Floyd 1981). Analyzing powers at 6.0, 7.0, 8.0, 9.0, and 10.0 MeV for inelastic neutron scattering from the first excited state of ^{208}Pb ($J^\pi=3^-$, Q=-2.614 MeV) are shown in Figure 4.11. The curves in Figures 4.9, 4.10 and 4.11 are associated Legendre polynomial fits.

Corrected analyzing power data for ^{208}Pb are tabulated in Appendix B. The tabulations include coefficients derived from associated Legendre polynomial fits to the data, uncorrected lab data, corrected center-of-mass data and relative uncertainties.

6. Compound nucleus contributions

A compound nucleus is formed when the target nucleus absorbs an incident particle and forms a compound system in which the total energy of the incoming particle is shared with all of the other nucleons in the system and the identity of the incoming particle is lost. Since the scattering models used later in this work calculate only shape elastic results (i.e., processes that occur without formation of a compound nucleus), compound elastic contributions to elastic scattering results must be determined and measured values adjusted.

After a compound nucleus is formed, it decays either through photon emission, neutron emission, or other massive-particle emission, if kinematically allowed. The decay of a compound nucleus is independent of its mode of formation, and the probability of a compound nucleus decaying through the entrance or elastic channel is largest when few other reactions are kinematically allowed (i.e., at lower compound nucleus excitation energies). Because the lifetime of the compound nucleus is extremely short (~10^{-16} s), the particles that are emitted from the decay of the compound system back into the ground state of the target nucleus are experimentally indistinguishable from

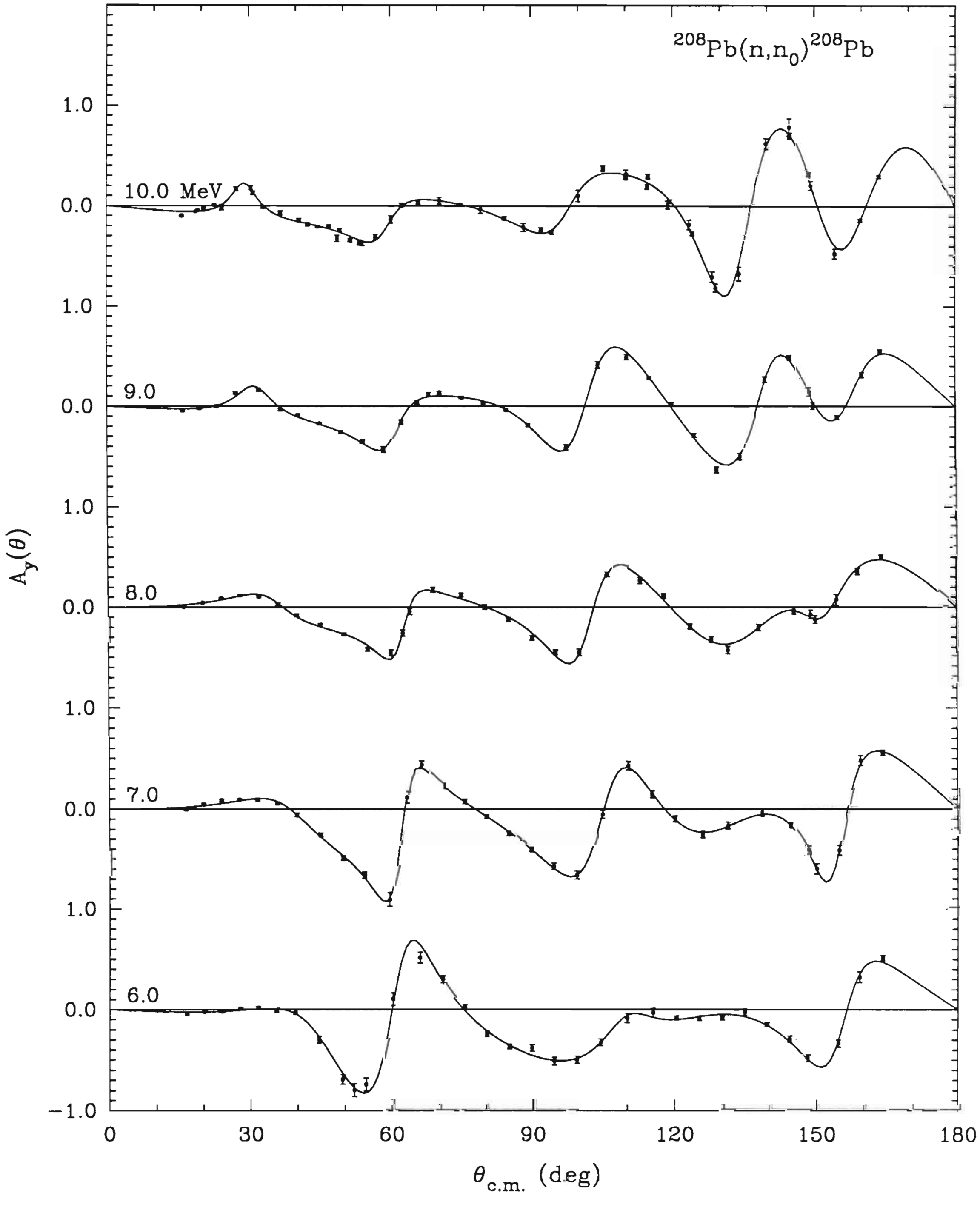

Figure 4.9. Analyzing powers for elastic neutron scattering from ^{208}Pb at 6.0, 7.0, 8.0, 9.0, and 10.0 MeV in the center-of-mass system. The curves are associated Legendre polynomial fits. The data shown at 10.0 MeV include data measured for the present work and data measured by Floyd (Floyd 1981).

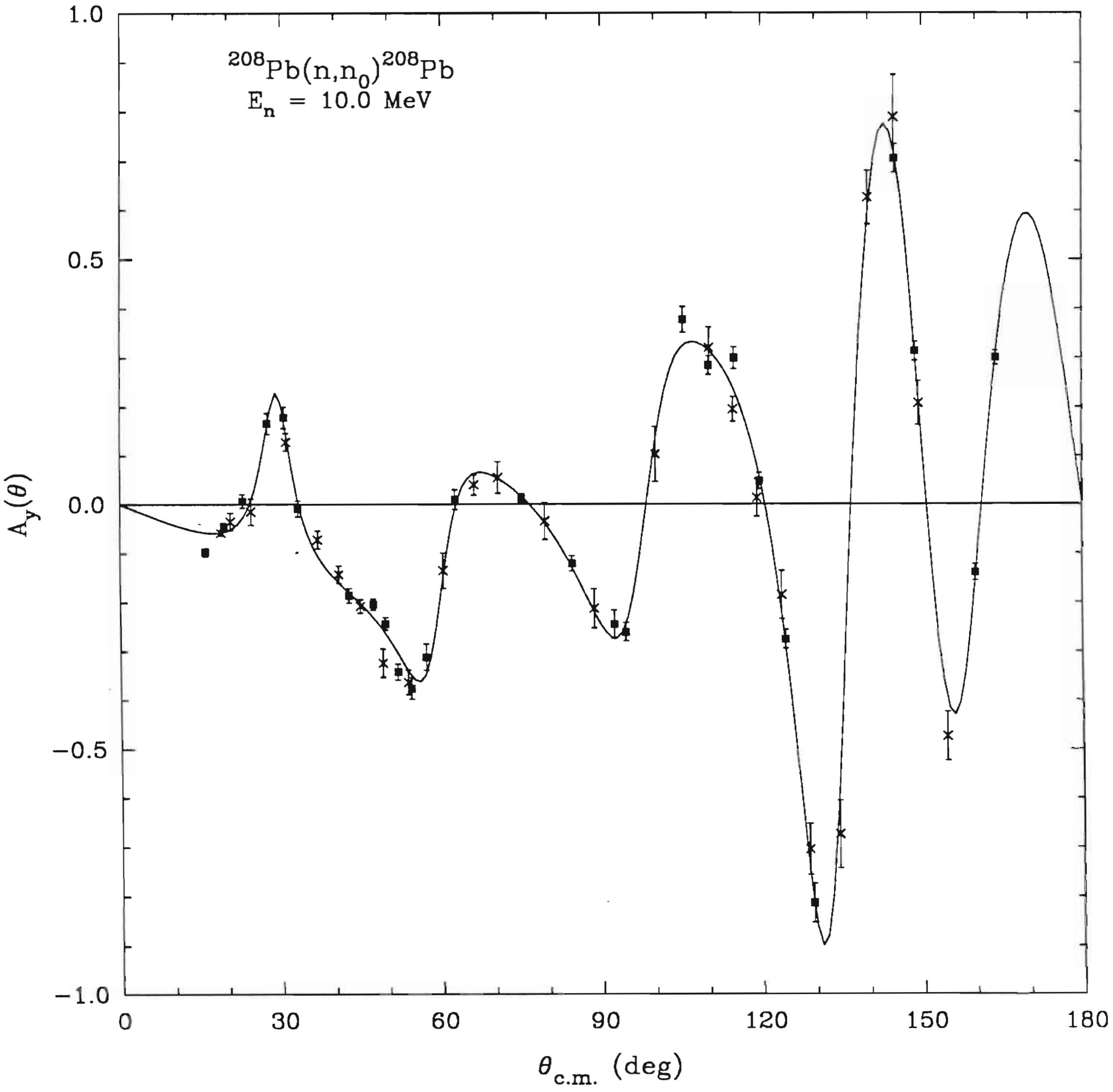

Figure 4.10. Comparison of the present 10.0 MeV elastic neutron analyzing power data from ^{208}Pb to data measured previously by Floyd (Floyd 1981). Data measured for the present work are indicated by closed squares while data measured by Floyd (Floyd 1981) are represented by x's. The curve is an associated Legendre polynomial fit to both sets of data.

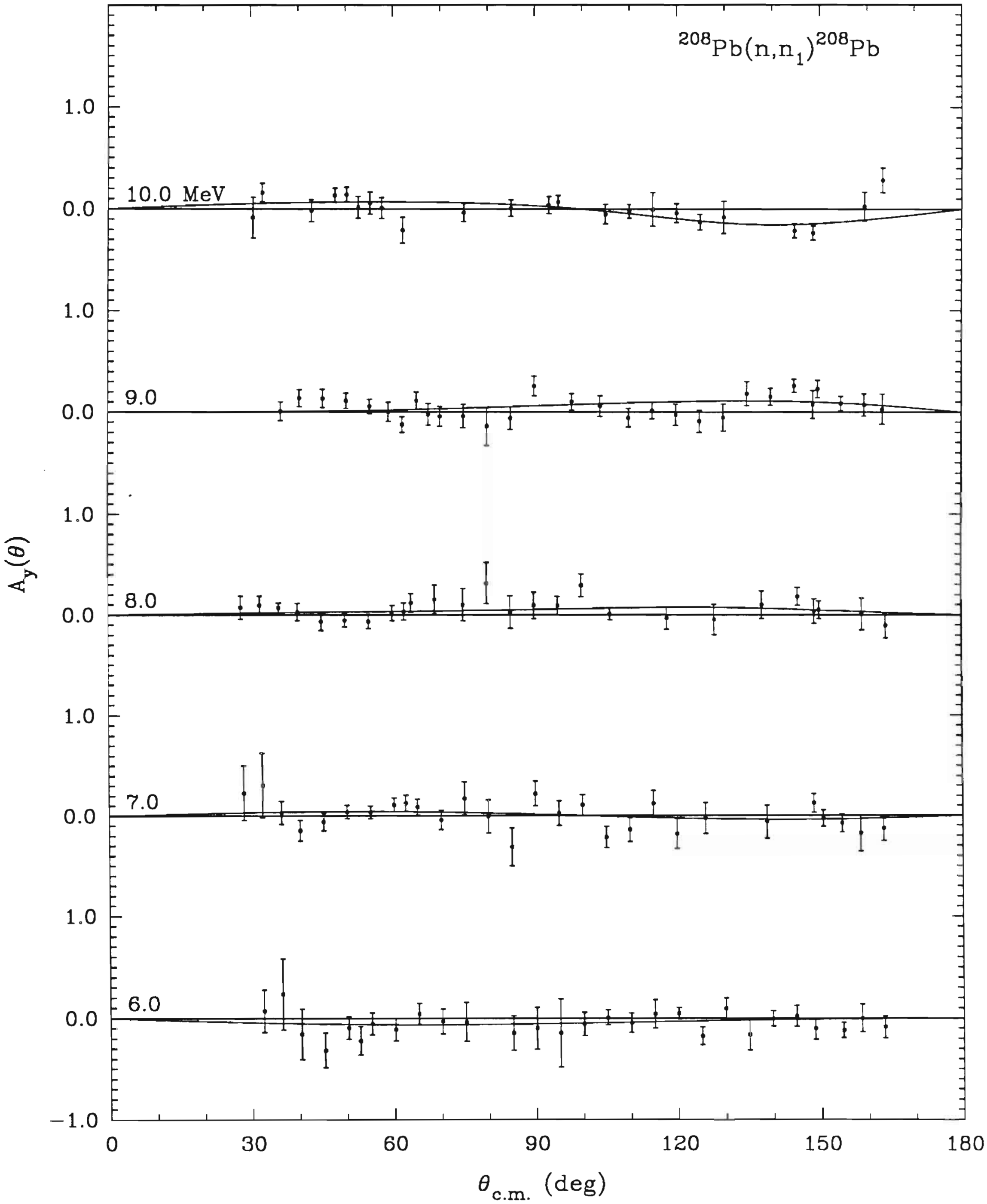

Figure 4.11. Analyzing powers for inelastic neutron scattering from the first excited state ($J^\pi=3^-$, Q=-2.614 MeV) of ^{208}Pb at 6.0, 7.0, 8.0, 9.0, and 10.0 MeV in the center-of-mass system. The curves are associated Legendre polynomial fits.

identical particles that result from shape elastic processes. As the incident particle energy rises, more reaction channels open up and the probability of a compound nucleus decaying through the entrance channel becomes increasingly smaller. Data taken for this work spans the transition region between where compound nucleus effects for ^{208}Pb become important (E<~7 MeV) and the region where compound nucleus effects become negligible (E>~8 MeV).

Observed neutron elastic cross sections ($\sigma^{OBS}(\theta)$) can be expressed as an incoherent sum of shape elastic ($\sigma^{SE}(\theta)$) and compound elastic ($\sigma^{CE}(\theta)$) cross sections:

$$\sigma^{\mathrm{OBS}}(\theta) = \sigma^{\mathrm{SE}}(\theta) + \sigma^{\mathrm{CE}}(\theta)\,, \tag{4-21}$$

while the observed analyzing power ($A_y^{OBS}(\theta)$) can be expressed as a weighted sum of the shape elastic ($A_y^{SE}(\theta)$) and compound elastic analyzing powers ($A_y^{CE}(\theta)$):

$$A_y^{\mathrm{OBS}}(\theta) = \frac{\sigma^{\mathrm{SE}}(\theta)}{\sigma^{\mathrm{OBS}}(\theta)} \cdot A_y^{\mathrm{SE}}(\theta) + \frac{\sigma^{\mathrm{CE}}(\theta)}{\sigma^{\mathrm{OBS}}(\theta)} \cdot A_y^{\mathrm{CE}}(\theta)\,. \tag{4-22}$$

In the process of compound nucleus formation the incident particle loses its spin orientation causing the compound elastic analyzing power to become zero ($A_y^{CE}=0$). Therefore, the shape elastic analyzing power is:

$$A_y^{\mathrm{SE}}(\theta) = \frac{\sigma^{\mathrm{OBS}}(\theta)}{\sigma^{\mathrm{SE}}(\theta)} \cdot A_y^{\mathrm{OBS}}(\theta)\,. \tag{4-23}$$

For the present ^{208}Pb(n,n)^{208}Pb elastic scattering analyzing power data at 8.0, 9.0, and 10.0 MeV, the compound elastic cross sections were negligible and effects upon shape elastic analyzing powers were ignored. For elastic analyzing power data at 6.0 and 7.0 MeV, compound elastic cross sections were not negligible and corrections to the data were made using Equation 4-21. For both the 6.0 and 7.0 MeV data, compound elastic cross sections were derived from observed and shape elastic cross sections reported by Annand *et al.* (Annand 1985). Figure 4.12 shows the compound nucleus effects on $A_y(\theta)$ at 6.0 MeV for ^{208}Pb(n,n)^{208}Pb elastic scattering. Compound nucleus effects on $A_y(\theta)$ at 7.0 MeV for ^{208}Pb(n,n)^{208}Pb elastic scattering were much smaller. Appendix C

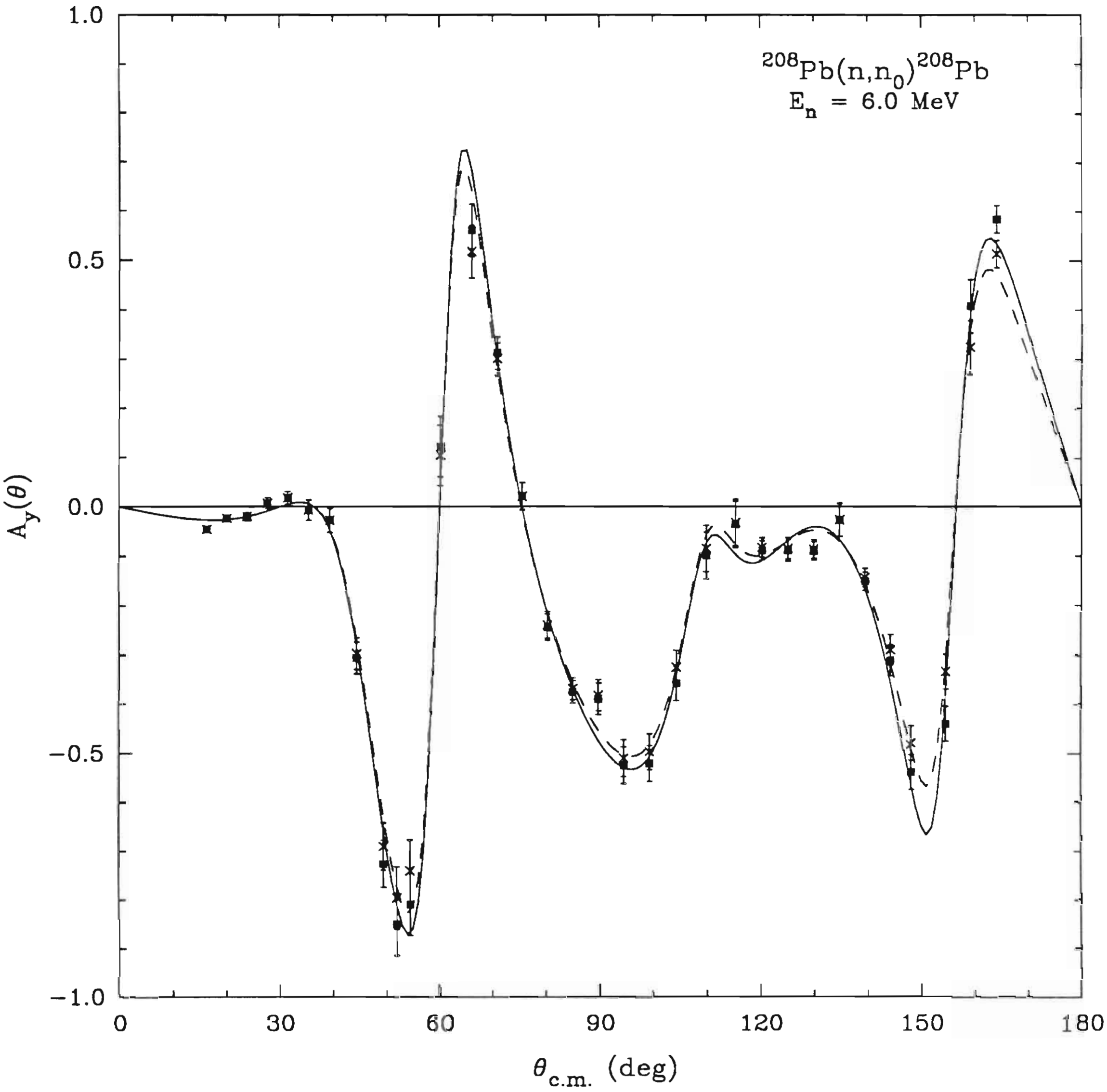

Figure 4.12. Compound nucleus contributions to elastic $^{208}Pb(n,n)^{208}Pb$ $A_y(\theta)$ data at E_n=6.0 MeV. Observed analyzing powers are indicated by x's and are connected by a dashed curve calculated from an associated Legendre polynomial fit. Shape elastic analyzing powers are indicated by closed squares and are connected by a solid curve that was also calculated from an associated Legendre polynomial fit.

contains the observed and shape elastic differential cross section data reported by Annand *et al.* (Annand 1985) and observed and shape elastic analyzing powers for ^{208}Pb(n,n)^{208}Pb elastic scattering at 6.0 and 7.0 MeV. Since the focus of this work was to be on elastic neutron scattering from ^{208}Pb, analyzing powers for inelastic scattering from the first excited state of ^{208}Pb ($J^{\pi}=3^{-}$, Q=-2.614 MeV) at 6.0 and 7.0 MeV were not corrected for compound nucleus effects.

CHAPTER V

OPTICAL MODEL ANALYSIS OF NEUTRON SCATTERING FROM ^{208}Pb

A. The optical model

The optical model of nucleon-nucleus scattering has a long history of theoretical and phenomenological study (see Hodgson 1971 or Satchler 1983). The nucleon-nucleus optical model is the reduction of the complicated many-body problem of scattering of a nucleon from a nucleus to the scattering of a single particle from a complex-valued one-body potential. The optical model potential is complex in order to account for the loss of flux from the incident channel into available inelastic and reaction channels. Though the optical model is unable to reproduce fine resonance features in cross sections and analyzing powers, it has had great success in describing the average behavior of elastic scattering observables and the total and reaction cross sections as a function of energy and mass. The optical model derives it name from the analog between the description of scattering and absorption of nucleons by a nucleus using a complex potential and the scattering and absorption of light by a cloudy crystal ball using a complex index of refraction.

The nucleon-nucleus optical-model potential normally includes central and spin-orbit components. The radial shape most often used for the optical model potential is based on the Woods-Saxon form factor, sometimes called the two-parameter-Fermi shape:

$$f_{WS}(r,R_i,a_i) = \frac{1}{1 + \exp\left[\dfrac{r - R_i}{a_i}\right]} , \tag{5-1}$$

where $R_i=r_iA^{1/3}$ is the nuclear radius and a_i is the surface diffuseness. The Woods-Saxon form factor is used because it has a shape similar to nuclear matter density distributions, and the short range of the nuclear force suggests that the real part of the optical model potential should resemble the nuclear density. In addition to a volume form factor, a surface-peaked form factor can be generated by taking a derivative of the Woods-Saxon form factor:

$$g_{WS}(r,R_i,a_i) = -4a_i \frac{d}{dr} f_{WS}(r,R_i,a_i) \ . \tag{5-2}$$

The factor of $-4a_i$ in Equation 5-2 allows $g_{ws}(r,R_i,a_i)$ to be equal to unity at $r=R_i$ (i.e., $g_{ws}(r=R_i,R_i,a_i)=1.0$).

Given the Woods-Saxon form factors, the optical model potential for neutron-nucleus scattering is usually written as:

$$\begin{aligned} U(r) &= -V_V(E)\cdot f_{WS}(r,R_V,a_V) \\ &\quad + -i(W_V\cdot f_{WS}(r,R_I,a_I) + W_S\cdot g_{WS}(r,R_I,a_I)) \\ &\quad + 2(V_{SO} + i\cdot W_{SO})\left[\frac{1}{r}\cdot\frac{d}{dr} f_{WS}(r,R_{SO},a_{SO})\ \mathbf{l}\cdot\sigma \right] , \end{aligned} \tag{5-3}$$

where the successive terms are the real central potential, the imaginary central potential (composed of a volume and a surface peaked term), and the spin-orbit potential (composed of real and imaginary parts).

As has been discussed earlier, the real central part of the optical model potential has a simple, volume-dominated shape, similar to nuclear matter density distributions. In the energy range of the present investigation, the real central part of the optical model potential is much stronger than any other component of the potential.

The imaginary or absorptive central potential is usually represented as a combination of volume and surface-peaked potentials. Surface peaking of the imaginary potential is most prominent for low energy nucleon scattering, while at higher energies the imaginary potential is dominated by volume absorption. Because nucleons in the interior of a nucleus are more tightly bound than nucleons at the surface and need more energy to be excited into an unoccupied state, the absorption of the wave function occurs mainly at the nuclear surface at low incident energies and is modeled using a surface-peaked derivative Woods-Saxon form factor. At higher incident energies, projectiles penetrate the nuclear interior and the absorption is from nucleon-nucleon collisions throughout the nucleus. Because the probability of a nucleon-nucleon collision in the interior of a nucleus is related to the mean free path of a nucleon in a nucleus, absorption at higher energies resembles the bulk distribution of target nucleons and is modeled using a volume-type

Woods-Saxon form factor. For the energy range of the present investigation, the overall strength of the imaginary potential increases with incident nucleon energy and most analyses have shown that its radial extent is usually greater than that of the real central potential.

The spin-orbit potential is the non-central part of the optical model potential and arises from a two-body spin-orbit coupling in the underlying nucleon-nucleon interaction. The spin-orbit potential is surface peaked and can be complex. The surface peaking of the spin-orbit potential can be understood on the basis of simple arguments. In the case of uniform nuclear matter, there is no meaningful point about which to establish the orbital angular momentum and the direction of spin relative to the orbital angular momentum is undefined. In a finite nucleus, where the center of mass provides a significant reference point, symmetry arguments show that the spin-orbit interaction averages to zero for an incident nucleon which crosses through the interior of a nucleus. Only when the incident nucleon crosses at or near the surface of a nucleus can the spin-orbit potential have a non-zero value.

B. Summary of data used in the ^{208}Pb optical model parametrization

Differential neutron scattering data used in the present analysis came from three facilities, the TUNL neutron time-of-flight facility, the Ohio University Accelerator Laboratory, and the Michigan State University Cyclotron Laboratory. Differential cross sections for elastic neutron scattering from ^{208}Pb were measured at TUNL by the present author at 8.0 MeV and by Floyd (Floyd 1981) at 10.0, 14.0, and 16.9 MeV. Differential cross sections for elastic neutron scattering from ^{208}Pb were measured at Ohio University at 4.0, 4.5, 5.0, 5.5, 6.0, 6.5, and 7.0 MeV by Annand *et al.* (Annand 1985), at 20.0, 22.0, and 24.0 MeV by Finlay *et al.* (Finlay 1984), and at 9.0, 11.0, and 25.7 MeV by Rapaport *et al.* (Rapaport 1978). Differential cross sections for elastic neutron scattering from ^{208}Pb were measured at Michigan State University at 30.3 and 40.0 MeV by DeVito *et al.* (DeVito 1979). The 4.0 to 7.0 MeV ^{208}Pb differential cross sections measured by Annand *et al.* (Annand 1985) were adjusted by Annand *et al.* for compound nucleus contributions using calculated compound nucleus cross section values.

The polarized neutron scattering data were obtained using the time-of-flight facility at TUNL. Analyzing powers for elastic neutron scattering from ^{208}Pb were measured by the present author at 6.0, 7.0, 8.0, 9.0, and 10.0 MeV and by Floyd (Floyd 1981) at 10.0 and 14.0 MeV.

Average ^{nat}Pb (52% ^{208}Pb) total cross sections values were communicated to us by Larson *et al.* (Larson 1980) from 4.0 to 80.0 MeV in steps of 2.0 MeV. Total cross section values at intermediate values (i.e., 7.0, 9.0, 11.0 MeV, etc.) were obtained through interpolation. An uncertainty of 3.0% was assigned to all total cross section values.

C. Analysis of scattering data

1. Introduction

Since obtaining details of the optical model potential directly from experimental data is a complicated problem, it is customary to begin with a suitable potential and iterate the numerical values of its parameters in order to optimize fits to data. In these iterations, however, it is important to begin with a physically reasonable potential, as determined by theoretical considerations or from previous analyses, to avoid excessive numerical work or the danger of obtaining an unphysical solution. An unphysical solution is a solution that is inconsistent with fundamental knowledge of the nucleon-nucleus interaction. For the present analysis, iterations of the optical model parameters were performed using a modified version of the computer code GENOA (originally obtained from F. Perey, Oak Ridge National Laboratory). The computer code GENOA has been modified to include the effects of the Mott-Schwinger electromagnetic interaction. For a detailed discussion of the Mott-Schwinger interaction and discussion of the associated modifications to the computer code see Floyd (Floyd 1981). The computer code GENOA calculates theoretical cross sections and analyzing powers from a one-body Schrödinger equation using the chosen potential $U(r)$. At each stage of the iteration process, GENOA calculates chi-square (χ^2), a quantitative measure of agreement between theoretical predictions and experimental values:

$$\frac{\chi^2}{N} = \frac{1}{N_S}\sum_{i=1}^{N_S}\left[\frac{\sigma^{exp}(\theta_i) - \sigma^{th}(\theta_i)}{\Delta\sigma^{exp}(\theta_i)}\right]^2 + \tag{5-4}$$

$$\frac{1}{N_P}\sum_{i=1}^{N_P}\left[\frac{A_y^{exp}(\theta_i) - A_y^{th}(\theta_i)}{\Delta A_y^{exp}(\theta_i)}\right]^2 ,$$

where χ^2/N is the average chi-square per data point, $\sigma^{exp}(\theta_i)$ is the experimental cross section measured at θ_i , $\sigma^{th}(\theta_i)$ is the theoretical cross section calculated from the optical model potential at θ_i, $\Delta\sigma^{exp}(\theta_i)$ is the error in the experimental cross section, N_S is the number of experimental cross section points, $A_y^{exp}(\theta_i)$ is the experimental analyzing power measured at θ_i, $A_y^{th}(\theta_i)$ is the theoretical analyzing power calculated from the optical model potential at θ_i, $\Delta A_y^{exp}(\theta_i)$ is the error in the analyzing power, and N_P is the number of experimental analyzing power points. In the iteration procedure, values of one or more parameters are varied using an automatic search routine to minimize χ^2.

2. Individual fits

Optimum potential parameters were obtained at each individual energy by searching on as many optical model parameters as possible. Starting parameters for the 4.0 to 6.5 MeV data were the ^{208}Pb parameters reported by Annand *et al.* (Annand 1985) while the starting parameters for the 7.0 to 40.0 MeV data were the ^{208}Pb global parameters reported by Finlay *et al.* (Finlay 1984). In addition to these parameters, an imaginary spin-orbit term was introduced early in the analysis. Best fits were obtained at each energy using an iterative procedure. Using GENOA, potential well strengths were searched upon first, followed by geometrical parameters, and finally by potential strengths and geometrical parameters simultaneously. In order to provide spin-orbit parameters at energies where analyzing power data were not available, energies at which both cross section and analyzing power data were available were considered first. Using these initial searches, the mean real spin-orbit strength, spin-orbit radius, and spin-orbit diffuseness were obtained by taking an unweighted average of the strength, radius, and diffuseness from each search. The imaginary spin-orbit strength, which was assumed to vary linearly with energy, was obtained by forcing the imaginary spin-orbit strength to be approximately -0.650 MeV at an incident energy of 80 MeV, as suggested by the proton scattering analysis of Schwandt *et al.* (Schwandt 1982), and then searching on the slope and y-intercept required to obtain best fits to the present data. At energies where no $A_y(\theta)$ data were available, these mean spin-orbit parameters were used and held fixed. Final optical model parameters for these individual fits are listed in Table 5.1 while corresponding fits are shown in Figures 5.1 through 5.4. Table 5.1 also contains the volume integral per nucleon defined as:

$$(J/A) = -\frac{1}{A}\int V(r)\cdot d^3r\,. \qquad (5\text{-}5)$$

Table 5-1

Single energy n + ^{208}Pb optical model parameters

E_n (MeV)	V_V (MeV)	r_{V_V} (fm)	a_{V_V} (fm)	W_V (MeV)	W_S (MeV)	r_I (fm)	a_I (fm)	V_{SO} (MeV)	r_{SO} (fm)	a_{SO} (fm)	W_{SO} (MeV)	J_V/A ($\mathrm{MeV\cdot fm^3}$)	J_W/A ($\mathrm{MeV\cdot fm^3}$)	χ^2/N_S	χ^2/N_P
4.000	47.373	1.222	0.726	0.000	6.240	1.302	0.351	6.583[a]	1.147[a]	0.488[a]	0.536[a]	398.04	31.71	1.36	---
4.500	47.617	1.207	0.789	0.000	6.480	1.355	0.308	6.583[a]	1.147[a]	0.488[a]	0.528[a]	392.87	31.24	2.62	---
5.000	44.436	1.272	0.662	0.000	6.511	1.343	0.300	6.583[a]	1.147[a]	0.488[a]	0.520[a]	412.25	30.03	1.67	---
5.500	41.766	1.313	0.748	0.000	9.073	1.388	0.325	6.583[a]	1.147[a]	0.488[a]	0.512[a]	432.15	48.44	2.85	---
6.000	43.122	1.289	0.672	0.000	8.425	1.338	0.316	6.590	1.256	0.349	1.279	416.42	40.65	6.88	6.07
6.500	43.666	1.275	0.666	0.000	9.015	1.333	0.311	6.583[a]	1.147[a]	0.488[a]	0.496[a]	408.19	42.48	7.20	---
7.000	43.602	1.271	0.670	0.000	7.820	1.306	0.375	5.710	0.956	0.434	0.601	404.30	42.76	3.43	5.09
8.000	43.715	1.263	0.675	0.000	8.512	1.304	0.388	5.664	1.003	0.595	0.484	398.54	48.04	3.49	5.07
9.000	44.907	1.232	0.738	0.000	8.242	1.281	0.440	7.037	1.235	0.503	0.720	387.24	51.05	5.61	4.52
10.000	45.220	1.225	0.726	0.000	7.224	1.285	0.506	6.892	1.201	0.523	0.522	382.59	51.95	12.55	9.62
11.000	43.729	1.262	0.585	0.000	9.244	0.923	0.490	6.583[a]	1.147[a]	0.488[a]	0.424[a]	390.40	33.60	0.42	---
13.950	44.664	1.226	0.743	0.497	7.402	1.276	0.526	7.611	1.230	0.526	1.081	380.37	59.18	5.03	4.32
16.910	41.289	1.266	0.655	0.000	8.292	1.205	0.523	6.583[a]	1.147[a]	0.488[a]	0.329[a]	377.34	54.36	26.59	---
20.000	43.672	1.218	0.718	1.627	6.318	1.254	0.515	6.583[a]	1.147[a]	0.488[a]	0.280[a]	362.85	58.18	5.57	---
22.000	44.976	1.189	0.715	2.211	4.789	1.301	0.542	6.583[a]	1.147[a]	0.488[a]	0.248[a]	348.87	59.27	5.75	---
24.000	46.483	1.152	0.722	2.027	3.726	1.297	0.663	6.583[a]	1.147[a]	0.488[a]	0.216[a]	330.55	56.00	8.91	---
25.700	43.251	1.195	0.725	2.321	4.836	1.278	0.580	6.583[a]	1.147[a]	0.488[a]	0.189[a]	341.17	61.09	3.30	---
30.300	43.489	1.159	0.693	4.135	0.794	1.500	0.413	6.583[a]	1.147[a]	0.488[a]	0.115[a]	312.12	66.01	1.97	---
40.000	37.390	1.240	0.752	5.434	4.291	1.274	0.527	6.583[a]	1.147[a]	0.488[a]	0.000[a]	329.49	80.97	3.90	---

[a] These parameters were held constant in the search.

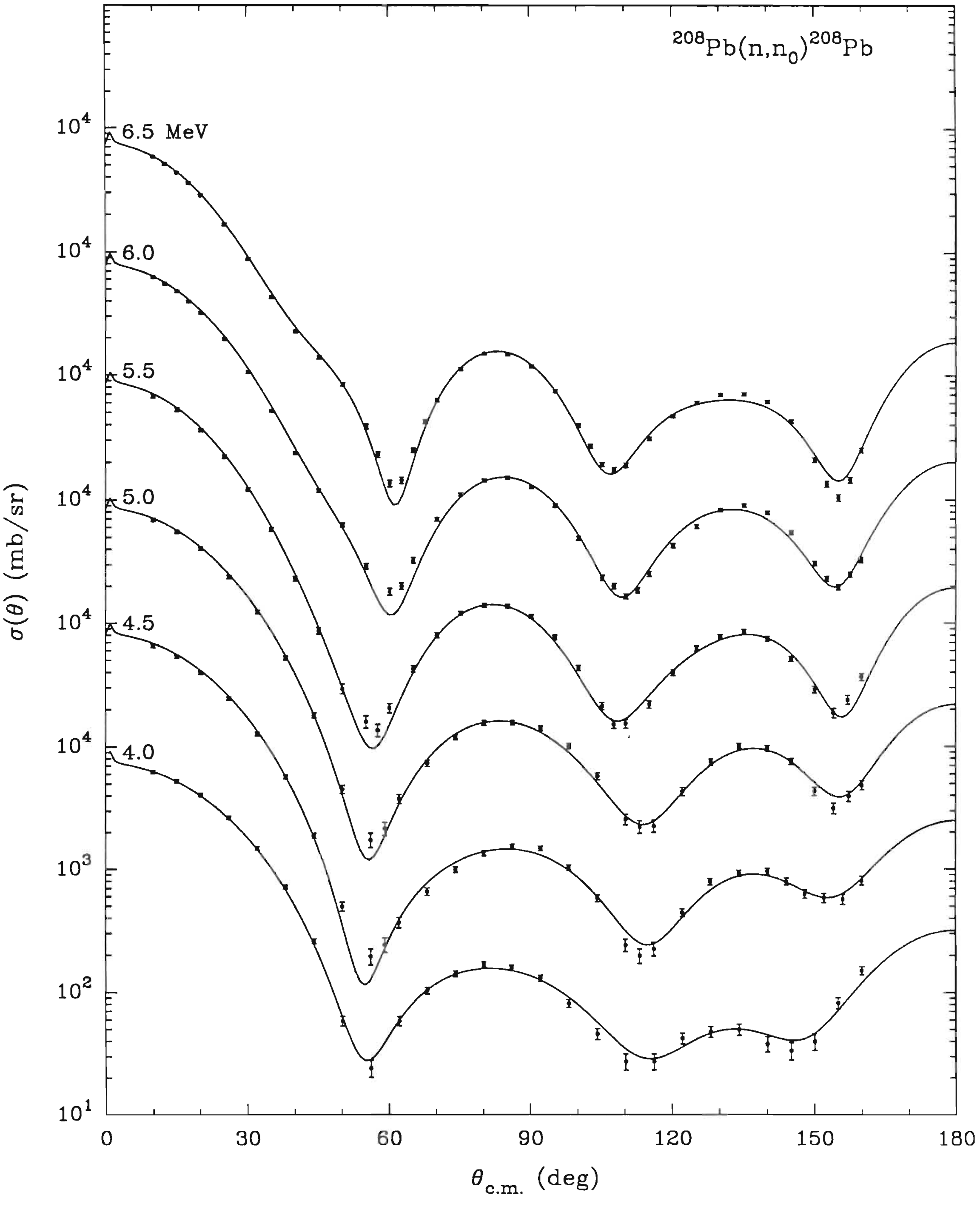

Figure 5.1. Optical model calculations compared to $\sigma(\theta)$ data for neutron elastic scattering from ^{208}Pb at 4.0 to 6.5 MeV. The curves are optimum fits at each individual energy using the parameters listed in Table 5.1. The data from 4.0 to 6.5 MeV have been adjusted for compound nucleus contributions (see Section B of this chapter).

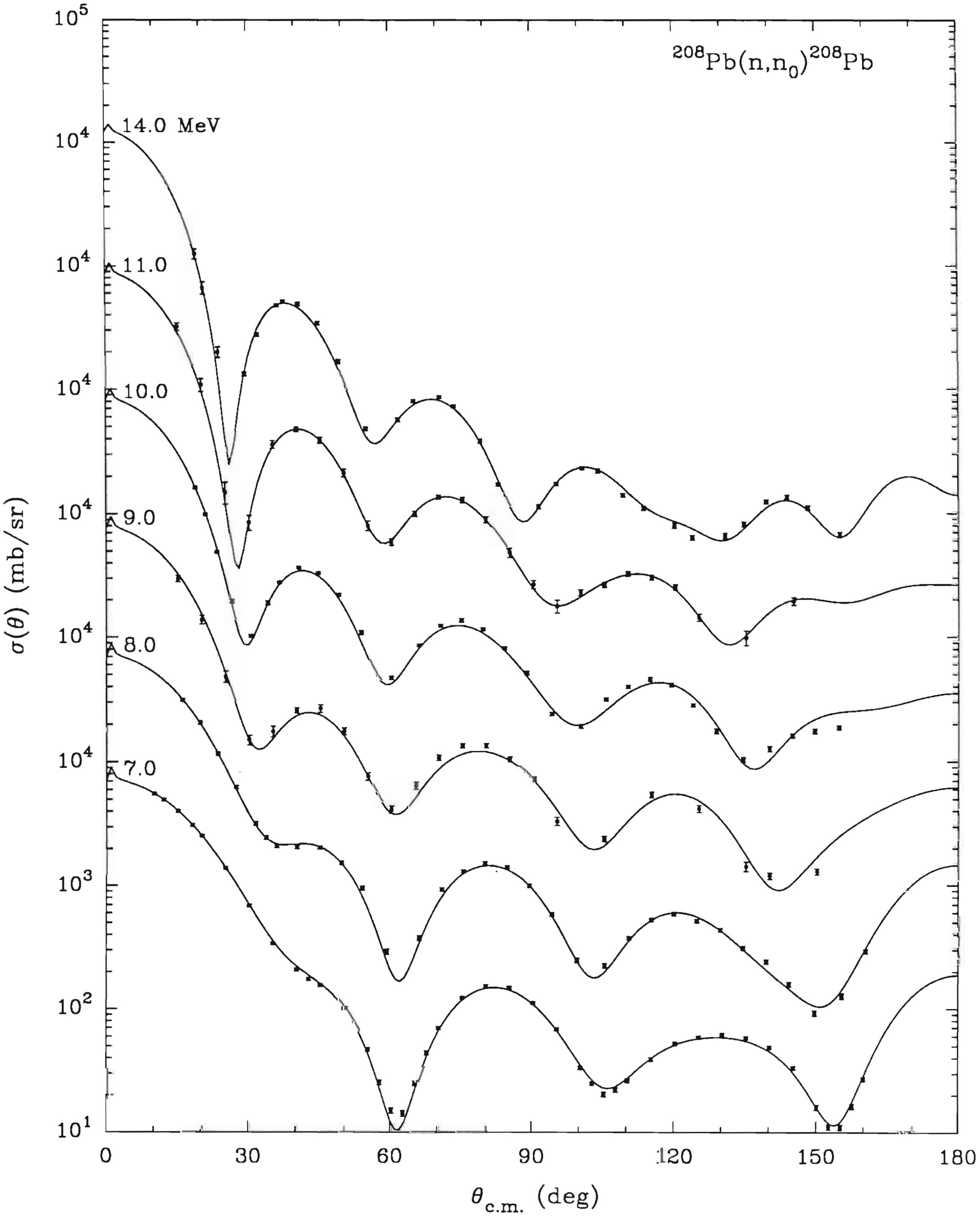

Figure 5.2. Continuation of Figure 5.1. Optical model calculations compared to σ(θ) data for neutron elastic scattering from ^{208}Pb at 7.0 to 14.0 MeV. The curves are optimum fits at each individual energy using the parameters listed in Table 5.1. The data at 7.0 MeV have been adjusted for compound nucleus contributions (see Section B of this chapter).

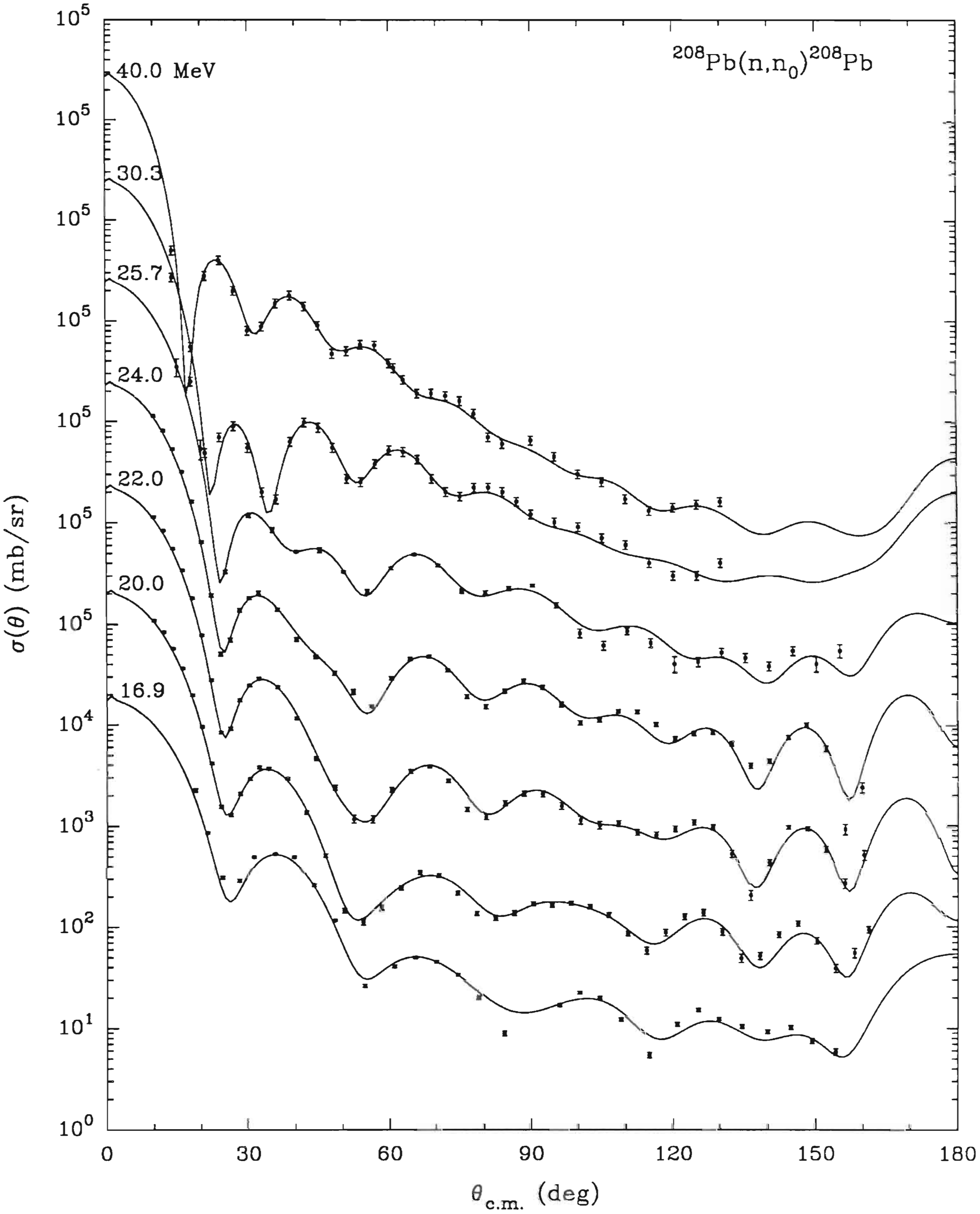

Figure 5.3. Continuation of Figure 5.1. Optical model calculations compared to $\sigma(\theta)$ data for neutron elastic scattering from ^{208}Pb at 16.9 to 40.0 MeV. The curves are optimum fits at each individual energy using the parameters listed in Table 5.1.

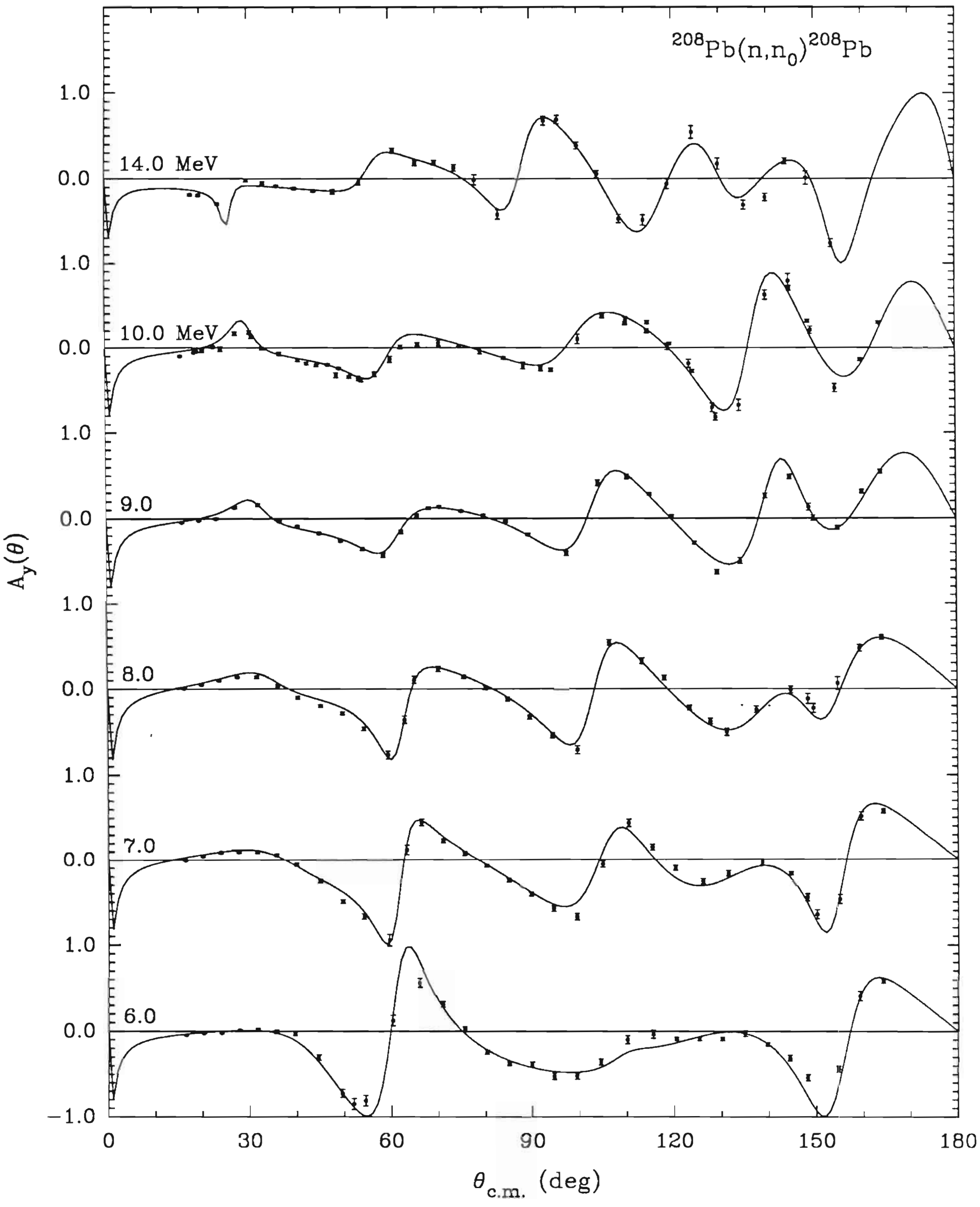

Figure 5.4. Optical model calculations compared to $A_y(\theta)$ data for neutron elastic scattering from ^{208}Pb. The curves are optimum fits at each individual energy using the parameters listed in Table 5.1. The data at 6.0 and 7.0 MeV have been adjusted for compound nucleus contributions (see Chapter IV, Section B-6).

For the present single-energy searches, the sum over all points and all energies of the χ^2 from the differential cross sections, analyzing powers, and total cross sections was obtained. This value is 5 200 and is defined as the "total single-energy χ^2 ". The total single-energy χ^2 is important for comparison purposes to average optical model potentials made in later sections.

3. Constant geometry fits

In order to ascertain the average energy dependence of the real and imaginary optical model potential, it is common practice, for the energy range of the present work, to assign linear energy dependences to potential strengths and constant values to the geometrical parameters. These values can be assigned either by averaging the values found in the individual fits or by searching for values that provide the best overall fit to the data. A combination of both approaches was adopted for the present work.

First, an energy averaged parameter set was obtained by taking an unweighted average of the geometrical parameters and a linear least square fit to the potential strengths found for the individual fits that were discussed in Section C-2 of this chapter. Using this energy averaged parameter set as a starting point, the entire data set was fit simultaneously, with potential well depths and geometrical parameters, including the real spin-orbit strength and spin-orbit geometry, being allowed to vary. In the search, geometrical parameters were constrained to be energy independent while potential strengths were constrained to have a linear energy dependence summarized as follows:

$$V_V = V_V' - \alpha_{V_V} \cdot E \tag{5-6}$$

$$W_V = W_V' + \alpha_{W_V} \cdot E$$

$$W_S = W_S' - \alpha_{W_S} \cdot E$$

$$V_{SO} = V_{SO}' - \alpha_{V_{SO}} \cdot E$$

As the search proceeded, the real spin-orbit potential strength was forced to be energy independent, because little variation in its strength was seen as a function of energy. As before, potential well strengths and energy dependences were searched upon first, followed by geometrical parameters, and finally by potential strengths and geometrical parameters simultaneously. The imaginary spin-orbit potential, however, was not searched upon in this procedure and was held fixed to the linear energy dependent function determined by the individual fits discussed in Section C-2 of this chapter. Optical model parameters resulting from this constant geometry search are given in Table 5.2, while corresponding fits to the differential scattering cross sections and analyzing powers are shown in Figures 5.5 thru 5.8. A comparison of the averaged ^{nat}Pb total cross section data to the current constant geometry ^{208}Pb optical model predictions is shown in Figure 5.9. The total χ^2 of 12 200 listed in Table 5.2 for the 4.0 to 40.0 MeV data set can be compared to the total single-energy χ^2 of 5 200 obtained in the individual fits discussed in the previous section.

Table 5.2 also contains a list of the constant geometry parameters for neutron scattering from ^{208}Pb obtained by Annand *et al.* (Annand 1985) from 4.0 to 11.0 MeV and by Finlay *et al.* (Finlay 1984) from 7.0 to 50.0 MeV. Comparisons of the present model to the models of Annand and Finlay are shown in Figures 5.5 thru 5.8.

4. Energy dependent geometry fits

Recently, based on optical-model fits to n+^{208}Pb scattering data, Annand *et al.* (Annand 1985) have suggested that the radius of the real central potential and the radius and diffuseness of the imaginary central potential vary with energy. In the Annand model or parametrization, the real and imaginary radii were seen to decrease with increasing energy while the imaginary diffuseness increased with increasing energy. In order to investigate the energy dependence of the geometrical parameters using our larger data set, an optical model search was performed in which the real and imaginary central potential geometries were permitted to vary linearly with energy:

$$r_{V_v} = r'_{V_v} - \alpha_{r_{V_v}} \cdot E \qquad (5\text{-}7)$$

$$a_{V_v} = a'_{V_v} - \alpha_{a_{V_v}} \cdot E$$

$$r_I = r'_I - \alpha_{r_I} \cdot E$$

$$a_I = a'_I - \alpha_{a_I} \cdot E$$

Starting parameters for the optical model search were linear least squares fits to the potential strengths and geometries found for the individual fits discussed in section C-2 of this chapter. Using these starting parameters, the entire data set was fit

Table 5.2

Constant geometry n + ^{208}Pb optical model parameters

Parameter		Present Analysis		Annand *et al.*[a]	Finlay *et al.*[b]	
V_V	(MeV)	46.727-0.230·E		45.640-0.280·E	49.130-0.310·E	
rv_V	(fm)	1.245		1.265	1.205	
av_V	(fm)	0.690		0.698	0.685	
W_V	(MeV)	0.000	E<10.5 MeV	0.000	0.000	E<11.2 MeV
		-1.845+0.176·E	E>10.5 MeV		-2.030+0.180·E	E>11.2 MeV
W_S	(MeV)	2.744+0.544·E	E<10.5 MeV	4.046+0.710·E	1.326+0.470·E	E<10.7 MeV
		10.031-0.150·E	E>10.5 MeV		7.752-0.130·E	E>10.7 MeV
r_I	(fm)	1.294		1.332	1.283	
a_I	(fm)	0.450		0.320	0.499	
V_{SO}	(MeV)	6.112		5.750	5.750	
r_{SO}	(fm)	1.174		1.105	1.105	
a_{SO}	(fm)	0.517		0.499	0.499	
W_{SO}	(MeV)	0.600-0.016·E		0.000	0.000	
χ^2 from 4.0 to 40.0 MeV		12200				
χ^2 from 4.0 to 11.0 MeV		7050		13200		
χ^2 from 7.0 to 40.0 MeV		9020			16900	

[a] Constant geometry optical model parameters of Annand *et al.* (Annand 1985)
[b] Constant geometry optical model parameters of Finlay *et al.* (Finlay 1984)

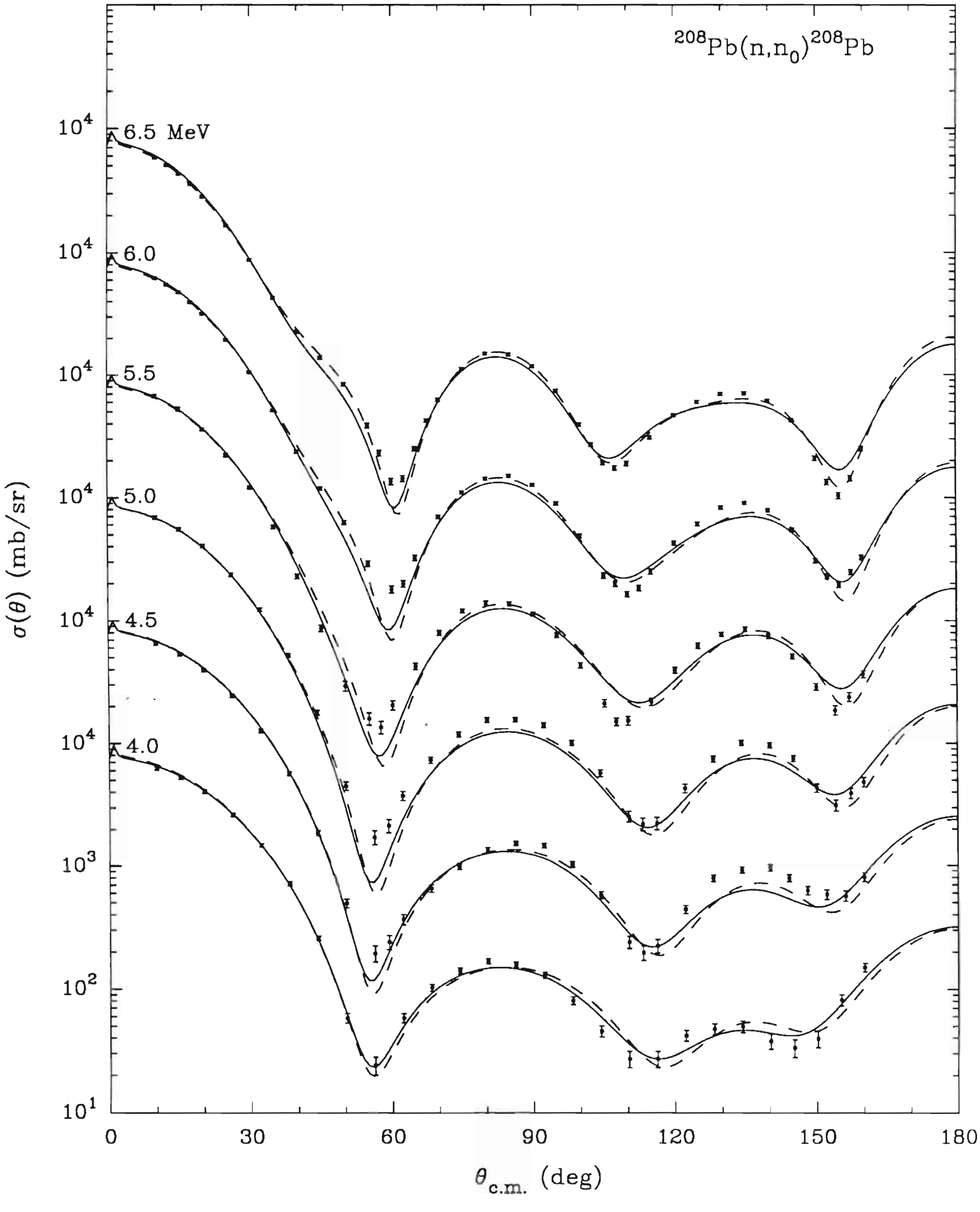

Figure 5.5. Optical model calculations compared to $\sigma(\theta)$ data for neutron elastic scattering from ^{208}Pb at 4.0 to 6.5 MeV. Solid curves are from a constant geometry fit whose parameters are listed in Table 5.2. Dashed curves are the Annand *et al.* 4.0 to 11.0 MeV predictions. The data from 4.0 to 7.0 MeV have been adjusted for compound nucleus contributions (see Section B of this chapter).

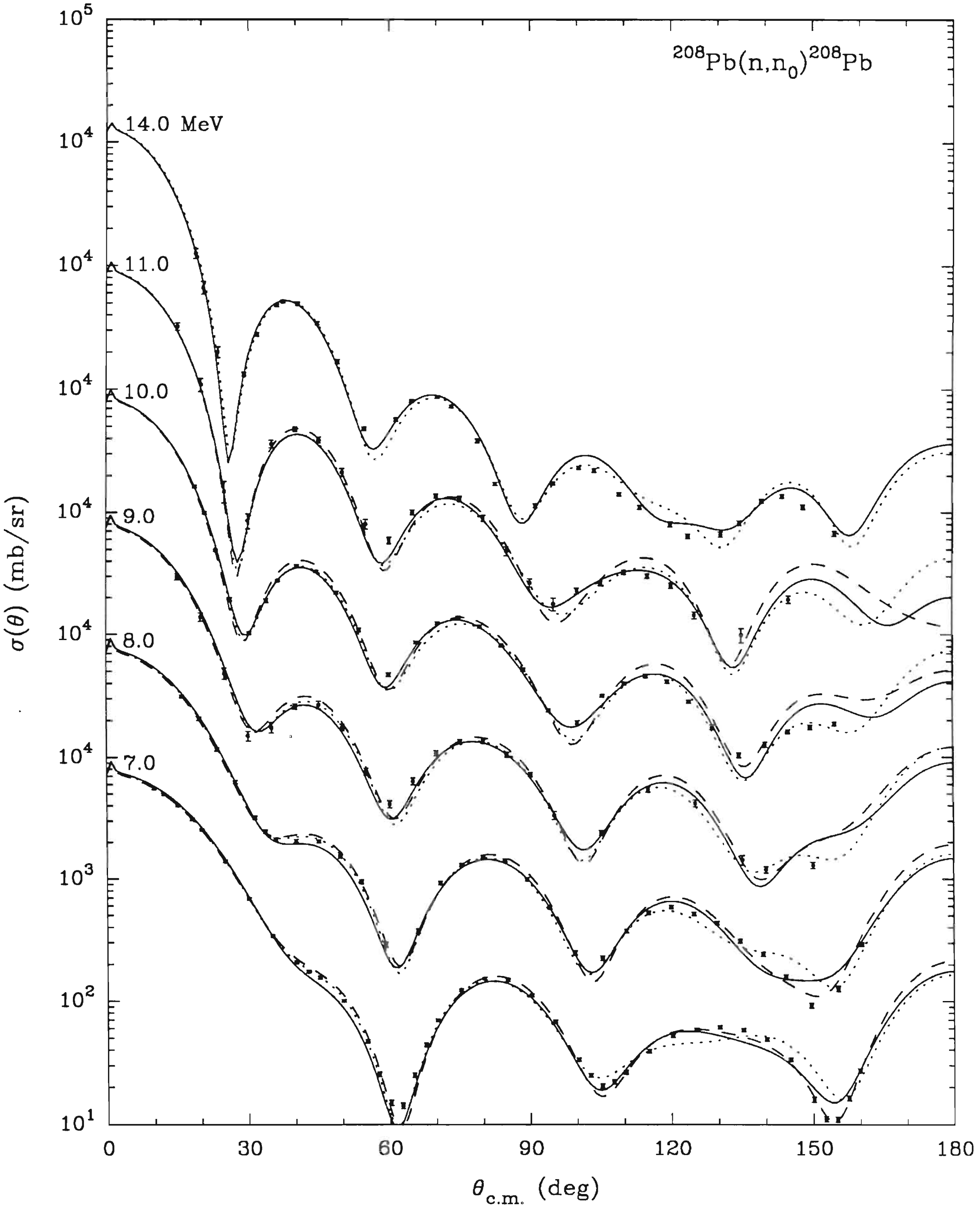

Figure 5.6. Continuation of Figure 5.5. Optical model calculations compared to σ(θ) data for neutron elastic scattering from ^{208}Pb at 7.0 to 14.0 MeV. Solid curves are from a constant geometry fit whose parameters are listed in Table 5.2. Dashed curves are the Annand *et al.* 4.0 to 11.0 MeV predictions. Dotted curves are the Finlay *et al.* 7.0 to 50.0 MeV predictions.

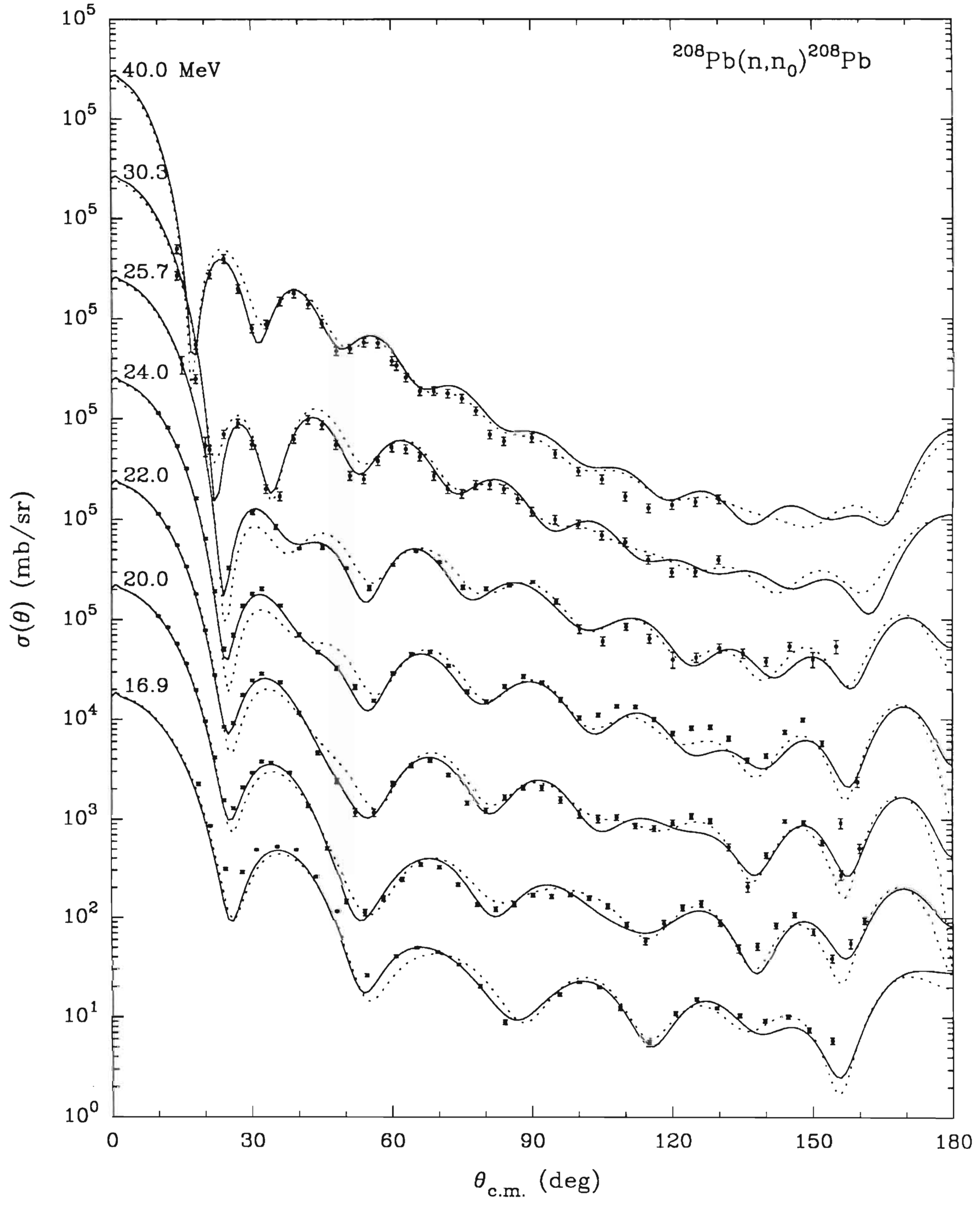

Figure 5.7. Continuation of Figure 5.5. Optical model calculations compared to σ(θ) data for neutron elastic scattering from ^{208}Pb at 16.9 to 40.0 MeV. Solid curves are from a constant geometry fit whose parameters are listed in Table 5.2. Dotted curves are the Finlay *et al.* 7.0 to 50.0 MeV predictions.

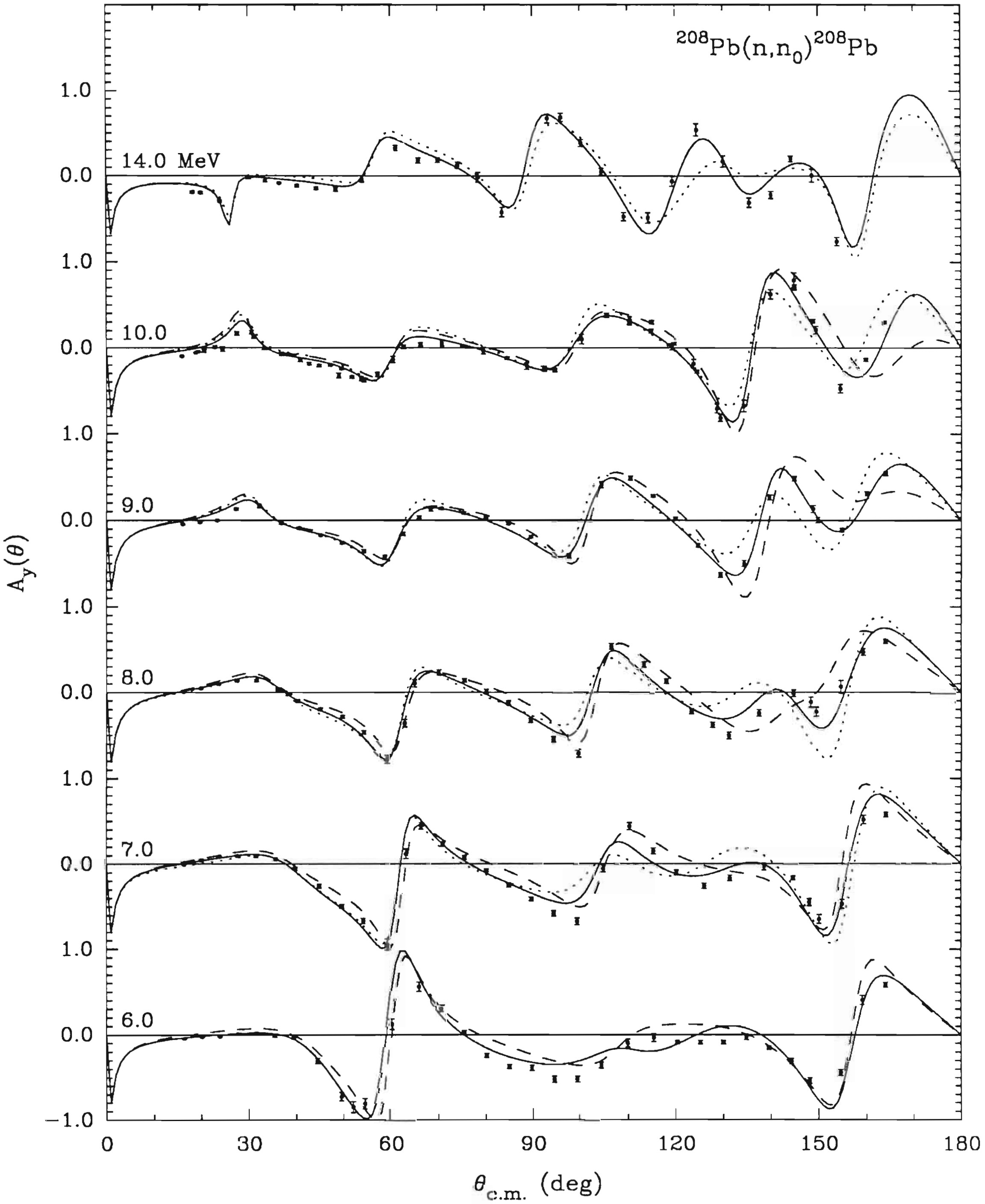

Figure 5.8. Optical model calculations compared to $A_y(\theta)$ data for neutron elastic scattering from ^{208}Pb. Solid curves are from a constant geometry fit whose parameters are listed in Table 5.2. Dashed curves are the Annand *et al.* 4.0 to 11.0 MeV predictions. Dotted curves are the Finlay *et al.* 7.0 to 50.0 MeV predictions. The data at 6.0 and 7.0 MeV have been adjusted for compound nucleus contributions (see Chapter IV, Section B-6).

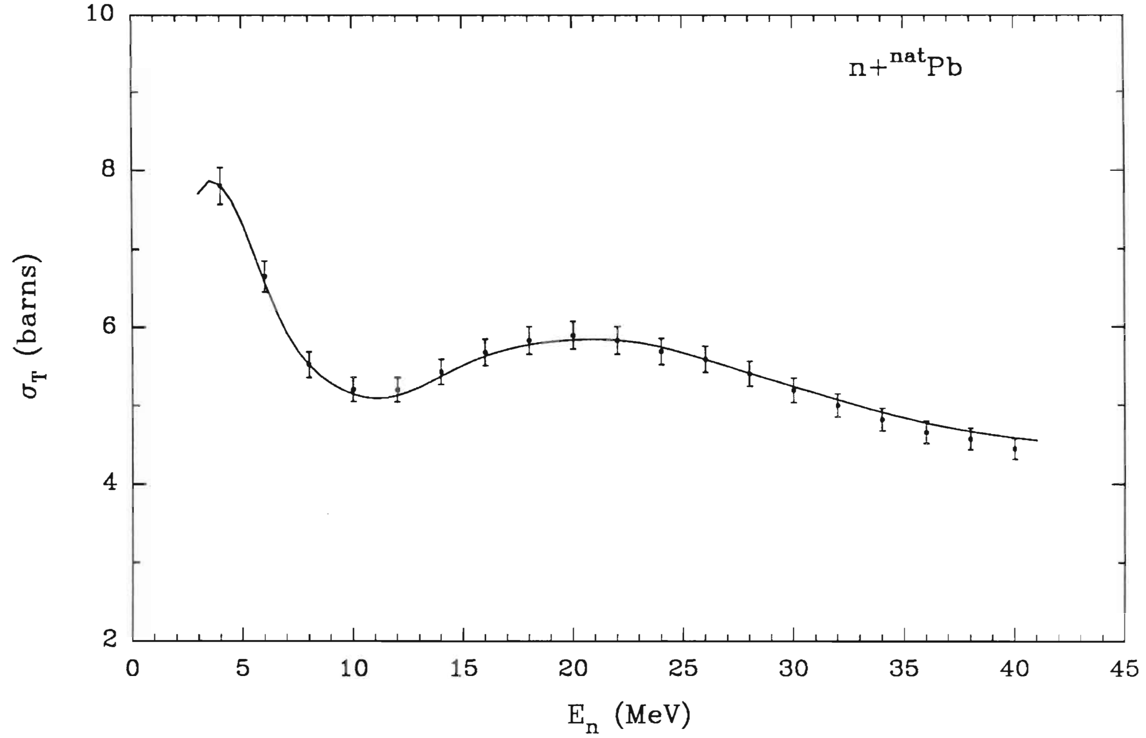

Figure 5.9. Comparison of the averaged $n+^{nat}Pb$ total cross section data to $n+^{208}Pb$ optical model predictions using the constant geometry parameters listed in Table 5.2.

simultaneously, with potential well depths and geometries, including the real spin-orbit parameters, being allowed to vary. Potential well strengths and energy dependences were searched upon first, followed by potential geometries, and finally by potential strengths and potential geometries simultaneously. However, as with the constant geometry fits, the imaginary spin-orbit potential strength was not searched upon in this procedure and was held fixed to the linear energy dependent function determined by the individual fits discussed in Section C-2 of this chapter. Optical model parameters resulting from this energy-dependent geometry search are given in Table 5.3, while corresponding fits to the differential scattering cross sections and analyzing powers are shown in Figures 5.10 through 5.13. A comparison of the averaged ^{nat}Pb total cross section data to the current energy-dependent geometry ^{208}Pb optical model predictions is shown in Figure 5.14. Also listed in Table 5.3 are the energy-dependent geometry parameters of the Annand model while a comparison of the differential cross sections and analyzing powers predicted by the Annand model to the present energy-dependent geometry fit are shown in Figures 5.10 through 5.13.

Two differences between the current parameters and the parameters of the Annand model should be noted. First, in our searches, potential geometries were varied linearly over the entire 4.0 to 40.0 MeV range, while in the search by Annand the geometrical parameters were forced to retain their 24.0 MeV values at energies above 24.0 MeV (i.e., $r_{V_V}(E>24.0\ MeV) = r_{V_V}(E=24.0\ MeV),\ a_{V_V}(E>24.0\ MeV)) = a_{V_V}(E=24.0\ MeV)$, etc.). Second, the real and imaginary potential strengths were constrained to have a linear energy dependence in our searches while in the Annand model, individual values for the real and imaginary potential strengths were reported at each energy and were not explicitly parameterized with a single function.

As can be seen by comparing the total χ^2 for the energy-dependent geometry fit listed in Table 5.3 and the total χ^2 for the constant geometry fit listed in Table 5.2, a slight improvement in χ^2 can be achieved by letting geometrical parameters of the optical model have an energy dependence. However, there is a reluctance to introduce four new energy dependences in order to achieve a reduction in χ^2 of 6%. It is interesting to note, however, that when an energy-dependent geometry is introduced into the real central potential, the strength of the real central potential becomes nearly energy independent. This ambiguity between energy dependence in the real central potential strength and energy dependence in the real central geometry has also been noted by Annand *et al.* (Annand 1985) and by Johnson *et al.* (Johnson 1987).

Table 5.3

Energy-dependent geometry n + ^{208}Pb optical model parameters

Parameter		Present Analysis		Annand *et al.*$^{a)}$
V_V	(MeV)	45.299-0.083·E		---$^{b)}$
rV_V	(fm)	1.277-0.003·E		1.302-0.0055·E
aV_V	(fm)	0.640+0.005·E		0.700
W_V	(MeV)	0.000	E<10.5 MeV	---$^{b)}$
		-1.110+0.112·E	E>10.5 MeV	
W_S	(MeV)	4.057+0.447·E	E<10.5 MeV	---$^{b)}$
		10.284-0.146·E	E>10.5 MeV	
r_I	(fm)	1.321-0.002·E		1.363-0.0042·E
a_I	(fm)	0.344+0.008·E		0.162+0.0189·E
V_{SO}	(MeV)	6.152		5.750
r_{SO}	(fm)	1.178		1.150
a_{SO}	(fm)	0.541		0.499
W_{SO}	(MeV)	0.600-0.016·E		0.000
χ^2 from 4.0 to 40.0 MeV		11400		
χ^2 from 4.0 to 40.0 MeV$^{c)}$		6400		10400

a) Energy-dependent geometry optical model parameters of Annand *et al.* (Annand 1985)

b) In the searches by Annand *et al.*, values for the real and imaginary strengths were not given explicitly as a single function of energy and were reported individually at 15 energies which excluded 8.0, 10.0, 14.0, and 16.9 MeV.

c) Sum of χ^2 at the 15 energies where Annand *et al.* reported values for the real and imaginary strengths. See b) above.

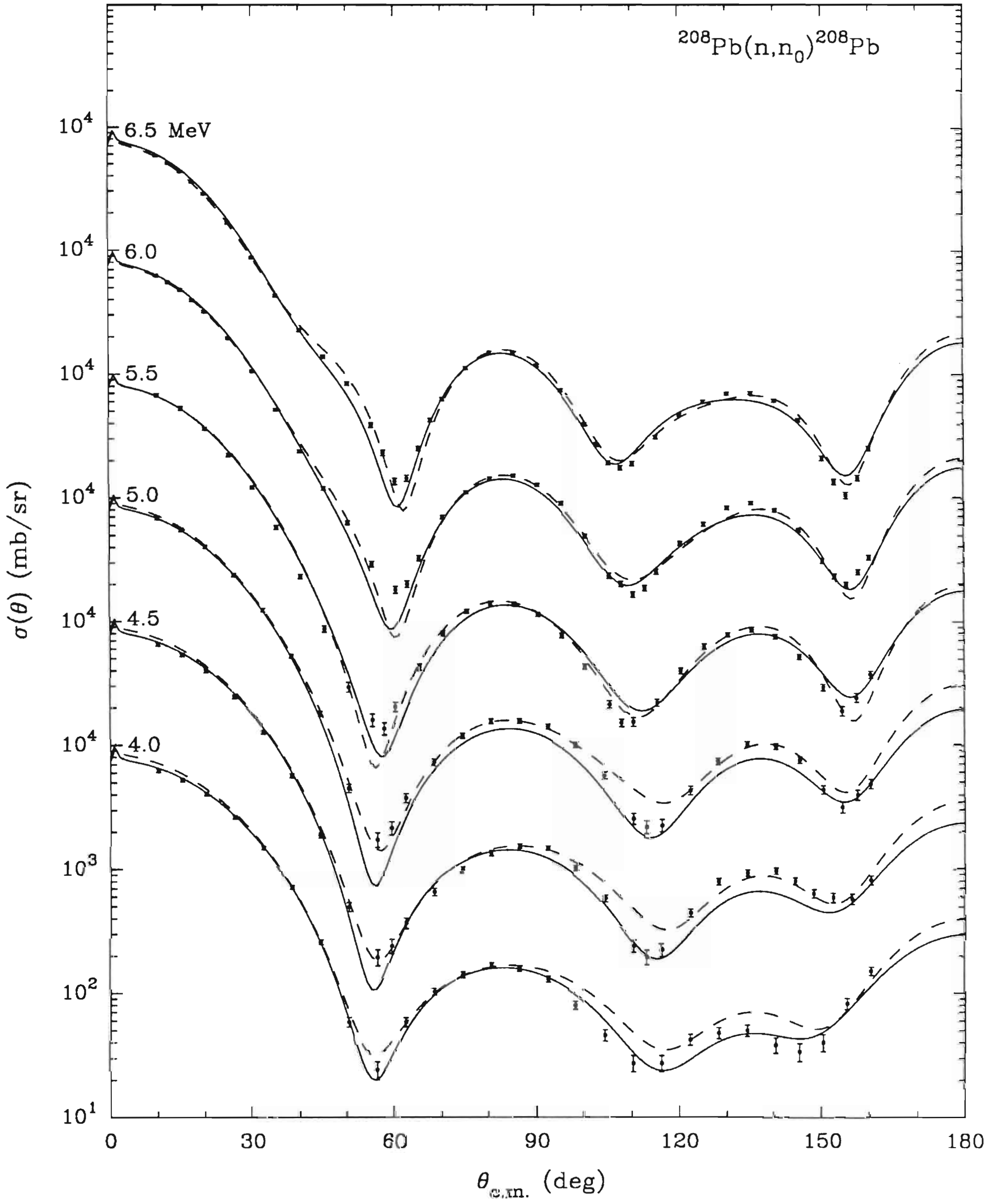

Figure 5.10. Optical model calculations compared to σ(θ) data for neutron elastic scattering from ^{208}Pb at 4.0 to 6.5 MeV. Solid curves are from an energy-dependent geometry fit whose parameters are listed in Table 5.3. Dashed curves are the Annand *et al.* predictions. The data from 4.0 to 6.5 MeV have been adjusted for compound nucleus contributions (see Section B of this chapter).

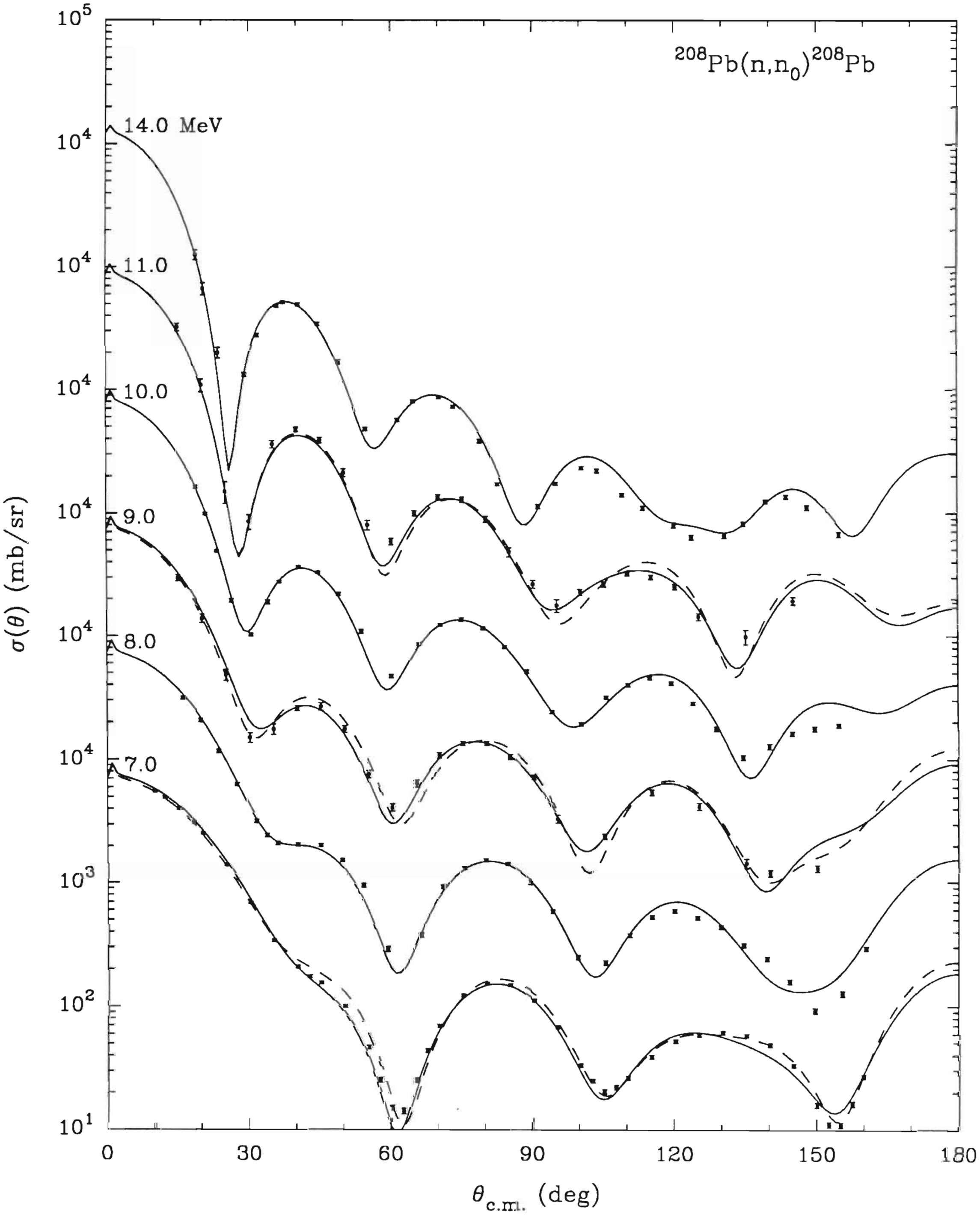

Figure 5.11. Continuation of Figure 5.10. Optical model calculations compared to $\sigma(\theta)$ data for neutron elastic scattering from ^{208}Pb at 7.0 to 14.0 MeV. Solid curves are from an energy-dependent geometry fit whose parameters are listed in Table 5.3. Dashed curves are the Annand *et al.* predictions. The data at 7.0 MeV have been adjusted for compound nucleus contributions (see Section B of this chapter).

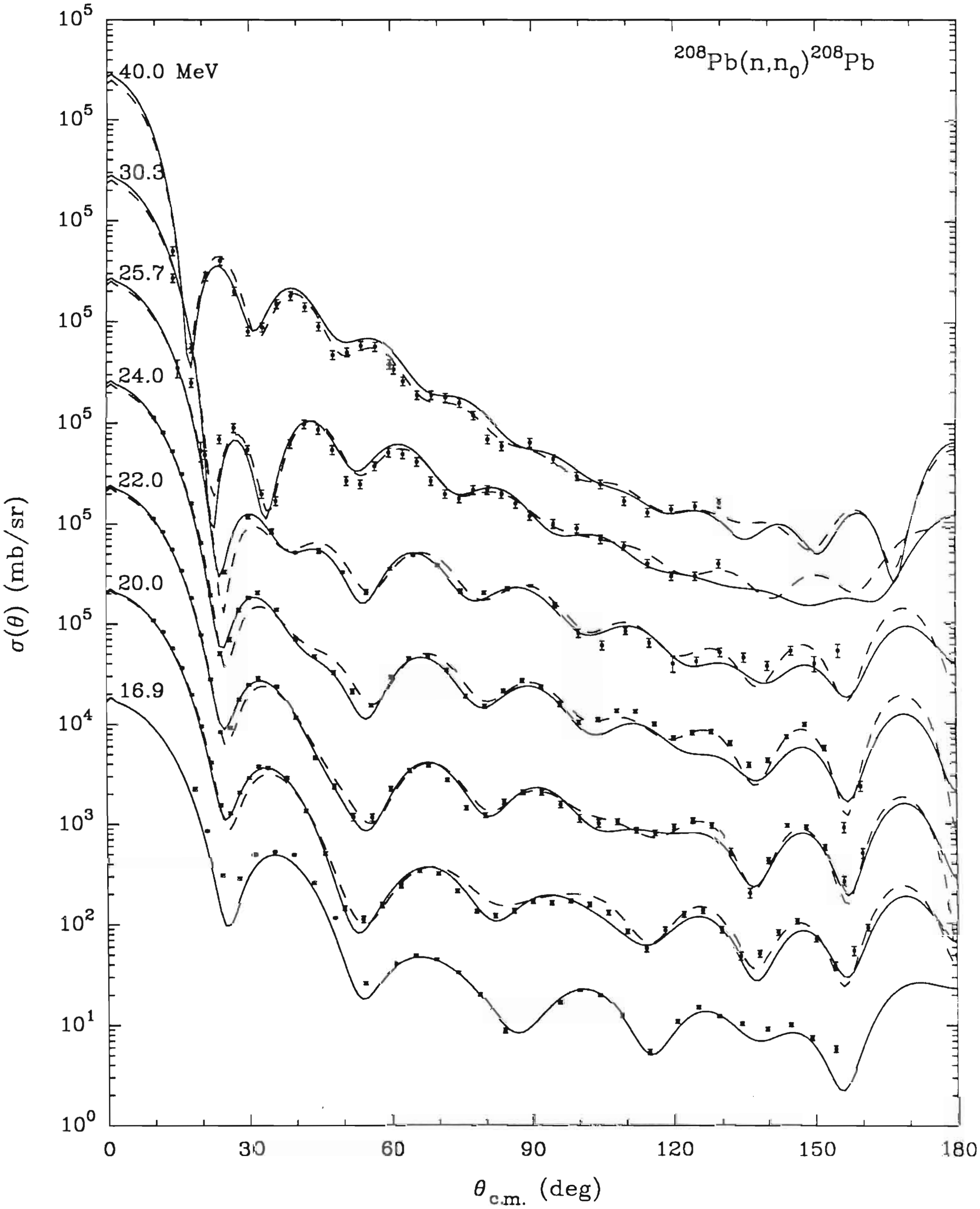

Figure 5.12. Continuation of Figure 5.10. Optical model calculations compared to $\sigma(\theta)$ data for neutron elastic scattering from ^{208}Pb at 16.9 to 40.0 MeV. Solid curves are from an energy-dependent geometry fit whose parameters are listed in Table 5.3. Dashed curves are the Annand *et al.* predictions.

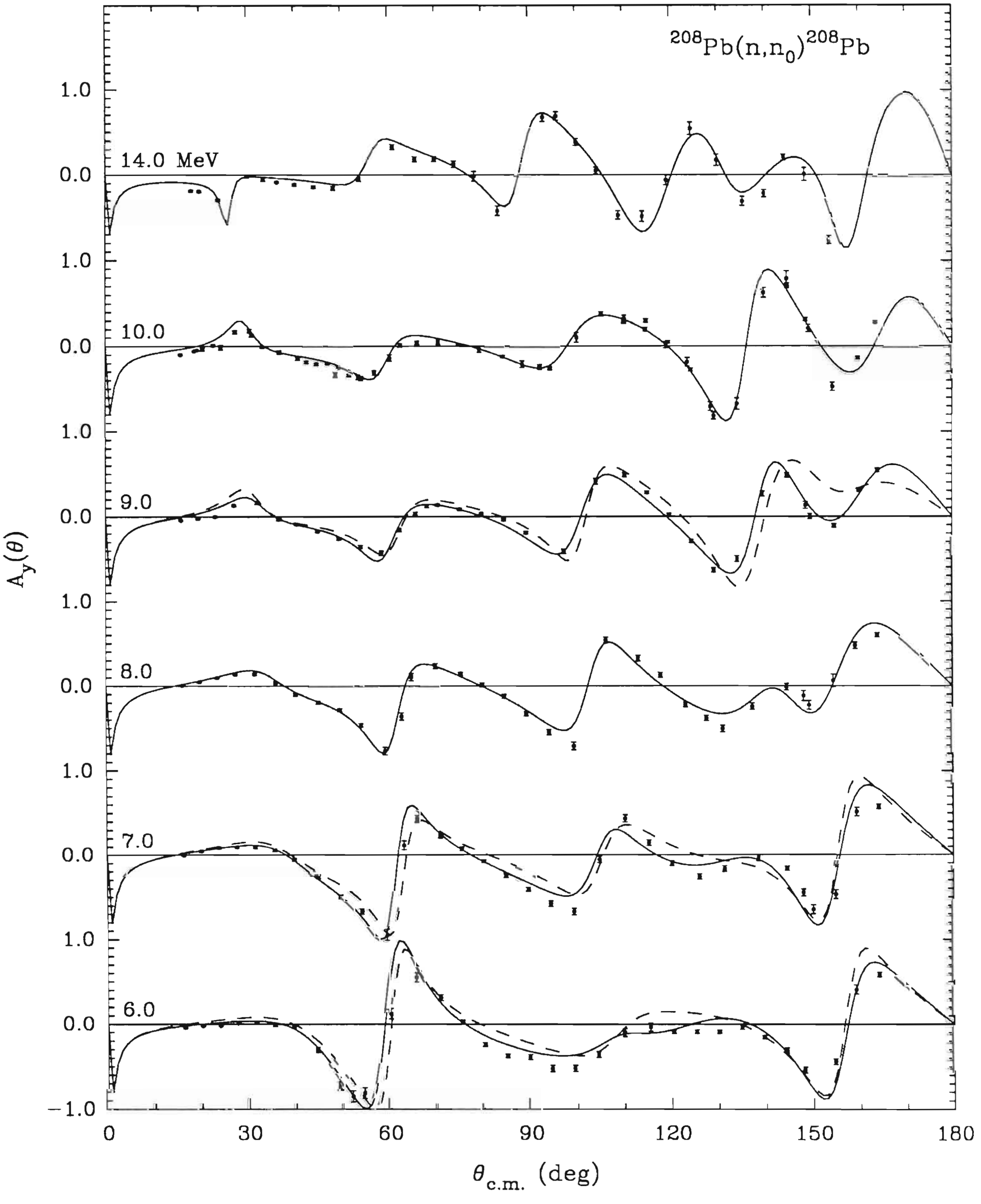

Figure 5.13. Optical model calculations compared to $A_y(\theta)$ data for neutron elastic scattering from ^{208}Pb. Solid curves are from an energy-dependent geometry fit whose parameters are listed in Table 5.3. Dashed curves are the Annand *et al.* predictions. The data at 6.0 and 7.0 MeV have been adjusted for compound nucleus contributions (see Chapter IV, Section B-6).

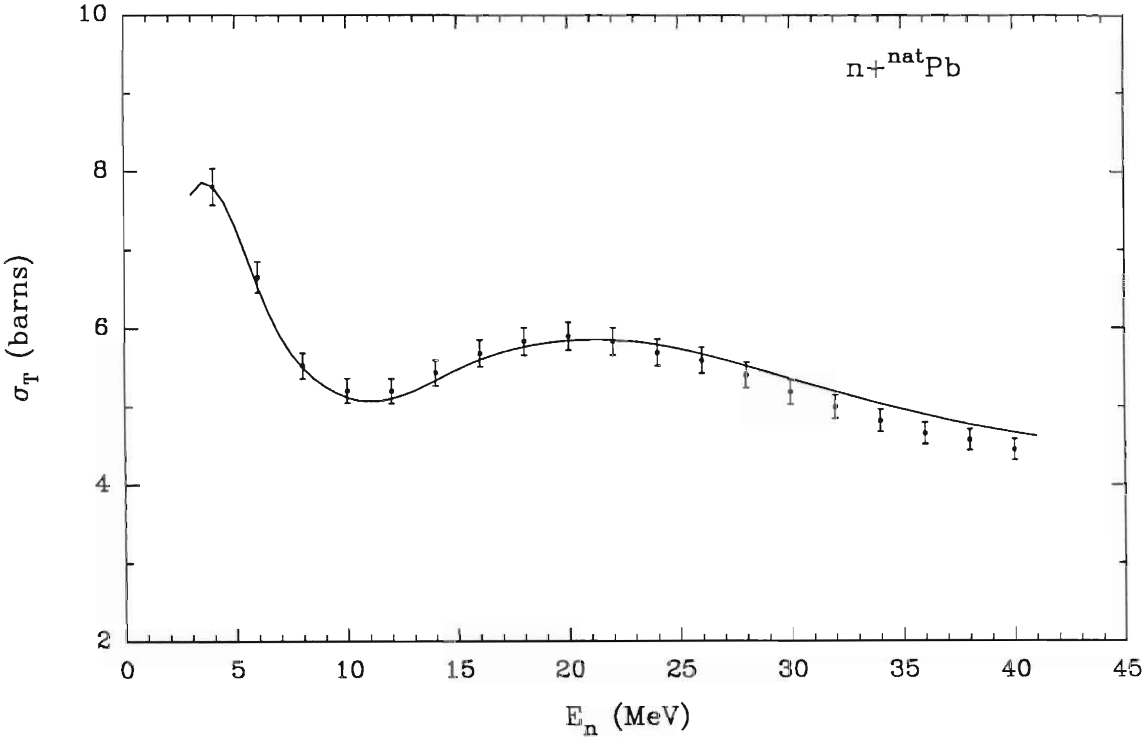

Figure 5.14. Comparison of the averaged n+^{nat}Pb total cross section data to n+^{208}Pb optical model predictions using the energy-dependent geometry parameters listed in Table 5.3.

5. Extrapolation of the optical model potential to negative energies

The average potential $V_V(r,E)$ is a continuous function of energy which varies smoothly as the bombarding neutron or nucleon energy E changes sign. When E is positive, $V_V(r,E)$ is the real part of the optical-model potential, and when E is negative, $V_V(r,E)$ is the shell-model potential. The fact that data from all energies can be utilized for parametrizing $V_V(r,E)$ is especially useful for the shell model because the few data available for negative E are strongly augmented by the abundant and varied scattering data for positive E. Essentially, the information for negative E reduces to the energies of the single-particle bound states. The primary purpose of the work described in this section, therefore, is to extrapolate the optical-model potential from positive to negative energies and compare the single-particle bound state energies predicted by our model to the reported experimentally bound state values.

The energy dependence of $V_V(r,E)$ is quite complicated in the region near the Fermi energy, which separates the occupied and unoccupied single-particle states at negative energies. This complicated behavior is described in terms of the dispersion relation. The dispersion relation connects the real and imaginary parts of the optical-model potential, and occurs because the target does not remain in its ground state during the elastic scattering process. In the dispersion relation, the real part of the optical-model potential is written:

$$V_V(r,E) = V_{HF}(r,E) + \Delta V_S(r,E) + \Delta V_V(r,E) \ , \qquad (5\text{-}8)$$

where $V_{HF}(r,E)$, $\Delta V_S(r,E)$, and $\Delta V_V(r,E)$ are the Hartree-Fock, surface dispersive, and volume dispersive contributions to the mean field, respectively. The dispersive contributions $\Delta V_S(r,E)$ and $\Delta V_V(r,E)$ are connected to the imaginary surface (W_S) and imaginary volume (W_V) parts of the optical model potential by the dispersion relations:

$$\Delta V_S(r,E) = \frac{P}{\pi}\int_{-\infty}^{+\infty} \frac{W_S(r,E')}{E' - E}\, dE' \qquad (5\text{-}9)$$

$$\Delta V_V(r,E) = \frac{P}{\pi}\int_{-\infty}^{+\infty} \frac{W_V(r,E')}{E' - E}\, dE' \ , \qquad (5\text{-}10)$$

where P denotes a principal value integral.

While the energy dependence of $V_{HF}(r,E)$ is expected to be smooth, this is not the case for $\Delta V_S(r,E)$ and $\Delta V_V(r,E)$. Since $W_S(r,E)$ and $W_V(r,E)$ decrease rapidly with decreasing energy due to threshold effects, both $\Delta V_S(r,E)$ and $\Delta V_V(r,E)$ have a distinct energy dependence for small E. Therefore, any complicated energy dependence observed in $V_V(r,E)$ at low energies is expected to be a result of the dispersive contributions.

To implement the dispersion relation, a new optical model search was performed in which the entire data set was fit simultaneously. As a starting point for this search, the constant geometry parameters discussed in Section C-3 of this chapter and listed in Table 5.2 were used. However, in this search procedure, the imaginary spin-orbit potential strength was taken to be zero at all energies and the geometry of the volume imaginary potential was forced to be identical to the geometry of the real volume potential. The imaginary spin-orbit potential was taken to be zero because of difficulty in computing single-particle bound-state values with an imaginary spin-orbit potential strength other than zero. The volume imaginary potential was forced to be identical to the geometry of the real volume potential so that the volume dispersive contribution to the mean field could be added directly to the Hartree-Fock potential strength. Using these initial starting parameters and conditions, surface and volume dispersive contributions to the mean field were calculated using Equations 5-9 and 5-10. An optical model search was then initiated using the computer code GENOA . In this search, dispersive contributions to the real central potential were held fixed, but Hartree-Fock, imaginary, and spin-orbit potential strengths and geometries were allowed to vary. After the optical model search, surface and volume dispersive contributions to the mean field were recalculated using the new imaginary potential parameters and another GENOA search was begun. This entire process was repeated until no improvement was seen in the fits to the scattering data. Final parameters of the last iteration are listed in Table 5.4, while corresponding fits to the differential cross section and analyzing power data are shown by the solid curves in Figures 5.15 through 5.18. Optical model predictions of the ^{208}Pb total cross section are shown in Figure 5.19 in comparison to energy averaged ^{nat}Pb total cross section data of Larson *et al.* (Larson 1980) and to ^{208}Pb total cross section data measured by Schutt *et al.* (Schutt 1988). Energy dependences of V_{HF}, $V_{HF}+\Delta V_V$, W_V, ΔV_V, W_S, and ΔV_S are shown in Figure 5.20.

To compute single-particle bound state energies, the real part of the Hartree-Fock optical-model potential $V_{HF}(r,E)$ was extrapolated to negative energies. At energies above the Fermi surface (ε_f=-6 MeV) the Hartree-Fock potential obtained in the above search and listed in Table 5.4 was used:

Table 5.4

Optical model parameters used in extrapolating the $n+^{208}Pb$ optical potential to negative energies

Parameter		Value	
V_{HF}	(MeV)	$46.338e^{-0.261(E-\varepsilon_f)/46.338}$	$\varepsilon_f = -6$ MeV
r_{V_V}	(fm)	1.221	
a_{V_V}	(fm)	0.720	
W_V	(MeV)	0.000	$E<11.4$ MeV
		$-2.032+0.178\cdot E$	11.4 MeV$<E<50.7$ MeV
		7.000[a]	50.7 MeV$<E$
r_{W_V}	(fm)	$= r_{V_V}$	
a_{W_V}	(fm)	$= a_{V_V}$	
ΔV_V		Calculated from Equation 5-10 and W_V above	
W_S	(MeV)	$2.966+0.512\cdot E$	$E<10.5$ MeV
		$9.749-0.134\cdot E$	10.5 MeV$<E<72.8$ MeV
		0.000	72.8 MeV$<E$
r_{W_S}	(fm)	1.291	
a_{W_S}	(fm)	0.463	
ΔV_S		Calculated from Equation 5-9 and W_S above	
V_{SO}	(MeV)	6.214	
r_{SO}	(fm)	1.147	
a_{SO}	(fm)	0.546	
χ^2 from 4.0 to 40.0 MeV		14500	

[a] In order to apply the dispersion relation to the $n+^{208}Pb$ data set, the value of $W_V(E)$ for E larger than 40.0 MeV is needed. Johnson *et al.* (Johnson 1987) determined, from fits to a peak in ^{208}Pb total cross section data, that W_V is approximately 7 MeV at 80 MeV. Therefore, $W_V(E)$ was parameterized by the listed linear expression up to $E = 50.7$ MeV, beyond which the constant value of $W_V(E) = 7.0$ MeV was taken.

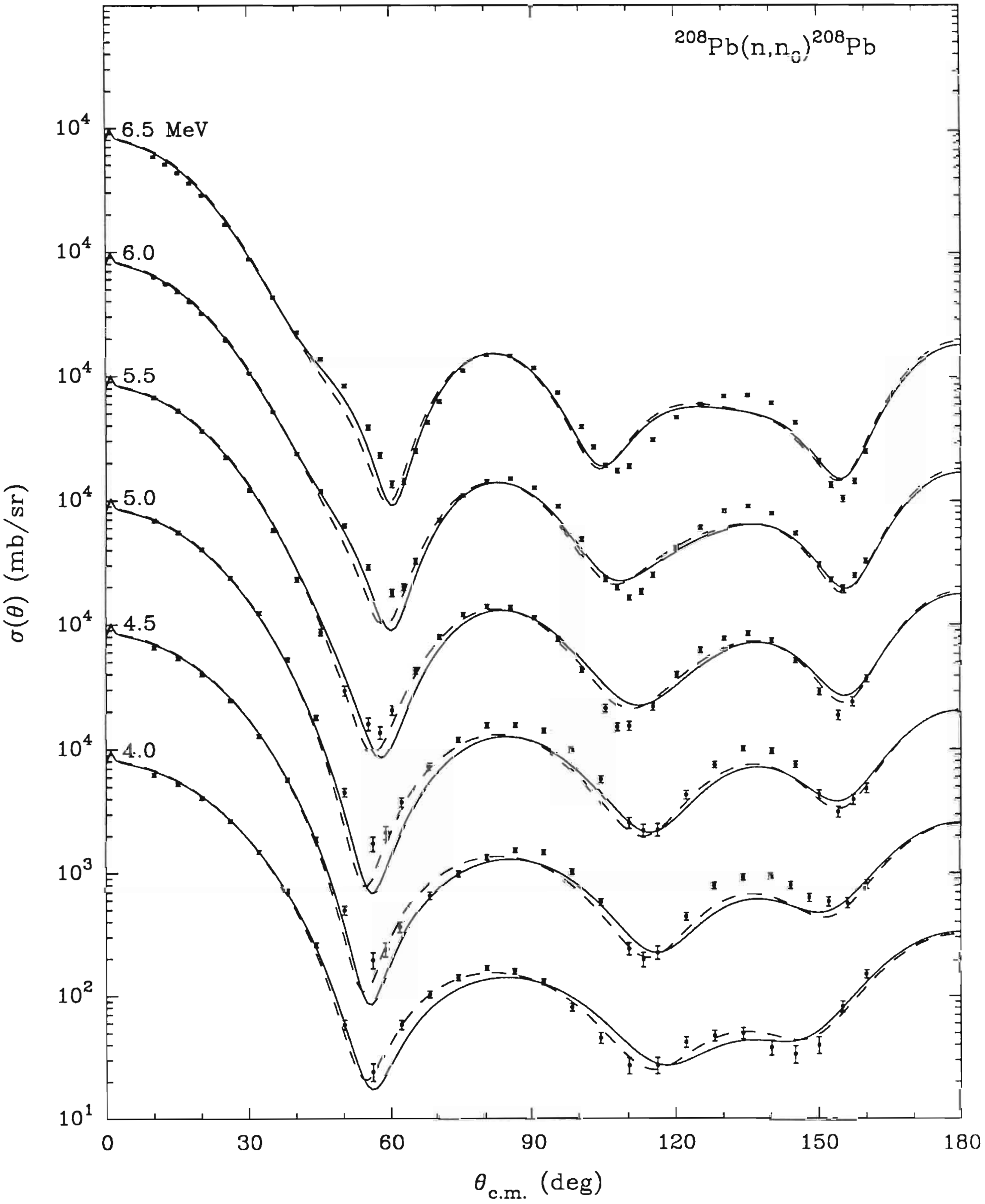

Figure 5.15. Optical model calculations compared to $\sigma(\theta)$ data for neutron elastic scattering from ^{208}Pb at 4.0 to 6.5 MeV. Curves are optical model fits using the dispersion relation. The solid curve is a fit to scattering data only, while the dashed curve is a fit to neutron single-particle bound state values as well as to scattering data. The data from 4.0 to 7.0 MeV have been adjusted for compound nucleus contributions (see Sect. B of this chapter).

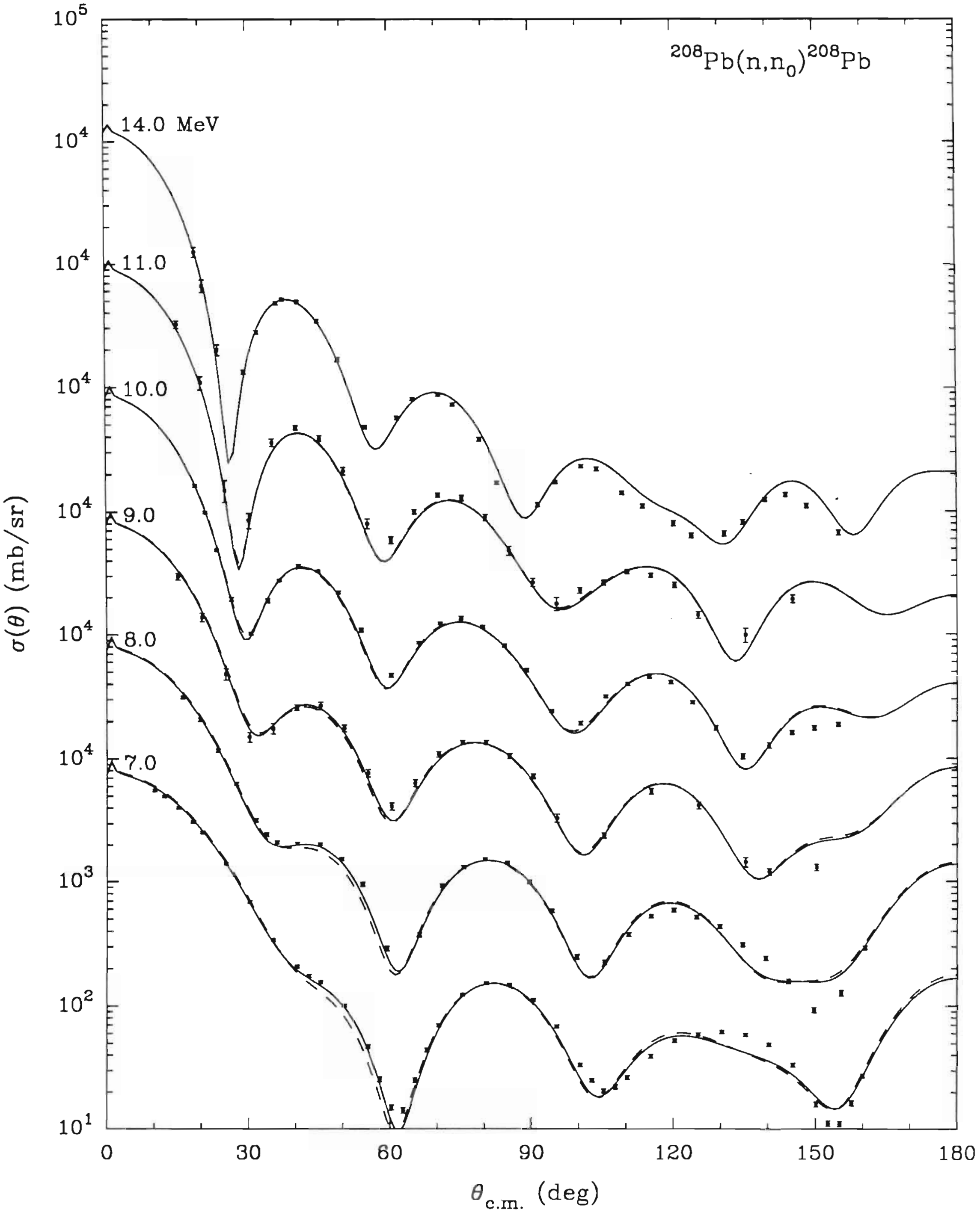

Figure 5.16. Continuation of Figure 5.15. Optical model calculations compared to σ(θ) data for neutron elastic scattering from ^{208}Pb at 7.0 to 14.0 MeV. Curves are optical model fits using the dispersion relation. The solid curve is a fit to scattering data only, while the dashed curve is a fit to neutron single-particle bound state values as well as to scattering data.

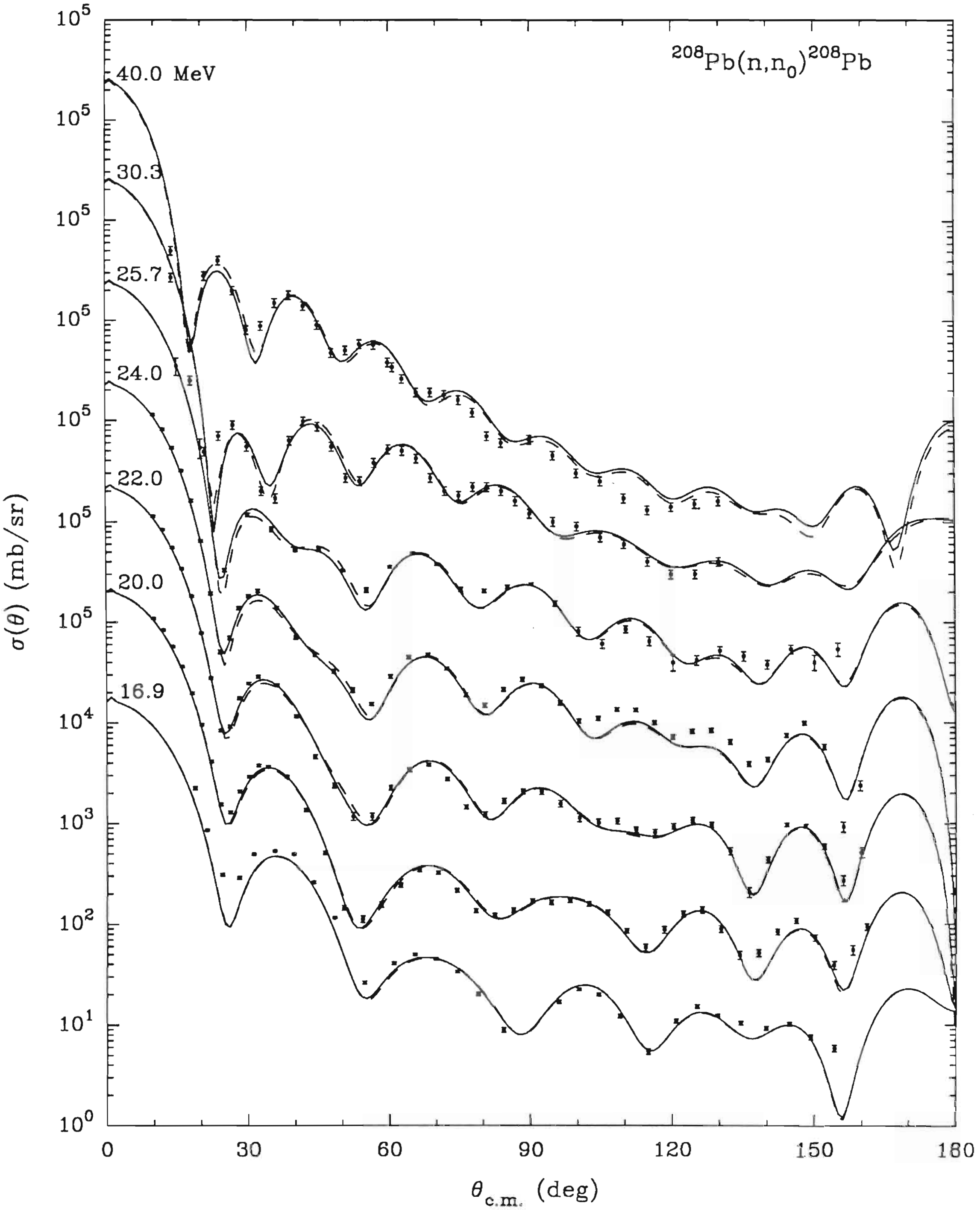

Figure 5.17. Continuation of Figure 5.15. Optical model calculations compared to σ(θ) data for neutron elastic scattering from ^{208}Pb at 16.9 to 40.0 MeV. Curves are optical model fits using the dispersion relation. The solid curve is a fit to scattering data only, while the dashed curve is a fit to neutron single-particle bound state values as well as to scattering data.

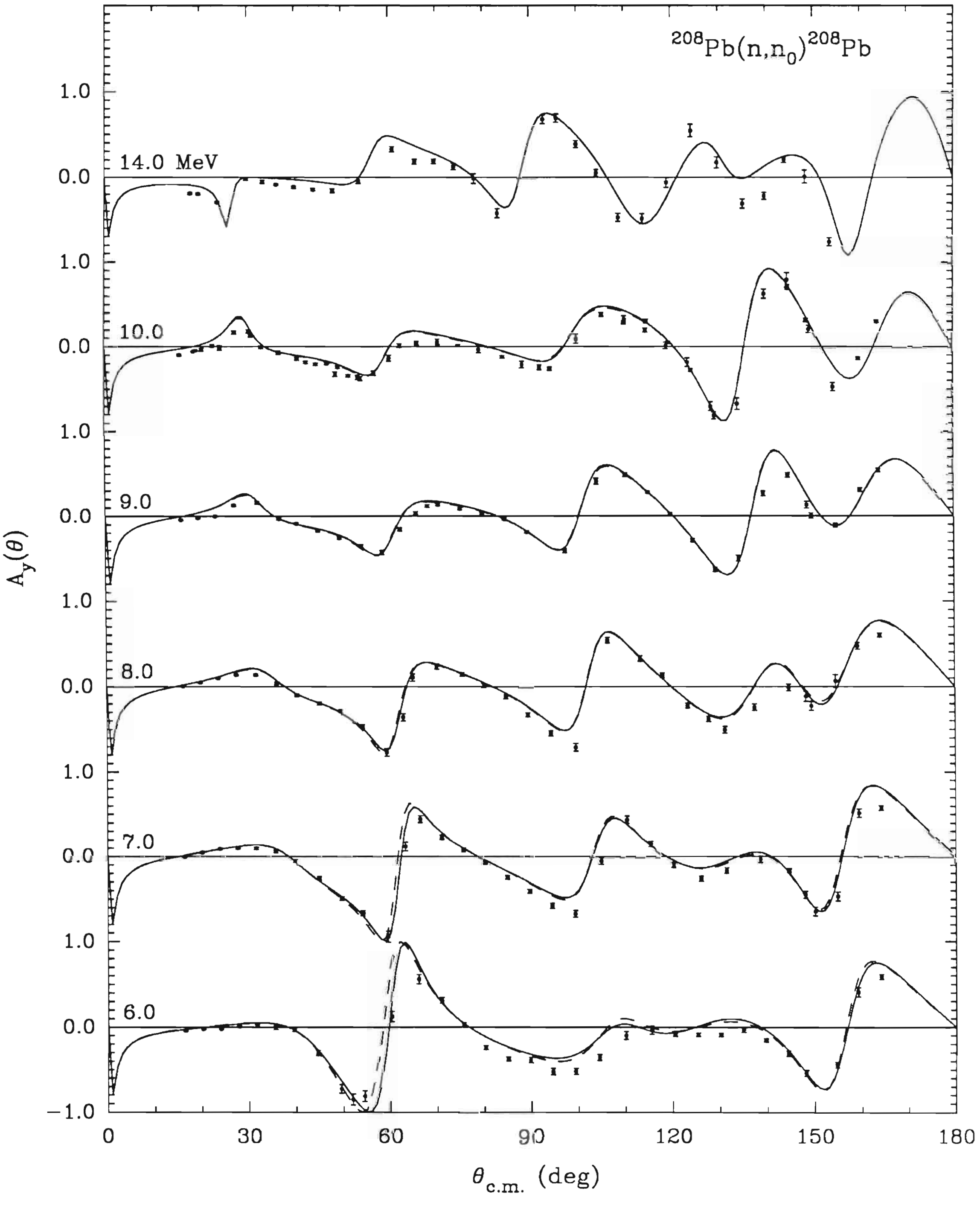

Figure 5.18. Optical model calculations compared to $A_y(\theta)$ data for neutron elastic scattering from ^{208}Pb. Curves are optical model fits using the dispersion relation. The solid curve is a fit to scattering data only, while the dashed curve is a fit to neutron single-particle bound state values as well as to scattering data. The data at 6.0 and 7.0 MeV have been adjusted for compound nucleus contributions (see Chapter IV, Section B-6).

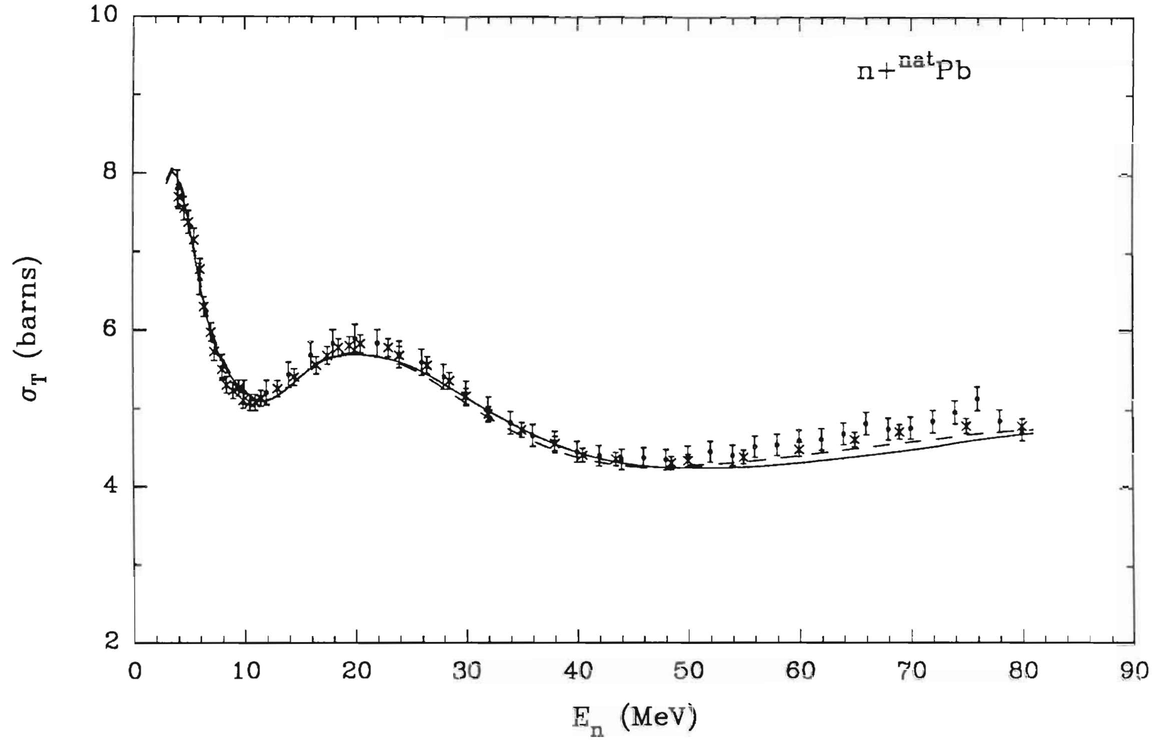

Figure 5.19. Optical model predictions of the ^{208}Pb total cross section compared to measured data. The solid curve is a prediction of the total cross section based on scattering data only, while the dashed curve is a prediction using neutron single-particle bound state values as well as scattering data. The energy averaged ^{nat}Pb total cross section data of Larson *et al.* (Larson 1980) are shown as circles while the total cross section data measured by Schutt *et al.* (Schutt 1988) are shown by x's.

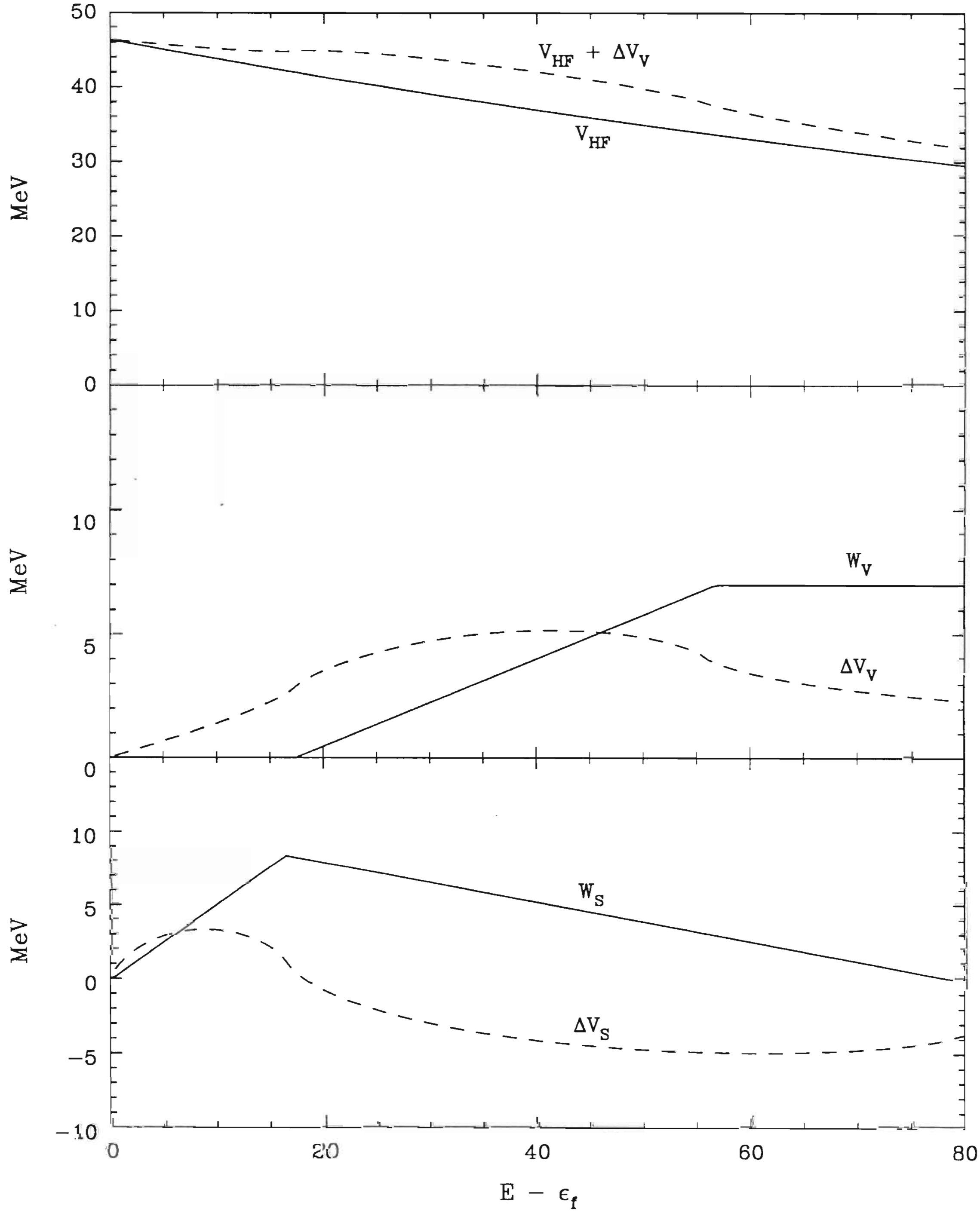

Figure 5.20. Energy dependences of the Hartree-Fock (V_{HF}), Hartree-Fock plus volume dispersive ($V_{HF}+\Delta V_V$), imaginary volume (W_V), volume dispersive (ΔV_V), imaginary surface (W_S), and surface dispersive (ΔV_S) parts of the optical model potential in the dispersion relation formalism.

$$V_{HF}(E) = 46.338 \cdot \exp[-0.261 \cdot (E - \varepsilon_f)/46.338] , \qquad (5\text{-}11)$$

while at energies below the Fermi surface, the Hartree-Fock potential was approximated by:

$$V_{HF}(E) = 46.338 - 0.261 \cdot (E - \varepsilon_f) . \qquad (5\text{-}12)$$

Using the computer code BOUNDSTATE (provided by C. Johnson, Oak Ridge National Laboratory), eigenvalues associated with $V_V(r,E)$ were calculated and compared to experimental energies of the weakly and deeply bound single-particle valence and hole states. Table 5.5 lists the neutron single-particle bound state energies (E_{nlj}) predicted by our extrapolated optical model compared to the experimental values of the neutron single-particle bound state energies of ^{208}Pb. In Table 5.5 the left-hand column specifies the principal, orbital, and total angular momentum quantum numbers. Experimental values of the single particle bound state energies were taken from Table III of Johnson *et al.* (Johnson 1987) and are listed in the column labeled 'Experimental E_{nlj}'. The column labeled 'Extrapolated V_{HF}' lists the extrapolated Hartree-Fock potential strengths from Equations 5-11 and 5-12. Predicted single-particle bound state energies of the extrapolated potential are listed in the column labeled 'Predicted E_{nlj}'. The column labeled 'Required V_{HF}' specifies the Hartree-Fock potential strength required to fit the single-particle bound states exactly.

To better determine the energy dependence of the Hartree-Fock potential at negative energies, Hartree-Fock potential strengths required to fit the single-particle bound states exactly and Hartree-Fock potential strengths obtained from single energy searches to the scattering data were fit using a least squares fitting routine to obtain:

$$V_{HF}(E) = 47.591 \cdot \exp[-0.332 \cdot (E - \varepsilon_f)/47.591] \qquad (5\text{-}13)$$

at energies above the Fermi surface and:

$$V_{HF}(E) = 47.591 - 0.332 \cdot (E - \varepsilon_f) \qquad (5\text{-}14)$$

Table 5.5

Neutron single-particle bound state energies E_{nlj} for n + ^{208}Pb

nlj	Experimental E_{nlj} (MeV)	Extrapolated V_{HF} (MeV)	Predicted E_{nlj} (MeV)	Required V_{HF} (MeV)	Fit V_{HF} (MeV)	Fit E_{nlj} (MeV)
$^3d_{3/2}$	-1.40	45.153	-1.02	45.983	46.088	-1.45
$^2g_{7/2}$	-1.44	45.163	-0.94	46.047	46.101	-1.47
$^4s_{1/2}$	-1.90	45.280	-1.38	46.480	46.249	-1.80
$^3d_{5/2}$	-2.37	45.400	-1.78	46.536	46.401	-2.30
$^1j_{15/2}$	-2.51	45.436	-1.02	47.682	46.446	-1.69
$^1i_{11/2}$	-3.16	45.603	-1.70	47.583	46.657	-2.47
$^2g_{9/2}$	-3.94	45.803	-3.25	46.886	46.912	-3.96
$^3p_{1/2}$	-7.37	46.696	-6.70	47.691	48.046	-7.61
$^2f_{5/2}$	-7.94	46.844	-7.21	47.837	48.235	-8.24
$^3p_{3/2}$	-8.26	46.928	-7.41	48.156	48.341	-8.39
$^1i_{13/2}$	-9.00	47.121	-7.24	49.461	48.587	-8.34
$^2f_{7/2}$	-9.71	47.306	-9.46	47.639	49.823	-10.61
$^1h_{9/2}$	-10.78	47.586	-9.70	48.877	49.178	-10.88
$^1h_{11/2}$	-16.50	49.079	-14.76	51.228	51.077	-16.38

at energies below the Fermi surface. Using this new Hartree-Fock potential, the single-particle bound state energies and scattering data were recalculated. The column labeled 'Fit V_{HF}' lists the Hartree-Fock potential strengths at the single-particle bound state energies using Equations 5-13 and 5-14. Predicted single-particle bound state energies using this new Hartree-Fock potential are listed in the column labeled 'Fit E_{nlj}'. Fits to differential cross section and analyzing power scattering data are shown as dashed curves in Figures 5.15 through 5.18, while the predicted ^{208}Pb total cross section is shown as a dashed curve in Figure 5.20. The total χ^2 for fits to the 4.0 to 40.0 MeV n+^{208}Pb scattering data set increased from 14 500 to 16 100 when using the new Hartree-Fock potential given by Equation 5-13.

A similar potential, also utilizing the dispersion relation, has recently been reported by Johnson *et al.* (Johnson 1987). When compared to our model or parametrization, the Johnson model predicts similar single-particle bound state energies while giving slightly poorer descriptions of the n+^{208}Pb scattering data. A quantitative comparison of the two models gives a total χ^2 to the 4.0 to 40.0 MeV ^{208}Pb scattering data of 20 400 for the Johnson model as opposed to a total χ^2 of 16 100 when using our parametrization.

D. Summary of the optical model analyses of neutron scattering from ^{208}Pb

The n+^{208}Pb differential cross section and analyzing power data obtained for the present work have proved to be a valuable addition to the existing data used in determining the optical model potential for neutron scattering from ^{208}Pb. The accuracy and precision of the new data have placed stringent constraints on optical model parameters and have specifically served to reduce ambiguity in spin-orbit parameters.

Using a conventional optical model, based on average geometries and systematic linear variations of potential strengths with energy, it has been possible to obtain an excellent description of the entire 4.0 to 40.0 MeV n+^{208}Pb data set. While small systematic discrepancies in the fits occur at backward angles of both the cross section and analyzing power data, the current constant geometry optical model potential represents a considerable improvement in quality of fit over the previous conventional n+^{208}Pb optical model work of Annand *et al.* (Annand 1985) and Finlay *et al.* (Finlay 1984).

In addition to the constant geometry potential obtained, an optical model potential in which the geometries of the real and imaginary central potentials varied linearly with energy was obtained and compared to the energy-dependent geometry potential of Annand *et al.* (Annand 1985). While a reduction in total χ^2 of approximately 6% to the 4.0 to 40.0 MeV n+^{208}Pb data set was achieved in these energy-dependent geometry fits in comparison to constant geometry fits, we are reluctant to introduce four new energy dependences into a model already laden with parameters.

In both the constant geometry and energy-dependent geometry searches, the real part of the spin-orbit potential was found to be energy independent. The imaginary part of the spin-orbit potential, however, was found to be energy dependent and positive at energies below 50 MeV.

In order to extrapolate our optical model potential from positive to negative energies and predict single-particle bound state energies, we have also utilized the dispersion relation in analyzing the n+^{208}Pb data set. Using a simple, fixed geometry model, in which the Hartree-Fock potential has an exponential energy dependence, we have been able to obtain a reasonable description of the 4.0 to 40.0 MeV n+^{208}Pb scattering data set and predict single-particle bound state energies that are in good agreement with experimental observations. In general, however, the present dispersion relation model is only a slight improvement over the n+^{208}Pb dispersion relation model reported by Johnson *et al.* (Johnson 1987). Both models are limited in the low-energy region (4.0 to 10.0 MeV), in that predicted differential cross sections do not fit the data well at large scattering angles. This failure might reflect an inadequacy of the imaginary potential used in the low-energy region since, for both models, the imaginary potential involves only one function of energy for $E < 10.5$ MeV.

CHAPTER VI

FOURIER-BESSEL ANALYSIS OF NEUTRON SCATTERING FROM ^{208}Pb

A. Introduction

In almost all optical model descriptions of nucleon elastic scattering there is some residual dependence on the final results from the initial shape or form factor chosen for each potential. The Woods-Saxon form factor was used in the previous chapter and has been widely used elsewhere to describe optical potentials for the scattering of nucleons as well as composite projectiles. The Woods-Saxon form factor, however, contains an implicit coupling between the surface region and the interior of the potential which could introduce undesirable constraints in an analysis and obscure information about the true shape of the nuclear potential. Attempts have been made to improve upon the Woods-Saxon form factor. Goldberg (Goldberg 1975) has shown that better fits to α-scattering data could be obtained by using a square of the Woods-Saxon form factor for the real part of the optical potential or by adding to the Woods-Saxon potential an extra term which is centered near the nuclear surface. More recently, Clement (Clement 1985) and Leeb (1985) have demonstrated that better fits to d+^{116}Sn and α+^{40}Ca elastic scattering data, respectively, could be obtained by expanding the real and imaginary central potentials in terms of a Fourier-Bessel series.

To further study the shape or form factor of the nuclear potential, we have expanded the n+^{208}Pb optical model potentials in terms of a Fourier-Bessel series. The application of the Fourier-Bessel method to neutron scattering is straightforward and should yield direct information on nuclear matter density since the Coulomb interaction is absent in neutron scattering. The Fourier-Bessel method, however, requires a large number of high accuracy data points and it was felt that only with the addition of the present n+^{208}Pb cross section and analyzing power data did we have the quality and quantity of data required to perform a Fourier-Bessel analysis and even then only in the limited energy range of 6.0 to 10.0 MeV. To our knowledge the current Fourier-Bessel study of neutron scattering from ^{208}Pb is unique in that, only two previous attempts have been made to fit neutron elastic scattering data using the Fourier-Bessel method, and both of these attempts (Alarcon *et al.* (Alarcon (1987) and Tornow *et al.* (Tornow 1982)) were for neutron scattering from ^{40}Ca.

B. Fourier-Bessel optical potential

Following Friedman and Batty (Friedman 1978) the conventional Woods-Saxon form factor employed in phenomenological descriptions of the optical potential was modified by taking a Fourier-Bessel expansion of the real central potential:

$$V(r) = V_V \cdot f_{WS}(r, R_{V_V}, a_{V_V}) + \sum_{n=1}^{N} b_n \cdot \frac{\sin(n\pi r/R_C)}{n\pi r/R_C}, \qquad (6\text{-}1)$$

where, in the first term of Equation 6-1, f_{WS} is the Woods-Saxon form factor defined in Chapter 5 and V_V, $R_{V_V}=r_{V_V}A^{1/3}$ and a_{V_V} are the "best-fit" Woods-Saxon potential parameters obtained in a conventional optical model search. In the second term of Equation 6-1, b_n are the Fourier-Bessel expansion coefficients determined by a least-squares fit to the experimental data, N is the number of terms used in the Fourier-Bessel expansion, and R_C is a suitably chosen Fourier-Bessel cut-off radius beyond which the second term in Equation 6-1 vanishes (i.e., for $r \geq R_C$ only the first term or Woods-Saxon part remains).

In the Fourier-Bessel analysis, the extra term given by the Fourier-Bessel series in Equation 6-1 was not assumed to be small, and no constraints were imposed on the b_n coefficients. In fact, it was possible to obtain excellent fits to the data without including the Woods-Saxon term in Equation 6-1. However, in this case, lengthy calculations were required for the least-square fits to converge, and the cutoff of the optical potential at the Fourier-Bessel cutoff radius was an undesirable feature. It should be noted that although this Fourier-Bessel method is somewhat analogous to the method used for analyses of elastic scattering of electrons, in which case the coefficients are directly related to the charge form factor of the nucleus, neither the number of Fourier-Bessel terms used in the Fourier-Bessel expansion nor the values of the Fourier-Bessel expansion coefficients have any direct relation to the charge form factor.

In addition to the real central potential, the imaginary and spin-orbit parts of the optical potential were also expanded in terms of a Fourier-Bessel series. However, resulting improvements in total χ^2 were usually small, and it was difficult to assess the significance of the results. Therefore, only expansions of the real central potential were examined in detail and are discussed here. In all the cases shown here, an independent Woods-Saxon form for the imaginary and spin-orbit parts of the potential was used, while the real central part of the optical potential was parameterized by Equation 6-1.

The uncertainty $\Delta V(r)$ in $V(r)$ can be calculated from the matrix M :

$$[\Delta V(r)]^2 = \sum_{m,n=1}^{N} (M^{-1})_{mn} \cdot \frac{\sin(m\pi r/R_C)}{m\pi r/R_C} \cdot \frac{\sin(n\pi r/R_C)}{n\pi r/R_C} , \qquad (6\text{-}2)$$

where the matrix M is formed from the partial derivatives of χ^2 and is given by $M_{mn}=(\partial^2\chi^2/\partial b_m\partial b_n)$, and the uncertainty Δb_n of parameter b_n is defined as $(\Delta b_n)^2=(M^{-1})_{nn}\chi^2$.

To expand the optical model potentials in terms of a Fourier-Bessel series and iterate on the numerical values of the various parameters, the computer code GOMFIL (written by H. Leeb, unpublished) was used. This code, however, does not include the Mott-Schwinger electromagnetic interaction, which causes a large negative analyzing power at far forward angles and small changes at other angles. To account for this limitation, it was necessary to adjust the analyzing power data using corrections estimated with the TUNL version of the optical model code GENOA (which calculates analyzing powers either with or without the Mott-Schwinger interaction). For all the ^{208}Pb data shown in this chapter, this adjustment is included.

C. Analysis of scattering data

1. Individual fits

As a first step in the Fourier-Bessel analysis of the ^{208}Pb scattering data, a conventional complex Woods-Saxon potential was obtained at each energy by a standard optical model fit to each data set. Using the optical model parameters listed in Table 5.2 of Chapter 5 as a starting point, parameters of the real, imaginary, and spin-orbit potentials were searched upon to obtain a "best-fit" Woods-Saxon potential at each individual energy. However, the imaginary spin-orbit potential strength was not searched upon here and was held fixed to the value obtained from the energy dependent function discussed in Section C-2 of Chapter 5. After obtaining "best-fit" Woods-Saxon potentials, Fourier-Bessel searches were begun in which values of both the Fourier-Bessel coefficients and parameters of the imaginary and real spin-orbit Woods-Saxon potentials were allowed to vary. Initial values of the Fourier-Bessel coefficients b_n were set to zero and no constraints were imposed on the coefficients. In these Fourier-Bessel searches, both the underlying Woods-Saxon part (first term in Equation 6-1) of the real central potential and the strength of the imaginary spin-orbit potential were held fixed.

Values of the Fourier-Bessel cutoff radius and the number of Fourier-Bessel coefficients (R_C and N, respectively) were determined by systematic searches. Figure 6-1 shows a plot of total χ^2 at 8.0 MeV versus number of Fourier-Bessel coefficients N for several values of the Fourier-Bessel cutoff radius R_C. As can be seen, the total χ^2 was rather insensitive to the particular value of R_C chosen. However, with increasing N the potential became more flexible and better fits to the data were achieved. Values of N between 8 and 10 were found to give adequate fits.

Using 10 Fourier-Bessel coefficients and a Fourier-Bessel cutoff radius of 12 fm ($N=10$ and $R_C=12\,fm$, respectively), elastic neutron scattering data for ^{208}Pb at 6.0, 7.0, 8.0, 9.0, and 10.0 MeV were individually fit using a Fourier-Bessel expansion of the real central potential. In these fits, improvement in values of total χ^2 as large as a factor of 3.5 were achieved in comparison to fits using only a Woods-Saxon form factor for the real central potential. Fourier-Bessel potentials obtained at each energy are shown in Figure 6.2 in comparison to the "best-fit" Woods-Saxon potentials. Corresponding fits to differential cross sections and analyzing powers are shown in Figures 6.3 through 6.7. At each energy, estimated uncertainties in the shape of the real central potential were obtained using Equation 6-2 and are shown in Figure 6.2 as a series of vertical error bars. Table 6.1 lists the n+^{208}Pb "best-fit" single energy Woods-Saxon optical model parameters obtained in the present analysis and parameters obtained when using the additional Fourier-Bessel term in the description of the real central potential. In Table 6.1, the column labeled 'χ^2_σ/N_σ' is the average chi-square per point for the cross section data, while the column labeled '$\chi^2_{A_y}/N_P$' is the average chi-square per point for the analyzing power data.

2. Average fits

In order to ascertain the energy-averaged form factor of the real central potential, a Fourier-Bessel analysis was performed on the combined 6.0 to 10.0 MeV ^{208}Pb neutron elastic scattering data set. In this analysis, the same energy-independent Fourier-Bessel term was added at each energy to an underlying "best-fit" energy-dependent Woods-Saxon potential. As with the individual fits, the first step was to obtain a "best-fit" energy-dependent Woods-Saxon potential. Using the optical model parameters listed in Table 5.2 as a starting point, parameters of the real, imaginary, and spin-orbit potentials were searched upon to obtain a constant geometry Woods-Saxon potential for the combined 6.0 to 10.0 MeV data set. In this search, real and imaginary central potential strengths were allowed to vary linearly as a function of energy, while the spin-orbit potential strength was forced to be energy independent. Geometries of the

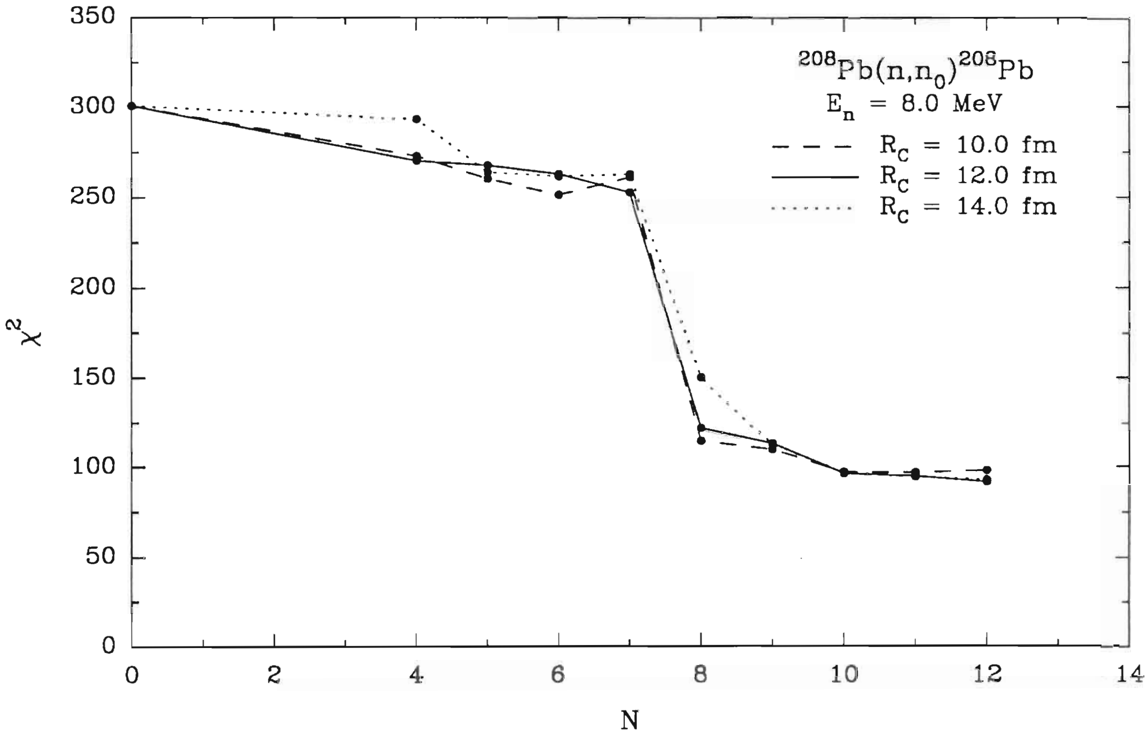

Figure 6.1. Total chi-square (χ^2) at 8.0 MeV versus number of Fourier-Bessel coefficients (N) for several values of the Fourier-Bessel cutoff radius (R_C).

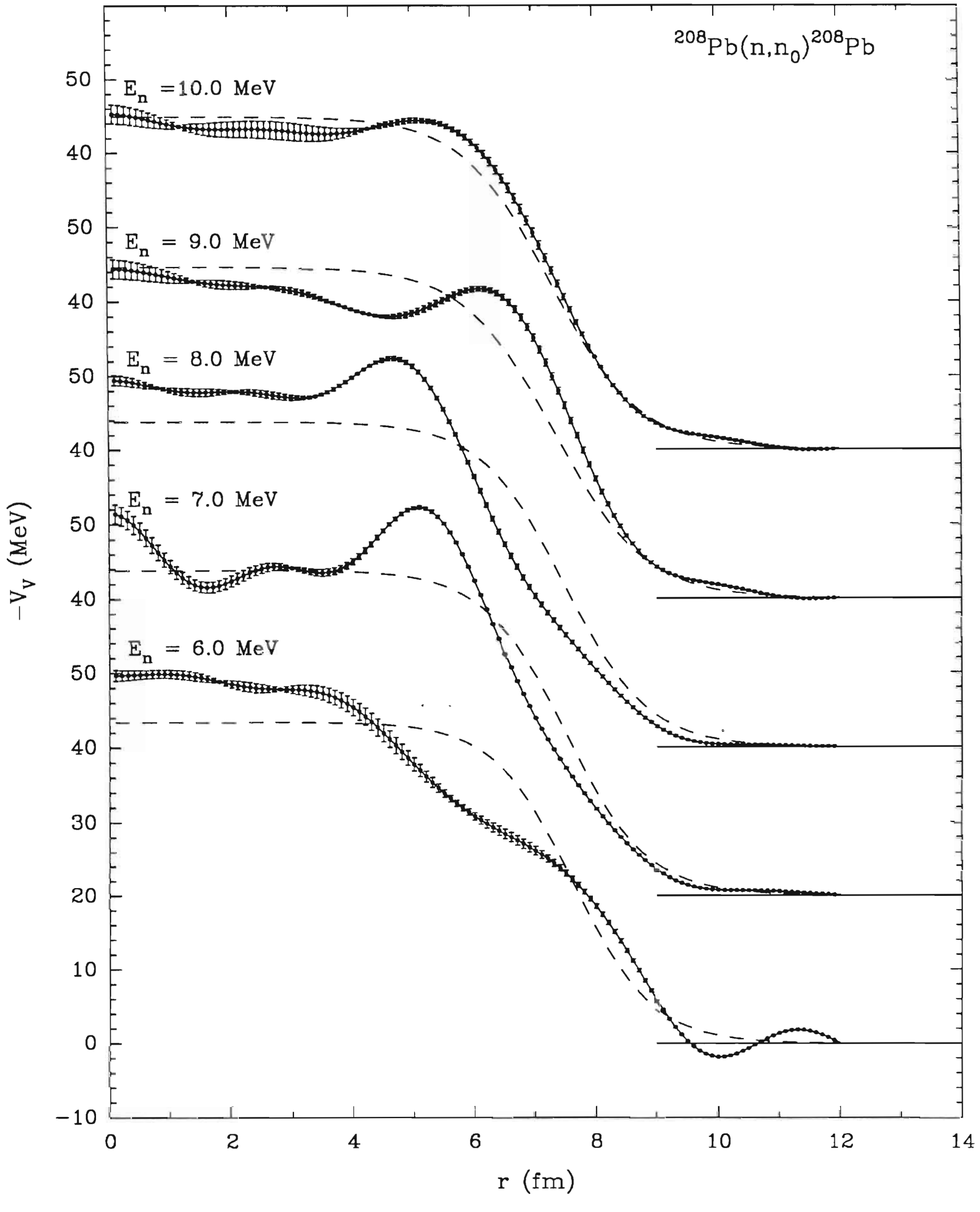

Figure 6.2. Fourier-Bessel potentials obtained at each energy compared to "best-fit" Woods-Saxon potentials.

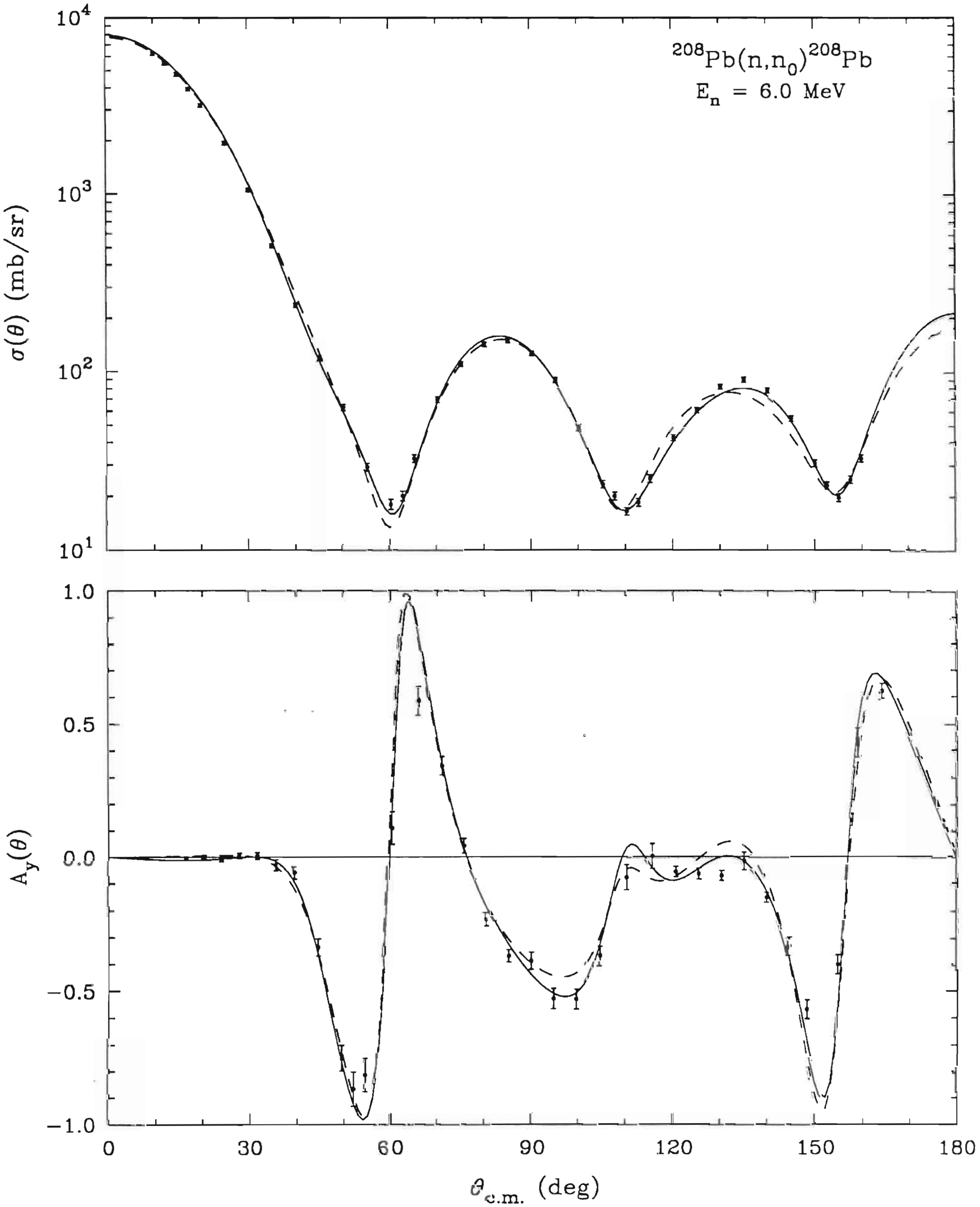

Figure 6.3. Comparison of fits to ^{208}Pb neutron elastic σ(θ) and A_y(θ) data at 6.0 MeV using a Fourier-Bessel or a Woods-Saxon potential. The solid line is a fit using a Fourier-Bessel potential while the dashed line is the "best-fit" obtained with a Woods-Saxon potential. The A_y(θ) data have been adjusted to compensate for the effect of the Mott-Schwinger interaction (see Section B of this chapter).

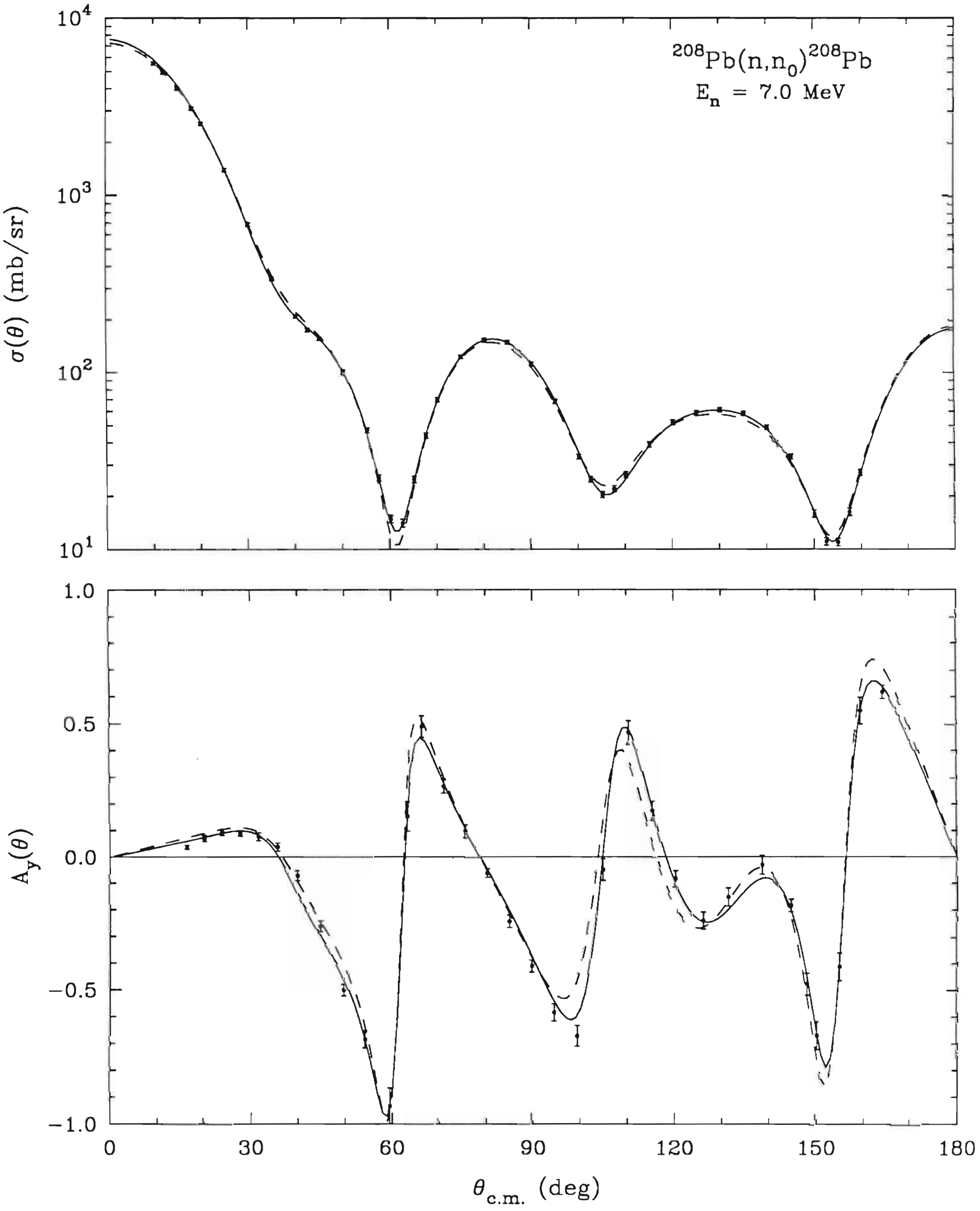

Figure 6.4. Comparison of fits to ^{208}Pb neutron elastic $\sigma(\theta)$ and $A_y(\theta)$ data at 7.0 MeV using a Fourier-Bessel or a Woods-Saxon potential. The solid line is a fit using a Fourier-Bessel potential while the dashed line is the "best-fit" obtained with a Woods-Saxon potential. The $A_y(\theta)$ data have been adjusted to compensate for the effect of the Mott-Schwinger interaction (see Section B of this chapter).

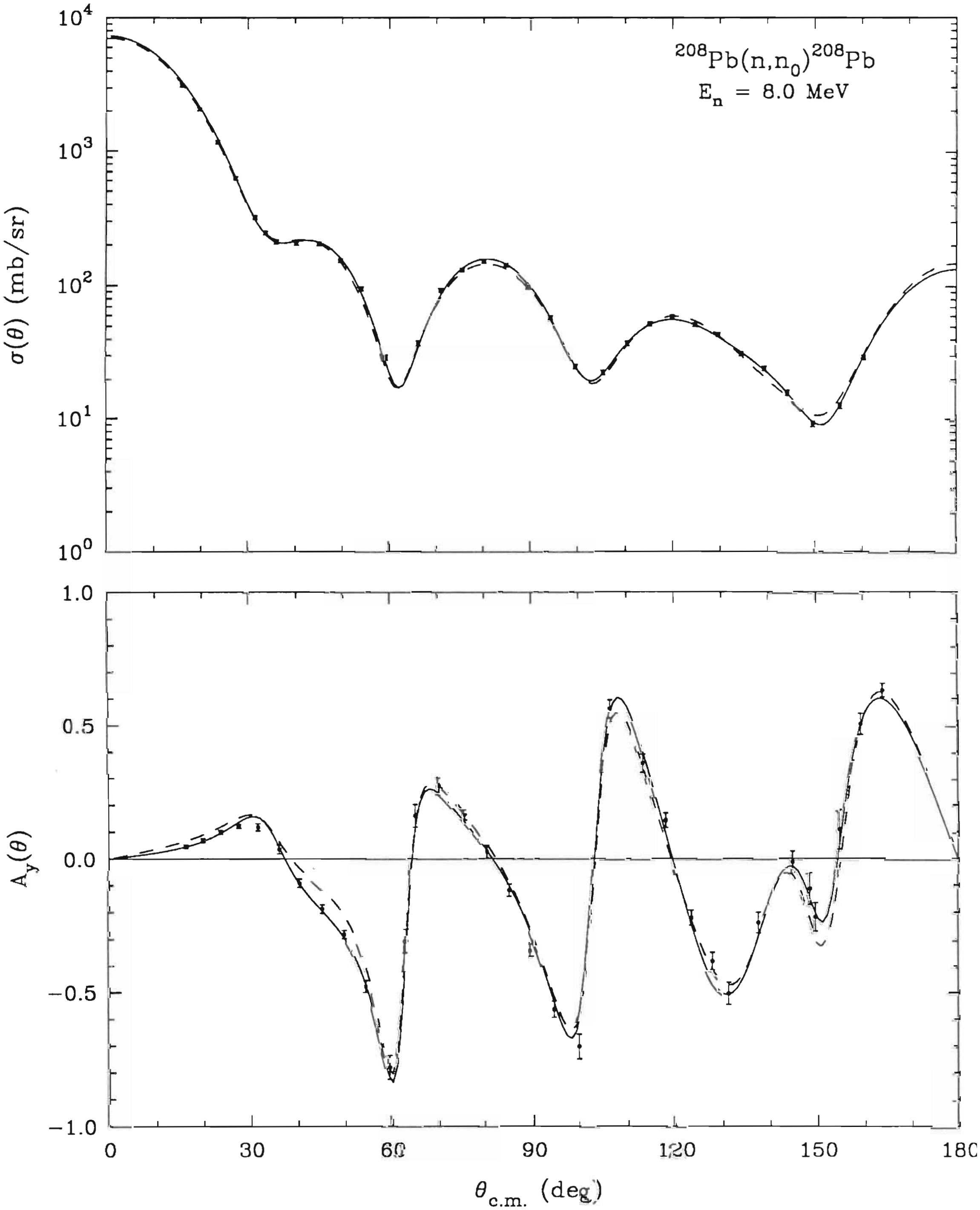

Figure 6.5. Comparison of fits to ^{208}Pb neutron elastic σ(θ) and A_y(θ) data at 8.0 MeV using a Fourier-Bessel or a Woods-Saxon potential. The solid line is a fit using a Fourier-Bessel potential while the dashed line is the "best-fit" obtained with a Woods-Saxon potential. The A_y(θ) data have been adjusted to compensate for the effect of the Mott-Schwinger interaction (see Section B of this chapter).

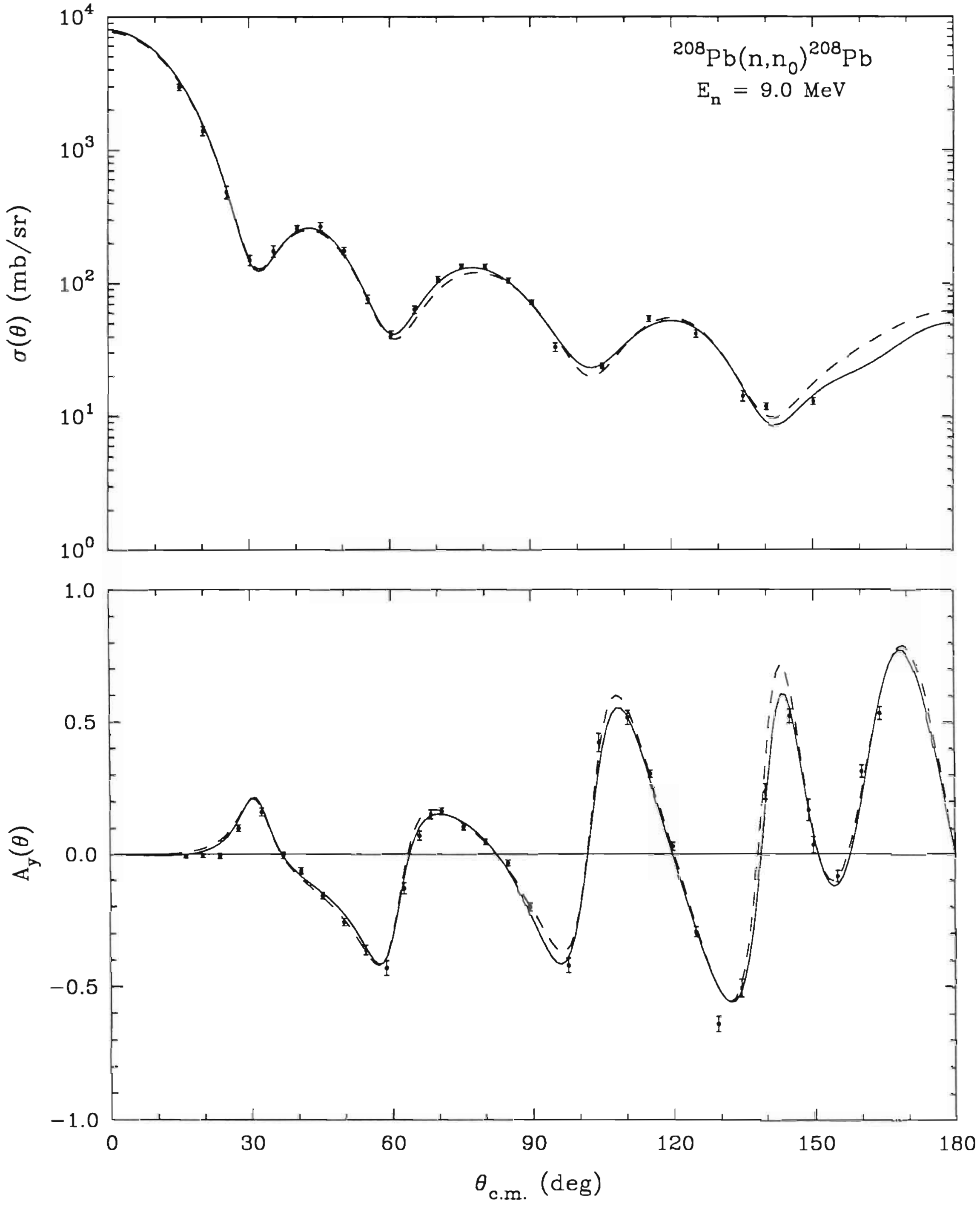

Figure 6.6. Comparison of fits to ^{208}Pb neutron elastic $\sigma(\theta)$ and $A_y(\theta)$ data at 9.0 MeV using a Fourier-Bessel or a Woods-Saxon potential. The solid line is a fit using a Fourier-Bessel potential while the dashed line is the "best-fit" obtained with a Woods-Saxon potential. The $A_y(\theta)$ data have been adjusted to compensate for the effect of the Mott-Schwinger interaction (see Section B of this chapter).

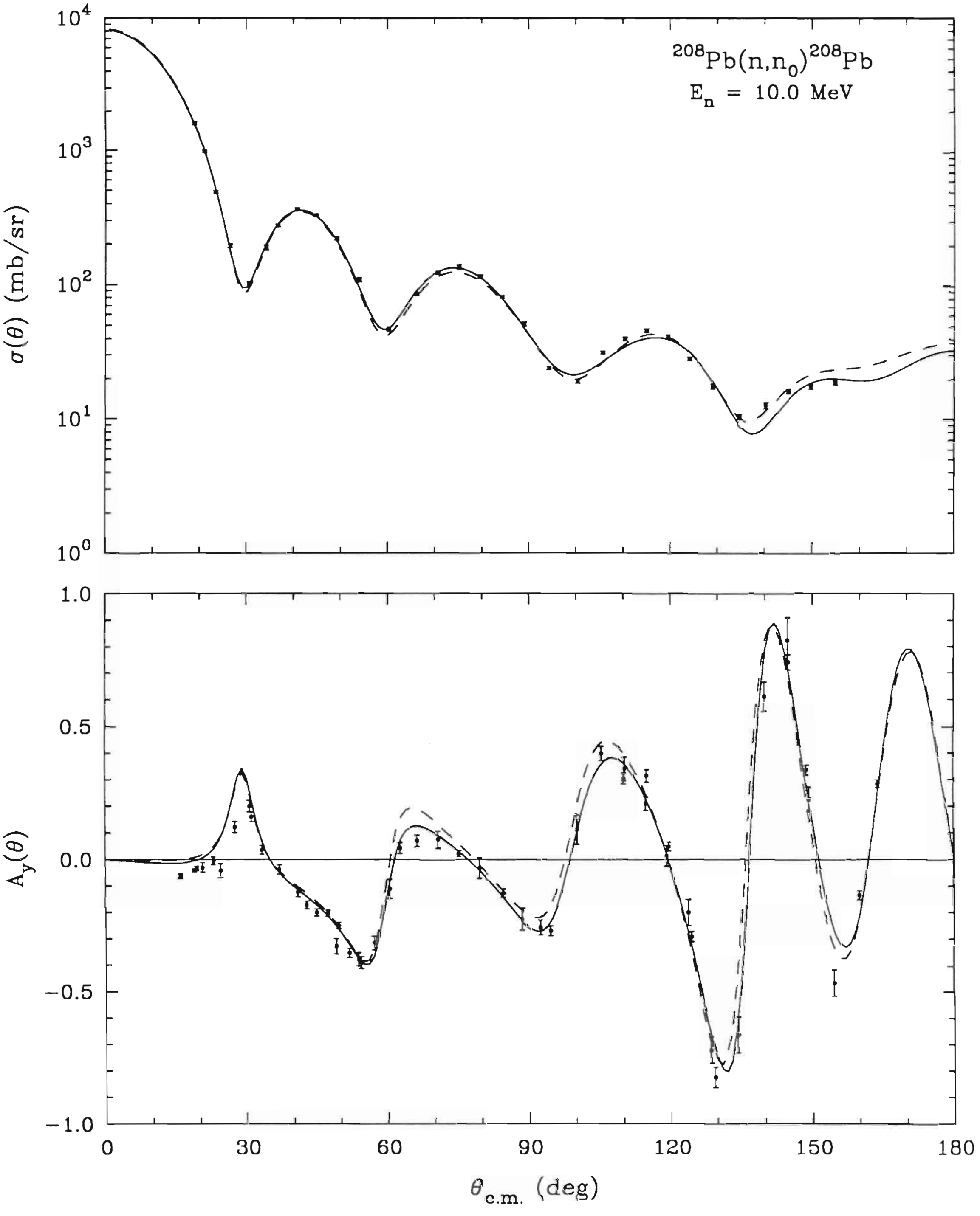

Figure 6.7. Comparison of fits to ^{208}Pb neutron elastic $\sigma(\theta)$ and $A_y(\theta)$ data at 10.0 MeV using a Fourier-Bessel or a Woods-Saxon potential. The solid line is a fit using a Fourier-Bessel potential while the dashed line is the "best-fit" obtained with a Woods-Saxon potential. The $A_y(\theta)$ data have been adjusted to compensate for the effect of the Mott-Schwinger interaction (see Section B of this chapter).

Table 6.1

Parameters obtained in "best-fit" single-energy Woods-Saxon (W-S) optical model searches and parameters obtained when using an additional Fourier-Bessel (F-B) term in the description of the real central potential for n+^{208}Pb elastic scattering

E_n (MeV)		6.0 MeV		7.0 MeV		8.0 MeV		9.0 MeV		10.0 MeV	
		W-S	F-B	W-S	F-B	W-S	F-B	W-S	F-B	W-S	F-B
V_V	(MeV)	43.393	43.393a)	43.842	43.842a)	43.782	43.782a)	44.635	44.635a)	44.929	44.929a)
r_V	(fm)	1.286	1.286a)	1.265	1.265a)	1.262	1.262a)	1.237	1.237a)	1.230	1.230a)
a_V	(fm)	0.652	0.652a)	0.675	0.675a)	0.681	0.681a)	0.732	0.732a)	0.717	0.717a)
W_S	(MeV)	7.377	8.149	7.268	5.870	8.482	6.276	8.303	9.435	7.173	7.612
r_I	(fm)	1.325	1.286	1.307	1.309	1.305	1.257	1.282	1.286	1.284	1.292
a_I	(fm)	0.348	0.350	0.398	0.441	0.389	0.471	0.438	0.420	0.510	0.470
V_{SO}	(MeV)	6.764	6.733	5.664	6.962	5.545	5.819	6.931	7.541	6.830	6.687
r_{SO}	(fm)	1.244	1.216	0.958	0.919	1.013	0.902	1.220	1.205	1.182	1.164
a_{SO}	(fm)	0.349	0.343	0.437	0.327	0.587	0.484	0.489	0.482	0.531	0.560
W_{SO}	(MeV)	0.504b)	0.504b)	0.488b)	0.488b)	0.472b)	0.472b)	0.456b)	0.456b)	0.440b)	0.440b)
R_C	(fm)	—	12.000	—	12.000	—	12.000	—	12.000	—	12.000
b_1		—	-3.232	—	0.293	—	-1.729	—	2.177	—	1.357
b_2		—	2.326	—	6.187	—	11.990	—	-8.688	—	-2.176
b_3		—	14.315	—	-3.863	—	4.365	—	-6.232	—	-4.965
b_4		—	5.594	—	-17.124	—	-20.984	—	16.955	—	1.628
b_5		—	-23.362	—	7.604	—	-2.855	—	6.066	—	6.821
b_6		—	0.767	—	19.855	—	22.760	—	-17.706	—	-1.856
b_7		—	24.181	—	-4.708	—	4.678	—	-1.042	—	-3.589
b_8		—	-22.157	—	-19.944	—	-18.914	—	12.437	—	2.781
b_9		—	14.545	—	6.670	—	-2.044	—	-5.232	—	-3.061
b_{10}		—	-6.713	—	12.696	—	8.442	—	1.046	—	3.414
χ^2_σ/N		8.91	3.63	3.68	1.01	3.64	1.41	5.24	2.45	9.04	7.01
$\chi^2_{A_y}/N$		6.62	3.62	5.70	1.80	5.05	1.36	5.46	4.17	11.29	6.79

a) In the Fourier-Bessel descriptions, parameters of the underlying Woods-Saxon part of the real central potential were not searched upon and were held fixed to their "best-fit" values.

b) In both the "best-fit" Woods-Saxon and Fourier-Bessel searches, the imaginary spin-orbit potential strength was not searched upon and was held fixed to the value obtained from the energy dependent function discussed in Section C-2 of Chapter 5.

real, imaginary, and spin-orbit potential were required to be energy-independent. As in the individual fits, the imaginary spin-orbit potential strength was not searched upon and was held fixed to the linear energy dependent function listed in Table 5.2.

After obtaining a "best-fit" energy-dependent Woods-Saxon potential, a Fourier-Bessel search was initiated using a Fourier-Bessel cutoff radius of 12 fm ($R_C=12$ *fm*) and 10 Fourier-Bessel coefficients ($N=10$). As with the individual fits, initial values of the Fourier-Bessel coefficients b_n were set to zero and no constraints were imposed. In this search, both the underlying Woods-Saxon part of the real central potential and the strength of the imaginary spin-orbit potential were held fixed while parameters of the imaginary central potential and real spin-orbit potential were allowed to vary. After searching, an improvement in total χ^2 of approximately 15% was obtained for the n+^{208}Pb data set when using a Fourier-Bessel description of the real central potential as opposed to the analysis using a conventional Woods-Saxon form factor. The Fourier-Bessel potentials and associated potential uncertainties obtained at each energy are shown in Figure 6.8 in comparison to the "best-fit" energy-dependent Woods-Saxon potentials. Corresponding fits to differential cross sections and analyzing powers are shown in Figures 6.9 and 6.10. The estimated uncertainty in the shape of the real central potential was obtained using Equation 6-2 and is shown at each energy in Figure 6.8 as a series of vertical error bars. Table 6.2 lists the n+^{208}Pb "best-fit" energy-dependent Woods-Saxon parameters obtained in the present analysis and parameters obtained when using the additional Fourier-Bessel term in the description of the real central potential. In Table 6.2 the column labeled 'χ^2 ' is the total chi-square from 6.0 to 10.0 MeV.

D. Summary of the Fourier-Bessel analyses of neutron scattering from ^{208}Pb

In optical model fits to n+^{208}Pb data, improvements in total χ^2 as large as a factor of 3.5 were observed for individual fits when using a Fourier-Bessel description of the real central potential as opposed to analyses using a conventional Woods-Saxon form factor. In these individual fits, radial distributions of the potentials were also seen to deviate significantly from Woods-Saxon shapes. These large deviations could be caused by small systematic discrepancies in the data or by an insensitivity of the scattering observables to the shape of the real central potential for small radii.

In a Fourier-Bessel analysis of the combined 6.0 to 10.0 MeV n+^{208}Pb elastic scattering data set, in which the same energy-independent Fourier-Bessel term was added at each energy, improvements in total χ^2 were small when compared to the optical model analysis using conventional Woods-Saxon form factors, and radial distributions of the real central potentials deviated only slightly from Woods-Saxon shapes. It is interesting

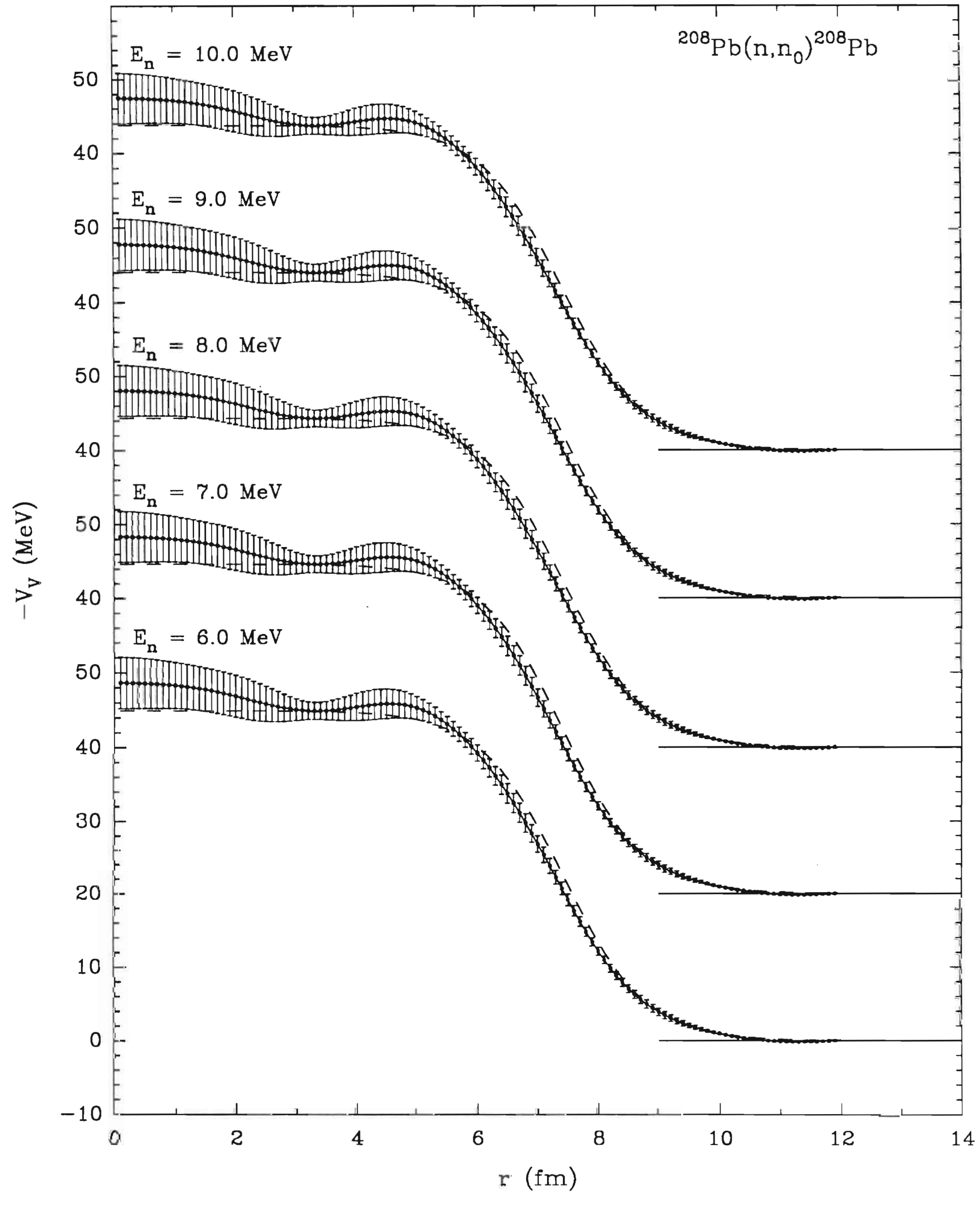

Figure 6.8. Average Fourier-Bessel potentials obtained compared to "best-fit" energy dependent Woods-Saxon potentials.

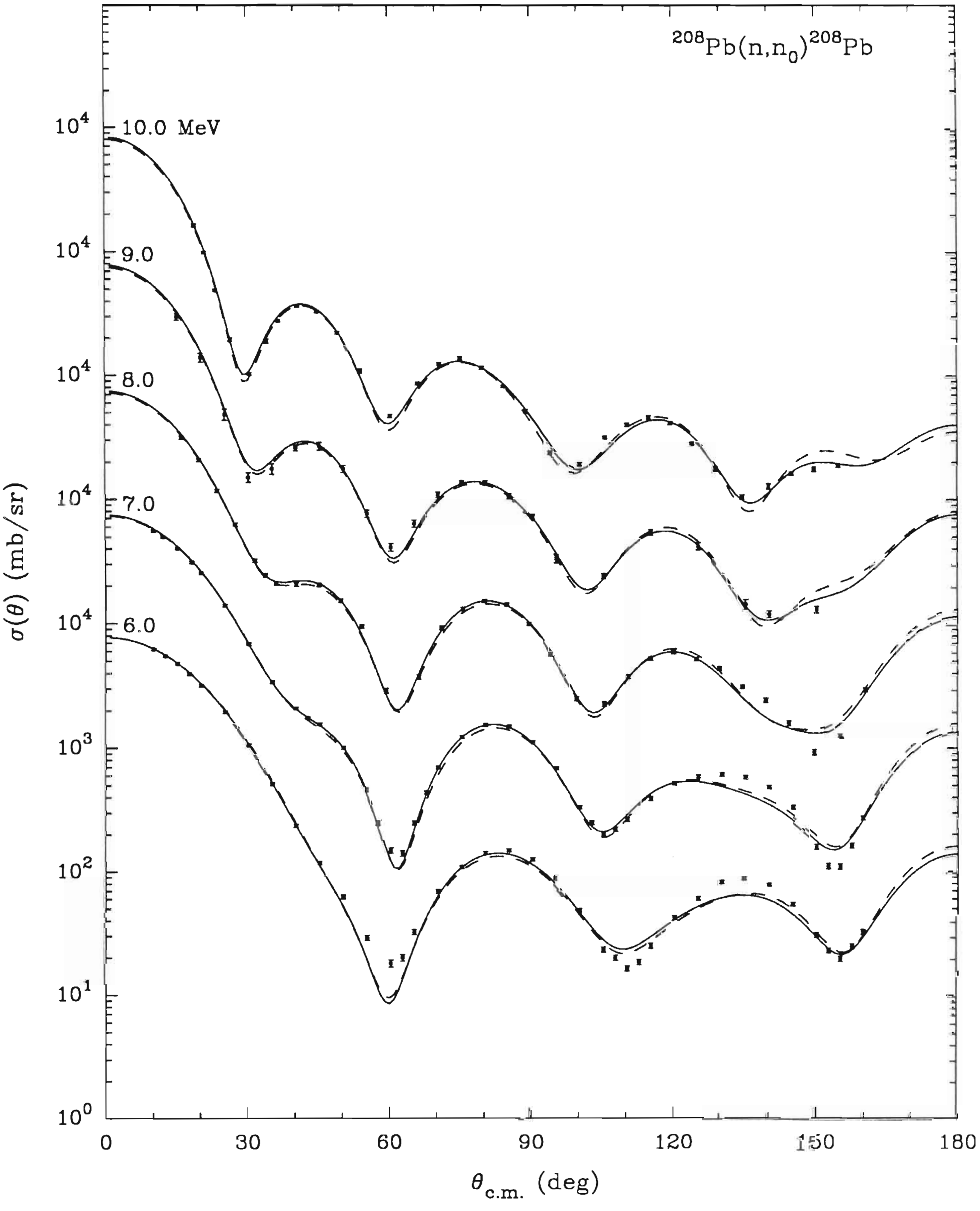

Figure 6.9. Comparison of fits to ^{208}Pb neutron elastic $\sigma(\theta)$ data from 6.0 to 10.0 MeV using a Fourier-Bessel or a Woods-Saxon potential. The solid line is a fit using an average Fourier-Bessel potential while the dashed line is the "best-fit" obtained using an energy dependent Woods-Saxon potential.

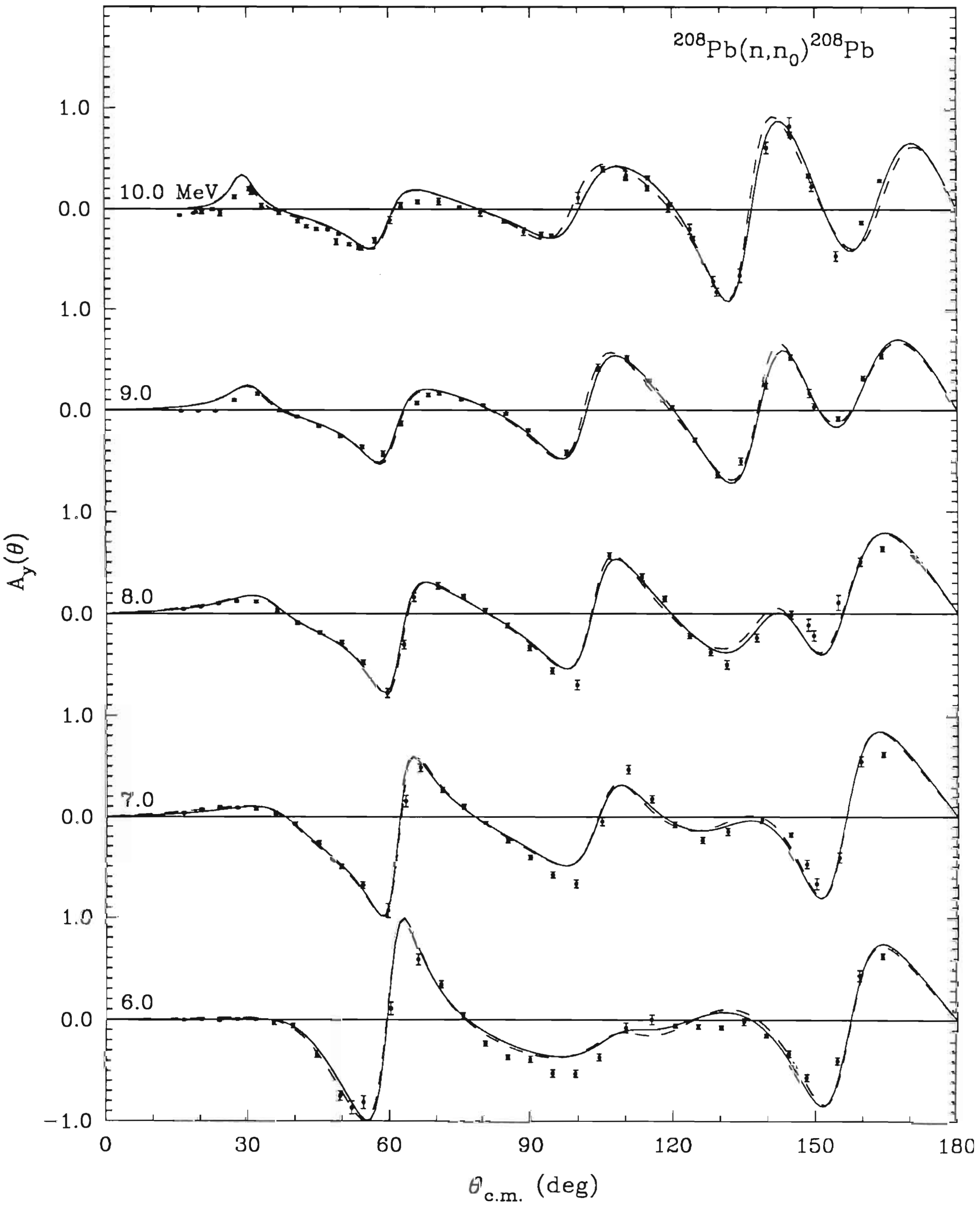

Figure 6.10. Comparison of fits to ^{208}Pb neutron elastic $A_y(\theta)$ data at 6.0 to 10.0 MeV using a Fourier-Bessel or a Woods-Saxon potential. The solid line is a fit using an average Fourier-Bessel potential while the dashed line is the "best-fit" obtained using an energy dependent Woods-Saxon potential. The data have been adjusted to compensate for the effect of the Mott-Schwinger interaction (see Section B of this chapter).

Table 6.2

Parameters obtained in a "best-fit" energy-dependent Woods-Saxon (W-S) optical model search and parameters obtained when using an additional Fourier-Bessel (F-B) term in the description of the real central potential for n+^{208}Pb elastic scattering

	W-S	F-B
V_V (MeV)	46.674 - 0.293·E	46.674 - 0.293·E[a)]
r_V (fm)	1.253	1.253[a)]
a_V (fm)	0.674	0.674[a)]
W_S (MeV)	2.632 + 0.592·E	3.245 + 0.485·E
r_I (fm)	1.291	1.284
a_I (fm)	0.441	0.447
V_{SO} (MeV)	6.334	6.259
r_{SO} (fm)	1.166	1.142
a_{SO} (fm)	0.529	0.551
W_{SO} (MeV)	0.600 - 0.016·E[b)]	0.600 - 0.016·E[b)]
R_C (fm)	—	12.000
b_1	—	-0.771
b_2	—	2.758
b_3	—	2.010
b_4	—	-4.066
b_5	—	0.037
b_6	—	8.060
b_7	—	-1.683
b_8	—	-2.745
b_9	—	-0.895
b_{10}	—	1.024
χ^2	4 574	3 911

a) In the Fourier-Bessel descriptions, parameters of the underlying Woods-Saxon part of the real central potential were not searched upon and were held fixed to their "best-fit" values.

b) In both the "best-fit" Woods-Saxon and Fourier-Bessel searches, the imaginary spin-orbit potential strength was not searched upon and was held fixed to the linear energy dependent function discussed in Section C-2 of Chapter 5.

to note, however, that the general shape of the real central potential obtained from this energy-averaged Fourier-Bessel analysis is similar to the ^{208}Pb charge distribution, determined from high-momentum-transfer electron scattering (Frois 1977), in that a small surface peaking of the potential is observed between 4.0 and 5.0 fm.

In both individual and energy averaged fits, estimated potential uncertainties indicate that the real central potential is rather poorly determined in the nuclear interior but seems to be well determined near the nuclear surface. This agrees with commonly accepted knowledge that low-energy neutron scattering data are rather insensitive to the nuclear interior.

In summary, when the Fourier-Bessel method is applied to the real central potential, much better descriptions of n+^{208}Pb elastic scattering data can be obtained than analyses performed when using only a Woods-Saxon form factor. Although the improvement in fits, in both the individual and energy averaged cases, is partly due to an increased number of parameters or degrees of freedom, the Fourier-Bessel method indicates that a different shape or form factor for the real central potential can greatly improve the quality of fits to neutron scattering data.

CHAPTER VII

SUMMARY

Differential cross sections and analyzing powers have been obtained for the scattering of neutrons from the ground and first excited states of ^{208}Pb. These new measurements include differential cross sections for elastic and inelastic neutron scattering at 8.0 MeV, and analyzing powers for elastic and inelastic neutron scattering at 6.0, 7.0, 8.0, 9.0, and 10.0 MeV. All data were obtained using the Triangle Universities Nuclear Laboratory (TUNL) pulsed beam facility and time-of-flight spectrometer. The data have been corrected for the effects of finite geometry, flux attenuation, and multiple scattering. At 6.0 and 7.0 MeV the elastic scattering analyzing power data were adjusted for compound nucleus contributions using the observed cross sections and calculated compound nucleus cross sections reported by Annand *et al.* (Annand 1985). Although the cross sections and analyzing powers for inelastic neutron scattering from ^{208}Pb were not used in the present analyses, they would be appropriate for future descriptions of n+^{208}Pb scattering in the coupled-channels formalism.

The present n+^{208}Pb elastic scattering data have been combined with the differential cross section and analyzing power data previously measured at TUNL (Floyd 1981), differential cross section data from Ohio (Annand 1985, Finlay 1984, and Rapaport 1978) and Michigan State University (DeVito 1979), and total cross section data (Larson 1980) to obtain a detailed and high accuracy data set for neutron elastic scattering from ^{208}Pb from 4.0 to 40.0 MeV. This comprehensive n+^{208}Pb data set has been described using the spherical optical model in which constant geometry fits, energy-dependent geometry fits, and fits incorporating the dispersion relation were performed.

Using a conventional constant geometry optical model, it was possible to obtain an excellent description of the entire n+^{208}Pb 4.0 to 40.0 MeV data set. While small systematic discrepancies in the fits occurred at backward angles of both the cross section and analyzing power data, the current constant geometry optical model potential represents a considerable improvement in quality of fit over the previous conventional n+^{208}Pb optical model work of Annand *et al.* (Annand 1985) and Finlay *et al.* (Finlay 1984).

In addition to the constant geometry potential obtained, an optical model potential in which the geometries of the real and imaginary central potentials varied linearly with energy was obtained and compared to the energy-dependent geometry potential of Annand *et al.* (Annand 1985). While a reduction in total χ^2 of approximately 6% to the 4.0 to 40.0 MeV n+^{208}Pb data set was achieved in these energy-dependent geometry fits in comparison to constant geometry fits, we are reluctant to introduce four new energy dependences into a model already laden with parameters.

In order to extrapolate the real central potential to negative energies and so further test energy dependences by comparing predicted single-particle bound state energies to experimentally reported values, we have also utilized the dispersion relation in analyzing the n+^{208}Pb data set. Using a simple, fixed geometry model, in which the Hartree-Fock potential had an exponential energy dependence, we were able to obtain a reasonable description of the 4.0 to 40.0 MeV n+^{208}Pb scattering data set and predict single-particle bound state energies that were in good agreement with experimental observations. In general, however, the present dispersion relation model is only a slight improvement over the n+^{208}Pb dispersion relation model reported by Johnson *et al.* (Johnson 1987). Both models are limited in the low-energy region (4.0 to 10.0 MeV), in that predicted differential cross sections do not fit the data well at large scattering angles.

Although the overall description of the elastic n+^{208}Pb scattering data was reasonably good using the various optical potentials, small systematic discrepancies remained at the backward angles for both the cross section and analyzing power, and no optical model solution based on conventional Woods-Saxon form factors was found which could describe all of the details seen in the scattering data. To relax the constraint of having a Woods-Saxon form factor, the real central part of the optical model potential was modified using a Fourier-Bessel expansion of the real central potential. Individual fits at 6.0, 7.0, 8.0, 9.0, and 10.0 MeV and fits to the combined 6.0 to 10.0 MeV ^{208}Pb data set were performed using a Fourier-Bessel expansion of the real central potential and compared to analyses using a conventional Woods-Saxon form factor.

In individual fits, improvements in χ^2 as large as a factor of 3.5 were observed when using a Fourier-Bessel description of the real central potential as opposed to a conventional Woods-Saxon form factor. However, in a Fourier-Bessel analysis of the combined 6.0 to 10.0 MeV n+^{208}Pb elastic scattering data set, in which the same energy-independent Fourier-Bessel term was added at each energy, improvements in χ^2 were small when compared to optical model analyses using conventional Woods-Saxon form factors, and radial distributions of the real central potentials deviated only slightly from Woods-Saxon shapes. Nevertheless, when the Fourier-Bessel method is applied to the real central potential, much better descriptions of n+^{208}Pb elastic scattering data can be obtained than in analyses performed when using only a Woods-Saxon form factor.

In addition to the ^{208}Pb data obtained, differential cross sections for elastic neutron scattering from ^{12}C and for inelastic neutron scattering from the first excited state of ^{12}C ($J^{\pi} = 2^{+}$, $Q = -4.439$ MeV) were measured at 11.01 and 13.76 MeV to provide a confirmation of the 11.05 and 13.75 MeV calibration data obtained at Physikalisch-Technische Bundesanstalt (PTB), Braunschweig, Federal Republic of Germany. These PTB results are in disagreement with the ^{12}C cross section evaluation reported in ENDF/B-V (Evaluated Nuclear Data File, Library B, Version V, National Neutron Cross Section Center, Brookhaven National Laboratory, USA) and call into question earlier data obtained at TUNL and Bruyères-le-Châtel. Legendre polynomial expansion coefficients were derived from fits to our data and compared to polynomial coefficients derived by PTB from their calibrated data. Our polynomial coefficients for elastic neutron scattering from ^{12}C are in close agreement with the PTB findings and indicate a possible need for revising the ENDF/B-V evaluation. However, our polynomial coefficients for inelastic neutron scattering from ^{12}C seem to disagree with the PTB results. A more accurate comparison of the ^{12}C differential cross section data can be made when the actual PTB data are released and can supplement the current Legendre polynomial coefficients.

APPENDIX A

DIFFERENTIAL CROSS SECTION TABULATIONS

Cross section data measured by the present author are tabulated in this appendix. Coefficients calculated from Legendre polynomial fits to the data and various parameters associated with the fits and experiment are also presented. The procedure for the data analysis is described in chapter IV. The following equation was used to fit the data:

$$\sigma(\theta,E) = \sum_{l=0}^{n} A_l(E)\cdot P_l(\cos\theta) \qquad \text{(A-1)}$$

$$= \frac{\sigma_{int}}{4\pi}\left[a_0 + \sum_{l=1}^{n} (2l+1)\cdot a_l(E)\cdot P_l(\cos\theta) \right]$$

where the parameters of the fits and symbols used in the tables are defined as follows:

l-Value - order of the Legendre polynomial in the expansion.

A_l - l^{th} coefficient $A_l(E)$ of the Legendre polynomial expansion.

ΔA_l - absolute uncertainty in the coefficient $A_l(E)$.

σ_{int} - integrated differential cross section over a 4π solid angle, obtained by integrating the fits to the cross section over 4π.

a_l - reduced expansion coefficients in ENDF/B-V form, defined to be:

$$a_0 = 1$$
$$a_l = A_l / A_0(2l+1)$$

Δa_l - absolute uncertainty in the reduced coefficient a_l.

θ_{lab} - experimental laboratory angle at which the center of the detector viewed the center of the sample.

$\sigma(\theta_{lab})$ - normalized differential cross section as measured in the laboratory, before corrections for multiple scattering, finite geometry, attenuation, and detector efficiency.

$\Delta\sigma_{lab}$ - absolute error of $\sigma(\theta_{lab})$. This error does not include uncertainties due to data normalization.

$\theta_{c.m.}$ - reaction angle in the center-of-mass system.

$\sigma(\theta_{c.m.})$ - corrected differential cross section in the center-of-mass system.

$\Delta\sigma_{c.m.}$ - absolute error of $\sigma(\theta_{c.m.})$. This error does not include uncertainties due to data normalization.

%Dev. - percentage deviation of the calculated cross section from the experimental value.

χ^2 - χ^2 per point for the calculation at that angle.

F-Test - integral probability

$$P_F(F,\gamma_1,\gamma_2) = \int_F^{\infty} P_f(f,\gamma_1,\gamma_2)df$$

where γ_1 and γ_2 are the respective degrees of freedom.

F-value -

$$\text{F-value} = F_\chi = \frac{\chi^2_{n-1} - \chi^2_n}{\chi^2_n}(N-n-1)$$

where N is the number of data points, and n is the number of terms in the fit.

The σ_T values for ^{12}C at 11.01 MeV and 13.76 MeV are from ENDF/B-V. The Pb total cross section value at 8.0 MeV is the energy averaged ^{nat}Pb value obtained from Larson *et al.* (Larson 1980). The calculated Wick's Limits and accompanying uncertainties are based on the σ_T values used. The zero degree cross sections are calculated from the fits to the data.

^{12}C NEUTRON ELASTIC SCATTERING CROSS SECTIONS

Neutron Energy ± Energy Spread	11.010 ± 0.118 MeV
Excitation Energy (J^{π})	0.000 MeV (0^{+})
Total Cross Section	1.396 ± 0.070 barns
Integrated Cross Section	0.735 ± 0.006 barns
Calculated Wick's Limit	604.480 ± 60.4 mb/sr
Zero Degree Cross Section	518.350 ± 3.57 mb/sr
Normalization Uncertainty	3.000 %
Chi-square/degree-of-freedom	0.761

l-Value	A_l	ΔA_l	a_l	Δa_l	F-Value	F-Test
0	58.47	0.495	1.00000	0.00000	20.000	0.472
1	104.89	1.309	0.59800	0.00746	0.503	0.473
2	130.02	1.769	0.44473	0.00605	2.711	0.474
3	129.73	1.780	0.31698	0.00435	22.483	0.475
4	69.28	1.580	0.13165	0.00300	131.983	0.476
5	21.19	1.187	0.03295	0.00185	162.311	0.478
6	4.77	0.774	0.00627	0.00102	36.671	0.479

Uncorrected			Corrected			Calculation		
θ_{lab}	$\sigma(\theta_{lab})$	$\Delta\sigma_{lab}$	$\theta_{c.m.}$	$\sigma(\theta_{c.m.})$	$\Delta\sigma_{c.m.}$	$\sigma(\theta_{c.m.})$	%Dev.	χ^2
20.0	314.29	2.23	21.8	363.55	9.80	369.08	-1.5	0.32
25.0	266.15	1.72	27.0	310.32	8.34	305.54	1.5	0.33
28.0	224.27	1.46	30.1	262.69	7.07	266.60	-1.5	0.31
30.0	208.58	1.38	32.2	245.17	6.61	240.99	1.7	0.40
35.0	153.06	1.09	37.4	181.15	4.93	180.23	0.5	0.03
40.0	106.29	0.82	42.6	126.98	3.50	126.96	0.0	0.00
50.0	40.71	0.29	52.9	49.39	1.39	50.56	-2.4	0.71
60.0	11.70	0.14	63.2	13.51	0.44	13.76	-1.8	0.30
65.0	7.07	0.11	68.8	7.10	0.26	6.84	3.7	1.03
70.0	5.95	0.10	74.7	6.21	0.23	6.25	-0.7	0.03
75.0	7.66	0.12	80.2	9.26	0.31	9.35	-0.9	0.07
80.0	10.59	0.14	85.2	13.30	0.42	13.59	-2.2	0.51
90.0	17.33	0.18	95.0	22.18	0.49	21.95	1.1	0.23
100.0	21.06	0.18	104.7	26.70	0.41	26.93	-0.9	0.31
110.0	22.09	0.20	114.4	28.00	0.32	27.52	1.7	2.24
120.0	19.05	0.18	123.9	24.38	0.27	24.61	-0.9	0.69
130.0	15.22	0.14	133.3	19.63	0.26	19.77	-0.7	0.29
140.0	11.71	0.15	142.7	14.76	0.28	14.65	0.7	0.14
150.0	9.32	0.14	152.0	10.76	0.27	10.58	1.7	0.46
159.0	7.98	0.16	160.3	8.15	0.26	8.28	-1.5	0.22

^{12}C NEUTRON INELASTIC SCATTERING CROSS SECTIONS

Neutron Energy ± Energy Spread	11.010 ± 0.118 MeV
Excitation Energy (J^{π})	-4.439 MeV (2^{+})
Integrated Cross Section	0.364 ± 0.002 barn
Zero Degree Cross Section	87.610 ± 1.13 mb/sr
Normalization Uncertainty	3.000 %
Chi-square/degree-of-freedom	0.735

l-Value	A_l	ΔA_l	a_l	Δa_l	F-Value	F-Test
0	28.940	0.194	1.00000	0.00000	19.000	0.473
1	17.017	0.409	0.19601	0.00471	2.139	0.474
2	27.907	0.515	0.19286	0.00356	167.581	0.475
3	9.806	0.571	0.04841	0.00282	98.159	0.476
4	3.942	0.698	0.01514	0.00268	43.476	0.478

Uncorrected			Corrected			Calculation		
θ_{lab}	$\sigma(\theta_{lab})$	$\Delta\sigma_{lab}$	$\theta_{c.m.}$	$\sigma(\theta_{c.m.})$	$\Delta\sigma_{c.m.}$	$\sigma(\theta_{c.m.})$	%Dev.	χ^2
20.0	81.26	0.70	22.5	71.03	1.99	73.64	-3.7	1.73
25.0	74.20	0.67	27.8	65.94	1.86	67.17	-1.9	0.44
28.0	68.77	0.61	31.1	61.53	1.74	62.99	-2.4	0.71
30.0	68.33	0.61	33.2	61.63	1.74	60.14	2.4	0.73
35.0	60.09	0.56	38.6	54.95	1.57	52.93	3.7	1.65
40.0	52.22	0.51	44.0	48.33	1.40	45.90	5.0	3.02
50.0	35.96	0.27	54.7	33.86	0.97	33.50	1.1	0.14
60.0	24.85	0.21	65.3	23.81	0.70	24.46	-2.7	0.87
65.0	21.65	0.19	70.6	21.00	0.62	21.32	-1.5	0.27
70.0	19.36	0.17	75.8	19.17	0.56	19.08	0.5	0.03
75.0	17.27	0.17	81.0	17.42	0.53	17.58	-0.9	0.10
80.0	16.00	0.18	86.2	16.68	0.51	16.75	-0.4	0.02
90.0	15.41	0.18	96.3	16.88	0.52	16.51	2.2	0.51
100.0	15.21	0.16	106.2	17.75	0.53	17.51	1.4	0.22
110.0	15.86	0.18	116.0	19.15	0.58	19.22	-0.4	0.02
120.0	17.36	0.18	125.5	21.11	0.65	21.41	-1.4	0.21
130.0	19.97	0.17	134.8	23.93	0.73	23.96	-0.1	0.00
140.0	22.34	0.20	144.0	26.37	0.83	26.73	-1.3	0.18
150.0	25.72	0.23	153.0	29.56	0.93	29.44	0.4	0.02
159.0	27.81	0.28	161.0	31.97	1.01	31.56	1.3	0.17

^{12}C NEUTRON ELASTIC SCATTERING CROSS SECTIONS

Neutron Energy ± Energy Spread	13.759 ± 0.091 MeV
Excitation Energy (J^{π})	0.000 MeV (0^+)
Total Cross Section	1.306 ± 0.065 barns
Integrated Cross Section	0.858 ± 0.007 barn
Calculated Wick's Limit	661.110 ±66.1 mb/sr
Zero Degree Cross Section	607.180 ± 4.62 mb/sr
Normalization Uncertainty	3.000 %
Chi-square/degree-of-freedom	0.796

l-Value	A_l	ΔA_l	a_l	Δa_l	F-Value	F-Test
0	68.30	0.575	1.00000	0.00000	19.000	0.473
1	114.50	1.509	0.55880	0.00737	0.464	0.474
2	143.38	2.117	0.41984	0.00620	0.099	0.475
3	140.63	2.208	0.29412	0.00462	4.768	0.476
4	102.19	2.216	0.16624	0.00360	248.741	0.478
5	28.84	1.742	0.03838	0.00232	55.332	0.479
6	9.33	1.195	0.01051	0.00135	61.105	0.480

Uncorrected			Corrected			Calculation		
θ_{lab}	$\sigma(\theta_{lab})$	$\Delta\sigma_{lab}$	$\theta_{c.m.}$	$\sigma(\theta_{c.m.})$	$\Delta\sigma_{c.m.}$	$\sigma(\theta_{c.m.})$	%Dev.	χ^2
20.0	365.25	2.78	21.7	438.39	11.91	420.72	4.0	2.20
25.0	286.16	2.19	26.9	346.48	9.45	342.56	1.1	0.17
28.0	240.08	2.17	30.0	291.88	8.12	295.28	-1.2	0.18
30.0	216.87	1.74	32.1	264.63	7.29	264.50	0.0	0.00
35.0	152.26	1.32	37.3	187.07	5.24	192.70	-3.0	1.15
40.0	103.43	0.98	42.5	128.08	3.68	131.60	-2.7	0.91
50.0	39.81	0.48	52.9	48.70	1.56	49.04	-0.7	0.05
60.0	15.51	0.27	63.7	16.32	0.65	15.92	2.5	0.38
65.0	13.22	0.27	69.4	14.15	0.58	13.71	3.1	0.55
70.0	14.12	0.19	74.8	16.39	0.57	16.94	-3.4	0.94
80.0	21.26	0.21	85.0	26.84	0.82	27.55	-2.7	0.77
90.0	27.93	0.36	94.8	35.54	1.02	34.78	2.1	0.57
100.0	27.80	0.24	104.6	35.32	0.65	35.19	0.4	0.04
110.0	24.11	0.39	114.2	30.51	0.59	30.02	1.6	0.68
120.0	18.01	0.19	123.8	22.41	0.27	22.55	-0.6	0.25
130.0	13.53	0.18	133.3	16.54	0.29	16.59	-0.3	0.03
140.0	12.39	0.28	142.9	15.63	0.48	15.42	1.3	0.19
150.0	15.08	0.19	152.3	20.29	0.50	20.05	1.2	0.24
159.0	19.37	0.23	160.5	26.91	0.69	27.33	-1.6	0.36

^{12}C NEUTRON INELASTIC SCATTERING CROSS SECTIONS

Neutron Energy ± Energy Spread	13.759 ± 0.091 MeV
Excitation Energy (J^{π})	-4.439 MeV (2^+)
Integrated Cross Section	0.177 ± 0.001 barn
Zero Degree Cross Section	36.90 ± 0.65 mb/sr
Normalization Uncertainty	3.000 %
Chi-square/degree-of-freedom	3.184

l-Value	A_l	ΔA_l	a_l	Δa_l	F-Value	F-Test
0	14.099	0.116	1.00000	0.00000	18.000	0.474
1	9.310	0.221	0.22011	0.00522	7.204	0.475
2	11.283	0.282	0.16005	0.00400	236.930	0.476
3	2.508	0.346	0.02541	0.00350	23.435	0.478
4	-0.298	0.403	-0.00235	0.00317	0.172	0.479

Uncorrected			Corrected			Calculation		
θ_{lab}	$\sigma(\theta_{lab})$	$\Delta\sigma_{lab}$	$\theta_{c.m.}$	$\sigma(\theta_{c.m.})$	$\Delta\sigma_{c.m.}$	$\sigma(\theta_{c.m.})$	%Dev.	χ^2
20.0	34.19	0.59	22.4	31.42	1.02	32.91	-4.8	2.15
25.0	31.35	0.53	27.7	28.74	0.93	30.95	-7.7	5.60
28.0	32.92	0.63	30.9	30.21	1.02	29.63	1.9	0.32
30.0	31.51	0.52	33.1	28.80	0.93	28.71	0.3	0.01
35.0	30.04	0.50	38.4	27.57	0.89	26.29	4.6	2.09
40.0	28.03	0.47	43.8	25.87	0.84	23.78	8.1	6.25
50.0	22.08	0.38	54.4	20.56	0.69	18.79	8.6	6.61
60.0	15.18	0.29	64.9	14.27	0.52	14.38	-0.8	0.04
65.0	12.54	0.28	70.1	11.97	0.47	12.57	-5.0	1.61
70.0	10.82	0.19	75.3	10.43	0.39	11.01	-5.6	2.21
80.0	8.48	0.16	85.7	8.38	0.32	8.87	-5.8	2.30
90.0	8.49	0.23	95.9	8.43	0.37	7.96	5.5	1.58
100.0	8.73	0.15	105.9	8.46	0.30	8.04	5.0	2.00
110.0	9.48	0.28	115.5	9.25	0.40	8.76	5.3	1.49
120.0	10.06	0.16	125.1	9.88	0.33	9.78	1.0	0.09
130.0	10.49	0.17	134.4	10.12	0.35	10.84	-7.1	4.29
140.0	11.46	0.27	143.7	11.08	0.44	11.76	-6.2	2.42
150.0	12.99	0.19	152.8	12.42	0.42	12.46	-0.3	0.01
159.0	14.30	0.21	160.8	13.73	0.45	12.88	6.2	3.51

^{208}Pb NEUTRON ELASTIC SCATTERING CROSS SECTIONS AT 8 MeV

Neutron Energy ± Energy Spread	7.970 ± 0.180 MeV
Excitation Energy (J^{π})	0.000 MeV (0^{+})
Total Cross Section	5.522 ± 0.276 barns
Integrated Cross Section	2.785 ± 0.030 barn
Calculated Wick's Limit	7391.550 ±739.2 mb/sr
Zero Degree Cross Section	6078.480±36.45 mb/sr
Normalization Uncertainty	3.000 %
Chi-square/degree-of-freedom	1.997

l-Value	A_l	ΔA_l	a_l	Δa_l	F-Value	F-Test
0	221.61	2.353	1.00000	0.00000	32.000	0.464
1	476.57	6.774	0.71683	0.01019	13.661	0.465
2	636.55	10.166	0.57447	0.00917	0.399	0.466
3	759.20	12.907	0.48940	0.00832	5.422	0.466
4	839.89	14.179	0.42110	0.00711	4.723	0.466
5	788.50	14.998	0.32346	0.00615	3.047	0.466
6	676.02	13.806	0.23465	0.00479	15.411	0.467
7	512.38	12.785	0.15414	0.00385	3.457	0.468
8	512.39	10.269	0.13601	0.00273	0.010	0.469
9	406.73	8.631	0.09660	0.00205	15.738	0.469
10	210.45	5.771	0.04522	0.00124	316.126	0.470
11	38.19	3.704	0.00749	0.00073	48.022	0.471

Uncorrected			Corrected			Calculation		
θ_{lab}	$\sigma(\theta_{lab})$	$\Delta\sigma_{lab}$	$\theta_{c.m.}$	$\sigma(\theta_{c.m.})$	$\Delta\sigma_{c.m.}$	$\sigma(\theta_{c.m.})$	%Dev.	χ^2
16.0	1952.70	19.23	16.0	3134.62	89.43	2965.53	5.4	3.57
20.0	1268.21	12.45	19.7	2062.62	59.51	1997.76	3.1	1.19
24.0	717.11	6.77	23.5	1164.29	34.44	1205.93	-3.6	1.46
28.0	392.99	3.56	27.3	626.23	19.23	650.52	-3.9	1.60
32.0	227.16	2.14	31.5	319.81	10.40	326.50	-2.1	0.41
34.0	186.04	0.87	33.7	245.04	7.74	244.91	0.1	0.00
36.0	163.30	1.49	36.0	210.54	6.99	206.71	1.8	0.30
40.0	149.18	1.26	40.2	205.63	6.60	199.02	3.2	1.00
45.0	138.32	0.86	45.1	204.00	6.18	199.92	2.0	0.44
50.0	99.81	0.80	49.6	152.64	4.74	159.92	-4.8	2.36
55.0	61.04	0.57	54.1	94.85	3.25	92.49	2.5	0.53
60.0	27.07	0.41	59.3	28.99	1.37	30.10	-3.8	0.66
65.0	30.80	0.39	66.2	37.29	1.62	35.56	4.6	1.14
70.0	60.90	0.60	71.0	92.72	3.12	88.51	4.5	1.82
75.0	86.15	0.70	75.5	131.04	3.99	138.38	-5.6	3.38
80.0	100.12	0.81	80.1	151.98	4.52	160.44	-5.6	3.51
85.0	93.51	0.74	84.8	142.01	4.24	143.95	-1.4	0.21
90.0	65.71	0.63	89.5	99.33	3.14	100.93	-1.6	0.26
95.0	40.57	0.38	94.2	58.11	2.00	54.58	6.1	3.11

Uncorrected			Corrected			Calculation		
θ_{lab}	$\sigma(\theta_{lab})$	$\Delta\sigma_{lab}$	$\theta_{c.m.}$	$\sigma(\theta_{c.m.})$	$\Delta\sigma_{c.m.}$	$\sigma(\theta_{c.m.})$	%Dev.	χ^2
100.0	22.23	0.24	99.5	24.85	1.00	24.27	2.3	0.33
105.0	19.30	0.28	105.4	22.53	0.94	23.66	-5.0	1.44
110.0	26.92	0.37	110.5	37.49	1.37	38.42	-2.5	0.47
115.0	36.37	0.44	115.2	52.47	1.75	51.14	2.5	0.58
120.0	40.91	0.46	120.0	59.09	1.91	55.65	5.8	3.25
125.0	36.28	0.44	124.8	51.82	1.70	51.81	0.0	0.00
130.0	30.98	0.40	129.7	43.52	1.48	43.22	0.7	0.04
135.0	22.58	0.33	134.5	31.14	1.12	33.37	-7.1	3.98
140.0	18.19	0.31	139.4	24.22	0.96	23.80	1.8	0.20
145.0	13.02	0.25	144.3	15.78	0.72	15.11	4.3	0.86
150.0	9.50	0.15	149.6	9.24	0.45	9.26	-0.3	0.00
155.0	10.85	0.23	155.4	12.64	0.63	13.03	-3.1	0.39
160.0	20.93	0.32	160.4	29.34	1.12	28.72	2.1	0.31

^{208}Pb NEUTRON INELASTIC SCATTERING CROSS SECTIONS AT 8 MeV

Neutron Energy ± Energy Spread	7.970 ± 0.180 MeV
Excitation Energy (J^{π})	-2.614 MeV (3^-)
Integrated Cross Section	0.093 ± 0.001 barn
Zero Degree Cross Section	8.040 ± 0.34 mb/sr
Normalization Uncertainty	3.000 %
Chi-square/degree-of-freedom	1.999

l-Value	A_l	ΔA_l	a_l	Δa_l	F-Value	F-Test
0	7.362	0.076	1.00000	0.00000	28.000	0.466
1	2.853	0.126	0.12918	0.00571	145.094	0.466
2	-0.354	0.189	-0.00962	0.00514	0.322	0.467
3	-1.824	0.241	-0.03540	0.00468	28.567	0.468

Uncorrected			Corrected			Calculation		
θ_{lab}	$\sigma(\theta_{lab})$	$\Delta\sigma_{lab}$	$\theta_{c.m.}$	$\sigma(\theta_{c.m.})$	$\Delta\sigma_{c.m.}$	$\sigma(\theta_{c.m.})$	%Dev.	χ^2
28.0	6.48	0.44	28.4	8.52	0.73	8.94	-4.9	0.33
32.0	7.01	0.41	32.3	9.10	0.63	9.13	-0.3	0.00
34.0	7.29	0.19	34.3	9.03	0.31	9.22	-2.1	0.40
36.0	7.42	0.34	36.3	9.17	0.53	9.31	-1.5	0.07
40.0	7.98	0.33	40.3	9.79	0.52	9.47	3.3	0.39
45.0	8.46	0.28	45.2	10.32	0.45	9.62	6.8	2.45
50.0	7.90	0.27	50.2	9.56	0.44	9.70	-1.6	0.12
55.0	9.24	0.27	55.2	11.08	0.43	9.71	12.4	10.06
60.0	7.56	0.29	60.1	9.03	0.46	9.63	-6.7	1.68
65.0	7.87	0.29	65.1	9.37	0.47	9.46	-1.0	0.04
70.0	6.50	0.30	70.1	7.86	0.47	9.20	-17.1	8.08
75.0	7.21	0.32	75.0	8.66	0.50	8.87	-2.4	0.17
80.0	6.36	0.30	80.0	7.64	0.47	8.47	-10.9	3.13
85.0	6.95	0.33	85.0	8.35	0.53	8.02	4.0	0.39
90.0	5.77	0.25	90.0	6.81	0.40	7.54	-10.7	3.34
95.0	6.39	0.23	95.0	7.53	0.38	7.05	6.3	1.58
100.0	6.15	0.18	100.0	7.16	0.29	6.58	8.1	4.06
105.0	5.54	0.22	105.0	6.42	0.35	6.14	4.3	0.63
110.0	5.85	0.23	109.9	6.64	0.37	5.75	13.3	5.71
115.0	4.40	0.21	114.9	5.03	0.34	5.43	-8.0	1.43
120.0	4.68	0.22	119.9	5.29	0.35	5.18	2.0	0.09
125.0	3.93	0.20	124.9	4.47	0.32	5.02	-12.2	2.93
130.0	4.22	0.22	129.9	4.75	0.35	4.94	-4.0	0.29
135.0	4.17	0.24	134.9	4.67	0.37	4.93	-5.6	0.49
140.0	4.26	0.22	139.9	4.73	0.36	4.99	-5.6	0.55
145.0	4.50	0.21	144.9	4.99	0.33	5.11	-2.3	0.11
150.0	4.83	0.15	149.8	5.39	0.25	5.26	2.5	0.28
155.0	4.85	0.25	154.7	5.45	0.40	5.42	0.5	0.00
160.0	5.31	0.25	159.6	6.03	0.41	5.59	7.4	1.19

APPENDIX B

ANALYZING POWER TABULATIONS

Analyzing power data measured by the present author and by Floyd (Floyd 1981) are tabulated in this appendix. Coefficients calculated from associated Legendre polynomial fits to the product of analyzing powers and differential cross sections and various parameters associated with the fits and experiment are also presented. The procedure for the data analysis is described in chapter IV. The following equation was used to fit the data:

$$A_y(\theta,E)\cdot\sigma(\theta,E) = \sum_{l=1}^{n} B_l(E)\cdot P_l^1(\cos\theta) \qquad \text{(B-1)}$$

where $\sigma(\theta)$ used in calculating the fits was determined from Legendre polynomial fits to $\sigma(\theta)$ data. Other parameters and symbols used in the tables are defined as follows:

l-value - order of the Legendre polynomial in the expansion.

B_l - l^{th} coefficient $B_l(E)$ of the associated Legendre polynomial expansion.

ΔB_l - absolute uncertainty in the coefficient $B_l(E)$.

Ratio - $B_l(E)/B_1(E)$

θ_{lab} - experimental laboratory angle at which the center of the detector viewed the center of the sample.

$A_y(\theta_{lab})$ - analyzing power as measured in the laboratory before corrections for multiple scattering, finite geometry, and attenuation.

ΔA_{ylab} - absolute error of $A_y(\theta_{lab})$. This error does not include normalization uncertainties.

$\theta_{c.m.}$ - scattering angle in the center-of-mass system.

$A_y(\theta_{c.m.})$ - corrected analyzing power in the center-of-mass system.

$\Delta A_{yc.m.}$ - absolute error of $A_y(\theta_{c.m.})$. This error does not include normalization uncertainties.

Dev. - absolute deviation of the calculated analyzing power from the experimental value.

χ^2 - χ^2 per point for the calculation at that angle.

F-Test - integral probability

$$P_F(F,\gamma_1,\gamma_2) = \int_F^\infty P_f(f,\gamma_1,\gamma_2)df$$

where γ_1 and γ_2 are the respective degrees of freedom.

F-value -

$$\text{F-value} = F_\chi = \frac{\chi^2_{n-1} - \chi^2_n}{\chi^2_n}(N-n-1)$$

where N is the number of data points, and n is the number of terms in the fit.

^{208}Pb NEUTRON ELASTIC SCATTERING ANALYZING POWERS AT 6 MeV

Neutron Energy ± Energy Spread	5.969 ± 0.353 MeV
Excitation Energy (J^{π})	0.000 MeV (0^+)
Normalization ± Calibration Error	1.000 ± 0.030
Chi-square/degree-of-freedom	0.927

l-Value	B_l	ΔB_l	Ratio	F-Value	F-Test
1	-19.9884	0.7425	1.0000	32.000	0.464
2	-4.2187	0.7101	0.2111	0.002	0.465
3	-0.5264	0.8098	0.0263	0.284	0.466
4	-5.8438	0.7851	0.2924	0.254	0.466
5	-7.7693	0.7784	0.3887	2.921	0.466
6	-2.9630	0.7271	0.1482	4.594	0.466
7	3.6186	0.6570	-0.1810	25.339	0.467
8	-5.8602	0.5511	0.2932	1.103	0.468
9	-6.5517	0.4773	0.3278	0.000	0.469
10	-6.1444	0.3655	0.3074	331.393	0.469
11	0.6440	0.2402	-0.0322	3.584	0.470

Uncorrected			Corrected			Calculation		
θ_{lab}	$A_y(\theta_{lab})$	ΔA_{ylab}	$\theta_{c.m.}$	$A_y(\theta_{c.m.})$	$\Delta A_{yc.m.}$	$A_y(\theta_{c.m.})$	Dev.	χ^2
16.0	-0.040	0.006	16.4	-0.046	0.007	-0.027	-0.019	7.86
20.0	-0.019	0.007	20.1	-0.023	0.007	-0.026	0.003	0.17
24.0	-0.017	0.008	23.9	-0.020	0.008	-0.020	0.000	0.00
28.0	0.007	0.010	27.7	0.007	0.011	-0.009	0.016	2.08
32.0	0.013	0.011	31.5	0.018	0.013	0.005	0.013	1.00
36.0	-0.017	0.018	35.4	-0.007	0.021	0.007	-0.014	0.45
40.0	-0.042	0.019	39.4	-0.027	0.024	-0.043	0.016	0.41
45.0	-0.240	0.023	44.4	-0.297	0.032	-0.269	-0.029	0.78
50.0	-0.472	0.030	49.5	-0.690	0.048	-0.630	-0.060	1.54
52.5	-0.511	0.036	52.0	-0.796	0.064	-0.774	-0.022	0.12
55.0	-0.422	0.035	54.5	-0.740	0.064	-0.824	0.084	1.73
60.0	-0.009	0.036	60.2	0.105	0.062	0.050	0.055	0.80
65.0	0.263	0.036	66.0	0.517	0.053	0.644	-0.127	5.66
70.0	0.232	0.027	70.8	0.301	0.034	0.277	0.025	0.52
75.0	0.015	0.024	75.5	0.021	0.027	-0.013	0.033	1.48
80.0	-0.217	0.023	80.2	-0.239	0.027	-0.213	-0.027	1.00
85.0	-0.336	0.020	85.0	-0.369	0.023	-0.355	-0.014	0.39
90.0	-0.351	0.029	89.7	-0.382	0.032	-0.453	0.071	4.91
95.0	-0.460	0.032	94.5	-0.511	0.038	-0.505	-0.006	0.03
100.0	-0.426	0.028	99.3	-0.498	0.037	-0.483	-0.014	0.15
105.0	-0.273	0.023	104.4	-0.326	0.035	-0.323	-0.003	0.01
110.0	-0.125	0.031	110.0	-0.085	0.047	-0.056	-0.029	0.37
115.0	-0.052	0.035	115.4	-0.032	0.047	-0.077	0.045	0.90
120.0	-0.082	0.016	120.4	-0.083	0.020	-0.099	0.016	0.66
125.0	-0.089	0.018	125.2	-0.084	0.022	-0.069	-0.015	0.51
130.0	-0.092	0.016	130.0	-0.086	0.019	-0.047	-0.038	4.20

Uncorrected			Corrected			Calculation		
θ_{lab}	$A_y(\theta_{lab})$	ΔA_{ylab}	$\theta_{c.m.}$	$A_y(\theta_{c.m.})$	$\Delta A_{yc.m.}$	$A_y(\theta_{c.m.})$	Dev.	χ^2
135.0	-0.038	0.029	134.8	-0.026	0.034	-0.070	0.044	1.72
140.0	-0.139	0.016	139.6	-0.144	0.019	-0.156	0.012	0.43
145.0	-0.250	0.026	144.3	-0.290	0.031	-0.316	0.027	0.74
149.0	-0.365	0.027	148.1	-0.480	0.035	-0.491	0.011	0.09
155.0	-0.182	0.023	154.6	-0.334	0.036	-0.305	-0.029	0.68
159.0	0.186	0.041	159.1	0.325	0.054	0.358	-0.033	0.38
164.0	0.393	0.022	164.0	0.514	0.028	0.471	0.043	2.32

^{208}Pb NEUTRON INELASTIC SCATTERING ANALYZING POWERS AT 6 MeV

Neutron Energy ± Energy Spread	5.969 ± 0.353 MeV
Excitation Energy (J^{π})	-2.620 MeV (3^-)
Normalization ± Calibration Error	1.000 ± 0.030
Chi-square/degree-of-freedom	0.696

l-Value	B_l	ΔB_l	Ratio	F-Value	F-Test
1	-1.1162	0.5802	1.0000	27.000	0.466
2	-0.3096	0.3653	0.2774	1.032	0.467

Uncorrected			Corrected			Calculation		
θ_{lab}	$A_y(\theta_{lab})$	ΔA_{ylab}	$\theta_{c.m.}$	$A_y(\theta_{c.m.})$	$\Delta A_{yc.m.}$	$A_y(\theta_{c.m.})$	Dev.	χ^2
32.0	0.055	0.166	32.4	0.071	0.208	-0.046	0.117	0.32
36.0	0.183	0.274	36.4	0.235	0.348	-0.050	0.285	0.67
40.0	-0.127	0.194	40.3	-0.159	0.248	-0.054	-0.105	0.18
45.0	-0.253	0.135	45.3	-0.315	0.170	-0.058	-0.257	2.28
50.0	-0.077	0.088	50.2	-0.094	0.112	-0.061	-0.033	0.09
52.5	-0.180	0.112	52.7	-0.220	0.139	-0.062	-0.158	1.28
55.0	-0.047	0.086	55.2	-0.055	0.108	-0.063	0.008	0.01
60.0	-0.092	0.088	60.2	-0.112	0.110	-0.065	-0.047	0.18
65.0	0.030	0.084	65.2	0.042	0.105	-0.065	0.108	1.05
70.0	-0.030	0.097	70.1	-0.032	0.124	-0.065	0.033	0.07
75.0	-0.034	0.153	75.1	-0.037	0.191	-0.064	0.027	0.02
85.0	-0.120	0.134	85.1	-0.147	0.170	-0.060	-0.087	0.26
90.0	-0.083	0.165	90.1	-0.099	0.206	-0.056	-0.043	0.04
95.0	-0.120	0.268	95.1	-0.146	0.335	-0.053	-0.093	0.08
100.0	-0.049	0.091	100.0	-0.057	0.115	-0.049	-0.008	0.01
105.0	0.001	0.059	105.0	0.007	0.075	-0.044	0.051	0.47
110.0	-0.040	0.075	110.0	-0.045	0.096	-0.040	-0.006	0.00
115.0	0.029	0.111	115.0	0.042	0.141	-0.035	0.077	0.30
120.0	0.034	0.045	119.9	0.048	0.056	-0.031	0.079	1.94
125.0	-0.141	0.069	124.9	-0.175	0.087	-0.026	-0.149	2.90
130.0	0.072	0.080	129.9	0.096	0.101	-0.022	0.118	1.36
135.0	-0.130	0.119	134.9	-0.162	0.153	-0.018	-0.144	0.89
140.0	-0.007	0.061	139.8	-0.005	0.076	-0.015	0.010	0.02
145.0	0.014	0.081	144.8	0.021	0.103	-0.012	0.033	0.10
149.0	-0.084	0.084	148.7	-0.102	0.106	-0.010	-0.092	0.76
155.0	-0.095	0.058	154.6	-0.118	0.074	-0.007	-0.111	2.26
159.0	-0.001	0.110	158.5	0.002	0.138	-0.005	0.007	0.00
164.0	-0.069	0.084	163.3	-0.085	0.108	-0.004	-0.082	0.57

^{208}Pb NEUTRON ELASTIC SCATTERING ANALYZING POWERS AT 7 MeV

Neutron Energy ± Energy Spread	6.967 ± 0.329 MeV
Excitation Energy (J^{π})	0.000 MeV (0^+)
Normalization ± Calibration Error	1.000 ± 0.030
Chi-square/degree-of-freedom	0.196

l-Value	B_l	ΔB_l	Ratio	F-Value	F-Test
1	-10.6990	0.5991	1.0000	32.000	0.464
2	1.9318	0.6049	-0.1806	0.072	0.465
3	7.7136	0.7056	-0.7210	0.408	0.466
4	5.5215	0.7141	-0.5161	0.634	0.466
5	5.9665	0.7248	-0.5577	0.149	0.466
6	6.8233	0.7261	-0.6377	0.351	0.466
7	9.5721	0.6577	-0.8947	43.548	0.467
8	-1.2533	0.5739	0.1171	7.791	0.468
9	-4.6173	0.4619	0.4316	0.499	0.469
10	-3.1120	0.3670	0.2909	35.355	0.469
11	1.5827	0.2897	-0.1479	67.490	0.470
12	-1.4928	0.1911	0.1395	42.196	0.471

Uncorrected			Corrected			Calculation		
θ_{lab}	$A_y(\theta_{lab})$	ΔA_{ylab}	$\theta_{c.m.}$	$A_y(\theta_{c.m.})$	$\Delta A_{yc.m.}$	$A_y(\theta_{c.m.})$	Dev.	χ^2
16.0	-0.005	0.007	16.3	-0.005	0.007	0.021	-0.025	11.64
20.0	0.043	0.011	20.0	0.047	0.011	0.035	0.012	1.05
24.0	0.078	0.011	23.8	0.086	0.012	0.056	0.030	6.65
28.0	0.084	0.009	27.6	0.094	0.009	0.083	0.011	1.38
32.0	0.074	0.013	31.5	0.094	0.015	0.104	-0.010	0.49
36.0	0.036	0.013	35.6	0.058	0.015	0.076	-0.018	1.45
40.0	-0.054	0.016	39.8	-0.059	0.019	-0.058	-0.001	0.00
45.0	-0.213	0.017	44.9	-0.257	0.020	-0.281	0.024	1.43
50.0	-0.419	0.017	49.6	-0.491	0.021	-0.470	-0.021	0.95
55.0	-0.516	0.022	54.2	-0.661	0.032	-0.688	0.027	0.71
60.0	-0.422	0.032	59.5	-0.906	0.068	-0.895	-0.011	0.03
62.5	-0.097	0.032	63.2	0.114	0.056	0.143	-0.030	0.28
65.0	0.185	0.027	66.3	0.437	0.040	0.407	0.030	0.54
70.0	0.183	0.022	71.0	0.228	0.025	0.230	-0.001	0.00
75.0	0.057	0.021	75.5	0.074	0.023	0.068	0.005	0.05
80.0	-0.078	0.015	80.2	-0.075	0.016	-0.075	0.001	0.00
85.0	-0.236	0.021	84.9	-0.246	0.023	-0.227	-0.019	0.70
90.0	-0.377	0.020	89.6	-0.405	0.023	-0.404	-0.001	0.00
95.0	-0.493	0.026	94.4	-0.573	0.032	-0.595	0.022	0.49
100.0	-0.490	0.029	99.3	-0.661	0.039	-0.660	-0.001	0.00
105.0	-0.089	0.029	104.8	-0.054	0.041	-0.040	-0.014	0.11
110.0	0.244	0.032	110.3	0.428	0.043	0.409	0.019	0.20
115.0	0.103	0.029	115.3	0.147	0.036	0.157	-0.011	0.09
120.0	-0.082	0.025	120.2	-0.099	0.029	-0.110	0.011	0.15
126.0	-0.219	0.028	126.0	-0.255	0.032	-0.233	-0.023	0.50

Uncorrected			Corrected			Calculation		
θ_{lab}	$A_y(\theta_{lab})$	ΔA_{ylab}	$\theta_{c.m.}$	$A_y(\theta_{c.m.})$	$\Delta A_{yc.m.}$	$A_y(\theta_{c.m.})$	Dev.	χ^2
131.5	-0.152	0.030	131.4	-0.164	0.034	-0.171	0.007	0.04
139.0	-0.052	0.032	138.5	-0.034	0.036	-0.052	0.019	0.27
145.4	-0.162	0.019	144.6	-0.162	0.023	-0.163	0.001	0.00
149.0	-0.329	0.031	148.0	-0.425	0.041	-0.404	-0.021	0.27
151.0	-0.359	0.035	150.1	-0.599	0.053	-0.606	0.008	0.02
155.0	-0.188	0.034	154.9	-0.414	0.051	-0.410	-0.003	0.00
159.0	0.301	0.036	159.4	0.482	0.049	0.445	0.037	0.56
164.0	0.444	0.021	164.1	0.557	0.025	0.571	-0.014	0.32

^{208}Pb NEUTRON INELASTIC SCATTERING ANALYZING POWERS AT 7 MeV

Neutron Energy ± Energy Spread	6.967 ± 0.329 MeV
Excitation Energy (J^{π})	-2.620 MeV (3^-)
Normalization ± Calibration Error	1.000 ± 0.030
Chi-square/degree-of-freedom	1.093

l-Value	B_l	ΔB_l	Ratio	F-Value	F-Test
1	0.1488	0.2520	1.0000	27.000	0.466
2	0.2651	0.1591	1.7812	2.540	0.467

Uncorrected			Corrected			Calculation		
θ_{lab}	$A_y(\theta_{lab})$	ΔA_{ylab}	$\theta_{c.m.}$	$A_y(\theta_{c.m.})$	$\Delta A_{yc.m.}$	$A_y(\theta_{c.m.})$	Dev.	χ^2
28.0	0.186	0.223	28.4	0.228	0.273	0.031	0.197	0.52
32.0	0.248	0.263	32.4	0.305	0.325	0.034	0.271	0.70
36.0	0.024	0.094	36.3	0.029	0.116	0.037	-0.007	0.00
40.0	-0.120	0.083	40.3	-0.147	0.102	0.039	-0.186	3.32
45.0	-0.051	0.072	45.2	-0.063	0.088	0.041	-0.103	1.38
50.0	0.031	0.055	50.2	0.038	0.067	0.042	-0.003	0.00
55.0	0.027	0.051	55.2	0.034	0.063	0.041	-0.008	0.01
60.0	0.087	0.056	60.2	0.109	0.069	0.040	0.068	0.96
62.5	0.101	0.068	62.6	0.125	0.083	0.040	0.085	1.05
65.0	0.071	0.064	65.1	0.088	0.080	0.038	0.050	0.39
70.0	-0.036	0.080	70.1	-0.042	0.098	0.035	-0.078	0.64
75.0	0.138	0.132	75.1	0.173	0.164	0.032	0.141	0.74
80.0	-0.006	0.135	80.1	-0.007	0.167	0.027	-0.034	0.04
85.0	-0.255	0.153	85.0	-0.312	0.189	0.021	-0.333	3.13
90.0	0.180	0.101	90.0	0.221	0.124	0.015	0.206	2.78
95.0	0.019	0.100	95.0	0.024	0.125	0.008	0.016	0.02
100.0	0.085	0.085	100.0	0.106	0.106	0.001	0.105	0.98
105.0	-0.173	0.086	105.0	-0.216	0.107	-0.006	-0.210	3.82
110.0	-0.112	0.096	109.9	-0.141	0.121	-0.013	-0.128	1.12
115.0	0.095	0.104	114.9	0.120	0.131	-0.020	0.140	1.15
120.0	-0.146	0.119	119.9	-0.182	0.149	-0.026	-0.155	1.08
126.0	-0.023	0.123	125.9	-0.028	0.155	-0.033	0.005	0.00
139.0	-0.051	0.133	138.8	-0.063	0.166	-0.041	-0.022	0.02
149.0	0.099	0.075	148.7	0.125	0.095	-0.040	0.165	3.05
151.0	-0.023	0.065	150.6	-0.028	0.083	-0.039	0.011	0.02
155.0	-0.061	0.073	154.6	-0.076	0.091	-0.036	-0.040	0.19
159.0	-0.138	0.143	158.5	-0.176	0.182	-0.033	-0.143	0.62
164.0	-0.102	0.098	163.3	-0.129	0.123	-0.027	-0.102	0.68

^{208}Pb NEUTRON ELASTIC SCATTERING ANALYZING POWERS AT 8 MeV

Neutron Energy ± Energy Spread	7.962 ± 0.361 MeV
Excitation Energy (J^{π})	0.000 MeV (0^{+})
Normalization ± Calibration Error	1.000 ± 0.030
Chi-square/degree-of-freedom	0.537

l-Value	B_l	ΔB_l	Ratio	F-Value	F-Test
1	-5.3071	0.5381	1.0000	32.000	0.464
2	0.7318	0.4119	-0.1379	1.696	0.465
3	4.6277	0.4360	-0.8720	0.036	0.466
4	5.9618	0.4012	-1.1234	0.026	0.466
5	8.3323	0.4155	-1.5700	2.847	0.466
6	6.9645	0.4381	-1.3123	0.034	0.466
7	9.4265	0.4027	-1.7762	33.562	0.467
8	-0.5680	0.3759	0.1070	9.905	0.468
9	-4.0222	0.3129	0.7579	4.503	0.469
10	-0.9054	0.2785	0.1706	12.199	0.469
11	1.7468	0.2403	-0.3291	67.059	0.470
12	-1.7494	0.1719	0.3296	47.825	0.471

Uncorrected			Corrected			Calculation		
θ_{lab}	$A_y(\theta_{lab})$	ΔA_{ylab}	$\theta_{c.m.}$	$A_y(\theta_{c.m.})$	$\Delta A_{yc.m.}$	$A_y(\theta_{c.m.})$	Dev.	χ^2
16.0	0.003	0.006	16.2	0.005	0.007	0.032	-0.027	16.01
20.0	0.044	0.007	19.9	0.047	0.008	0.051	-0.003	0.20
24.0	0.088	0.006	23.6	0.095	0.007	0.081	0.015	5.12
28.0	0.118	0.007	27.5	0.134	0.008	0.123	0.011	2.06
32.0	0.104	0.012	31.6	0.137	0.014	0.151	-0.014	1.05
36.0	0.026	0.014	36.0	0.037	0.016	0.056	-0.019	1.45
40.0	-0.083	0.014	40.3	-0.103	0.016	-0.099	-0.004	0.08
45.0	-0.181	0.014	45.1	-0.199	0.016	-0.212	0.013	0.68
50.0	-0.271	0.014	49.7	-0.285	0.016	-0.305	0.020	1.57
55.0	-0.422	0.019	54.2	-0.465	0.023	-0.452	-0.013	0.31
60.0	-0.457	0.029	59.3	-0.770	0.045	-0.751	-0.019	0.18
62.5	-0.260	0.029	62.9	-0.359	0.043	-0.342	-0.017	0.15
64.0	-0.047	0.031	65.0	0.105	0.043	0.079	0.026	0.39
69.0	0.172	0.027	70.1	0.231	0.032	0.221	0.010	0.10
75.0	0.120	0.019	75.5	0.139	0.021	0.126	0.013	0.39
80.0	0.002	0.023	80.1	0.011	0.024	0.026	-0.015	0.39
85.0	-0.126	0.022	84.8	-0.123	0.023	-0.108	-0.015	0.40
90.0	-0.309	0.022	89.5	-0.331	0.025	-0.307	-0.024	0.87
95.0	-0.452	0.025	94.2	-0.546	0.030	-0.595	0.049	2.62
100.0	-0.452	0.034	99.5	-0.709	0.047	-0.659	-0.050	1.14
106.0	0.325	0.024	106.4	0.538	0.032	0.508	0.029	0.80
113.0	0.266	0.030	113.3	0.325	0.034	0.400	-0.075	4.77
118.0	0.107	0.025	118.0	0.127	0.028	0.100	0.027	0.92
123.5	-0.194	0.025	123.3	-0.222	0.028	-0.230	0.007	0.07
128.0	-0.324	0.029	127.7	-0.380	0.033	-0.412	0.032	0.93

Uncorrected			Corrected			Calculation		
θ_{lab}	$A_y(\theta_{lab})$	ΔA_{ylab}	$\theta_{c.m.}$	$A_y(\theta_{c.m.})$	$\Delta A_{yc.m.}$	$A_y(\theta_{c.m.})$	Dev.	χ^2
131.5	-0.431	0.037	131.1	-0.505	0.041	-0.445	-0.060	2.12
138.0	-0.206	0.033	137.5	-0.243	0.038	-0.242	-0.001	0.00
145.5	-0.039	0.032	144.7	-0.013	0.040	-0.021	0.008	0.04
149.0	-0.072	0.043	148.4	-0.117	0.059	-0.147	0.030	0.27
150.0	-0.125	0.038	149.5	-0.226	0.052	-0.198	-0.029	0.30
154.5	0.074	0.054	154.7	0.063	0.074	0.050	0.013	0.03
159.0	0.358	0.032	159.3	0.472	0.040	0.481	-0.009	0.05
164.0	0.499	0.023	164.0	0.599	0.026	0.594	0.004	0.03

^{208}Pb NEUTRON INELASTIC SCATTERING ANALYZING POWERS AT 8 MeV

Neutron Energy ± Energy Spread	7.962 ± 0.361 MeV
Excitation Energy (J^{π})	-2.614 MeV (3^-)
Normalization ± Calibration Error	1.000 ± 0.030
Chi-square/degree-of-freedom	0.866

l-Value	B_l	ΔB_l	Ratio	F-Value	F-Test
1	0.4710	0.2214	1.0000	25.000	0.468
2	-0.0444	0.1333	-0.0943	0.136	0.469
3	0.0083	0.1104	0.0175	0.006	0.469

Uncorrected			Corrected			Calculation		
θ_{lab}	$A_y(\theta_{lab})$	ΔA_{ylab}	$\theta_{c.m.}$	$A_y(\theta_{c.m.})$	$\Delta A_{yc.m.}$	$A_y(\theta_{c.m.})$	Dev.	χ^2
28.0	0.073	0.115	28.5	0.086	0.138	0.021	0.066	0.23
32.0	0.094	0.093	32.4	0.111	0.112	0.023	0.088	0.62
36.0	0.069	0.049	36.4	0.080	0.059	0.025	0.055	0.89
40.0	0.027	0.086	40.3	0.030	0.102	0.027	0.003	0.00
45.0	-0.068	0.088	45.3	-0.082	0.103	0.029	-0.112	1.16
50.0	-0.054	0.066	50.3	-0.067	0.079	0.032	-0.099	1.58
55.0	-0.066	0.071	55.2	-0.082	0.084	0.034	-0.116	1.91
60.0	0.018	0.076	60.2	0.018	0.090	0.037	-0.018	0.04
62.5	0.033	0.085	62.7	0.036	0.101	0.038	-0.002	0.00
64.0	0.117	0.094	64.2	0.135	0.110	0.039	0.096	0.76
69.0	0.153	0.141	69.1	0.179	0.169	0.042	0.137	0.65
75.0	0.098	0.160	75.1	0.113	0.190	0.047	0.066	0.12
80.0	0.312	0.204	80.1	0.367	0.242	0.051	0.316	1.70
85.0	0.027	0.162	85.0	0.029	0.191	0.056	-0.027	0.02
90.0	0.094	0.130	90.0	0.108	0.156	0.061	0.047	0.09
95.0	0.090	0.094	95.0	0.104	0.112	0.066	0.037	0.11
100.0	0.290	0.111	100.0	0.346	0.134	0.072	0.274	4.16
106.0	0.009	0.059	105.9	0.007	0.072	0.079	-0.072	1.00
118.0	-0.033	0.111	117.9	-0.044	0.136	0.090	-0.133	0.96
128.0	-0.047	0.149	127.9	-0.062	0.184	0.090	-0.151	0.67
138.0	0.098	0.136	137.8	0.117	0.164	0.080	0.037	0.05
145.5	0.181	0.087	145.3	0.218	0.105	0.068	0.150	2.04
149.0	0.036	0.123	148.7	0.042	0.149	0.061	-0.019	0.02
150.0	0.049	0.087	149.7	0.059	0.105	0.059	-0.001	0.00
159.0	0.008	0.157	158.5	0.009	0.189	0.042	-0.033	0.03
164.0	-0.105	0.125	163.4	-0.126	0.151	0.032	-0.158	1.10

^{208}Pb NEUTRON ELASTIC SCATTERING ANALYZING POWERS AT 9 MeV

Neutron Energy ± Energy Spread	8.958 ± 0.345 MeV
Excitation Energy (J^{π})	0.000 MeV (0^+)
Normalization ± Calibration Error	1.000 ± 0.030
Chi-square/degree-of-freedom	0.017

l-Value	B_l	ΔB_l	Ratio	F-Value	F-Test
1	-5.4353	0.3365	1.0000	33.000	0.463
2	-6.2613	0.3223	1.1520	2.131	0.464
3	-4.3047	0.3273	0.7920	0.256	0.465
4	-1.5373	0.3229	0.2828	0.391	0.466
5	1.4487	0.3299	-0.2665	1.051	0.466
6	-0.1184	0.3394	0.0218	0.005	0.466
7	1.7645	0.3144	-0.3246	4.887	0.466
8	-4.2429	0.2868	0.7806	7.311	0.467
9	-6.8078	0.2442	1.2525	2.687	0.468
10	-3.6775	0.2150	0.6766	16.408	0.469
11	-0.8255	0.1718	0.1519	20.330	0.469
12	-2.9369	0.1034	0.5403	288.364	0.470

Uncorrected			Corrected			Calculation		
θ_{lab}	$A_y(\theta_{lab})$	ΔA_{ylab}	$\theta_{c.m.}$	$A_y(\theta_{c.m.})$	$\Delta A_{yc.m.}$	$A_y(\theta_{c.m.})$	Dev.	χ^2
16.0	-0.041	0.006	16.0	-0.046	0.007	-0.029	-0.017	6.07
20.0	-0.018	0.008	19.6	-0.023	0.008	-0.023	0.000	0.00
24.0	0.007	0.009	23.3	-0.002	0.010	0.004	-0.006	0.35
28.0	0.108	0.010	27.3	0.129	0.012	0.094	0.035	8.26
32.0	0.089	0.013	32.2	0.161	0.015	0.179	-0.019	1.46
36.0	-0.023	0.011	36.8	-0.036	0.013	-0.016	-0.020	2.58
40.0	-0.081	0.010	40.6	-0.091	0.011	-0.110	0.019	2.69
45.0	-0.166	0.011	45.1	-0.174	0.012	-0.181	0.008	0.40
50.0	-0.252	0.013	49.6	-0.261	0.014	-0.256	-0.004	0.10
55.0	-0.316	0.015	54.3	-0.354	0.018	-0.370	0.016	0.79
59.0	-0.301	0.021	58.7	-0.430	0.028	-0.429	-0.001	0.00
62.0	-0.159	0.017	62.5	-0.160	0.021	-0.137	-0.024	1.27
65.0	-0.011	0.014	65.9	0.036	0.017	0.054	-0.018	1.11
67.5	0.088	0.015	68.3	0.120	0.017	0.093	0.027	2.46
70.0	0.115	0.012	70.6	0.134	0.013	0.101	0.033	6.06
75.0	0.074	0.012	75.3	0.084	0.012	0.089	-0.004	0.12
80.0	0.023	0.011	80.0	0.034	0.012	0.050	-0.016	1.96
85.0	-0.049	0.011	84.7	-0.039	0.012	-0.033	-0.006	0.22
90.0	-0.184	0.013	89.5	-0.191	0.015	-0.191	0.001	0.00
98.0	-0.267	0.022	97.5	-0.411	0.027	-0.430	0.018	0.44
104.0	0.271	0.027	104.3	0.413	0.034	0.398	0.015	0.18
110.0	0.398	0.023	110.4	0.487	0.027	0.542	-0.055	4.34
115.0	0.249	0.012	115.2	0.281	0.014	0.289	-0.008	0.36
120.0	0.020	0.014	119.9	0.022	0.016	-0.015	0.037	5.50
125.0	-0.258	0.016	124.6	-0.289	0.019	-0.314	0.025	1.87

Uncorrected			Corrected			Calculation		
θ_{lab}	$A_y(\theta_{lab})$	ΔA_{ylab}	$\theta_{c.m.}$	$A_y(\theta_{c.m.})$	$\Delta A_{yc.m.}$	$A_y(\theta_{c.m.})$	Dev.	χ^2
130.0	-0.538	0.024	129.4	-0.631	0.029	-0.548	-0.083	8.10
135.0	-0.363	0.027	134.3	-0.500	0.034	-0.486	-0.013	0.16
140.0	0.150	0.023	139.6	0.265	0.029	0.258	0.007	0.06
145.0	0.336	0.021	144.8	0.484	0.026	0.459	0.025	0.89
149.0	0.117	0.033	148.8	0.132	0.041	0.135	-0.003	0.01
150.0	0.026	0.026	149.8	0.003	0.031	0.048	-0.045	2.07
155.0	-0.012	0.017	154.9	-0.110	0.022	-0.122	0.013	0.33
160.0	0.242	0.019	160.1	0.312	0.023	0.330	-0.018	0.62
164.0	0.441	0.021	164.0	0.543	0.024	0.522	0.021	0.76

^{208}Pb NEUTRON INELASTIC SCATTERING ANALYZING POWERS AT 9 MeV

Neutron Energy ± Energy Spread	8.958 ± 0.345 MeV
Excitation Energy (J^{π})	-2.614 MeV (3^-)
Normalization ± Calibration Error	1.000 ± 0.030
Chi-square/degree-of-freedom	1.359

l-Value	B_l	ΔB_l	Ratio	F-Value	F-Test
1	0.4041	0.1508	1.0000	28.000	0.466
2	-0.1454	0.0873	-0.3597	2.041	0.466

Uncorrected			Corrected			Calculation		
θ_{lab}	$A_y(\theta_{lab})$	ΔA_{ylab}	$\theta_{c.m.}$	$A_y(\theta_{c.m.})$	$\Delta A_{yc.m.}$	$A_y(\theta_{c.m.})$	Dev.	χ^2
36.0	0.008	0.079	36.4	0.007	0.092	0.004	0.004	0.00
40.0	0.120	0.074	40.4	0.136	0.086	0.005	0.131	2.32
45.0	0.116	0.077	45.3	0.133	0.091	0.008	0.125	1.87
50.0	0.099	0.067	50.3	0.110	0.077	0.011	0.099	1.66
55.0	0.051	0.061	55.2	0.055	0.071	0.015	0.039	0.31
59.0	0.004	0.082	59.2	0.001	0.095	0.019	-0.018	0.04
62.0	-0.105	0.067	62.2	-0.125	0.078	0.022	-0.147	3.57
65.0	0.099	0.074	65.1	0.112	0.086	0.025	0.087	1.01
67.5	-0.018	0.092	67.6	-0.024	0.106	0.028	-0.052	0.24
70.0	-0.034	0.084	70.1	-0.043	0.097	0.031	-0.074	0.58
75.0	-0.032	0.100	75.1	-0.041	0.116	0.037	-0.078	0.46
80.0	-0.117	0.163	80.1	-0.140	0.190	0.044	-0.184	0.94
85.0	-0.050	0.097	85.0	-0.061	0.113	0.051	-0.113	1.00
90.0	0.224	0.083	90.0	0.257	0.097	0.059	0.198	4.16
98.0	0.088	0.069	98.0	0.100	0.082	0.071	0.028	0.12
104.0	0.052	0.086	104.0	0.058	0.102	0.081	-0.022	0.05
110.0	-0.047	0.078	110.0	-0.058	0.093	0.089	-0.147	2.53
115.0	0.012	0.067	115.0	0.012	0.080	0.096	-0.084	1.09
120.0	-0.023	0.088	119.9	-0.029	0.105	0.102	-0.130	1.54
125.0	-0.075	0.093	124.9	-0.091	0.111	0.106	-0.197	3.15
130.0	-0.045	0.111	129.9	-0.056	0.133	0.109	-0.165	1.52
135.0	0.151	0.101	134.9	0.181	0.120	0.110	0.071	0.35
140.0	0.127	0.071	139.8	0.151	0.084	0.108	0.043	0.26
145.0	0.218	0.056	144.8	0.259	0.065	0.104	0.154	5.55
149.0	0.062	0.118	148.7	0.075	0.139	0.099	-0.024	0.03
150.0	0.191	0.073	149.7	0.228	0.086	0.098	0.130	2.28
155.0	0.068	0.061	154.6	0.083	0.072	0.088	-0.005	0.00
160.0	0.057	0.093	159.5	0.070	0.110	0.076	-0.005	0.00
164.0	0.021	0.127	163.3	0.029	0.148	0.064	-0.035	0.06

^{208}Pb NEUTRON ELASTIC SCATTERING ANALYZING POWERS AT 10 MeV

Neutron Energy ± Energy Spread	9.950 ± 0.441 MeV
Excitation Energy (J^π)	0.000 MeV (0^+)
Normalization ± Calibration Error	1.000 ± 0.030
Chi-square/degree-of-freedom	0.271

l-Value	B_l	ΔB_l	Ratio	F-Value	F-Test
1	-8.6539	0.3472	1.0000	51.000	0.461
2	-11.3075	0.3202	1.3066	8.051	0.461
3	-8.0708	0.3304	0.9326	0.301	0.461
4	-4.6118	0.3188	0.5329	0.533	0.461
5	-1.8130	0.2993	0.2095	3.891	0.461
6	-2.0335	0.3116	0.2350	0.027	0.461
7	-0.3121	0.2931	0.0361	1.344	0.461
8	-4.2046	0.2768	0.4859	33.012	0.461
9	-7.7709	0.2475	0.8980	4.823	0.461
10	-6.7679	0.2372	0.7821	24.342	0.461
11	-3.6499	0.2189	0.4218	0.481	0.462
12	-4.2215	0.2042	0.4878	147.100	0.463
13	-0.6413	0.1603	0.0741	12.488	0.463
14	-1.3143	0.1041	0.1519	63.583	0.463

Uncorrected			Corrected			Calculation		
θ_{lab}	$A_y(\theta_{lab})$	ΔA_{ylab}	$\theta_{c.m.}$	$A_y(\theta_{c.m.})$	$\Delta A_{yc.m.}$	$A_y(\theta_{c.m.})$	Dev.	χ^2
16.0	-0.090	0.008	15.9	-0.098	0.008	-0.058	-0.040	22.29
-----a)	-----a)	-----a)	18.8	-0.058	0.006	-0.058	0.000	0.00
20.0	-0.038	0.008	19.4	-0.046	0.009	-0.057	0.011	1.79
-----a)	-----a)	-----a)	20.6	-0.035	0.018	-0.052	0.017	0.88
24.0	0.017	0.013	22.9	0.007	0.014	-0.028	0.035	6.51
-----a)	-----a)	-----a)	24.4	-0.015	0.027	0.007	-0.023	0.71
28.0	0.073	0.017	27.5	0.166	0.021	0.164	0.002	0.01
30.0	0.078	0.017	30.6	0.179	0.022	0.173	0.006	0.07
-----a)	-----a)	-----a)	31.0	0.128	0.018	0.144	-0.016	0.74
32.0	0.003	0.014	33.2	-0.009	0.016	0.005	-0.014	0.77
-----a)	-----a)	-----a)	36.9	-0.073	0.018	-0.106	0.034	3.44
-----a)	-----a)	-----a)	40.8	-0.143	0.018	-0.160	0.017	0.86
42.5	-0.177	0.014	42.7	-0.186	0.015	-0.180	-0.006	0.18
-----a)	-----a)	-----a)	44.8	-0.208	0.014	-0.202	-0.006	0.18
47.5	-0.198	0.010	47.2	-0.204	0.011	-0.230	0.026	5.25
-----a)	-----a)	-----a)	49.0	-0.324	0.029	-0.255	-0.069	5.58
50.0	-0.232	0.012	49.5	-0.244	0.013	-0.263	0.019	2.31
52.5	-0.314	0.014	51.8	-0.342	0.016	-0.303	-0.039	5.62
-----a)	-----a)	-----a)	53.7	-0.364	0.026	-0.339	-0.024	0.91
55.0	-0.318	0.019	54.3	-0.376	0.022	-0.349	-0.027	1.50

a) denotes data measured by Floyd (Floyd 1983) for which uncorrected data are unavailable.

Uncorrected			Corrected			Calculation		
θ_{lab}	$A_y(\theta_{lab})$	ΔA_{ylab}	$\theta_{c.m.}$	$A_y(\theta_{c.m.})$	$\Delta A_{yc.m.}$	$A_y(\theta_{c.m.})$	Dev.	χ^2
57.5	-0.230	0.022	57.1	-0.312	0.027	-0.346	0.034	1.54
-----a)	-----a)	-----a)	60.4	-0.135	0.036	-0.148	0.013	0.13
62.0	-0.038	0.017	62.7	0.010	0.021	-0.007	0.017	0.65
-----a)	-----a)	-----a)	66.2	0.040	0.021	0.064	-0.024	1.26
-----a)	-----a)	-----a)	70.7	0.055	0.033	0.053	0.002	0.00
75.0	0.009	0.010	75.1	0.011	0.011	0.017	-0.006	0.26
-----a)	-----a)	-----a)	79.5	-0.035	0.038	-0.039	0.004	0.01
85.0	-0.116	0.014	84.6	-0.121	0.015	-0.130	0.008	0.28
-----a)	-----a)	-----a)	88.7	-0.213	0.040	-0.220	0.007	0.03
93.0	-0.186	0.024	92.4	-0.245	0.029	-0.273	0.028	0.99
95.0	-0.183	0.015	94.6	-0.261	0.019	-0.246	-0.015	0.66
-----a)	-----a)	-----a)	100.3	0.103	0.056	0.137	-0.034	0.37
105.0	0.312	0.023	105.4	0.378	0.027	0.326	0.052	3.89
110.0	0.250	0.017	110.3	0.285	0.019	0.316	-0.031	2.71
-----a)	-----a)	-----a)	110.3	0.320	0.043	0.315	0.005	0.02
-----a)	-----a)	-----a)	114.8	0.195	0.025	0.239	-0.044	3.04
115.0	0.260	0.020	115.0	0.300	0.022	0.235	0.064	8.43
-----a)	-----a)	-----a)	119.2	0.013	0.039	0.083	-0.070	3.19
120.0	0.023	0.015	119.7	0.048	0.017	0.061	-0.013	0.56
-----a)	-----a)	-----a)	123.8	-0.185	0.049	-0.226	0.041	0.68
125.0	-0.257	0.017	124.4	-0.276	0.019	-0.287	0.011	0.34
-----a)	-----a)	-----a)	128.6	-0.704	0.052	-0.744	0.040	0.60
130.0	-0.604	0.031	129.3	-0.813	0.040	-0.812	-0.001	0.00
-----a)	-----a)	-----a)	134.3	-0.674	0.068	-0.582	-0.091	1.78
-----a)	-----a)	-----a)	139.9	0.626	0.055	0.600	0.025	0.21
145.0	0.529	0.024	144.8	0.790	0.086	0.722	0.067	0.61
-----a)	-----a)	-----a)	144.9	0.706	0.029	0.715	-0.009	0.09
149.0	0.246	0.017	148.8	0.314	0.020	0.306	0.008	0.17
-----a)	-----a)	-----a)	149.4	0.208	0.045	0.216	-0.008	0.03
-----a)	-----a)	-----a)	154.5	-0.474	0.050	-0.393	-0.081	2.63
160.0	-0.076	0.015	159.9	-0.140	0.017	-0.151	0.011	0.38
164.0	0.251	0.013	163.8	0.300	0.015	0.304	-0.004	0.07

a) denotes data measured by Floyd (Floyd 1983) for which uncorrected data are unavailable.

^{208}Pb NEUTRON INELASTIC SCATTERING ANALYZING POWERS AT 10 MeV

Neutron Energy ± Energy Spread	9.950 ± 0.441 MeV
Excitation Energy (J^{π})	-2.615 MeV (3^-)
Normalization ± Calibration Error	1.000 ± 0.030
Chi-square/degree-of-freedom	1.254

l-Value	B_l	ΔB_l	Ratio	F-Value	F-Test
1	0.1140	0.1438	1.0000	22.000	0.470
2	0.3632	0.1022	3.1860	14.116	0.471
3	-0.0565	0.0746	-0.4957	0.458	0.472

Uncorrected			Corrected			Calculation		
θ_{lab}	$A_y(\theta_{lab})$	ΔA_{ylab}	$\theta_{c.m.}$	$A_y(\theta_{c.m.})$	$\Delta A_{yc.m.}$	$A_y(\theta_{c.m.})$	Dev.	χ^2
30.0	-0.074	0.174	30.5	-0.085	0.201	0.052	-0.137	0.47
32.0	0.140	0.080	32.5	0.160	0.092	0.054	0.106	1.33
42.5	-0.015	0.095	42.8	-0.017	0.108	0.063	-0.081	0.56
47.5	0.118	0.060	47.8	0.133	0.069	0.066	0.067	0.94
50.0	0.127	0.063	50.3	0.143	0.072	0.067	0.076	1.11
52.5	0.017	0.094	52.7	0.018	0.108	0.068	-0.050	0.22
55.0	0.051	0.095	55.2	0.057	0.109	0.069	-0.012	0.01
57.5	0.010	0.090	57.7	0.010	0.102	0.069	-0.059	0.33
62.0	-0.180	0.112	62.2	-0.208	0.128	0.068	-0.277	4.64
75.0	-0.029	0.079	75.1	-0.035	0.090	0.060	-0.095	1.12
85.0	0.010	0.071	85.0	0.009	0.081	0.044	-0.035	0.18
93.0	0.034	0.072	93.0	0.038	0.083	0.024	0.014	0.03
95.0	0.060	0.055	95.0	0.068	0.065	0.017	0.051	0.61
105.0	-0.042	0.082	105.0	-0.051	0.096	-0.022	-0.029	0.09
110.0	-0.019	0.057	110.0	-0.023	0.068	-0.045	0.022	0.10
115.0	-0.002	0.140	115.0	-0.004	0.165	-0.070	0.067	0.17
120.0	-0.032	0.080	120.0	-0.040	0.095	-0.096	0.056	0.35
125.0	-0.108	0.065	124.9	-0.128	0.076	-0.118	-0.010	0.02
130.0	-0.067	0.136	129.9	-0.081	0.160	-0.137	0.056	0.12
145.0	-0.180	0.061	144.8	-0.213	0.071	-0.152	-0.061	0.74
149.0	-0.200	0.060	148.7	-0.235	0.069	-0.145	-0.090	1.70
160.0	0.025	0.122	159.5	0.025	0.142	-0.107	0.133	0.87
164.0	0.247	0.105	163.3	0.283	0.122	-0.090	0.373	9.38

^{208}Pb NEUTRON ELASTIC SCATTERING ANALYZING POWERS AT 14 MeV

Neutron Energy ± Energy Spread	13.950 ± 0.441 MeV
Excitation Energy (J^{π})	0.000 MeV (0^{+})
Normalization ± Calibration Error	1.000 ± 0.030
Chi-square/degree-of-freedom	1.700

l-Value	B_l	ΔB_l	Ratio	F-Value	F-Test
1	-6.0260	0.4761	1.0000	29.000	0.466
2	-10.9852	0.6473	1.8230	0.353	0.466
3	-15.4011	0.6232	2.5558	5.162	0.466
4	-14.7509	0.8896	2.4479	3.847	0.467
5	-12.7817	0.7332	2.1211	7.764	0.468
6	-10.2241	1.0735	1.6967	0.055	0.469
7	-9.5782	0.7594	1.5895	2.722	0.469
8	-9.2771	1.0279	1.5395	0.036	0.470
9	-10.7608	0.7029	1.7857	0.780	0.471
10	-12.0664	0.8687	2.0024	0.798	0.472
11	-9.6331	0.5539	1.5986	68.868	0.473
12	-6.3779	0.6420	1.0584	0.165	0.474
13	-4.3265	0.3901	0.7180	5.607	0.475
14	-3.7891	0.4284	0.6288	45.487	0.476
15	-1.0599	0.2107	0.1759	7.607	0.478
16	-0.5256	0.2177	0.0872	2.477	0.479

Uncorrected			Corrected			Calculation		
θ_{lab}	$A_y(\theta_{lab})$	ΔA_{ylab}	$\theta_{c.m.}$	$A_y(\theta_{c.m.})$	$\Delta A_{yc.m.}$	$A_y(\theta_{c.m.})$	Dev.	χ^2
-----a)	-----a)	-----a)	18.2	-0.191	0.012	-0.175	-0.016	1.98
-----a)	-----a)	-----a)	19.9	-0.197	0.011	-0.202	0.005	0.24
-----a)	-----a)	-----a)	23.9	-0.297	0.010	-0.300	0.003	0.09
-----a)	-----a)	-----a)	30.0	-0.022	0.017	-0.005	-0.017	0.97
-----a)	-----a)	-----a)	33.5	-0.052	0.019	-0.063	0.011	0.33
-----a)	-----a)	-----a)	36.4	-0.087	0.009	-0.094	0.007	0.66
-----a)	-----a)	-----a)	40.2	-0.115	0.014	-0.120	0.005	0.12
-----a)	-----a)	-----a)	44.2	-0.144	0.013	-0.137	-0.007	0.33
-----a)	-----a)	-----a)	48.4	-0.156	0.024	-0.144	-0.011	0.23
-----a)	-----a)	-----a)	53.9	-0.038	0.036	-0.039	0.001	0.00
-----a)	-----a)	-----a)	61.0	0.325	0.031	0.299	0.026	0.72
-----a)	-----a)	-----a)	65.8	0.179	0.031	0.236	-0.057	3.46
-----a)	-----a)	-----a)	69.9	0.185	0.028	0.183	0.003	0.01
-----a)	-----a)	-----a)	74.1	0.126	0.037	0.100	0.026	0.50
-----a)	-----a)	-----a)	78.4	-0.015	0.057	-0.067	0.052	0.82
-----a)	-----a)	-----a)	83.4	-0.422	0.055	-0.396	-0.026	0.22
-----a)	-----a)	-----a)	93.1	0.676	0.049	0.692	-0.016	0.10
-----a)	-----a)	-----a)	95.9	0.690	0.050	0.634	0.057	1.26

a) denotes data measured by Floyd (Floyd 1983) for which uncorrected data are unavailable.

Uncorrected			Corrected			Calculation		
θ_{lab}	$A_y(\theta_{lab})$	ΔA_{ylab}	$\theta_{c.m.}$	$A_y(\theta_{c.m.})$	$\Delta A_{yc.m.}$	$A_y(\theta_{c.m.})$	Dev.	χ^2
-----a)	-----a)	-----a)	100.1	0.387	0.042	0.400	-0.013	0.09
-----a)	-----a)	-----a)	104.4	0.049	0.042	0.051	-0.002	0.00
-----a)	-----a)	-----a)	109.1	-0.473	0.049	-0.412	-0.061	1.54
-----a)	-----a)	-----a)	114.2	-0.488	0.062	-0.612	0.125	4.07
-----a)	-----a)	-----a)	119.3	-0.063	0.059	-0.009	-0.053	0.82
-----a)	-----a)	-----a)	124.4	0.544	0.075	0.574	-0.030	0.16
-----a)	-----a)	-----a)	130.0	0.173	0.065	0.130	0.043	0.44
-----a)	-----a)	-----a)	135.4	-0.311	0.053	-0.330	0.019	0.13
-----a)	-----a)	-----a)	140.0	-0.220	0.043	-0.120	-0.100	5.32
-----a)	-----a)	-----a)	144.2	0.205	0.035	0.127	0.078	4.93
-----a)	-----a)	-----a)	148.6	0.007	0.078	0.149	-0.143	3.37
-----a)	-----a)	-----a)	153.8	-0.761	0.047	-0.766	0.006	0.01

a) denotes data measured by Floyd (Floyd 1983) for which uncorrected data are unavailable.

APPENDIX C

COMPOUND NUCLEUS CONTRIBUTIONS

This appendix contains tabulations of the observed and shape elastic differential cross sections and the observed and shape elastic analyzing powers for elastic neutron scattering from ^{208}Pb at 6.0 and 7.0 MeV. Shape elastic analyzing powers ($A_y^{SE}(\theta)$) were calculated from observed analyzing powers ($A_y^{OBS}(\theta)$) using the observed ($\sigma^{OBS}(\theta)$) and shape elastic ($\sigma^{SE}(\theta)$) differential cross sections reported by Annand *et al.* (Annand 1985):

$$A_y^{SE}(\theta) = \frac{\sigma^{OBS}(\theta)}{\sigma^{SE}(\theta)} \cdot A_y^{OBS}(\theta) , \qquad \text{(C-1)}$$

where the observed differential cross section is the incoherent sum of the shape elastic and compound elastic cross sections:

$$\sigma^{OBS}(\theta) = \sigma^{SE}(\theta) + \sigma^{CE}(\theta) . \qquad \text{(C-2)}$$

The symbols used in the tables are defined as follows:

$\theta_{c.m.}$	-	reaction or scattering angle in the center-of-mass system.
$\sigma^{OBS}(\theta_{c.m.})$	-	observed or experimentally measured differential cross section at angle $\theta_{c.m.}$ in the center-of-mass system.
$\Delta\sigma^{OBS}(\theta_{c.m.})$	-	absolute error of $\sigma^{OBS}(\theta_{c.m.})$.
$\sigma^{SE}(\theta_{c.m.})$	-	shape elastic cross section at angle $\theta_{c.m.}$ in the center-of-mass system.
$\Delta\sigma^{SE}(\theta_{c.m.})$	-	absolute error of $\sigma^{SE}(\theta_{c.m.})$.
$\sigma^{CE}(\theta_{c.m.})$	-	compound elastic cross section at angle $\theta_{c.m.}$ in the center-of-mass system.

$A_y^{OBS}(\theta_{c.m.})$ - observed or experimentally measured analyzing power at angle $\theta_{c.m.}$ in the center-of-mass system.

$A_y^{SE}(\theta_{c.m.})$ - shape elastic analyzing power at angle $\theta_{c.m.}$ in the center-of-mass system.

For convenience, observed and shape elastic differential cross section values and uncertainties are reported to more digits than are significant. Observed and shape elastic cross section values are valid to three significant figures while uncertainties in the cross sections are valid to two significant figures.

^{208}Pb OBSERVED AND SHAPE ELASTIC NEUTRON SCATTERING CROSS SECTIONS AT 6 MeV

$\theta_{c.m.}$	$\sigma^{OBS}(\theta_{c.m.})$	$\Delta\sigma^{OBS}(\theta_{c.m.})$	$\sigma^{SE}(\theta_{c.m.})$	$\Delta\sigma^{SE}(\theta_{c.m.})$
10.1	6256.79	145.29	6245.27	145.26
12.6	5526.90	128.34	5516.23	128.36
15.1	4784.41	110.62	4774.68	110.63
17.6	3956.78	92.08	3947.98	92.07
20.1	3191.10	73.78	3183.18	73.79
25.1	1948.87	45.66	1942.47	45.67
30.1	1059.89	25.17	1054.59	25.17
35.2	516.87	12.83	512.31	12.83
40.2	240.05	6.56	235.98	6.56
45.2	121.98	3.75	118.28	3.75
50.2	66.09	2.43	62.69	2.43
55.2	32.18	1.49	29.01	1.49
60.2	21.01	1.17	18.00	1.17
62.7	22.97	1.21	20.02	1.21
65.3	35.25	1.63	32.34	1.63
70.3	72.23	2.53	69.39	2.53
75.3	112.45	3.42	109.68	3.42
80.3	144.49	4.05	141.79	4.05
85.3	151.82	4.24	149.17	4.24
90.3	128.47	3.64	125.84	3.64
95.3	92.05	2.82	89.40	2.82
100.3	51.30	1.75	48.59	1.75
105.3	26.05	1.12	23.27	1.12
107.8	22.81	1.02	20.00	1.02
110.3	19.25	0.81	16.41	0.81
112.8	21.35	0.92	18.47	0.92
115.3	27.92	1.23	25.01	1.23
120.2	45.44	1.68	42.42	1.68
125.2	63.90	2.16	60.71	2.16
130.2	85.84	2.64	82.42	2.64
135.2	93.68	2.79	89.95	2.79
140.2	82.47	2.51	78.37	2.51
145.2	58.98	1.95	54.38	1.95
150.1	35.87	1.33	30.52	1.33
152.6	28.78	1.04	22.93	1.04
155.1	26.06	0.98	19.60	0.98
157.6	31.88	1.17	24.71	1.17
159.9	40.40	1.51	32.49	1.51

^{208}Pb OBSERVED AND SHAPE ELASTIC NEUTRON SCATTERING CROSS SECTIONS AT 7 MeV

$\theta_{c.m.}$	$\sigma^{OBS}(\theta_{c.m.})$	$\Delta\sigma^{OBS}(\theta_{c.m.})$	$\sigma^{SE}(\theta_{c.m.})$	$\Delta\sigma^{SE}(\theta_{c.m.})$
10.1	5560.01	121.49	5557.19	121.48
12.1	4965.32	108.10	4962.69	108.09
15.1	4024.92	87.47	4022.60	87.45
18.1	3098.00	67.20	3095.98	67.21
20.1	2542.00	55.14	2540.17	55.15
25.1	1395.32	30.55	1393.87	30.55
30.1	687.16	15.30	685.97	15.30
35.2	340.51	7.86	339.48	7.86
40.2	208.92	5.01	207.99	5.01
42.7	175.20	4.32	174.32	4.32
45.2	156.42	3.90	155.58	3.90
50.2	101.03	2.72	100.26	2.72
55.2	47.56	1.55	46.84	1.55
57.7	25.98	1.00	25.28	1.00
60.2	15.59	0.73	14.91	0.73
62.7	14.76	0.73	14.09	0.73
65.3	25.52	1.04	24.86	1.04
67.8	44.37	1.50	43.72	1.50
70.3	70.42	2.03	69.78	2.03
75.3	123.45	3.13	122.82	3.13
80.3	153.54	3.73	152.93	3.73
85.3	149.32	3.61	148.72	3.61
90.3	112.31	2.78	111.71	2.78
95.3	69.11	1.84	68.51	1.84
100.3	33.90	1.05	33.29	1.05
102.8	25.44	0.88	24.82	0.88
105.3	20.94	0.81	20.31	0.81
107.8	22.66	0.90	22.02	0.90
110.3	26.97	1.02	26.33	1.02
115.3	39.67	1.38	39.01	1.38
120.2	52.87	1.65	52.18	1.65
125.2	59.54	1.73	58.82	1.73
130.2	61.99	1.79	61.21	1.79
135.2	59.05	1.70	58.20	1.70
140.2	49.60	1.50	48.67	1.50
145.2	34.34	1.13	33.30	1.13
150.1	17.07	0.75	15.87	0.75
152.6	12.40	0.54	11.08	0.54
155.1	12.45	0.54	10.99	0.54
157.6	17.89	0.77	16.25	0.77
159.9	28.93	1.03	27.10	1.03

^{208}Pb OBSERVED AND SHAPE ELASTIC NEUTRON SCATTERING ANALYZING POWERS AT 6 MeV

$\theta_{c.m.}$	$\sigma^{OBS}(\theta_{c.m.})$	$\sigma^{CE}(\theta_{c.m.})$	$\sigma^{SE}(\theta_{c.m.})$	$A_y^{OBS}(\theta_{c.m.})$	$A_y^{SE}(\theta_{c.m.})$
16.4	4319.37	9.35	4310.02	-0.046	-0.046
20.1	3247.32	7.96	3239.36	-0.023	-0.023
23.9	2271.01	6.73	2264.28	-0.020	-0.020
27.7	1476.59	5.75	1470.84	0.007	0.007
31.5	891.96	5.03	886.93	0.018	0.018
35.4	502.48	4.51	497.98	-0.007	-0.007
39.4	271.09	4.13	266.96	-0.027	-0.028
44.4	131.54	3.77	127.78	-0.297	-0.306
49.5	70.62	3.46	67.16	-0.690	-0.726
52.0	52.16	3.33	48.84	-0.796	-0.851
54.5	37.51	3.20	34.31	-0.741	-0.810
60.2	20.88	3.00	17.88	0.105	0.122
66.0	37.36	2.89	34.47	0.518	0.561
70.8	75.30	2.84	72.46	0.301	0.313
75.5	117.79	2.78	115.01	0.021	0.021
80.2	147.79	2.71	145.08	-0.239	-0.244
85.0	152.77	2.65	150.12	-0.369	-0.376
89.7	131.82	2.62	129.20	-0.382	-0.390
94.5	95.44	2.64	92.80	-0.511	-0.525
99.3	58.02	2.70	55.32	-0.498	-0.522
104.4	30.30	2.77	27.53	-0.326	-0.358
110.0	19.66	2.84	16.82	-0.085	-0.099
115.4	27.79	2.91	24.88	-0.032	-0.036
120.4	45.48	3.02	42.46	-0.083	-0.089
125.2	66.09	3.18	62.91	-0.085	-0.089
130.0	83.50	3.42	80.08	-0.086	-0.089
134.8	91.01	3.71	87.30	-0.026	-0.027
139.6	84.38	4.05	80.32	-0.144	-0.151
144.3	64.98	4.50	60.48	-0.290	-0.311
148.1	45.40	5.01	40.40	-0.480	-0.539
154.6	26.14	6.33	19.81	-0.334	-0.441
159.1	37.56	7.66	29.90	0.325	0.408
164.0	77.84	9.40	68.44	0.514	0.584

^{208}Pb OBSERVED AND SHAPE ELASTIC NEUTRON SCATTERING ANALYZING POWERS AT 7 MeV

$\theta_{c.m.}$	$\sigma^{OBS}(\theta_{c.m.})$	$\sigma^{CE}(\theta_{c.m.})$	$\sigma^{SE}(\theta_{c.m.})$	$A_y^{OBS}(\theta_{c.m.})$	$A_y^{SE}(\theta_{c.m.})$
16.3	3611.74	2.22	3609.52	-0.005	-0.005
20.0	2581.75	1.86	2579.89	0.046	0.047
23.8	1694.32	1.55	1692.77	0.086	0.086
27.6	1023.34	1.30	1022.03	0.094	0.094
31.5	577.59	1.13	576.46	0.094	0.094
35.6	324.76	1.01	323.75	0.058	0.058
39.8	210.69	0.93	209.76	-0.059	-0.059
44.9	153.95	0.85	153.09	-0.257	-0.258
49.6	109.18	0.79	108.39	-0.491	-0.494
54.2	59.65	0.73	58.92	-0.661	-0.669
59.5	17.79	0.68	17.11	-0.906	-0.942
63.2	15.48	0.66	14.82	0.114	0.119
66.3	32.80	0.65	32.15	0.437	0.446
71.0	80.40	0.64	79.76	0.228	0.230
75.5	129.17	0.63	128.54	0.074	0.074
80.2	156.99	0.62	156.37	-0.075	-0.075
84.9	151.02	0.60	150.42	-0.246	-0.247
89.6	117.07	0.59	116.48	-0.405	-0.407
94.4	73.73	0.60	73.13	-0.573	-0.577
99.3	38.48	0.61	37.87	-0.661	-0.672
104.8	22.29	0.63	21.66	-0.054	-0.055
110.3	26.85	0.64	26.21	0.428	0.438
115.3	38.98	0.66	38.32	0.147	0.149
120.2	50.80	0.68	50.12	-0.099	-0.100
126.0	60.61	0.73	59.87	-0.255	-0.258
131.4	63.45	0.80	62.66	-0.164	-0.166
138.5	54.27	0.90	53.36	-0.034	-0.034
144.6	34.82	1.02	33.80	-0.162	-0.167
148.0	22.88	1.12	21.76	-0.425	-0.447
150.1	16.99	1.20	15.80	-0.599	-0.644
154.9	12.47	1.45	11.02	-0.413	-0.468
159.4	25.73	1.79	23.94	0.482	0.518
164.1	58.57	2.21	56.36	0.557	0.578

LIST OF REFERENCES

Alarcon 1987	R. Alarcon, J. Rapaport, and R.W. Finlay, " Neutron Elastic Scattering from ^{40}Ca between 11 and 48 MeV," Nuclear Physics **A462** (1987) 413-444.
Annand 1985	J.R.M. Annand, R.W. Finlay, and F.S. Dietrich, "A Low-Energy Optical Model Analysis of ^{208}Pb and ^{209}Bi," Nuclear Physics **A443** (1985) 249-282.
Beyerle 1981	A.G. Beyerle, Jr., "Double Differential Continuum Neutron Scattering Cross Sections in Iron and Nickel for Incident Energies of 7.5, 10, and 12 MeV," Ph.D. Dissertation, North Carolina State University, 1981.
Byrd 1984	R.C. Byrd, C.E. Floyd, K. Murphy, P.P. Guss, and R.L. Walter, "The Analyzing Power for Neutron Scattering from ^{9}Be at 9 to 17 MeV," Nuclear Physics **A427** (1984) 36-60.
Clement 1985	H. Clement, "Fourier-Bessel Analysis of Polarized Deuteron Scattering," Lecture Notes in Physics **236** (Springer, Berlin 1985) 324-334.
DeVito 1979	R.P. DeVito, Ph.D. Dissertation, Michigan State University, 1979; R.P. DeVito, S.M. Austin, U.E.P. Berg, W. Sterrenberg, and L.E. Young, "Techniques for Measuring Neutron Scattering Cross Sections with a Beam Swinger," Nuclear Instruments and Methods **215** (1983) 423-430.
El-Kadi 1981	S.M. El-Kadi, "Neutron Elastic and Inelastic Scattering Studies on ^{54}Fe, ^{56}Fe, ^{63}Cu, and ^{65}Cu," Ph.D. Dissertation, Duke University, 1981.

El-Kadi 1982	S.M. El-Kadi, C.E. Nelson, F.O. Purser, R.L. Walter, A. Beyerle, C.R. Gould, and L.W. Seagondollar, "Elastic and Inelastic Scattering of Neutrons from ^{54,56}Fe, and ^{63,65}Cu (I). Measurements from 8 to 14 MeV and a Spherical Optical Model Analysis," Nuclear Physics **A390** (1982) 509-540.
Finlay 1984	R.W. Finlay, J.R.M. Annand, T.S. Cheema, and J. Rapaport, "Energy Dependence of Neutron Scattering from ^{208}Pb in the Energy Range 7-50 MeV," Physical Review **C30** (1984) 796-805.
Floyd 1981	C.E. Floyd, Jr., "Scattering of Polarized Fast Neutrons from ^{9}Be, ^{54}Fe, ^{65}Cu, and ^{208}Pb: The Determination of the Nucleon-Nucleus Spin-Orbit Interaction," Ph.D. Dissertation, Duke University, 1981.
Floyd 1983	C.E. Floyd, P.P. Guss, R.C. Byrd, K. Murphy, R.L. Walter, and J.P. Delaroche, "Spin-Orbit Potential Properties Derived from Measurements of Analyzing Powers for Neutron Scattering from ^{54}Fe and ^{65}Cu," Physical Review **C28** (1983) 1498-1503.
Friedman 1978	E. Friedman and C.J. Batty, "Method for Optical Model Analysis of Alpha-Nucleus Elastic Scattering," Physical Review **C17** (1978) 34-42.
Frois 1977	B. Frois, J.B. Bellicard, J.M. Cavedon, M. Huet, P. Leconte, P. Ludeau, A. Nakada, Phan Zuan Hô, and I. Sick, "High-Momentum-Transfer Electron Scattering from ^{208}Pb," Physical Review Letters **38** (1977) 152-155.
Goldberg 1975	D.A. Goldberg, "Improved Six-Parameter Alpha-Nucleus Optical Potentials," Physics Letters **55B** (1975) 59-62.
Gould 1981	C.R. Gould, L.G. Holzsweig, S.E. King, Y.C. Lau, R.V. Poore, N.R. Roberson, and S.A. Wender, "The XSYS Data Acquisition System at Triangle Universities Nuclear Laboratory," IEEE Transactions on Nuclear Science **NS-28** (1981) 3708-3714.

Guss 1982	P.P. Guss, "Elastic and Inelastic Neutron Scattering Cross Sections and Analyzing Powers for ^{58}Ni, ^{60}Ni, ^{116}Sn, and ^{120}Sn," Ph.D. Dissertation, Duke University, 1982.
Hodgson 1971	P.E. Hodgson, Nuclear Reactions and Nuclear Structure, (Clarendon Press, Oxford, 1971).
Hogue 1977	H.H. Hogue, "Elastic and Inelastic Scattering of Fast Neutrons by ^{6}Li, ^{7}Li, ^{9}Be, and ^{12}C," Ph.D. Dissertation, Duke University, 1977.
Hopkins 1971	J.C. Hopkins and G. Breit, "The ^{1}H(n,n)^{1}H Scattering Observables Required for High-Precision Fast-Neutron Measurements," Nuclear Data Tables **A9** (1971) 137-145.
Howell 1982	C.R. Howell and S.A. Wender, "A Linear Voltage Ramp Generator for a Three Stage Bunching System," Nuclear Instruments and Methods **195** (1982) 443-446.
Howell 1984	C.R. Howell, "Neutron Scattering from ^{28}Si and ^{32}S: Cross Sections and Analyzing Powers from 8 to 40 MeV," Ph.D. Dissertation, Duke University, 1984.
Johnson 1987	C.H. Johnson, D.J. Horen, and C. Mahaux, "Unified Description of the Neutron-^{208}Pb Mean Field between -20 and +165 MeV from the Dispersion Relation Constraint," Physical Review **C36** (1987) 2252-2273.
Larson 1980	D.C. Larson, D.M. Hetrick, and J.A. Harvey, "Comparison of the Neutron Total Cross Section Measurements with Optical Model Predictions from 2 to 80 MeV," Bulletin of the American Physical Society **25** (1980) 543; and private communication to R.L. Walter

Leeb 1985 H. Leeb, "Comparison of Model-Independent Optical Potential Analyses," Lecture Notes in Physics **236** (Springer, Berlin 1985) 269-282.

Lisowski 1973 P.W. Lisowski, "The Transfer Polarization of the D(d,n)^{3}He Reaction and the Scattering of Polarized Neutrons from ^{4}He and ^{3}He," Ph.D. Dissertation, Duke University, 1973.

Lisowski 1975 P.W. Lisowski, R.L. Walter, C.E. Busch, and T.B. Clegg, "Polarization Transfer in the ^{2}H(d,n)^{3}He Reaction at $\theta = 0°$," Nuclear Physics **A242** (1975) 298-308.

Mahaux 1987 C. Mahaux and R. Sartor, " Extrapolation from Positive to Negative Energy of the Woods-Saxon Parametrization of the n- ^{208}Pb Mean Field," Nuclear Physics **A468** (1987) 193-236.

Milner 1979 W.T. Milner, "Double-Drift Bunching Systems," IEEE Transactions on Nuclear Science **NS-26** (1979) 1445-1449.

Ohlsen 1973 G.G. Ohlsen and P.W. Keaton, Jr., "Techniques for Measurement of Spin-1/2 and Spin-1 Polarization and Analyzing Tensors," Nuclear Instruments and Methods **109** (1973) 41.

Pfützner 1987 H.G. Pfützner, "Cross Sections and Analyzing Powers for Nucleon Scattering from ^{6}Li and Proton Scattering for ^{27}Al," Ph.D. Dissertation, Duke University, 1987.

Rapaport 1978 J. Rapaport, T.S. Cheema, D.E. Bainum, R.W. Finlay, and J.D. Carlson, " Neutron Scattering from ^{208}Pb," Nuclear Physics **A296** (1978) 95-108.

Roberson 1981 N.R. Roberson and S.E. Edwards, "Interface for the TUNL VAX Data Acquisition Facility," IEEE Transactions on Nuclear Science **NS-28** (1981) 3834-3837.

Satchler	G.R. Satchler, Direct Nuclear Reactions, (Oxford Press, New York, 1983).
Schutt 1988	R.L. Schutt, R.E. Shamu, P.W. Lisowski, M.S. Moore, and G.L. Morgran, "Nucleon Scattering from ^{208}Pb at Low and Intermediate Energies," Physics Letters B **203** (1988) 22-25.
Schwandt 1982	P. Schwandt, H.O. Meyer, W.W. Jacobs, A.D. Bacher, S.E. Vigdor, M.D. Kaitchuck, and T.R. Donoghue, "Analyzing Power of Proton-Nucleus Elastic Scattering between 80 and 180 MeV," Physical Review **C26** (1982) 55-64.
Tornow 1988	W. Tornow, C.R. Howell, M.L. Roberts, P.D. Felsher, Z.M. Chen, R.L. Walter, G. Mertens, and I. Slaus, "Low-Energy Neutron-Proton Analyzing Power and the New Bonn Potential and Paris Potential Predictions," Physical Review **C37** (1988) 2326-2331.
Tornow 1982	W. Tornow, E. Woye, G. Mack, C.E. Floyd, K. Murphy, P.P. Guss, S.A. Wender, R.C. Byrd, R.L. Walter, T.B. Clegg, and H. Leeb, "Analyzing Power and Differential Cross Section at 9.9, 11.9, and 13.9 MeV for Ca(n,n)," Nuclear Physics **A385** (1982) 373-406.

BIOGRAPHY

Mark L. Roberts

Born: Springfield, Missouri
August 12, 1960

Education: B. S. North Carolina State University,
Raleigh, North Carolina, 1982

M. A. Duke University,
Durham, North Carolina, 1984

Positions: Research Assistant, Duke University, 1983-1988
Teaching Assistant, Duke University, 1982-1983

Memberships: American Physical Society
Sigma Pi Sigma

PUBLICATIONS

1. "Rigorous Calculations and Measurements of $A_y(\theta)$ for n+d Elastic-Scattering and Breakup Processes," C.R. Howell, W. Tornow, I. Slaus, P.D. Felsher, M.L. Roberts, H.G. Pfützner, Anli Li, K. Murphy, R.L. Walter, J.M. Lambert, P.A. Treado, H. Witala, W. Glöckle, and T. Cornelius, Physical Review Letters **61** (1988) 1565-1568.

2. "Low-Energy Neutron-Proton Analyzing Power and the New Bonn Potential and Paris Potential Predictions," W. Tornow, C.R. Howell, M.L. Roberts, P.D. Felsher, Z.M. Chen, R.L. Walter, G. Mertens, and I. Slaus, Physical Review **C37** (1988) 2326-2331.

3. "Analysing power for $^{12}C(n,n_{0,1})^{12}C$ and Evaluation of n-^{12}C Scattering at 18.2 MeV," W. Tornow, C.R. Howell, H.G. Pfützner, M.L. Roberts, P.D. Felsher, Z.M. Chen, M. AlOhali, G.J. Weisel, R.L. Walter, and A.A. Naqvi, Journal Physics G: Nuclear Physics **14** (1988) 49-64.

4. "Search for a Purported Resonance in ^{13}C at 20 MeV via Analyzing Power Measurements of $^{12}C(n,n)$," W. Tornow, C.R. Howell, H.G. Pfützner, M.L. Roberts, P.D. Felsher, Z.M. Chen, and R.L. Walter, Physical Review **C35** (1987) 1578-1580.

5. "Comparisons of Vector Analyzing Power Data and Calculations for Neutron-Deuteron Elastic Scattering from 10 to 14 MeV," C.R. Howell, W. Tornow, K. Murphy, H.G. Pfützner, M.L. Roberts, Anli Li, P.D. Felsher,

R.L. Walter, I. Slaus, P.A. Treado, and Y. Koike, Few-Body Systems **2** (1987) 19.

CONTRIBUTED ABSTRACTS / TALKS PRESENTED

1. "Neutron Scattering of 6 to 10 MeV Neutrons from ^{208}Pb," M.L. Roberts, W. Tornow, C.R. Howell, P.D. Felsher, G.J. Weisel, M.A. AlOhali, K. Murphy, H.G. Pfützner, Z.M. Chen, and R.L. Walter, Bulletin of the American Physical Society **33** (1988) 1061.

2. "New Ion Beam Pulsing System at TUNL," M.L. Roberts, C.R. Howell, T.B. Clegg, D. Pierce, and C.R. Westerfeldt, Bulletin of the American Physical Society **31** (1986) 1764.

3. "Neutron Scattering from ^{12}C at 11.0 and 13.8 MeV," M.L. Roberts, H.G. Pfützner, A.A. Naqvi, K. Murphy, Anli Li, C.R. Howell, and R.L. Walter, Bulletin of the American Physical Society **31** (1986) 854.

CO-AUTHORED ABSTRACTS

1. "Analyzing Power Data for Neutron Scattering from ^{209}Bi at 6 and 9 MeV," G.J. Weisel, W. Tornow, C.R. Howell, M.L. Roberts, P.D. Felsher, M.A. AlOhali, J.M. Hanly, R.L. Walter, and G. Mertens, Bulletin of the American Physical Society **33** (1988) 2195.

2. "Measurements of Polarization Observables for d-p and d-n Quasifree Scattering in the d+d System," C.R. Howell, W. Tornow, P.D. Felsher, I. Slaus, J.M. Hanly, M.L. Roberts, G. Weisel, M. AlOhali, R.L. Walter, G. Mertens, J.M. Lambert, and P.A. Treado, Bulletin of the American Physical Society **33** (1988) 1101.

3. "Experimental Techniques for Measuring Polarization Observables in the d+d→d+p+n Breakup Reaction at Low Energies," P.D. Felsher, C.R. Howell, W. Tornow, M.L. Roberts, I. Slaus, R.L. Walter, J.M. Lambert, and P.A. Treado, Bulletin of the American Physical Society **33** (1988) 1100.

4. "Measurements and Rigorous Calculations of $A_y(\theta)$ for n+d Elastic Scattering and Breakup Processes," W. Tornow, C.R. Howell, I. Slaus, P.D. Felsher, M.L. Roberts, K. Murphy, H.G. Pfützner, R.L. Walter, H. Witala, W. Glöckle, T. Cornelius, J.M. Lambert, and P.A. Treado, Bulletin of the American Physical Society **33** (1988) 1100.

5. "Search for a Narrow Resonance in the n-^{12}C System via Analyzing Power Measurements with 16 MeV Neutrons," W. Tornow, C.R. Howell, H.G. Pfützner, M.L. Roberts, P.D. Felsher, Z. Chen, and R.L. Walter, Bulletin of the American Physical Society **31** (1986) 1238.

6. "Comparison Between Predictions and Preliminary Data of 7-MeV Analyzing Power for ^{208}Pb," D.J. Horen, C.H. Johnson, M.L. Roberts, C.R. Howell, W.

Tornow, R.L. Walter, Z. Chen, K. Murphy, H.G. Pfützner, and P.D. Felsher, Bulletin of the American Physical Society **31** (1986) 1237.

7. "Extension of the Capability of $A_y(\theta)$ Measurements for Neutron Scattering to 19 MeV at TUNL," C.R. Howell, W. Tornow, M.L. Roberts, P.D. Felsher, H.G. Pfützner, A.A. Naqvi, Z. Chen, and R.L. Walter, Bulletin of the American Physical Society **31** (1986) 1225.

8. "Vector Analyzing Powers for n-d Elastic Scattering from 10 to 14 MeV," C.R. Howell, W. Tornow, I. Slaus, P.A. Treado, K. Murphy, H.G. Pfützner, M.L. Roberts, P.D. Felsher, and R.L. Walter, Bulletin of the American Physical Society **31** (1986) 854.

9. "A Study of the n-d Breakup Reaction with Polarized Neutrons," C.R. Howell, I. Slaus, W. Tornow, P.A. Treado, H.G. Pfützner, Anli Li, M.L. Roberts, K. Murphy, P.D. Felsher, A. Naqvi, and R.L. Walter, Bulletin of the American Physical Society **30** (1985) 1267.

10. "Analyzing Powers for Elastic Neutron Scattering from ^{27}Al," Ph. Martin, H.G. Pfützner, Anli Li, M.L. Roberts, B. Smith, C.R. Howell, and R.L. Walter, Bulletin of the American Physical Society **30** (1985) 1268.

11. "Vector Analyzing Power Data and Calculations for Nucleon-Deuteron Elastic Scattering from 10 to 14 MeV," W. Tornow, C.R. Howell, K. Murphy, H.G. Pfützner, M.L. Roberts, Anli Li, P.D. Felsher, and R.L. Walter, Proceedings of the International Symposium on the Three-Body Force in the Three Nucleon System (1985) 251-254.

12. "Vector Analyzing Powers for the n+d Breakup Reaction," C.R. Howell, I. Slaus, W. Tornow, P.A. Treado, H.G. Pfützner, Anli Li, M.L. Roberts, K. Murphy, P.D. Felsher, and R.L. Walter, Journal of the Physical Society of Japan **55** supplement, (1985) 866.

13. "Analyzing Power Measurements for Neutron Elastic Scattering from ^{14}N," Anli Li, H.G. Pfützner, M.L. Roberts, C.R. Howell, K. Murphy, and R.L. Walter, Journal of the Physical Society of Japan **55** supplement, (1985) 564.

14. "Measurements of $A_y(\theta)$ for Neutron and Proton Elastic Scattering from ^{6}Li between 5 and 17 MeV Compared to Resonating Group Calculations, H.G. Pfützner, Anli Li, K. Murphy, C.R. Howell, M.L. Roberts, I. Slaus, R.L. Walter, M. Herman, and H.M. Hofmann, Journal of the Physical Society of Japan **55** supplement, (1985) 556.

15. "Analyzing Powers for Elastic Neutron Scattering from ^{14}N and ^{16}O," Anli Li, C.R. Howell, R.K. Murphy, H.G. Pfützner, M.L. Roberts, and R.L. Walter, Bulletin of the American Physical Society **30** (1985) 797.

16. "Nucleon Scattering from ^{11}B," K. Murphy, C.R. Howell, H.G. Pfützner, M.L. Roberts, Anli Li, and R.L. Walter, Bulletin of the American Physical Society **30** (1985) 796.

17. "Analyzing Powers for Elastic and Inelastic Neutron Scattering from ^{6}Li," H.G. Pfützner, Anli Li, C.R. Howell, M.L. Roberts, I. Slaus, and R.L. Walter, Bulletin of the American Physical Society **29** (1984) 1036.

18. "Differential Cross Section and Analyzing Power for the Scattering of 17 MeV Neutrons from ^{54}Fe and ^{58}Ni," R.S. Pedroni, C.R. Howell, G.M. Honoré, H.G. Pfützner, M.L. Roberts, R.C. Byrd, and R.L. Walter, Bulletin of the American Physical Society **28** (1983) 998.